Croissance latérale MPCVD de diamant en homoépitaxie pour dispositifs électroniques de puissance

Fernando Lloret Vieira

Communauté
UNIVERSITÉ Grenoble Alpes

UCA | Universidad de Cádiz

THÈSE

Pour obtenir le grade de

DOCTEUR DE LA COMMUNAUTE UNIVERSITE GRENOBLE ALPES

préparée dans le cadre d'une cotutelle *entre la Communauté Université Grenoble Alpes* et la *Universidad de Cádiz*

Spécialité : **Physique, Physique des Matériaux**

Arrêté ministériel : le 6 janvier 2005 - 7 août 2006

Présentée par

« Fernando LLORET VIEIRA »

Thèse dirigée par **« Etienne BUSTARRET »** et **« Daniel ARAÚJO »**

préparée au sein des **Institut Néel-CNRS, Grenoble, et Universidad de Cádiz**
dans **les Écoles Doctorales de Physique et ED UCA**

Croissance latérale MPCVD de diamant en homoépitaxie pour dispositifs électroniques de puissance

Thèse soutenue publiquement le **15 juin 2017**,
devant le jury composé de :

M. François SILVA
Ingénieur de recherche, LPICM – CNRS Paris-Saclay, Rapporteur
M. Ken HAENEN
Professeur des universités, Hasselt University, Belgique, Rapporteur
Mme. Isabelle BERBEZIER
Directrice de recherche, IM2NP Marseille, Examinatrice
Mme. M.Pilar VILLAR
Maître de conférence, Universidad de Cádiz, Espagne, Examinatrice
Mme. Catherine BOUGEROL
Directrice de recherche, Institut Néel – CNRS Grenoble, Présidente
M. David EON
Maître de conférences, Institut Néel – CNRS Grenoble, Examinateur

Communauté
UNIVERSITÉ Grenoble Alpes

UCA | Universidad de Cádiz

TESIS

Para la obtención del título de

DOCTOR POR LA COMMUNAUTE UNIVERSITE GRENOBLE ALPES Y LA UNIVERSIDAD DE CADIZ

Preparada en el marco de cotutela entre la *Communauté Université Grenoble Alpes* y la *Universidad de Cádiz*

Physique, Physique des Matériaux y Doctor en Ciencias

Presentada por

« Fernando LLORET VIEIRA »

Tesis supervisada por **« Etienne BUSTARRET »** y **« Daniel ARAÚJO »**

Preparada en el seno del **Institut Néel-CNRS, Grenoble,** y la **Universidad de Cádiz**
en las **Écoles Doctorales de Physique** y **ED UCA**

Crecimiento lateral MPCVD de diamante homoepitaxial para dispositivos electrónicos de potencia

Tesis defendida públicamente el **15 de junio del 2017**,
frente al tribunal compuesto por:

D. François SILVA
Investigador Senior, LPICM – CNRS, Francia Informador
D. Ken HAENEN
Catedrático de Universidad, Hasselt University, Belgica, Informador
Dña. Isabelle BERBEZIER
Profesora de Investigación, IM2NP Marseille, Francia Examinadora
Dña. M.Pilar VILLAR
Profesora Titular de Universidad, Universidad de Cádiz, España, Examinadora
Dña. Catherine BOUGEROL
Profesora de investigación, Institut Néel – CNRS, Francia, Presidenta
D. David EON
Profesor Titular de Universidad, Institut Néel – CNRS, Francia, Examinador

Communauté
UNIVERSITÉ Grenoble Alpes

UCA | Universidad de Cádiz

THESIS

To obtain the degree of

PHD FROM COMMUNAUTE UNIVERSITE GRENOBLE ALPES AND UNIVERSIDAD DE CADIZ

prepared within the framework of a cotutelle between the *Communauté Université Grenoble Alpes* and the *Universidad de Cádiz*

Physique, Physique des Matériaux and Doctor en Ciencias

Presented by

« Fernando LLORET VIEIRA »

Thesis supervised by **« Etienne BUSTARRET »** and **« Daniel ARAÚJO »**

Prepared within the **Institut Néel-CNRS, Grenoble,** and **Universidad de Cádiz**
in the **Écoles Doctorales de Physique** and **ED UCA**

MPCVD homoepitaxial diamond lateral growth for power devices

Thesis defended publicly on **June 15th 2017**,
with a committee composed by:

Mr. François SILVA
Research Engineer, LPICM – CNRS, France, Reporter
Mr. Ken HAENEN
Professor, Hasselt University, Belgium, Reporter
Ms. Isabelle BERBEZIER
Professor, IM2NP, France Examiner
Ms. M.Pilar VILLAR
Reader, Universidad de Cádiz, Spain, Examiner
Ms. Catherine BOUGEROL
Professor, Institut Néel – CNRS, France, President
Mr. David EON
Reader, Institut Néel – CNRS, France, Examiner

Acknowledgements

During my PhD, I have been working in three different countries and using facilities from more than six different institutions that have allowed me to success in my work. During these years, I met many people who help me and teach me a lot. Now that all this experience is expressed in this manuscript, it is time to thank them their support and training.

I want to thank Daniel Araujo, who is my Spanish-Swiss supervisor. He gave me my first opportunity in research and supported me always. He "rescued" me when most blocked I was. From his expertise, I learnt (and I learn) a lot about CL, semiconductors, TEM, …. And his optimism and enthusiasm provided me this extra-energy needed for the PhD work. Moreover, his good mood makes it easy to be under his supervision. I really appreciate the confidence he had in me, granting to me a high independence and autonomy.

I wish to express my deep gratitude to Etienne Bustarret, who, despite his busy schedule, accepted the co-supervision of my PhD. He helped me a lot in my stage at Néel institut. I really appreciate the pedagogical meetings in which, through brief discussions, he helped me organize all the ideas I was collecting during the experiments. His expertise in diamond growth gave me the clues I was looking for in many of the stage of my work.

I wish to thank to Rafael Garcia, who accepted me in the research group TEP 0120 from which he is the leader. To be part of this group is not only a pride, it is a fortune because it allowed me to work together with friendly and great researchers.

I thank to Pilar Villar, who, as well as Daniel, always supported me. Her chemical expertise and TEM experience were very helpful. But also, her knowledge about the University rules and paperwork was very valuable.

I want to thank to David Eon his growth and electronics tutorials. He is one of the biggest author of my success in this business. I owe my experience on MPCVD growth to him and I have to thank his support and trust. He allows me to do these “crazily long” growths and provided me all the facilities and help that I needed. I really thank his inestimable help. And the time he spent on my training.

During the analysis of my samples, I was fortunate to have the help of an expertise in defects as Marina Gutierrez. She helped me in the understanding of their generations and gave me her expert point of view.

I want to thank to Kostantinos Zekentes, who spent a lot of time in teaching me about MBE growth, materials… and, especially, how to do research. Thank you for giving me the opportunity to work under your supervision at FORTH and your patience with me.

And thanks to all the FORTH workers and PhD students that made of my stage in Greece a really great experience. *Σας ευχαριστώ πάρα πολύ για όλα*.

The CL measurements would not be possible without Fabrice Donatini. I want to thank him for his kind help in the use of this technique.

I thank the support of the technicians from NANOFAB (Institut Néel) and, more in particular, to Bruno Fernandez, who made possible the lithography of my samples and did not have inconvenient with my hurries due to the continues traveling Grenoble-Cadiz.

I would like to thank to Paco Varela for his support with the TEM facilities of CITIUS. It is always a pleasure to go to Seville for TEM observation and share a coffee or beer with him.

I thank to Rocio Romero, her kindness during my visits to Malaga. I appreciate very much the FIB facilities from the SCBI.

I would like to thank to Paco Morales for his advices. He was always available to give me his point of view. I want to thank also his support and help in the PTA and the time he spent for me in its winning. And I want to thank him, as director of the IMEYMAT, for accept me as member of this institute.

I want to thank to Alexandre Fiori from whom I started this subject of work which was fascinating to me.

I want to thank to Didier Chaussende for the interesting discussions. His growth expertise was very helpful for me.

Of course, I want to thank to my fellow sufferers. I thank to my PhD student-mates who, “suffering” like me the PhD student life, were always friendly and shared with me their knowledge and help:

I thank to these PhD students than became in Doctors in Cádiz: Jose C. Piñero, who was together with me since the bachelor degree and whose passion for the science is always a motivation; Maria de la Paz Alegre, her tenacy is an example for me; Carlo Enzo, whose “italiandalucian” character makes everything easier; Daniel Fernandez, the person to who I asked my daily questions about microscopy; Jesus Hernandez, FIB sufferer like me; Jose Manuel Mánuel, and his kind advices. And the ones who are still on the way: Natalia Fernandez and her happiness, Veronica Braza, Jose Javier Relinque, Atif Khan, Gonzalo Alba, Juan Jesus Jimenez, Otman Batza,

…Those who are “exiled”: Andrés Raya and Rocio Félix; The “PhD student” Francisco Delgado, and “the people from the third floor”. Muchas gracias a todos.

I thank to who, during my work or just when I arrived, became Doctors in Grenoble: Aurèlien Merechal, Aboulaye Traoré and Jessica Bousquet, whose PhD thesis on diamond, together with the Alexandre Fiori, were my “bedtime books”, Zhihua Fang and Toan Pham. And the still PhD students, Oluwasayo Loto, Cédric Masante and, especially, Juliette Letellier (I still owe you a *tortilla*) who kindly helped me a lot in my experimental work at Grenoble. I want to thank to them and to all SC2G research group their help, these in particular to Julien Pernot, Etienne Gheeraert, Matthieu Florentin and Gauthier Chicot, for your hospitality and kindness. It was a fruitful and great time at Grenoble thanks to all of you. Merci beaucoup.

Finally, thanks to my family, my parents and sisters, who support me at any circumstance and who made easier overpass the difficulties. Thanks to Emil, who is my joy, and the just arrived Margot, the nicest nephews an uncle can have.

Thanks to my friends, whom I don't see since last months because the hard working required by the PhD, but I know they will be always there.

Diamond is the ultimate semiconductor for power electronic devices. Consequently, diamond growth techniques and diamond-base devices have been intensively investigated over the last two decades all over the world. Among these power devices, diamond based Schottky diodes are the most advanced. However, for diamond to substitute present Si and SiC for power electronics, a substantial technological progress is still needed.

The improvement of power devices depends not only on the intrinsic characteristic of the semiconductor, but also on the device architecture. Vertical and pseudo-vertical devices offer many advantages such as low-specific on-resistance, high breakdown voltage and a smaller size. Moreover, three-dimensional (3D) design allows to reduce the electric field inside the material and would make the most out of the superb material qualities of diamond, if only the diamond growth mechanism over patterned diamond substrates were better studied and understood.

Thus, the aim of this thesis manuscript is to understand the mechanisms governing the three-dimensional (3-D) shaped diamond substrates homoepitaxial overgrowth, in order to implement them in the design and fabrication of a Schottky device.

To reach this goal, the main mechanisms of CVD growth over patterned substrates were experimentally investigated by transmission electron microscopy using a novel stratigraphic approach that allowed to follow the growth direction and generation of defects at various stages. Evidence was provided for many sectors of growth, and a tendency to planarization, while the methane concentration and resulting growth rates were shown to be key parameters. Various interpretation models, from the atomistic to the macroscopic scale, were discussed. The origin of dislocations, and of other extended and superficial defects was determined. Low methane concentrations led to high quality 3-D overgrowth. The overgrowth of micro-terraces is proposed as a method to achieve large areas free of defects. A novel method based in solid solution strengthening was introduced as an alternative to cathodoluminescence to evaluate boron doping in dislocation-rich regions where extended defects usually hinder this approach. All the results obtained above have been taken into account to reduce the number of technological steps leading to a diamond based 3D device (Schottky diode or even MOSFET). In the case of Schottky diodes, a 3D design was proposed with the following advantages:

- To “filter” dislocations.
- To allow an arbitrary large field region.
- To spare photolithography steps.
- To improve ohmic contacts, as the p^+ layer is grown on a {111} facet.

El diamante es el material semiconductor definitivo para los dispositivos electrónicos de potencia. Por ello, las técnicas de crecimiento y los dispositivos basados en diamante han sido objeto de estudio mucho en todo el mundo durante las últimas dos décadas. De entre estos dispositivos de potencia, los diodos Schottky basados en diamante son los más avanzados. Sin embargo, sustituir los dispositivos de potencia actuales, basados en Si y SiC, aún requiere importantes avances tecnológicos.

La mejora de los dispositivos de potencia no solo depende de las características propias del material semiconductor, sino también de la arquitectura del dispositivo. Dispositivos verticales y pseudo-verticales ofrecen muchas ventajas, tales como baja resistencia activa (ON) específica, alto voltaje de ruptura y reducción del tamaño. Además, los diseños tridimensionales (3D) permiten reducir el campo eléctrico dentro del material y, tan solo comprendiendo mejor los mecanismos de crecimiento del diamante sobre sustratos de diamante grabados, se aprovecharían mejor las características excepcionales del diamante.

Por esto, la motivación de esta tesis es la de entender los mecanismos que gobiernan el crecimiento homoepitaxial de diamantes sobre sustratos grabados tridimensionalmente con el objetivo de implementarlo en el diseño y fabricación de un diodo Schottky.

Para lograr este objetivo, se han estudiado experimentalmente los principales mecanismos de crecimiento CVD sobre sustratos grabados usando para ello una novedosa aproximación estratigráfica que permite seguir la dirección de crecimiento y la generación de defectos en varias etapas. Se han evidenciado varios sectores de crecimiento y una tendencia a la “planarización”, mientras que la concentración de metano, y las consecuentes velocidades de crecimiento, se han mostrado claves. Se han tratado varias interpretaciones del modelo, desde la atomística hasta la escala macroscópica. Se ha determinado igualmente el origen de las dislocaciones y otros defectos planares y superficiales. Las condiciones de crecimiento a bajo metano dieron lugar a una gran calidad de recrecimiento 3D. Se propone el recrecimiento de micro-terrazas como método para la obtención de grandes regiones libres de defectos. Y un nuevo método basado en el endurecimiento por solución sólida se presenta como alternativa a la catodoluminiscencia en la evaluación del dopado por boro en regiones con alta densidad de dislocaciones, que habitualmente impiden esta estimación. Todos los resultados obtenidos, han sido utilizados en la reducción de pasos tecnológicos para la fabricación de dispositivos 3D basados en diamante (diodos Schottky o incluso MOSFET). En el caso de diodos Schottky, se propone un diseño 3D que tiene las ventajas siguientes:

- “Filtrar” dislocaciones.
- Permitir ampliar las regiones de campo arbitrariamente.
- Disminuir los procesos de fotolitografía.
- Mejorar los contactors óhmicos con el crecimiento de capas p^+ en planos {111}

Le diamant est le semi-conducteur par excellence pour les composants électroniques de puissance. Par conséquent, la technique de croissance du diamant et les dispositifs à base de diamant ont été largement étudiés dans le monde entier au cours des deux dernières décennies. A ce jour, les diodes Schottky à base de diamant sont les composants les plus avancés et les plus prometteurs. Cependant, pour remplacer Si et SiC dans cette filière technologique, des progrès importants dans la technologie du diamant sont nécessaires.

L'amélioration de l'électronique de puissance dépend non seulement des caractéristiques intrinsèques du semi-conducteur mais aussi de l'architecture du dispositif. Les dispositifs verticaux et pseudo-verticaux offrent nombreux avantages comme une faible résistance spécifique, une haute tension de rupture et une taille réduite. De plus, la conception tridimensionnelle (3D) permettrait de réduire le champ électrique à l'intérieur du matériau et de tirer parti des qualités exceptionnelles du diamant si le mécanisme de croissance de ce matériau sur un substrat structuré était plus étudié et mieux compris.

Ainsi, le but de ce manuscrit de thèse est de comprendre les mécanismes qui régissent la reprise de croissance en homoépitaxie sur un substrat structuré 3D en diamant. Pour atteindre cet objectif, les principaux mécanismes de la croissance CVD sur substrat gravé sont étudiés expérimentalement par microscopie électronique en transmission grâce à une approche stratigraphique originale qui permet de suivre la direction de croissance et la génération de défauts aux différentes étapes de la croissance. L'observation de divers secteurs de croissance, d'une tendance générale à la planarisation, et le rôle important joué par la concentration de méthane qui gouverne la vitesse de croissance, sont les principaux résultats de cette étude. Divers modèles d'interprétation allant de l'échelle atomistique à l'échelle macroscopique sont discutés. L'origine des dislocations, et des autres défauts étendus et superficiels a été déterminée. Les basses concentrations de méthane ont permis une croissance 3D de haute qualité. La reprise de croissance sur des micro-terrasses est présentée comme une alternative pour l'obtention de grandes surfaces sans défauts. Une nouvelle méthode basée sur le renforcement par solution solide est introduite comme alternative à la cathodoluminescence pour évaluer le dopage dans les régions riches en dislocations, où les défauts empêchent l'observation d'excitons. Tous les résultats obtenus ont été pris en compte pour réduire le nombre d'étapes technologiques nécessaires pour fabriquer des composants à architecture 3D en diamant (diode Schottky ou même MOSFET). Dans le cas des diodes Schottky, le procédé et l'architecture proposés ont les avantages suivants :

- « Filtrer » les dislocations.

- Permettre d'étendre la région de champ arbitrairement.

- Eviter certaines étapes de photolithographie.

- Améliorer le contact ohmique, par croissance d'une couche p^+ sur une facette {111}.

Contents

General introduction and thesis structure

Diamond is the ultimate semiconductor for power electronic devices. Diamond growth techniques and diamond-base devices have been widely investigated over the last two decades, but the 3D overgrowth expected to boost the performance of such devices was only rarely studied. This PhD thesis aims at contributing to such study. The manuscript is organized as follows:

Chapter 1: The motivation of diamond as a wide band gap material, its growth and doping, as well as its electronic applications, focusing on the Schottky diodes and the new architectures are discussed. The structural and electronic characterization techniques here used are also introduced.

Chapter 2: Engineering and technical details of the PhD work are highlighted. The selection of the substrate, the design of the mask and the etching conditions to obtain the patterned substrates required for the lateral/3D growth are described, as well as the choice of growth conditions based on previous works.

Chapter 3: The main mechanisms of CVD lateral growth are tentatively investigated in this chapter. A novel stratigraphic approach, based on the use of very thin doped layers to follow by transmission electron microscopy (TEM) the growth orientation at every time, is presented. The effect of the methane concentration during the growth process and of the geometrical characteristics of the substrate are investigated.

Chapter 4: The defects generated during lateral growth were studied with the help of TEM. The origin of dislocations and other extended and superficial defects was determined. Moreover, a mechanism based on the overgrowth on micro-terraces is proposed to achieve large areas free of defects.

Chapter 5: Boron doping content in diamond has been evaluated for the different growth sectors observed during lateral growth. Conventional TEM together with cathodoluminescence were used in order to estimate doping in a range where quantification is not trivial. Additionally, a novel method based in solid solution strengthening is introduced as alternative to evaluate doping on regions with dislocations, where CL is less powerful.

Chapter 6: Based on the previous chapter, this section envisions a future Schottky diode device. The design posed in this chapter drastically reduces the engineering steps usually required and reduces then the risk of failure during the fabrication process.

I Introduction

Contents

Diamond properties, diamond growth processes and diamond-based devices are introduced to motivate the current subject of thesis. The advantages of this material, the state of the art of the technology and devices, as well as the challenges to face, are pointed out in this first chapter, as well as the experimental approach specific to this work.

I.1 Diamond properties

Diamond is a metastable allotrope of carbon renowned as a material with superlative physical properties. The most remarkable are described in table I.I, and result from the strong covalent bonding between its atoms. Carbon atoms in diamond form tetrahedral covalent bonds involving sp^3-hybrid orbitals that configure two possible crystal system symmetries: (i) the very rare hexagonal symmetry; and (ii) the common in both, nature and synthetic, cubic diamond symmetry. This crystal structure awards to diamond the title of highest hardness and thermal conductivity of any bulk material.

Table I.I. Comparative properties of silicon and major wide band gap materials.

Property	Si	4H-SiC	GaN	Diamond
Band gap, E_G *(eV)*	1.12	3.23	3.39	5.45
Breakdown Voltage, E_C *($10^6 V \cdot cm^{-1}$)*	0.3	3	3	10
Electron mobility, μ_e *($cm^2 \cdot V^{-1} \cdot s^{-1}$)*	1500	980	1250	1000
Hole mobility, μ_h *($cm^2 \cdot V^{-1} \cdot s^{-1}$)*	480	100	200	2000
Thermal conductivity, λ *($W \cdot cm^{-1} \cdot K^{-1}$)*	1.5	5	1.5	22
Relative permittivity, ε_r	11.8	9.7	10.4	5.7
Saturated drift velocity *($10^7 cm^2 \cdot s^{-1}$)*	1.0	2.0	2.2	1.1
Maximal temperature, T_{max} *(K)*	140	760	800	1350

The cubic network of diamond, outlined in Fig.I.1, is formed by two face centered cubic (FCC) networks superimposed and displaced by a/4 along each dimension. In such a structure, the C-C bond length is 154.448 pm and the unit cell dimension is $a = \frac{4}{\sqrt{3}} r_{C-C} = 356.682$ pm, containing eight carbon per unit cell and resulting in a density of 3.515 $g \cdot cm^{-3}$. At room temperature, diamond has a maximum electron mobility of around 1000 $cm^2 \cdot V^{-1} \cdot s^{-1}$ [Pernot 2008] and 2000 $cm^2 \cdot V^{-1} \cdot s^{-1}$ for holes [Pernot 2010].

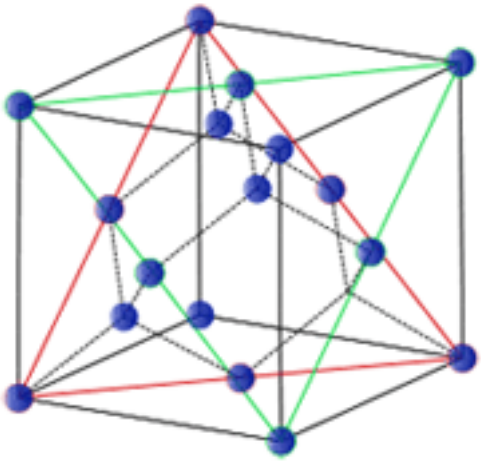

Fig.I.1. Diamond unit cell formed by two superimposed FCC networks.

Furthermore, diamond is optically transparent in the UV, visible, IR and far IR range; is extremely chemically inert, not being affected by any acid or other wet chemicals; is compatible with Si based devices, and non-toxic. These excellent mechanical, electrical and optical properties make diamond a quite versatile material that has been studied during last decades not only for gemstone applications, but also for tribology, biological or medical applications [Danker 2009, Zhang 2011 and Mochalin 2012]. Among these uses, electric and semiconductor diamond engineering has become the main objective thanks to the development of growth processes based on chemical vapor deposition [Matsumoto 1982, Matsumoto 1982-b, Kamo 1983 and Kobashi 1988]. Applications in the field of nuclear or X-ray detectors [Bergonzo 2001, Bergonzo 2006 and Morse 2010], electrochemical sensors [Tian 2007 and Kiran 2012] and power devices [Alvarez 2006, Ueda 2006, Umezawa 2007, El-Hajj 2008, Koné 2010, Conte 2010, Hirama 2010, Lin 2011, Achard 2011, Muret 2011, Thion 2011, Gaowei 2012 and Teraji 2012] have been developed with reproducible and promising results, opening the door to a new scientific-technological era.

I.2. CVD growth

Chemical vapor deposition (CVD) is a widely-used material-processing technology since the fifties [Powell 1966]. The majority of its applications involve applying solid thin-film coatings to surfaces, but it is also used to produce high-purity bulk materials and powders, as well as fabricating composite materials via infiltration techniques. It has been used to deposit a very wide range of materials. The majority of the elements in the periodic table have been deposited by CVD techniques, sometimes in the form of the pure element, but more often combined to form compounds.

In its simplest version, CVD involves flowing a precursor gas or gases into a chamber containing one or more heated objects to be coated. Chemical reactions occur on and near the hot surfaces, resulting on the deposition of a thin film on the surface. This is accompanied by the production of chemical gaseous byproducts that are exhausted out of the chamber along with unreacted precursor gases. As would be expected from the large variety of materials deposited and the wide range of applications, there are many variants of CVD. The deposition is undertaken in hot-wall reactors and cold-wall reactors, at sub-Torr total pressures as well as above-atmospheric pressures, with and without carrier gases, and at temperatures typically ranging from 200 to 1600°C. There are also a variety of enhanced CVD processes, which involve the use of plasma, ions, photons, lasers, hot filaments, or combustion reactions to increase deposition rates and/or lower deposition temperatures.

CVD has then applications across a wide range of industries. For example, depositions of coatings for a variety of applications such as wear resistance, corrosion resistance, high temperature protection, erosion protection and combinations thereof, are usually carried out by CVD. In addition, CVD can be used to produce components that are difficult or uneconomical to produce using conventional fabrication techniques. Dense structural parts produced via CVD are generally thin walled and maybe deposited onto a mandrel or former. Moreover, materials as optical fibres, powder production, catalysts products or composites are fabricated by CVD. In fact, performs can be infiltrated using CVD techniques to produce ceramic matrix composites such as carbon-carbon, carbon-silicon carbide and silicon carbide-silicon carbide composites.

An advantage of CVD is that, in addition to the wide variety of materials that can be deposited, they can be deposited with very high purity. This results from the relative ease with which impurities are removed from gaseous precursors using distillation techniques. Other assets include relatively high deposition rates, and the fact that CVD often does not require a vacuum as high as PVD processes. CVD also has a number of drawbacks. One of the primary disadvantages lies in the properties of the precursors. Ideally, the precursors need to be volatile at near-room temperatures. CVD precursors can also be highly toxic ($Ni(CO)_4$), explosive (B_2H_6), or corrosive ($SiCl_4$). The byproducts of CVD reactions can also be hazardous (CO, H_2, or HF). Some of these precursors, especially the metal-organic precursors, can also be quite expensive. The other major shortcoming is the fact that the films are usually deposited at elevated temperatures. This brings some restrictions on the kind of substrates that can be coated. More important, it leads to stresses in films deposited on materials with different thermal expansion coefficients, which can cause mechanical instabilities in the deposited films.

I.2.1. Diamond growth by CVD

For many years, the conventional wisdom was that diamond would form only under conditions of high pressure and high temperature (HPHT). This was the case of the first synthetic diamond produced, carried out by General Electric in 1955 [Bundy 1955]. A few years later, in 1962, the first diamond growth by CVD was patented [US3030188A]. However, it was necessary to wait until the late 1980s to see cheaper heteroepitaxial and reproducible grown diamond using CVD process [Spear 1994]. In heteroepitaxial diamond growth, the extremely high surface energy of diamond, that reflects the strength of the bonds that must be broken to create a new surface, leads to inefficient wetting of substrates surfaces by growing diamond species. In addition, the complexity of the chemical reactions requires a highly advanced understanding of the technique. The CVD process is quite different from the natural diamond formation. As its name implies, chemical vapor deposition involves chemical reaction inside a gas-phase as well as deposition onto a substrate surface. Growth of diamond films by CVD must be conducted under non-equilibrium conditions. This is because under normal conditions, graphite is a more stable phase of carbon than diamond. Furthermore, during the CVD process, hydrogen radicals (atomic hydrogen) must be present to, among others, remove non-diamond carbon, including graphite which is formed on the diamond surface. Methane is commonly used as the carbon source for CVD diamond growth. The process procedure with the whole range of selectable process parameters is shown in Fig.I.2 [Schwander 2011].

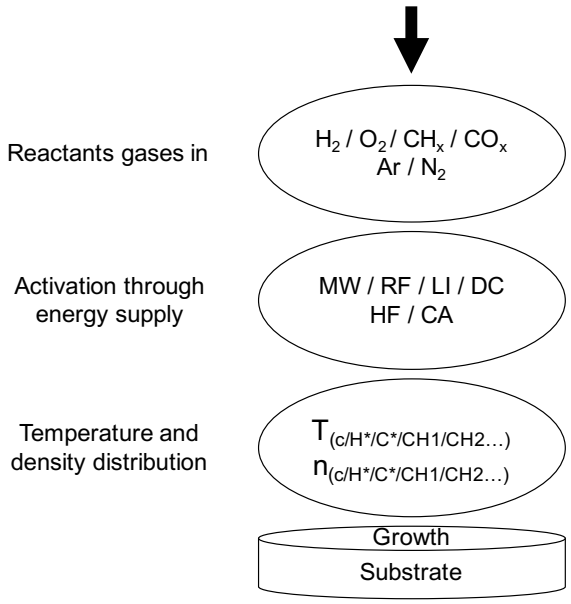

Fig.I.2. Schematic diagram of the mechanism from CVD processes for diamond growth.

This sketch illustrates the various direct and indirect adjustable parameters. The first group shows the different selectable process gases which can be used for CVD. The second group reflects a selection of energy sources for the activation of the chemical process, followed by ensuring parameters. Below that, there is the substrate with the growing diamond layer. The principal chemical mechanism relevant to the growth of diamond from gaseous hydrogen and hydrocarbon species was presented at 1993 by Butler *et al*. [Butler 1993]. However, the processes have been developed since this time [Schwander 2011 and Yang 2015]. For example, focusing on plasma enhanced CVD (PECVD), evaluations of the vapor phase have been studied based on optical emission spectroscopy (OES) and mass spectrometry (MS) [Giquel 1994, Benndorf 1994, Fujii 2007, Deák 2007, Zhou 2007, Ma 2009, Gicquel 2012, and Richley 2012]. These works established that the production and diffusion of hydrogen, CH_x radicals, and C_2H_y radicals were key processes. Along the same line, simulations were carried out to determine the distribution of radicals, gas and electron temperatures in such plasmas [Bou 1992, McMaster 1995, Larson 1999, Aubry 2004, Achard 2007, Yamada 2007, Ma 2008, Silva 2009, Hassouni 2010, Yamada 2011, and Yamada 2012].

I.2.2. Boron doped diamond growth

For the fabrication of diamond-based electronic devices, doping diamond by acceptor and donor impurities is necessary to control the carrier type and concentration and to control the electrical resistivity of diamond semiconductors. In contrast with other more common semiconductors, the highly compact lattice of diamond hinders the diffusion or incorporation of most impurities that could substitute carbon atoms. Consequently, only a few candidates are suitable for diamond doping.

Nitrogen, with a covalent radius of 0.079 nm close to that of carbon (0.077 nm) is the most common impurity in diamond and it is likely to form several types of complexes with vacancies. Nevertheless, nitrogen in substitutional site distorts the lattice, increasing the ionization energy of the resulting gap state up to 1.7 eV [Kajihara 1993], higher than the bandgap of silicon. This very deep level makes n-type doping with nitrogen unsuitable for the fabrication of devices. Nitrogen-vacancy center are common point defects originated on nitrogen doped diamond. It consists of a nearest-neighbor pair of a nitrogen atom, which substitutes for a carbon atom, and a lattice vancancy. Recently, this nitrogen-vacancy (N-V) center in diamond has attracted a lot of attention as a promising solid-state spin system for quantum information and sensing applications [Jelezko 2004, Childress 2006, Gurudev 2007, Neumann 2008, Balasubramanian 2009, Buckley 2010, Zhu 2011 and Lee 2011].

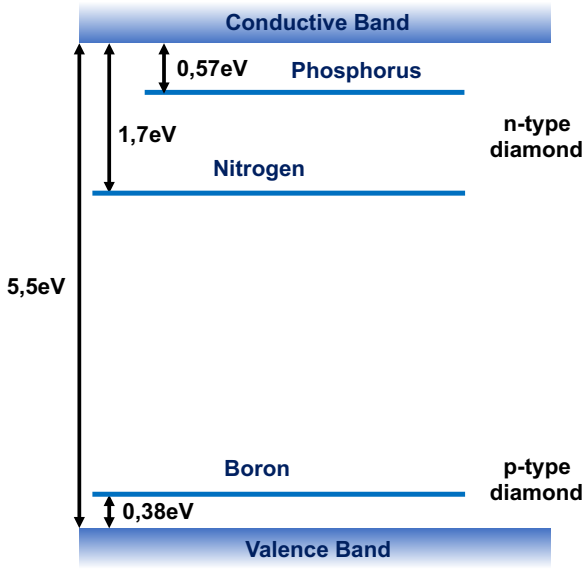

Fig.I.3. Ionization energy of dopants in diamond for *n*-type and *p*-type diamond.

Generally, boron and phosphorus are used as *p*- and *n*-type dopants of diamond semiconductors, respectively. The covalent radii of boron (0.088 nm) and carbon (0.077 nm) are close enough to allow the incorporation of boron as substitutional sites. The activation energy of boron-doped diamond is 0.37 eV [Lagrange 1998] and it was shown that in fact only this *p*-type dopant can be incorporated with a high reproducibility. Similarly, phosphorous has a covalent radius of 0.117 nm that makes its incorporation difficult and more effective on diamond substrates (111)-oriented. In fact, the first phosphorous doped {111}-oriented diamond was reported by Koizumi *et al*. at 1997 [Koizumi 1997] whereas the first phosphorous doping of {100}-oriented diamond was not achieved until 2005 [Makino 2005]. This donor has an ionization energy close to 0.57 eV [Katagiri 2004 and Kato 2005]. Fig.I.3 displays the ionization energy of dopants in diamond.

Doping into diamond may be carried out in situ by HPHT, PECVD, and a posteriori by ion implantation [Prings 1988, Uzan-Saguy 1998, Ueda 2007, Tsubouchi 2008 and Ratnikova 2011]. For device fabrication purposes, doped diamond films are mostly grown on HPHT or CVD diamond substrates by PECVD because doping by this technique provides both *p*- and *n*-type diamond with controlled concentrations of impurities. During homoepitaxial diamond growth by PECVD, boron and phosphorous doping is carried out by introducing diborane (or trimethylboron) and phosphine (or tertiarybutyl phosphine) gases, respectively. The highest Hall hole and electron mobility of PECVD diamond films reported are 1.860 $cm^2V^{-1}s^{-1}$ at 290 K [Yamanaka 1998] and 660 $cm^2V^{-1}s^{-1}$ at 300 K [Katagiri 2004], respectively. Carrier mobility decreases with increasing boron or phosphorous concentrations in diamond films. However, as dopant deliver more carriers, it reduces the resistivity of diamond. For $[B]<10^{19}cm^{-3}$, conduction is dominated by thermally

activated free holes in the valence band. At higher doping concentrations, variable-range hopping conduction between gap states appears, and then the metal-insulator transition and superconductivity occurs above $3x10^{20}$ [B] atoms·cm^{-3} [Lagrange 1998, Ekimov 2004, Yokoya 2005 and Bustarret 2008-a]. The resistivity of heavily boron-doped diamond {100} films with $3x10^{20}$ [B] atoms·cm^{-3} is 10 mΩ·cm or less at room temperature [Lagrange 1998, Tokuda 2007 and Tokuda 2007-b]. In contrast, the resistivity of heavily phosphorous-doped diamond {111} film with 10^{20} [P] atoms·cm^{-3} is around 70 Ω·cm at room temperature [Kato 2009]. These properties can lead to the fabrication of chemical/bio and electronic devices.

I.3. Diamond applications on power electronics

Silicon-based devices are the most advanced and mature technology for power applications. However, wide band gap (WBG)-based devices should enhance the energy efficiency in industrial-scale power electronics and clean energy technologies because of their superior electrical and thermal properties. Indeed, WBG materials may induce several energy-related benefits in power electronics systems, namely: (i) energy loss reduction up to 90% of those currently occurring in AC-to-DC and DC-to-AC electrical conversions [Tolbert 2005], (ii) higher voltage operation than for Si-based devices, which should greatly enhance the number of high-power applications [Ozpineci 2011], (iii) better tolerance of power systems to high operating temperatures resulting in smaller and lighter systems with reduced life cycle energy balance [Ozpineci 2011], (iv) higher frequency operations opening up a range of new applications such as radio frequency amplifiers [Ozpineci 2011], (v) more reliable and consistent power electronic device operation. These features promoted the use of wide band gap semiconductors in power electronics, an alternative to silicon that has been seriously considered since the 1980s [Baliga 1982].

Among WBG, diamond has exceptional electronic properties. These properties were already shown and compared with Si and other WBG semiconductors materials in Table.I.I. The excellent mobility of electrons and holes in diamond allows high current densities (which are an important parameter because of the current increase in power) and the high thermal conductivity enhances the heat dissipation capability. In fact, the first limitation on Si-based devices is the low thermal conductivity of silicon, limiting the maximum operating temperature to less than 150°C. Moreover, the wide band gap ensures greater immunity to radiation, which can be useful in space and nuclear applications, for example.

The improvement of power electronics not only depends on the intrinsic characteristics of the semiconductor but also on the device architecture. In this way, doped and undoped regions as well as contacts must be designed optimizing the diamond properties. Nevertheless, in the way to improve the electrical characteristics, the biggest progress probably would result from the design of three-dimensional (3D) devices. The argument is based on two main reasons: (i) 3D design allows to reduce the electric field inside the material, which makes possible higher voltage devices, (ii) better material qualities (dopant incorporation, generation of defects, …) can be reached using other growth directions (as for example the <111>, or the <311>) combined with that of the substrate [Tallaire 2017]. In addition, such devices offer many advantages such as low-specific on-resistance (see Fig.I.4 [Umezawa 2012]), high breakdown voltage (VB) and smaller size [Hoshino 2012, Umezawa 2012 and Sato 2014]. Such features have aroused interest to develop MESA-structures based devices [Biasol 2002, Hoshino 2012, Kato 2012, Ando 2012, Sato 2014 and Takeuchi 2014].

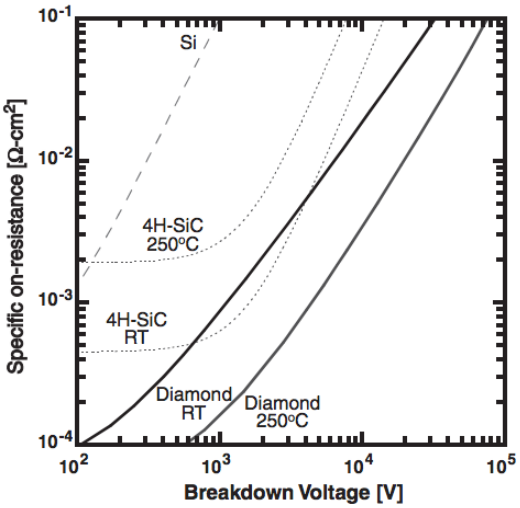

Fig.I.4. Specific ON-resistance and breakdown voltage characteristic for Si, 4H-SiC and diamond vertical Schottky diodes at RT and 250°C [Umezawa 2012].

I.3.1. Schottky diodes

A Schottky diode is one of the most common electronic components up to now. It is an unipolar device using the non-linear current transport behavior of rectifying metal semiconductor junction under applied bias voltage. Such a device behaves like a switch triggered by the bias voltage across its terminals. Schottky diodes are used in silicon-based power conversion systems because of their fast recovery time and their low turn-on voltage. When forward current flows through a diode, there is a small voltage drop across the terminals. A bipolar silicon diode has a

voltage drop between 0.6-0.7 volts, while a Schottky diode voltage drop is between approximately 0.15-0.45 volts. Besides their lower forward voltage, current transport through Schottky diodes consists of majority carrier, contrary to bipolar devices. Schottky diodes can thus switch rapidly from forward to reverse bias without minority carrier storage effects, a feature that improves the system efficiency. It makes them useful in voltage clamping and preventing transistor saturation applications.

Diamond Schottky diodes are made of an active *p*-type diamond sandwiched between the heavily doped p^+-type diamond and Schottky electrode. Compared to other diamond power devices (as bipolar [Kato 2012], junction field effect transistor [Iwasaki 2012], Schottky-pn diode [Makino 2009]), Schottky diode is the most promising because of highest breakdown voltage reported (2.5 kV [Umezawa 2013], 6.7 kV [Butler 2003], 10 kV [Volpe 2010], 8-12 kV [Chow 2004]) and architectural progress to minimize its serial resistance. Indeed, the high serial resistance of the lightly doped Schottky active layer required to get high breakdown field, is one of the main limitation of such a device.

Moreover, as the edges of the Schottky contact are fairly sharp, high electric field gradient occurs around them, limiting the reverse breakdown voltage. Several strategies are used, from guard rings to overlaps of metallization to spread out the field gradient. The guard rings consume valuable die area and are used primarily for large higher-voltage diodes, while overlapping metallization is employed primarily with smaller, low-voltage diodes.

I.3.2. Diamond lateral power devices

Some of the restrictions bearing upon diamond-based Schottky diodes can be solved by the use of 3D architectures. It is the case of pseudo vertical (with heavily boron doped buried layer) or vertical (with heavily boron doped substrate) architectures, whose use allowed a significant reduction of the diamond diode serial resistance. The reported forward current for these diodes architectures is higher than 100 A/cm^2. A 1 Ω serial resistance was recently demonstrated for a vertical diamond Schottky diode operating at 250 °C [Umezawa 2013]. However, the breakdown fields reached in pseudo vertical and vertical Schottky diodes (2.1 MV/cm [Umezawa 2013], 2.7 MV/cm [Kumaresan 2010]) even with a field plate structure used to avoid the edge field enhancement [Ikeda 2009] are much lower compared to those found for lateral diodes (7.7 MV/cm [Volpe 2010]) and to the very first value reported for bulk diamond (higher than 10 MV/cm) [Landstrass 1993]. It is generally admitted that the main reason of such a low breakdown fields and high reverse current values of pseudo vertical and vertical diamond Schottky

diodes lies in defects such as dislocations, which propagate from the heavily boron doped diamond substrate into the active layer [Ohmagari 2011].

Moreover, the high electric field gradient present around the fairly sharp Schottky contacts can be minimized by using 3D architectures. By reducing the electric field inside the device, it can be used at higher voltage. In this way, such architectures also reduce the ON state resistance by reducing the usually large drift zone necessary in the classical unipolar devices. In addition, Schottky diodes with 3D architecture can benefit from the use of nonconventional orientations (as <311> to avoid dislocations [Tallaire 2017]) or combine them in the most fruitful way (for example <111> for p+ doped region and <100> for undoped region).

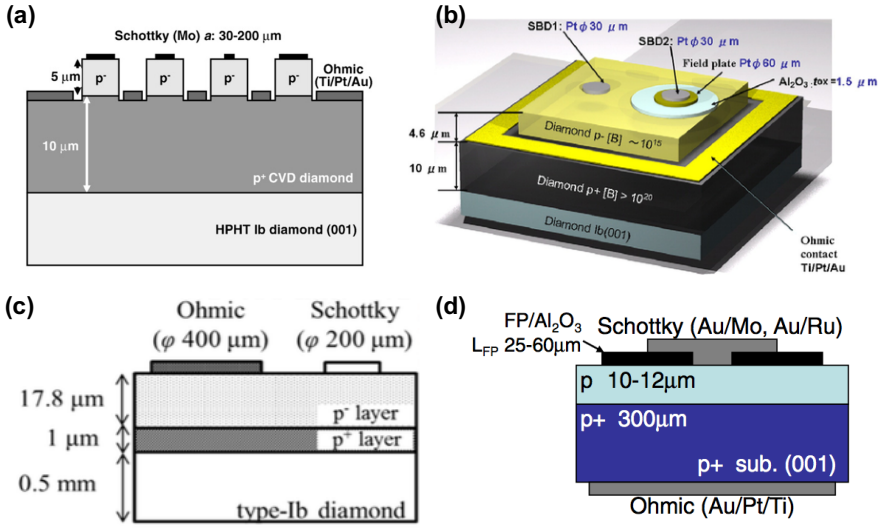

Fig.I.5. Cross-sectional views of diamond pseudo-vertical Schottky diode (a) [Umezawa 2009], (b) [Ikeda 2009], (c) [Kato 2015] and a vertical Schottky diode [Umezawa 2014].

All these advantages have encouraged 3D diamond growth and 3D devices design to become a relevant topic of research over the last years. Fig.I.5 shows cross-sectional view of some of the vertical and pseudo-vertical Schottky diodes designed. Fig.I.5 (a) shows a pseudo-vertical Schottky diode [Umezawa 2009] where, to decrease the parasitic resistance on diamond, the distance between Ohmic and Schottky electrodes was reduced using lithography techniques. Fig.I.5. (b) shows a pseudo-vertical Schottky diode with field plating (right), to avoid the edge field enhancement, and without (left) field plating [Ikeda 2009]. Fig.I.5 (c) shows another pseudo-vertical Schottky diode [Kato 2015] that was used in the study of dislocations and the correlation between defect density and device performance. Fig.I.5 (d) shows a vertical Schottky diode [Umezawa 2014] with a thick field plate (see arrow).

Fig.I.5 points out an interest of the community on such geometries that is not restricted to

the Schottky diodes. Many others electronic devices, such as *p-n* junctions, MOSFET, MESFET or MISFET, have been designed with vertical or pseudo-vertical geometries. Nevertheless, most of these studies are dedicated to the electrical characterization and the understanding of the growth mechanisms as well as defect correlation to leakage was not yet achieved. Fig.I.6 shows one of the few studies performed about selective diamond growth for device fabrication [Sato 2014]. It corresponds to a TEM study on selective growth of n-type diamond in lateral p–n junction diodes. One of the main reasons of the low number of similar studies is the difficulty to follow the growth at different times. For the Kato study, at least three different samples were needed, i.e. one for each time step (0 hours, 2 hours and 5 hours).

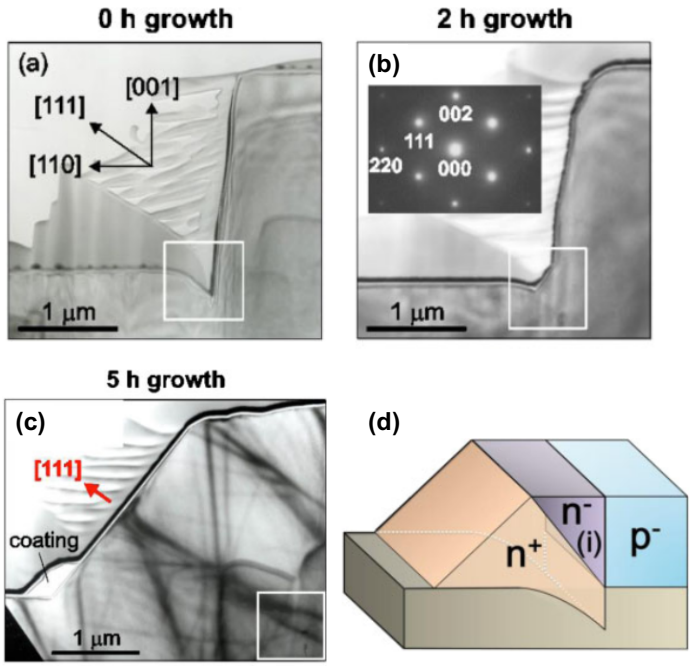

Fig.I.6. TEM cross-sectional micrographs of a *n*-type diamond patterned substrate after (a) 0 hours, (b) 2 hours and (c) 5 hours of overgrowth. (d) Schematic of the growth sectors during the selective overgrowth [Sato 2014].

Thus, the experimental work of this thesis has been carried out with the aim to understand the mechanisms governing the lateral growth and the defects generation during the process, in order to implement them in the design and fabrication of a Schottky device.

I.4. Characterization techniques

To study morphologic, chemical and structural properties at nanoscale, Electron Microscopy (EM)-related techniques are needed. EMs are capable of imaging at significantly higher resolution than light microscopes, owing to the small *de Broglie* wavelength of electrons. This

enables the instrument's user to examine fine details. There are two big families of EMs: (i) Scanning EM, in which the electron beam scans the surface of the sample and, in its basic mode, generates the image thanks to the synchronized detection of secondary electrons resulting from the interaction of the beam on such surfaces, thus providing mainly morphologic information; and (ii) Transmission EM, in which the electron beam goes through the sample to provide structural information and chemical information. To use TEM techniques, an electron-transparent sample (lamella) is required.

Microscopy equips used in the current thesis were: FEI Nova Nano SEM, SEM Dual Beam FEI Quanta 200 3D, TEM JEOL 2010 and TEM JEOL 2100 from the "Servicios Centrales de Ciencia y Tecnología – UCA", TEM Phillips CM 200 from the "Centro de Investigación Tecnología e Innovación – US" and SEM Dual Beam FEI Helios NanoLab 650 from the "Supercomputing and Bioinnovation Center – UMA".

I.4.1. SEM, FIB and CL

SEM has been employed in its basic Secondary Electrons (SE) mode. The most common imaging mode collects low-energy (<50 eV) secondary electrons that are ejected from the k-shell of the specimen atoms by inelastic scattering interactions with beam electrons. Due to their low energy, these electrons originate from within a few nanometers from the sample surface [Goldstein 1981]. The brightness of the signal depends on the number of secondary electrons reaching the detector. If the beam enters the sample perpendicular to the surface, then the activated region is uniform about the axis of the beam and a certain number of electrons "escape" from within the sample. As the angle of incidence increases, the interaction volume increases and the "escape" distance of one side of the beam decreases, resulting in more secondary electrons being emitted from the sample. Thus, steep surfaces and edges tend to be brighter than flat surfaces, which results in images with a well-defined, three-dimensional appearance. Using the signal of secondary electrons, image resolutions below 0.5 nm have been achieved.

The Focused Ion Beam is often packaged as a modification of a SEM in which an additional ion beam column has been added. When high energetic ions impinge the surface of a sample, some atoms of the bulk materials are sputtered. The high control of the size of the pattern (a common source of ions in FIB is Ga^+ that can be focused down to a very fine probe size, ~5 nm), as well as the 3D motion, allows very accurate nano-milling. The addition of a metal injector such as platinum or carbon turns this instrument into a very versatile tool that allows nano-lithography or, in our case, TEM sample preparation.

Due to the extreme hardness of diamond, electron-transparent samples of homoepitaxial diamond cannot be prepared by classical methods, and FIB techniques are required. The method used for the TEM lamellas preparation is an optimized version of the conventional ones reported in the bibliography [Giannuzzi 1999, Jin 2012, Schaffer 2012 and Chen 2013]. Fig.I.7 shows SEM micrographs describing the main steps followed during the FIB-lamellas preparation: platinum deposition to protect the sample, trench milling to extract the lamella, lamella extraction with a micromanipulator and, once it is glued on the grid, polishing of the lamella.

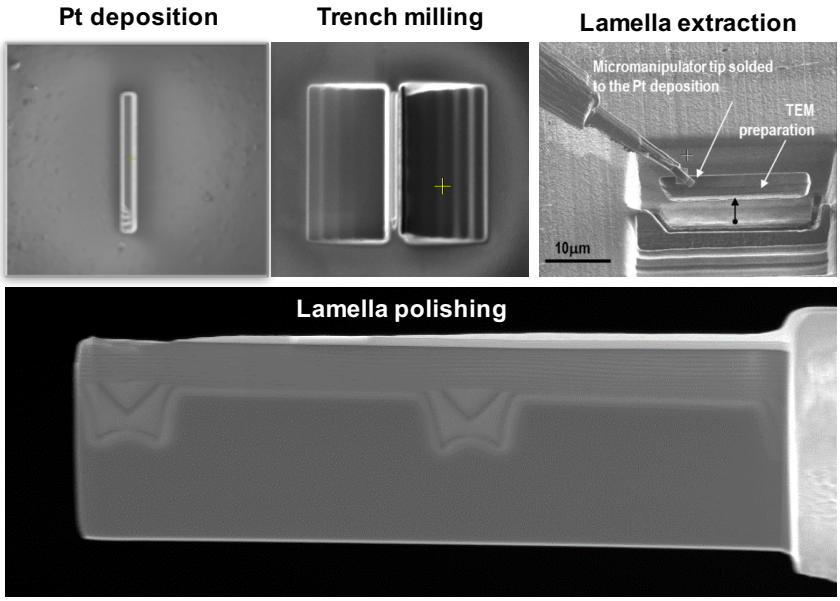

Fig.I.7. SEM micrographs of the main steps during the FIB-lamella preparation for TEM studies.

Cathodoluminescence allows the study of the light emission generated by SEM because of the impact of the electron beam on the semiconductor sample. After thermalisation such electronic bombardment results in the recombination of an electron from the conduction band with a hole in the valence band. The excess energy of this transition can be emitted in form of a photon. This photon is collected by a parabolic mirror and conducted to a detector. The energy of the photon (as well as the probability that a photon will be emitted rather than phonons) depends on the material, its purity and the presence of defects. It also depends strongly on temperature. In this way, cathodoluminescence provides chemical information about the sample.

In diamond the minimum of the conduction band is shifted by 0.76 π/a along the (100) direction of the first Brillouin zone. In this case, excitonic radiative transitions are assisted by phonon. Two kinds of phonons are present in the mechanism: transverse mode (TA for acoustic and TO for optic) and longitudinal mode (LA for acoustic and LO for optic). Free excitonic recombination assisted by TO phonon are called FE^{TO} and they are predominant. Other free excitonic recombinations, as FE^{TA} and FE^{LO}, are much weaker. When diamond (or another

semiconductor) is doped, excitons may bind to neutral impurities or-trapped carriers, leading to new possible transitions at different energies. They are generally assisted by transverse optic phonons and are labelled BE^{TO} [Zaitsev 2001].

I.4.2. TEM

In TEM a beam of electrons is transmitted through an ultra-thin specimen, interacting with the specimen as it passes through the solid matter. An image is formed from the interaction of the electrons transmitted through the specimen; the image is magnified and focused onto an imaging device. The main TEM techniques used during this thesis were:

(i) Bright field (BF) and High Resolution TEM (HRTEM): BF forms the contrast in the image directly by the occlusion and absorption of electrons in the sample. This technique is the simplest. Its name comes from the fact that regions with no sample in the beam path appear bright whilst regions with a high atomic number will appear dark. When magnification is very high (x500-x1M), and the crystal orientation perfect, it is possible to see columns of atoms. In such high-resolution situations, the method is called HRTEM.

(ii) Diffraction-contrast: Crystals may exhibit diffraction contrast whenever the electron beam undergoes Bragg scattering. Setting apertures in the back focal plane, i.e. the objective aperture, the desired Bragg reflections can be selected (or excluded), thus only parts of the sample that are causing the electrons to scatter to the selected reflections will end up projected onto the imaging apparatus. If the reflections that are selected do not include the unscattered beam (which will appear up at the focal point of the lens), then the image will appear dark wherever no sample scattering to the selected peak is present. Thus, a region without a specimen will appear dark. This is known as a dark-field image (DF).

There is one major difference between forming images to show mass-thickness contrast or diffraction contrast. We can use any scattered electrons to form a DF image showing mass-thickness contrast. However, to get good strong diffraction contrast in both BF and DF images we tilt the specimen to two-beam conditions. The electrons in the excited hkl beam have been diffracted by a specific set of hkl planes and so the area that appears bright in the DF image is the area where the hkl planes are at the Bragg condition. Hence the DF image contains specific orientation information, not just general scattering information, as is the case for mass-thickness contrast.

When the useful information from a diffraction-contrast image (usually in DF) is transferred by weakly excited beams, dislocations can be imaged as narrow lines which are

approximately 1.5 nm wide. Moreover, the positions of these lines are well defined with respect to the dislocation cores, they are also relatively insensitive to both the foil thickness and the position of the dislocations in the specimen. This mode of work is called weak-beam conditions or weak-beam microscopy (WB).

(iii) Electron Diffraction (ED) and Selected Area Electron Diffraction (SAED): As previously stated, by adjusting the magnetic lenses such that the back focal plane of the lens rather than the imaging plane is placed on the imaging apparatus, a diffraction pattern can be generated. For thin crystalline samples, this produces an image that consists of a pattern of dots in the case of a single crystal, rings made by the superposition of several dots patterns in the case of a polycrystalline material, or fuzzy rings in amorphous solid materials. For the single crystal case the diffraction pattern depends on the orientation of the specimen and on the structure of the sample illuminated by the electron beam. This image provides the investigator with information about the space group symmetries in the crystal and the crystal's orientation with respect to the beam path. This is typically done without utilizing any information but the position at which the diffraction spots appear and the observed image symmetries. When an intermediate aperture is used, the image region is restricted. The use of such aperture to analyze diffraction patterns of specific areas is called SAED.

(iv) Scanning transmission electron microscope (STEM): This mode differs from the previous TEM one described in that the electron beam is focused into a narrow spot which is scanned over the sample in a raster. The raster scan of the beam across the sample makes these microscopes suitable for analysis techniques such as energy dispersive X-ray (EDX) spectroscopy, electron energy loss spectroscopy (EELS) and annular dark-field imaging (ADF). These signals can be obtained simultaneously, allowing direct correlation of image and quantitative data. Usually STEM is a conventional transmission electron microscope equipped with additional scanning coils, detectors and needed circuitry; however dedicated STEMs are also manufactured.

a. Annular dark field (ADF): It is the only STEM technique used for this thesis work. In this technique, the signal is collected at diffraction angles around the main beam by an annular dark field detector. Images are formed of both incoherent scattered electron and Bragg scattered electrons. Atomic number variations of atoms of atoms in the sample (Z-contrast images) and dislocations are visible by this technique.

I.4.3. Electrical Characterization

Electrical characterization carried out in the current thesis was limited to the recording of some I-V curves. Such measurements were performed with a homemade probe station using a

source measurement unit single channel Keithley SMU 2601A. The set-up is equipped with an optical microscope and micro probes (0.5 μm size) that allow to perform measurements on very small contacts.

The SMU 2601A is characterized by a DC measurement mode and a Pulse mode for transient I-V. It has a bias voltage ranging from -40 V to 40 V, however, here it was used with a range from -20 V to 20 V. This SMU is generally used to investigate the forward state of fabricated diodes at the Institut Néel. The equipment can deliver high current up to 1 A in DC mode and 3 A in Pulse mode.

I.5. Summaries

I.5.1. Resumen

El diamante es un estado meta-estable del carbono, conocido por sus increíbles propiedades físicas. Estas cualidades tienen su origen en el fuerte enlace covalente sp^3 que forman los átomos de carbono. Estos se disponen de forma tetragonal construyendo dos posibles sistemas: (i) uno muy extraño con simetría hexagonal (prácticamente inexistente), y (ii) el más común, tanto sintética como naturalmente, de simetría cúbica.

Entre las propiedades más reseñables del diamante se encuentran su dureza (por lo que es comúnmente conocido) y su alta movilidad de portadores de carga (1000 $cm^2V^{-1}\cdot s^{-1}$ en electrones y 2000 $cm^2\cdot V^{-1}\cdot s^{-1}$ en huecos) y, sobre todo, su conductividad térmica (22 $W\cdot cm^{-1}\cdot K^{-1}$). El diamante es además un material muy interesante para muchas disciplinas gracias a ser químicamente inerte, silicio-compatible, no tóxico y transparente a un alto rango de radicación (rayos ultravioletas, visible e infrarrojo lejano y cercano).

Existen dos técnicas por las cuales se puede fabricar diamante sintético: alta presión-alta temperatura (HPHT) y deposición química de vapor (CVD). La deposición química de vapor es una técnica muy usada en la tecnología de procesado de materiales. Por medio de esta técnica se logran producir materiales y polvos de una gran pureza y su rango de uso abarca prácticamente la totalidad de los elementos de la tabla periódica.

En su modo más simple, el crecimiento por CVD se resume en la introducción de uno o varios gases precursores en una cámara que alberga, calentado, el material sobre el cual se quiere hacer la deposición. Debido a la gran versatilidad de la técnica, hay muchas variantes de la misma. Existen crecimientos por CVD a presiones que van desde por encima de la atmosférica hasta alto vacío, con tubo de reactor caliente y frío, con trasporte de gases y sin él y con temperaturas de trabajo que típicamente van desde los 200°C hasta los 1600°C.

El crecimiento de diamante sintético, sin embargo, ha sido siempre algo muy complejo y hasta hace bien poco se creía que solo sería posible por HPHT. Fue en 1962 cuando se patentó el primer diamante crecido por CVD pero hubo que esperar hasta los años ochenta para que la técnica fuera reproducible y menos costosa. Las dificultades encontradas están relacionadas con la complejidad de las reacciones químicas que tienen lugar durante la deposición de diamante por CVD. Este proceso es completamente diferente a la formación de diamante natural y se lleva a cabo en condiciones de no equilibrio dado que, en condiciones normales, es grafito, fase mucho más estable del carbono, lo que se obtiene. Para lograr el crecimiento de diamante, se hace uso de radicales de hidrógeno. Estos radicales son uno de los principales actores del crecimiento, participando en: la eliminación del grafito formado inintencionadamente, la activación de los enlaces superficiales del sustrato y la creación de radicales de carbono. Así pues, el metano, principal precursor de carbono durante la deposición de diamante por CVD, se diluye en hidrogeno antes de entrar en la cámara de crecimiento.

Pero para la fabricación de dispositivos electrónicos basados en diamante es necesario dopar a éste mediante la introducción de impurezas en su red cristalina. Al contrario de lo que ocurre con la mayoría de los semiconductores, el diamante tiene una celda unidad muy compacta que imposibilita el uso de la mayoría de los elementos para su dopado. El nitrógeno es el dopante más común debido a la similitud de su radio

covalente con el del carbono (0.079 y 0.077nm respectivamente). Sin embargo, la sustitución de un átomo de carbono por uno de nitrógeno distorsiona mucho la red incrementando la energía de ionización por encima de 1.7eV. Por eso, son el boro y el fósforo los elementos más usados como dopantes en diamante. Estos tienen radios covalentes lo suficientemente próximos al carbono como para introducirse en la red de forma sustitucional y las propiedades electrónicas que le proporcionan los hacen más interesantes desde el punto de vista electrónico.

Gracias a sus propiedades, el diamante se ha convertido en uno de los semiconductores más prometedores para sustituir al silicio en sus aplicaciones en alta potencia. El diamante es un material de ancha banda prohibida que podría reducir hasta en un 90% las pérdidas de energía de los conversores DC-AC y AC-DC. Además, puede trabajar a mucho más alto voltaje que el silicio y tolera temperaturas de trabajo muy elevadas.

Unos de los dispositivos electrónicos que pueden ser mejorados sustancialmente con el uso de diamante son los diodos Schottky. Un diodo Schottky es un dispositivo unipolar que utiliza el comportamiento de transporte de corriente no lineal de un rectificador de unión metal semiconductor bajo tensión de polarización aplicado. Dicho dispositivo se comporta como un interruptor accionado por la tensión de polarización a través de sus terminales. Los diodos Schottky se utilizan en sistemas de conversión de potencia basados en silicio debido a su rápido tiempo de recuperación y su bajo voltaje. Los diodos Schottky de diamante se presentan como los dispositivos más prometedores pues, a día de hoy, ya ha mostrado el mayor campo de ruptura logrado en semiconductores, así como una gran reducción de la resistencia de serie. Sin embargo, estos dispositivos aun adolecen de problemas técnicos tales como la resistencia en serie, que sigue siendo muy elevada, o los bordes de los contactos, que son muy cortantes y generan grandes campos eléctricos localizados que limitan el voltaje de ruptura de vuelta.

Por esto, la mejora de los dispositivos electrónicos de potencia basados en silicio no puede basarse únicamente en el uso de diamante, sino que la geometría en el diseño también debe jugar un papel fundamental. No en balde, muchos de los problemas encontrados en los diodos Schottky de diamante pueden ser solventado con el uso de geometrías tridimensionales. Por ejemplo, la resistencia en serie del diodo se reduce drásticamente con el uso de geometrías verticales y el uso de dichas geometrías facilita el diseño de contactos menos abruptos que evitan los fuertes campos eléctricos localizados en esos puntos. Además, existen ventajas adicionales, como son la reducción de la resistencia de estado activo (ON), la versatilidad que da poder jugar con el plano de crecimiento (mejores dopados sobre planos 111 o mayor calidad cristalina en los planos 311…) o la miniaturización del dispositivo.

En este sentido se está avanzado mucho en el plano internacional y son varios los grupos que trabajan en el desarrollo de dispositivos de diamante de geometría vertical o pseudo-vertical. Sin embargo, la mayoría de estos trabajos están encaminados a la fabricación y caracterización eléctrica de éstos dispositivos, encontrándose muchas dificultades. El desconocimiento de los mecanismos de crecimiento de diamante homoepitaxial que tienen lugar sobre sustratos grabados con estructuras tridimensionales es uno de los principales puntos débiles. Por ello, esta tesis tratará su estudio, así como el de la generación de defectos durante dicho crecimiento y la incorporación de dopante (boro) para su implementación en un diodo Schottky.

Durante este trabajo se realizarán estudios estructurales de las muestras que se llevarán a cabo principalmente mediante microscopía electrónica. La microscopía electrónica engloba las técnicas de caracterización que se basan en el estudio de las reacciones que tienen lugar en un material cuando sobre este impacta un haz de electrones. Cuando el haz barre la muestra, se tiene microscopía electrónica de barrido (SEM). La técnica SEM empleada detecta los electrones secundarios

generados en el material para dar una imagen en tres dimensiones de la superficie de la muestra.

La modificación de estos microscopios SEM incluyéndoles un cañón de iones permite la nanofabricación. Esta técnica, conocida como haz de iones focalizados (FIB por sus siglas en inglés), usa el haz de iones para el grabado de la muestra y, en nuestro caso, ha sido usado para la preparación de muestras electrón-transparentes para su observación por microscopía electrónica de transmisión.

Cuando el haz de electrones incide en la muestra también puede emitir luz. Esta es debida a la recombinación de electrones de la capa de conducción y huecos de la banda de valencia y su estudio proporciona información química y electrónica del material. Esta técnica es conocida como catodoluminiscencia (CL).

Por último, cuando el haz de electrones, en lugar de barrer la muestra, la atraviesa tenemos la microscopía electrónica de transmisión (TEM). Esta técnica requiere de muestras electrón-transparentes y permite altas magnificaciones.

Además de la caracterización estructural, en el presente trabajo se han realizado estudios simples de caracterización eléctrica. Se ha tratado de la obtención de curvas I-V con un rango de voltajes de -20V a 20V realizados con un equipo de fabricación propia equipado con sondas micrométricas, un microscópico óptico y una fuente de unidad de medida de canal simple Keithley SMU 2601A.

I.5.2. Résumé

Le diamant est un état métastable du carbone connu pour ses propriétés physiques étonnantes. Ces qualités résultent de la grande densité et la forte liaison covalente sp^3 que forment les atomes de carbone. Ceux-ci sont liés en symétrie tétraédrique au sein de deux systèmes possibles : (i) une

symétrie hexagonale (très rare), et (ii) le plus habituellement, une symétrie cubique, qu'il s'agisse d'un matériau naturel ou synthétique.

Parmi les propriétés les plus remarquables du diamant, on notera sa dureté, sa grande mobilité des porteurs de charge (1000 $cm^2 \cdot V^{-1} \cdot s^{-1}$ pour les électrons et 2000 $cm^2 \cdot V^{-1} \cdot s^{-1}$ pour les trous) et, surtout, sa très grande conductivité thermique (22 $W \cdot cm^{-1} \cdot K^{-1}$, 5 x le cuivre). En outre, le diamant est un matériau très intéressant dans de nombreux domaines parce qu'il est chimiquement inerte, compatible avec le silicium, non-toxique et transparent à un large spectre de radiation (ultraviolet, visible, infrarouge proche et lointain).

Il y a deux techniques avec lesquelles il est possible de faire croître le diamant synthétique, l'une à haute pression et haute température (HPHT), et l'autre par dépôt chimique en phase vapeur (CVD). Le dépôt chimique en phase vapeur est une technique largement utilisée depuis qu'elle a été brevetée en 1954. Grâce à cette technique, il est possible de produire des matériaux et des poudres de haute pureté. La gamme d'utilisation couvre la quasi-totalité des éléments de la table périodique.

Dans son mode le plus simple, la croissance CVD peut être résumée comme l'introduction d'un ou plusieurs précurseurs gazeux dans une chambre qui contient, chauffé, le matériau sur lequel doit être fait le dépôt. En raison de sa grande souplesse, il existe de nombreuses variantes de cette technique. La croissance par CVD est possible à des pressions allant d'au-dessus d'une atmosphère à un vide poussé, avec un réacteur à paroi chaude ou froide, avec transport de gaz ou sans, et à des températures de travail qui vont de 200 °C à 1600 °C.

La croissance du diamant synthétique, cependant, a toujours été très complexe et, jusqu'à récemment, on pensait qu'elle n'était possible que par HPHT. C'est en 1962, que le premier diamant cru par CVD a été obtenu. Il a fallu attendre jusqu'aux années quatre-vingts pour disposer d'une technique reproductible et moins coûteuse. Les difficultés sont liées à la complexité des réactions chimiques qui se produisent pendant le dépôt de

diamant par CVD. Ce procédé est complètement différent de la formation du diamant naturel et il est réalisé hors d'équilibre. Le graphite est la phase stable du carbone dans les conditions normales. C'est l'une des raisons pour lesquelles les radicaux d'hydrogène deviennent l'un des acteurs majeurs de la croissance. Ces radicaux participant à l'élimination du graphite formé, à l'activation des liens de surface de substrat et à la création des radicaux de carbone. Ainsi, le principal précurseur du carbone au cours du dépôt de diamant CVD est du méthane dilué dans l'hydrogène juste avant d'entrer dans la chambre de croissance.

Mais, pour la fabrication de dispositifs électroniques à base de diamant dopé, il est nécessaire d'introduire des impuretés. Contrairement à ce qui se passe avec la plupart des semi-conducteurs, le diamant possède une maille cristalline très compacte qui ne permet pas beaucoup de variété d'éléments pour le dopage. Ainsi, l'azote est le dopant le plus analogue au carbone en raison de la similitude de leurs rayons covalents (0.07nm et 0.079, respectivement). Cependant, la substitution d'un atome de carbone par un azote déforme beaucoup le réseau cristallin. En fait, ce sont le bore et le phosphore qui sont les plus utilisés comme dopants dans le diamant. Ces atomes ont des rayons covalents assez proches de celui du carbone et peuvent s'incorporer dans le réseau cristallin en substitution. Les propriétés électroniques qui résultent de ce dopage les rendent incontournables.

Grâce à ces propriétés, le diamant est devenu un des semi-conducteurs les plus prometteurs pour remplacer le silicium dans les applications de haute puissance. Le diamant est un matériau à large bande interdite qui pourrait réduire jusqu'à 90% de perte d'énergie des convertisseurs DC-AC et AC-DC. En outre, on peut travailler à beaucoup plus haute tension que le silicium et à des températures de travail beaucoup plus élevées.

Certains dispositifs électroniques peuvent être améliorés sensiblement avec l'utilisation du diamant : ce sont les diodes. Une diode Schottky est un dispositif unipolaire en utilisant le comportement de transport de courant

non linéaire de redresseur d'une jonction métallique semi-conducteur. Un tel dispositif se comporte comme un interrupteur déclenché par la tension de polarisation sur ses bornes. Les diodes Schottky sont utilisées dans les systèmes de conversion d'énergie à base de silicium en raison de leur temps de récupération rapide. Les diodes Schottky en diamant ont montré le plus grand champ de claquage jamais atteint par un semi-conducteur et une grande réduction de la résistance série. Cependant, ces dispositifs souffrent encore de problèmes techniques tels que la résistance série, qui est encore très élevée, ou les bords des contacts, qui sont très abrupts et génèrent des champs électriques localisés qui limitent la tension de claquage.

Par conséquent, l'amélioration des dispositifs électroniques de puissance à base de silicium ne peut pas résulter de la seule utilisation du diamant, mais la géométrie devrait également jouer un rôle clé dans la conception. La plupart des problèmes rencontrés par les diodes Schottky de diamant peuvent être résolus en utilisant des géométries tridimensionnelles. Par exemple, la résistance série de la diode est considérablement réduite par l'utilisation de géométries verticales et l'utilisation de telles géométries facilite la conception de contacts moins abrupts afin d'éviter de forts champs électriques localisés. En outre, des avantages supplémentaires, tels que la réduction de la résistance de l'état ON, la possibilité de jouer avec le plan de croissance (plus dopés sur les plans {111} ou avec une meilleure qualité cristalline dans les plans {311} ...) ou la miniaturisation du dispositif.

En ce sens, il y a plusieurs groupes internationaux qui travaille sur le développement de dispositifs de diamant avec géométrie verticale ou pseudo-verticale. Cependant, la plupart de ces travaux sont destinés à la fabrication et la caractérisation électrique de ces appareils. Mais, pour une bonne implémentation de la technologie 3D, la compréhension des mécanismes de croissance de diamant homoépitaxial sur substrats gravé avec des structures en trois dimensions est essentielle. Ils sont étudiés dans cette thèse, ainsi que la génération de défauts pendant la croissance et

l'incorporation de dopant (bore) pour la mise en œuvre dans une diode Schottky.

Au cours de ce travail, les études structurales des échantillons seront principalement réalisées par microscopie électronique. La microscopie électronique comprend des techniques de caractérisation basée sur l'étude des réactions qui se déroulent dans un matériau quand celui-ci est exposé à un faisceau d'électrons. Lorsque le faisceau balaie l'échantillon, c'est la microscopie électronique à balayage (MEB). Par MEB les électrons secondaires générés dans le matériau sont utilisés pour obtenir une image en trois dimensions de la surface de l'échantillon.

Une modification de ces microscopes MEB consiste à ajouter un canon à ions permettant la nanofabrication. Cette technique est connue sous le nom de faisceau d'ions focalisé (FIB). Dans notre cas, le faisceau d'ions utilisé pour la gravure de l'échantillon a été utilisé pour la préparation d'échantillons assez fins pour être transparents aux électrons, ce qui permet l'observation par microscopie électronique en transmission.

Le faisceau d'électrons qui vient frapper l'échantillon peut également provoquer une émission de lumière. Les recombinaisons des électrons de la bande de conduction avec des trous de la bande de valence donnent lieu à un émission de radiation dont l'étude fournit des informations chimiques et électroniques sur le matériau. Cette technique est connue sous le nom de cathodoluminescence (CL).

Enfin, lorsque le faisceau d'électrons, plutôt que de balayer l'échantillon, passe à travers l'échantillon, c'est la microscopie électronique à transmission (MET). Cette technique nécessite des échantillons transparents pour les électrons et permet de forts grandissements.

En plus de la caractérisation structurale, le présent travail comporte des études simples de caractérisation électrique. Nous avons essayé d'obtenir des courbes I-V avec une gamme de tensions de -20V à 20V réalisée avec un équipement fait maison équipé de sondes micrométriques, d'un microscope

optique en utilisant un seul canal de l'unité de mesure et d'alimentation Keithley SMU 2601a.

II Growth and technology: tuning parameters

Contents

Substrate preparation and growth process are discussed in this second chapter, introducing the techniques and facilities used. Growth resulted in a clearer faceting when using low methane concentrations. Moreover, such a lower concentration seemed to affect the crystal quality: a lower density of superficial defects was observed on such samples.

II.1. Substrate selection

Samples studied in the present thesis were grown under the supervision of Dr. David Eon at the Institut Néel (France) growth facility (DiamLab) during the stays carried out in the years 2015, 2016 and 2017. Diamond growth was performed following protocols already established in that research center. An introduction of such protocols is presented below.

Homoepitaxial overgrowth was performed on commercial {100}-oriented HPHT substrates. Selection of the substrate is not a trivial matter because many parameters such as roughness, crystalline defects or miscut angle (misorientation between the surface and the crystal orientation) are known to have a strong influence on the quality of the final overgrown sample [Martineau 2009]. In order to choose the best diamond substrate for the growth process, different characterization techniques are available. These techniques provide information about growth sectors, miscut, superficial and sub-superficial defects, as well as roughness. Growth sectors are mainly important on HPHT substrates [Bauer 2005]. In that case, growth velocity and superficial atomic bond density both depend on the growth orientation, implying different values of impurities incorporation. On the other hand, miscut angle controls the kinetic of the atomic superficial reconstructions modes during the growth process, playing a crucial role in the crystalline quality [Tsuno 1996, Battaile 1998, Watanabe 1999, Takeuchi 2000, Miyatake 2007, Maida 2008 and Friel 2009]. Superficial and sub-superficial defects play also an important role in the crystal quality of the overgrowth since has been proved that their presence generates new defects in the overgrown layer [Martineau 2009].

In our case, the selection was reduced due to the particularities of the overgrowth. This will be performed on etched substrate. Therefore, the initial roughness and superficial defects density will not play any crucial role (since the substrates will be etched prior the growth). Thus, the substrate characterization process has been reduced to only two studies carried out as described in the next sections.

II.1.1. Miscut angle

Miscut angle is defined as the crystallographic surface misorientation of the sample respect to a major crystallographic orientation. Such measurements are carried out by x-ray diffraction where symmetric Bragg reflections, i.e. [400], are used. The width of an x-ray diffraction peak is a sensitive function of the angle of incidence when the angle of incidence is less than 1°. In this way, the misorientation angles (miscut angles) are obtained as a function of the peak width. X-ray

diffractometer used here was a CrysoTAX model from the European Synchrotron Radiation Facility (ESRF), located at Grenoble.

II.1.2. Sub-superficial defects.

Sub-superficial defects such as dislocations have been revealed by White Beam Topography. This technique is based on diffraction processes. An incident white x-ray beam impinges on the sample and scan its surface. This beam is refracted providing a map of intensities of the signal refracted that reflects the distribution of scattering power inside the crystal. X-ray topography therefore reveal the irregularities in a non-ideal crystal lattice. Defects information is obtained from the modification that such defects generates in the crystal network. This maps provide then such information by showing the dislocations as black lines on the X-ray topography. Fig.II.1 shows an x-ray topography of a diamond substrate.

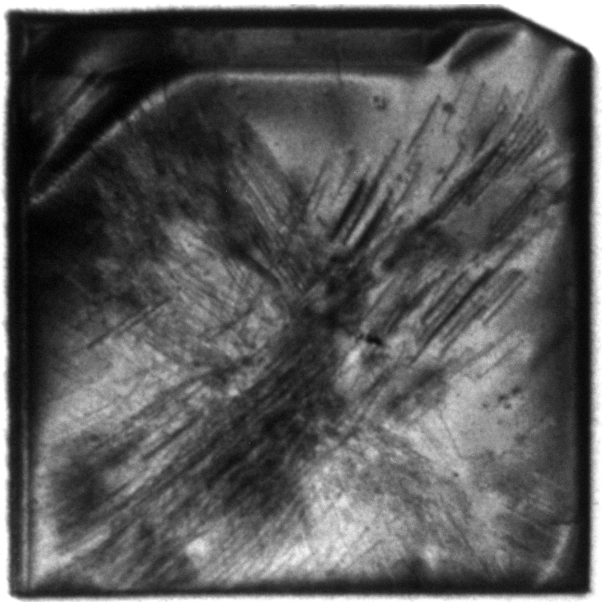

Fig.II.1. X-ray topography of a HPHT diamond substrate where black lines correspond to defects.

II.2. Lithography: Achieving a 3D surface

Overgrowth will be carried out on 3D patterned substrates. In addition to the etching itself, the process of etching includes the design of the mask, chemical cleaning, lithography and metallization. These processes were performed at the NANOFAB cleanroom from Institut Néel in collaboration with the Upstream Technological Platform (PTA-Grenoble) from CEA-Renatech, are schematized in Fig.II.2 and explained below.

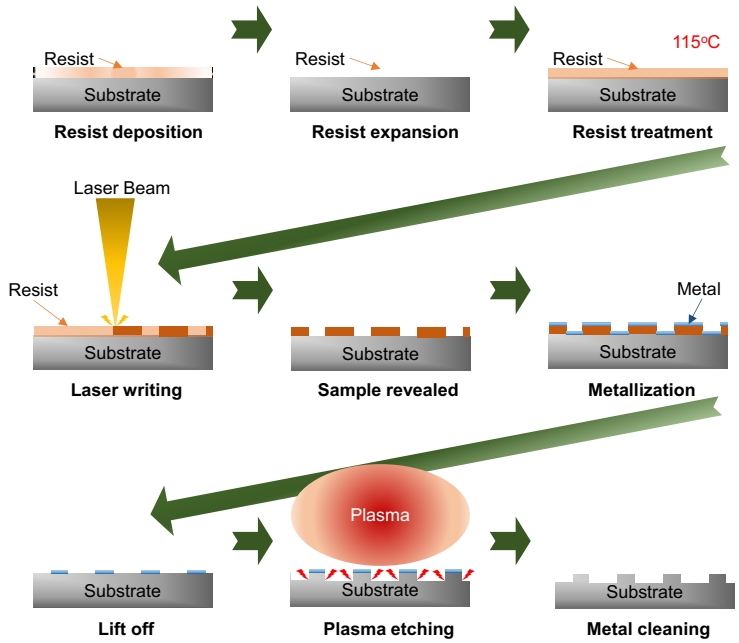

Fig.II.2. Flowchart of a lithographical etching process including all technological steps, from resist deposition to metal cleaning.

II.2.1. Mask design

Mask design, shown in Fig.II.3, was performed using the copyleft software *Klayout* (www.klayout.de). The mask, aiming at the study and understanding of lateral growth*, has been designed using two different patterns: (i) mesa rectangles (1μm, 2μm, 3μm, 5 μm and 10μm width) and (ii) mesa disks (1μm, 2μm, 3μm, 5μm and 10μm diameter). Mesa rectangles make it easier to study specific orientations because of the constant width. Different separations in between the mesa rectangles, have been used, as well as four different orientation (0º, 45º, 90º and 180º) in order to study terrace coalescence processes. Disks allow to perform an analysis of 3D-growth, to study growth orientations along each plane as well as to study coalescence along random directions. Thanks to the circular shape, studies of preferential faceting and oriented growth rates can be carried out.

* In the current thesis, lateral growth is understood as growth carried out along the lateral side of the mesa structures, *i.e.* any growth along a different orientation than the one from the substrate, it is the [100] one.

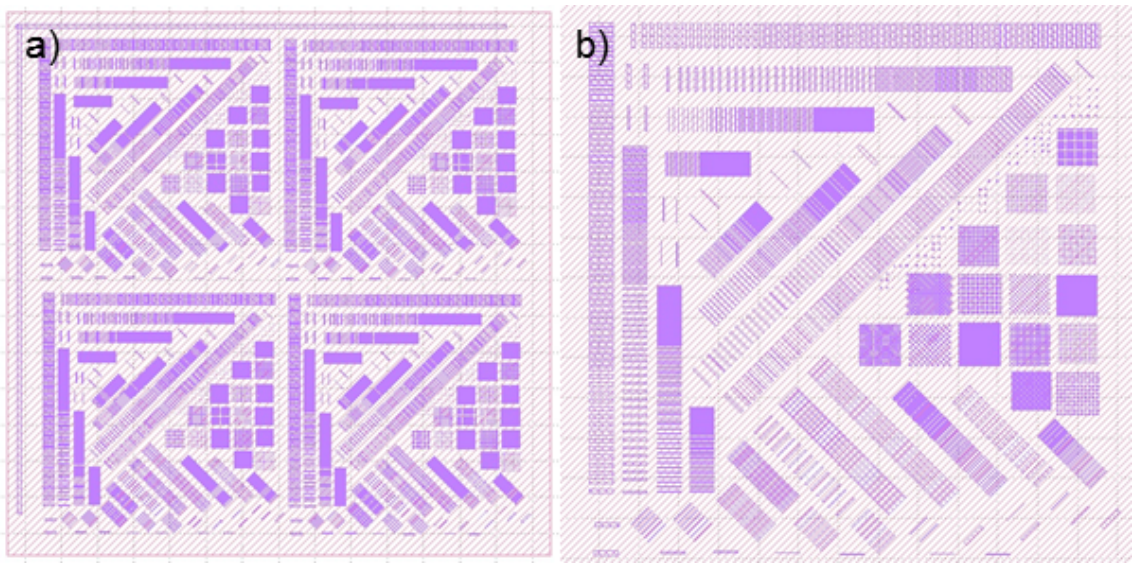

Fig.II.3. Design of mask. (a) full mask designed and (b) one of the patterns which are repeated four times on the full mask. There are combinations of structures (arrays of mesa disk and mesa rectangles), in order to study the different dynamic growth processes such as the coalescence, and individual structures, in order to study the growth of structures from an individual point of view.

Fig.II.4 shows SEM micrographs of one of the samples after the etching by using this mask. Different arrays of mesa structures (rectangles and disks) where obtained. For some patterns, distances were too close and the structures remained together (see Fig.II.4 (d)). Nevertheless, the variety and number of motifs was high enough to perform the desired studies.

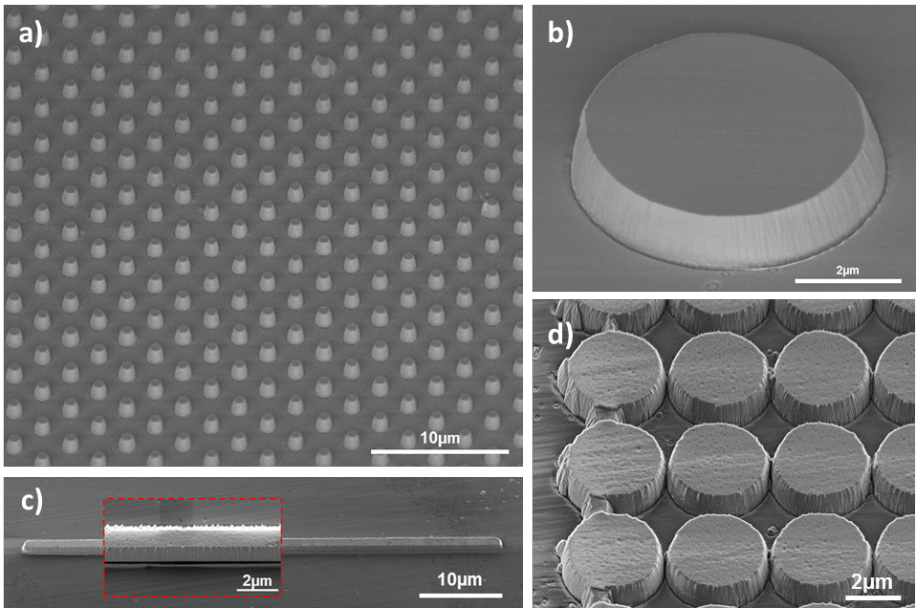

Fig. II.4. SEM micrographs of (a) general view of 1μm diameter mesa disk, (b) and individual mesa disk of 5μm diameter, (c) and individual mesa rectangle and (d) an array of very close 3μm diameter disk.

II.2.2. Chemical cleaning

Once substrates have been selected according to their miscut angles and density of superficial defects and before the lithography process, the following surface cleaning has been undertaken:

3 acid bath (objective: remove oxides and metal contaminations):

The solution is composed by 1 part of perchloric acid ($HClO_4$ 70%), 4 parts of nitric acid (HNO_3 67%) and 3 parts of sulfuric acid (H_2SO_4 98%). The aim of this step is to eliminate oxides and metal contaminants as well as superficial amorphous carbon (Sp_2 bonding). The sample was immersed in the bath and heated at 450ºC per 2 hours. During the process, solution turned yellow. Cleaning was finished only when the solution has come back to its transparent initial color.

Ultrasonic bath (objective remove organic contaminations)

To eliminate residual acid traces, the sample was rinsed with DI water and immersed in an acetone ultrasonic bath for 2 min. This bath cleans off the rests of acid and organic contamination. The sample is rinsed with ethanol after the acetone treatment, and then dried in a dry Ar flow.

II.2.3. Lithography

Laser lithography has been carried out with a Heidelberg DWL 66fs Laser Writer. The resist used was a S1805 that was expanded over the whole surface with a thickness of ~500nm by spinning the sample at 6000rpm. After that, the sample was heated at 115ºC per 1 min to treat the resist and introduced in the laser writer for lithography. Lithography process was carried at 3% of power and 56 of dose. The required exposure time was less than 4 min.

Afterward, the photo resist was developed in a 1:1 solution of Micro Dev water and DI water for 1 min. Samples were rinsed in DI water and dried with argon flow prior to checking under an optical microscope. The results of one of these checks are shown in Fig.II.5.

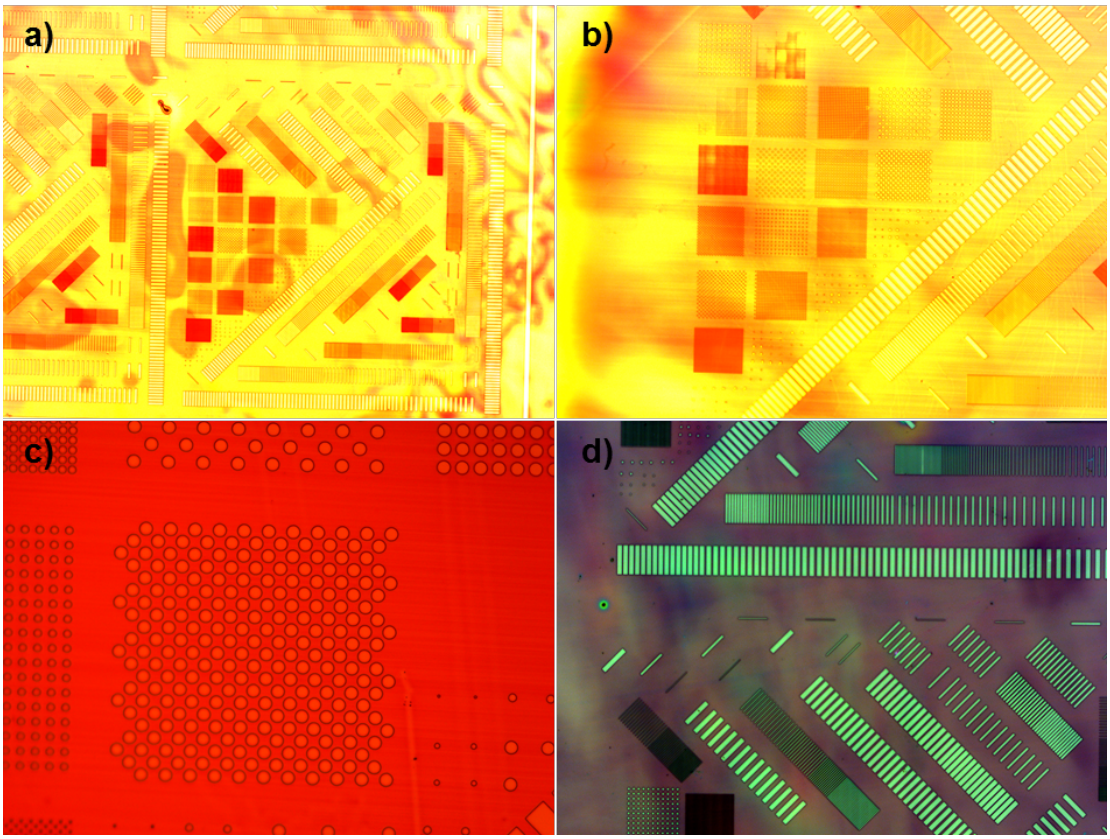

Fig.II.5. Optical micrograph of sample #8 (a, b and c) and #9 (d) after lithography. Structures are well defined as higher magnification micrographs (c and d) shown.

The spinning velocity during the cover of the surface by the resist is a critical parameter. If it is too slow, it generates a thicker and inhomogeneous resist layer. Under this condition, the laser writer cannot focus resulting in bad defined structures. If it is the case, samples must be cleaned by two baths of 1 minute in acetone and ethanol and the lithography process repeated using optimum spinning conditions.

II.2.4. Metallisation

The process of metallisation has been carried out in a Plassys MEB550S evaporator. It works at high vacuum (around 10^{-6} Torr). The system available at the NanoFab cleanroom has 8 different metals for depositions that include nickel, aluminum and gold. Based on the *rapport de stage* of Raphaël Fillon in 2012 [Fillon 2012], the metal used for the deposition of masks was aluminum. Deposition has been carried out at a pressure of $\sim 4 \times 10^{-6}$ Torr. The target consists in an aluminum source placed in a crucible on which an electron beam was focused by magnetic fields (see Fig.II.6). The beam was accelerated by HV and it scanned homogeneously the surface of the target to generate the metal evaporation avoiding the creation of craters. The current employed

for the electron gun was modified during the process from 300 mA to 350 mA increasing this way the ratio of deposition from 0.110 nm/s to 0.170 nm/s. The thickness of aluminum deposited was 150 nm (it was estimated in-situ by a piezoelectric sensor).

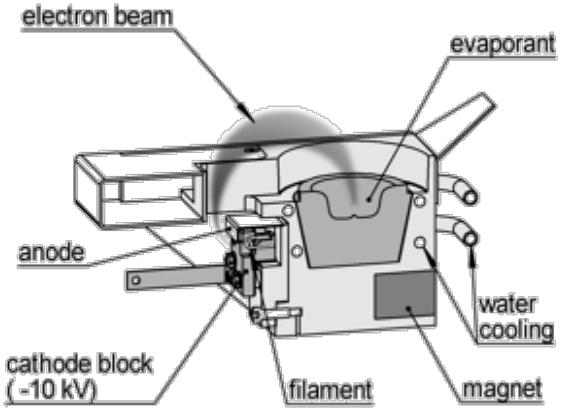

Fig.II.6. Schematics of a typical e-beam crucible. A tungsten filament is inside of a cavity and both (filament and cavity) are at the same negative potential. This cavity generates the electrostatic field which forms the beam. Electrons are directed to the ground potential of the material in the crucible. The electromagnetic coils direct the beam, and the surrounding magnetic fields guide and focus the beam on the target. The emission of electrons is carried out by the filament. These electrons are accelerated by the electrostatic field generated by the cavity. A beam is formed by carriers in movement so the cavity (as it is the generator of the electrostatic field) forms the beam.

After metal deposition, lift-off of the resist was carried out. Samples were introduced in an ultrasonic bath of acetone for two minutes and cleaned by alcohol for another two minutes. They were dried with argon flow and were observed by optical microscopy. Results are exposed on Fig.II.7.

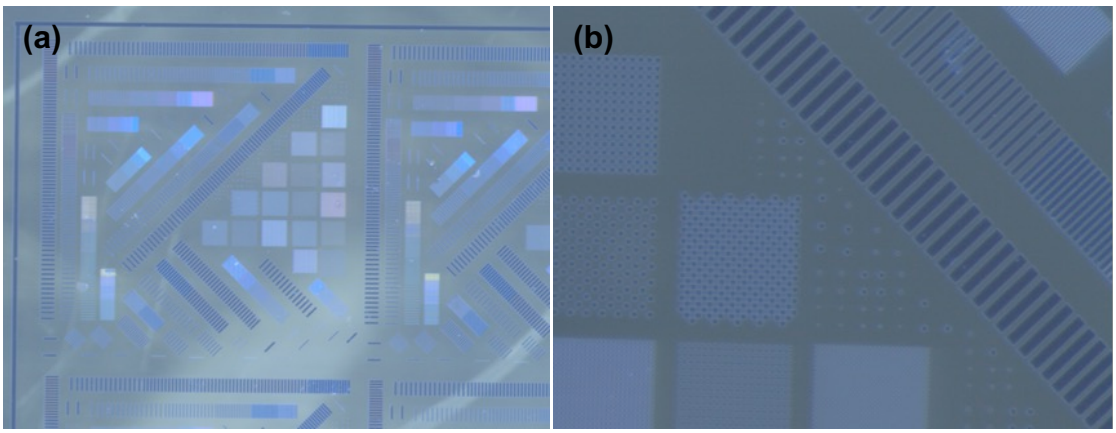

Fig.II.7. Optical micrographs of the substrates (sample #9-HMCU) after the lithography. Substrate remain marked with aluminum in the places where the resist was not exposed to ("written by") the laser beam.

II.2.5. Reactive Ion Etching

CNRS-Institut Néel gave us the opportunity to choose between two different dry etchings. One of them was the Reactive Ion Etching (RIE) that took place in a PLASSYS RIE reactor. Such technique consists in an oxygen plasma induced by radio-waves (13.56 MHz). The main etch process is a physical one that provides a quasi-perpendicular etching (not lateral etching). The conditions of etching were optimized to obtain the best quality of surface: 20 sccm of oxygen flow, 46 and 21 tune and load, 300 W of power, 1100 V Bias and $1x10^{-1}$ Torr of pressure. However, optical profilometry studies showed a very rough surface advising against this technique. Fig.II.8 shows as example one of the cases studied where a significant roughness is observed.

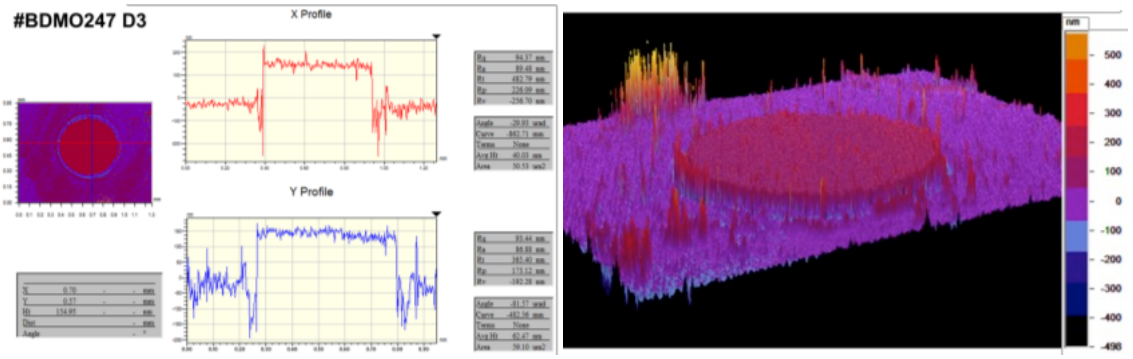

Fig.II.8. Profiles and 3D reproduction of the optical measurements performed on sample BDMO247 after etching. Height of the mesa disk (etched) was 200 nm. This study was carried out in a Veeco 3D optical profilometer Contour GT characterized by fair lateral resolution (0.5μm) and very high vertical resolution (<0.1nm).

II.2.6. Inductively Coupled Plasma – Reactive Ion Etching

Due to the unsatisfactory results using RIE, etching has been performed by inductively coupled plasma etching (ICP) in the Upstream Technological Platform of Grenoble (PTA-Grenoble). ICP etching is a reactive ion etching process that allows an independent control of plasma density and reactive ion energy onto the etched surface. Accordingly, two radio frequency (RF) sources are therefore used in such etching reactors (see Fig.II.9). The first RF source powers a coil generally wrapped around the etching chamber which, by an inductive coupling through a dielectric wall, allows plasma ignition and its control. The second RF source was used to power the substrate holder by capacitive coupling. Thus, a negative self-bias was generated on the holder that attracts the positive ions towards the etched surface and furthermore defines their kinetic energy. This second RF source defines both the etching rate and its anisotropy. The key parameters in such etching process are both the coil power (CP) and the substrate holder (SH) power. A high

CP power promotes a high density of reactive species. Conversely, a low SH power favors smooth etching by chemical reaction while a high SH power promotes a high etching rate and anisotropic etching by sputtering mechanism. Pure oxygen plasma etching was performed to delineate the pseudo-vertical structure with a 1000 W coil power, a 40 W substrate holder power, a 100 sccm gas flow, and 10 mTorr pressure. The CP and SH powers were selected to favor a smooth etching in order to preserve the selectivity of aluminum etching mask used.

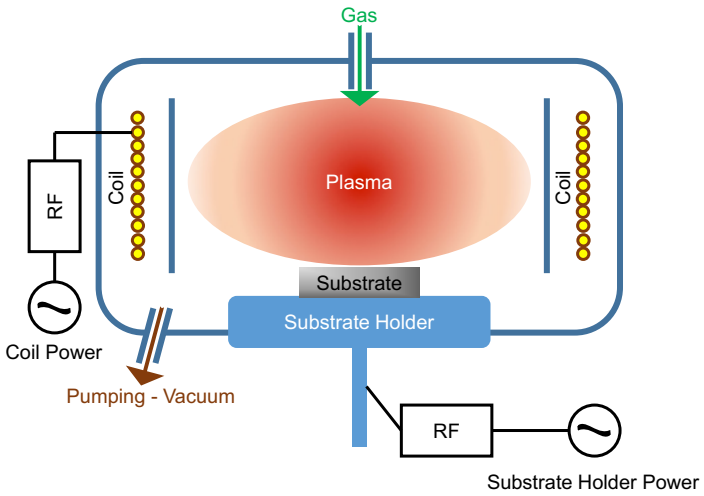

Fig.II.9. Schematics of the ICP reactor. The main parts of the reactor are indicated by labels.

II.3. Growth

Following the techniques and procedures described above, and after a new chemical bath, diamond epilayers have been grown in a home-made NIRIM type plasma enhanced chemical vapor deposition reactor. Fig.II.10 shows the schematic diagram of this growth apparatus [Fiori 2012]. This home-made reactor is a modified Japanese (NIMS lab) MPCVD reactor [Kamo 1983], which has the specificity of featuring a plasma ball located at the intersection of a rectangular waveguide and the cylindrical growth chamber. The gaseous mixture was injected from the top of growth chamber composed by an inner (25 mm diameter) and an outer (40 mm diameter) quartz tubes. A microwave generator, operating at 2.45 GHz (power range 0-2 KW), was used as plasma excitation source. The sample holder, formed by a patterned silicon substrate coated with a polycrystalline diamond layer, was located on the top of the inner tube fixed to a liner Z-axis guided UHV magnetically coupled metallic transporter. Thus, the deposition temperature could be set either by adjusting vertically the sample holder position compared to that of the plasma ball, or by changing the microwave power. A mono color pyrometer (960 nm), with an emissivity set

at 0.4, was used to estimate the sample temperatures taking in account the contribution of the sample holder.

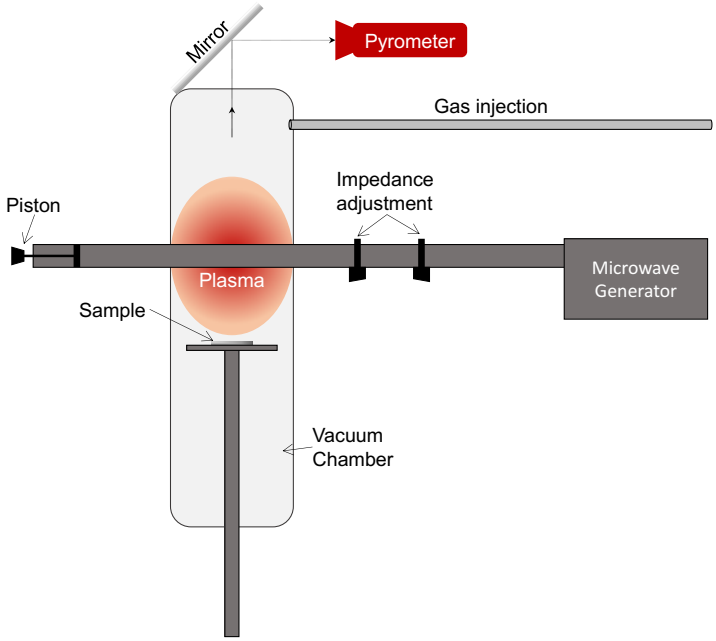

Fig.II.10. Schematic diagram of the home-made NIRIM type reactor used for the growth.

The growth pressure was set with a throttle valve actuated by a PID controller with five set points. The available pressures are 2.5, 4, 9, 33 and 50 Torr. In this thesis, 33 and 50 Torr were the pressure used for diamond growth, and 4 Torr for pure hydrogen plasma ignition.

Samples grown for the present study were doubly named: (i) by their order of use in the experiments and (ii) by a feature of their growth. For example, sample #3-LMCD is the third, **#3**, sample studied and it was grown at **L**ow **M**ethane **C**oncentration and with **D**oped layers.

II.3.1. Undoped layers growth

Chicot *et al.* [Chicot 2012] demonstrated high crystal quality of {100}-oriented undoped diamond with a gaseous mixture of 1 % CH_4 and 0.25 % O_2 in hydrogen gas, under 33 Torr pressure and 910°C substrate temperature. These conditions were reproduced in the growth of sample #1-F for a duration of 70 minutes [Fiori 2012]. Unfortunately, they led to a high density of surface defects as shown[†] in Fig.II.11. These defects were firstly attributed to surface

[†] The author would like to thank to A. Fiori for the figure.

contamination during the growth process [Traoré 2015], however their origin is investigated in Chapter IV where a full study of defects is presented.

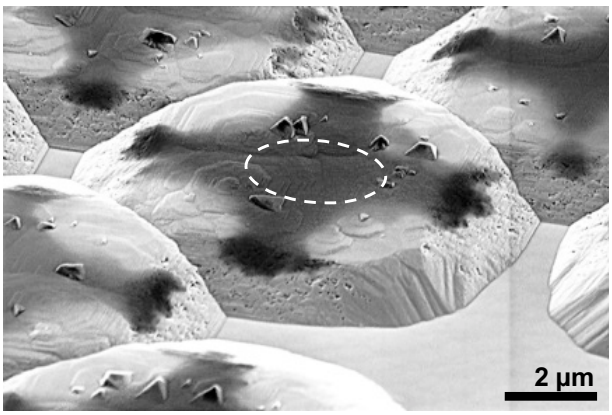

Fig.II.11. †Tilted SEM micrograph of sample #1-F. The initial shape of the etched mesa disk is marked by a dashed white circle. Many superficial defects are shown on the top of the overgrowth structures.

To assess if superficial defects observed on sample #1-F comes from extended crystallographic defects and substrate imperfections [Tallaire 2008], or by surface contamination [Traoré 2015], growth conditions were adjusted mainly reducing CH_4 flow which should result in the minimization of such surface contamination. In this way, sample #5-α16 was grown with 0.75% CH_4 and 0.25% O_2 in hydrogen gas, using 50 Torr pressure and a temperature of 910ºC. Duration of the growth was 30 min. It is worth to note that this overgrown sample looks less faceted, even though some isolated defects still persisted (see Fig.II.12).

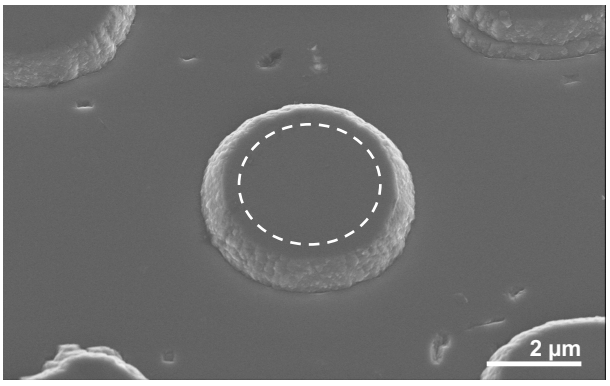

Fig.II.12. Tilted SEM micrograph of sample #5-α16. Sample surface seems cleaner but some superficial defects are still shown on the surface of the sample. Initial size of the mesa disk is marked by a dashed white circle. Final disk wall looks less facetted, probably due to the small overgrown thickness.

Based on such encouraging results, growth conditions used for sample #9-HMCU were similar. Methane concentration remained at 0.75% but oxygen ratio was increased to 0.32%. Pressure and temperature were set at 33 Torr and 900ºC respectively. Duration of growth was 140

min. Sample surface in Fig.II.13 also showed surface defects that were restricted to the top of the corner of the initial structures. However, mesa disk and rectangles are revealed to be highly facetted in the SEM micrograph of Fig.II.14. This indicates that those growing conditions are very selective versus crystalline orientation which is desirable for the present study. However, comparing to the growth conditions used in the literature, these are close to 100- standard growth parameters, mainly differing in the use of O_2. Oxygen has reported to influence in growth velocities and faces [Issaoui 2011], such influence will be discussed in the following chapters.

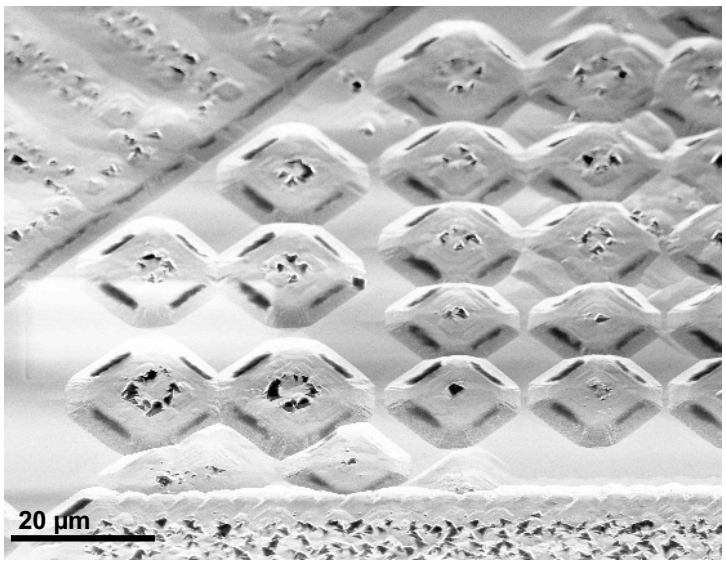

Fig.II.13. SEM micrograph of a group of mesa disk and mesa rectangles of sample #9-HMCU.

Table II.I shows a comparison of growth parameters used by different authors depending on the growth crystallographic direction (GD in the table) followed during the growth. The main differences are related to the pressure and methane concentration. Authors such as Hoshino *et al*. [Hoshino 2012] increase the pressure in order to grow along the {111}-orientation. In fact, along this orientation, pressure is always above 50 Torr (75 Torr in most of the cases). However, the same authors use lower pressures for {100} oriented growth (usually 25 Torr). The use of lower methane ratios during the growth along the 111 orientation is an obvious general trend. Except for one case in which the CH_4/H_2 was 0.15 % (even so, also very low), all cases studied used methane concentrations lower than 0.1% relative to hydrogen when the growth occurred along the 111 orientation. Nevertheless, these authors used higher concentrations (mainly between 0.4-0.6 %) for the cases of growth along the 100 direction. Table II.I points out the fact that authors modify the methane concentration according to the plane of growth and that such modifications correspond to an increase for growth along 100- orientations and, to a decrease for growth over 111- oriented substrates.

Table II.I. Comparative table of growth conditions used by authors from the bibliography. GD references to growth direction. Temperature is in Celsius, pressure in Torr, power in watts and CH_4/H_2, PH_3/CH_4 and B_2H_6/CH_4 are in %.

GD	Temp	Press	Power	CH_4/H_2	PH_3/CH_4	B_2H_6/CH_4	Substrate	Reference
100	900	25	750	0.2	-	-	HPHT 100	Hoshino 2012
111	930	75	750	0.05	50	-		
100	800	25	750	0.6	-	-	HPHT 100	Sato 2014
111	850	75	750	0.05	50	-		
100	950	25	750	0.4	5	-	HPHT 100	Kato 2009
111	930	75	750	0.05	50	-		
100	1200	50	900	0.6	-	0.8	HPHT 100	Makino 2014
100	750	25	900	0.4	5	-		
111	900	50	1200	0.05	-	-	HPHT 111	
111	800	50	750	0.05	0.01	-		
111	800	50	1200	0.15	-	0.1		
111	800	75	750	0.05	50	-		
111	900	50	1200	0.05	50			
100	1050	75	260	1.8	0.12	-	HPHT 100	Pinault-Thaury 2015

Nevertheless, growth conditions used by others authors for 111- oriented diamond involved an even higher pressure and lower methane concentration than that used in the growths here exposed [Hoshino 2012, Sato 2014, Makino 2014]. Aiming to favor this lateral growth against the normal 100, growth conditions were modified for sample #8-LMCU whereby CH_4 mixture was reduced to 0.1 %, near to the minimum detected by the flowmeters, and oxygen was not used. Pressure was kept at 33 Torr to have the sample in the middle of the plasma ball avoiding inhomogeneous growth [Johnston 1991], and temperature was set at 900ºC. At this methane concentration, growth is too slow. A duration of 840 min was required to yield a layer thickness similar to that of sample #9-HMCU. Fig.II.14 shows great differences in the final shape of this sample where the overgrown mesa disk (Fig.II.14 (a)) looks cross-like. In addition, superficial defects were drastically reduced, although a few still remained (see Fig.II.14 (b)).

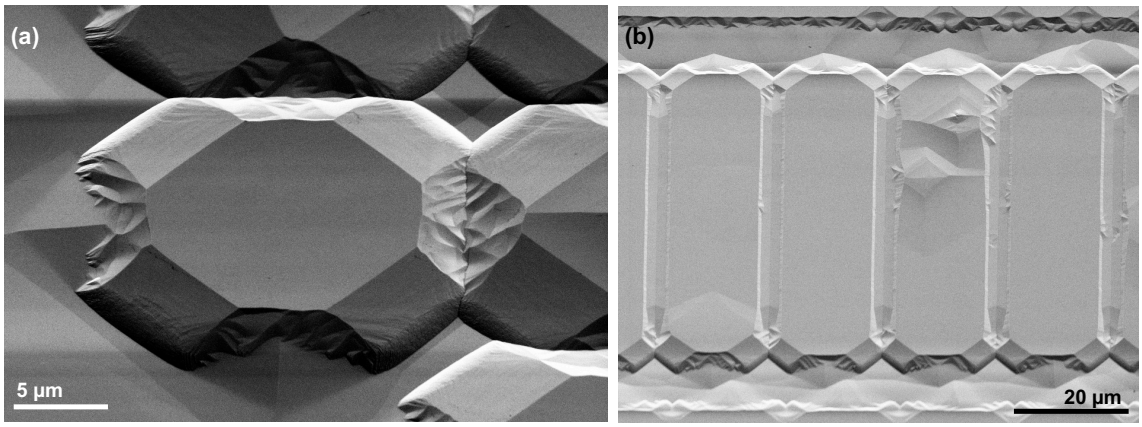

Fig.II.14. SEM micrograph of sample #8-LMCU of (a) a mesa disk overgrowth and (b) a group of mesa rectangles.

II.3.2. Boron doped layers growth

The goal of this thesis is to understand the mechanisms governing the lateral growth, in order to implement them in the design and fabrication of a Schottky device. Such applications require thin boron doped layers whose growth must also be studied. Conditions of 4% of methane in hydrogen and ([B]/[C]) of at least 10^3 ppm have been proposed as the most efficient in this reactor to lower the density of defects such as dislocations with a high growth rate (13-30 nm/min) [Traoré 2015]. In order to study the lateral growth of boron doped layers, sample #6-α10 was grown using these optimized conditions with a mixture of diborane of [B]/[C]=1200 ppm and a pressure of 33 Torr and 830°C temperature. Fig.II.15 shows an array of overgrown mesa disks where low facetting is observed. Mesa disks also shows fractures and dirtiness. Surface shows some pitch-like defects, however such superficial defects are likely attributed to plasma etching.

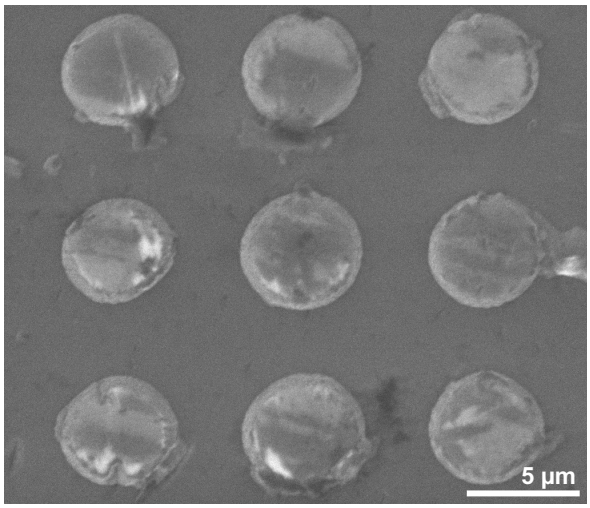

Fig.II.15. SEM micrograph of an array of overgrown mesa disks of sample #6-α10.

For sample #7-β10, methane concentration in hydrogen was reduced to 0.5% and diborane increased to 6000ppm with 50 Torr pressure and 830ºC temperature. Growth was performed for 10 min. These conditions were used in order to increase the facetting of the walls while keeping the boron incorporation into the layer. However, the final result, showed in Fig.II.16, does not show higher facetting than sample #6-α10. Nevertheless, surface is shown clean and smooth under the SEM microscope. Superficial defects were not observed indicating a better etch and growth process.

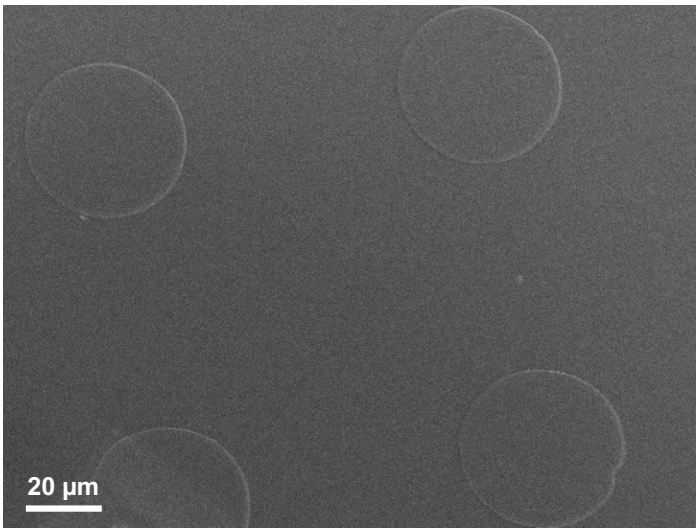

Fig.II.16. SEM micrograph of an array of overgrowth mesa disk of sample #7-ß10. A fist look shows the surface clean and free of superficial defects.

II.3.3. Multilayers growth

In addition to the monolayers samples growth, a group of samples have been grown including a superlattice structure. Sample #2-A is composed by stack of 10 boron-doped/undoped bilayers. Boron doped layers were grown with a mixture of 0.5% methane in hydrogen and 14000 ppm [B]/[C] and a duration of 11 min and 60 nm of nominal thickness. Undoped layers were grown with a methane concentration of 0.75% and gaseous mixture of 0.32% of oxygen, in hydrogen both. These layers were grown for 12 min with a nominal thickness of 100 nm. During the growth process, temperature and pressure were kept at 900ºC and 33 Torr, respectively. Fig.II.17 shows a SEM micrograph of sample #2-A with superficial hillocks-like defects filling the surface. Nevertheless, it was possible to identify at least two different kinds of hillocks: (i) some which were arbitrarily distributed on the top of the sample with almost the same size and square shape, and (ii) irregular hillocks appearing near the corner of the mesa structures. Many of the (i) and (ii) defects were marked by arrows on Fig.II.17 where they seem to be caused by different

mechanisms. The regular shape and size of all the (i) hillocks indeed indicates that they began to grow at the same time, probably at the beginning of the growth, and that they are somehow related to deficiencies in the plasma etching. In fact, they were likely generated on etch-pits. On the other hand, (ii) hillocks show random sizes and not regular shapes. It means they were not generated at the same time of the growth process and their mechanism of generation was attributed to the growth conditions and/or to the shape of the mesa structure, and not to the etching step.

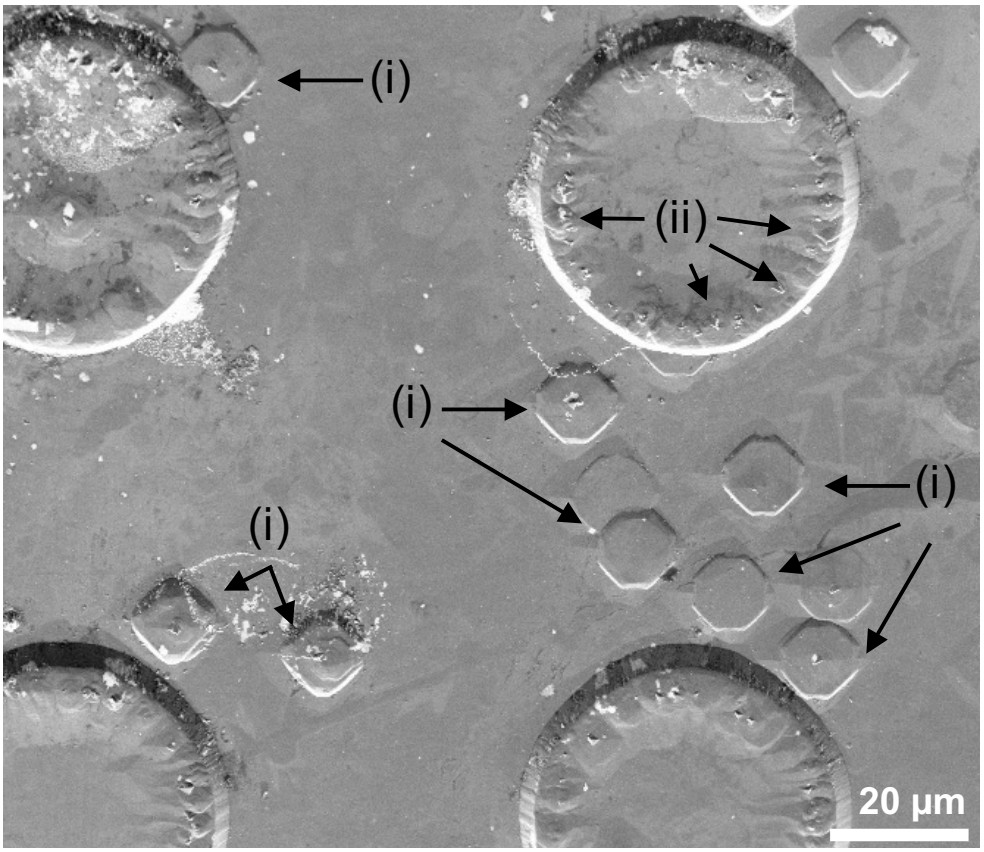

Fig.II.17. SEM micrograph of an array of overgrown mesa disks of sample #2-A. Superficial defects are indicated by arrows and identified by their shapes as type (i), regular, and (ii), irregular.

Sample #4-HMCD was grown with thirteen boron-doped/undoped bilayer as superlattice structures with growth conditions similar to sample #2-A. Undoped layers were grown with the same recipe but for a duration of 10 min. In contrast, boron concentration during the growth of the boron doped layer was reduced to 9600 ppm of diborane in hydrogen. The growth duration of these layers was also reduced to one minute. Fig.II.18 shows a general view of the overgrown surface that seemed very similar to Sample #9-HMCU, i.e. with plenty of superficial defects. By comparing such superficial defects with those observed in sample #2-A, the existence of both, (i) and (ii), types was apparent also in this case. However, the number of so-called (i) hillocks seemed smaller here.

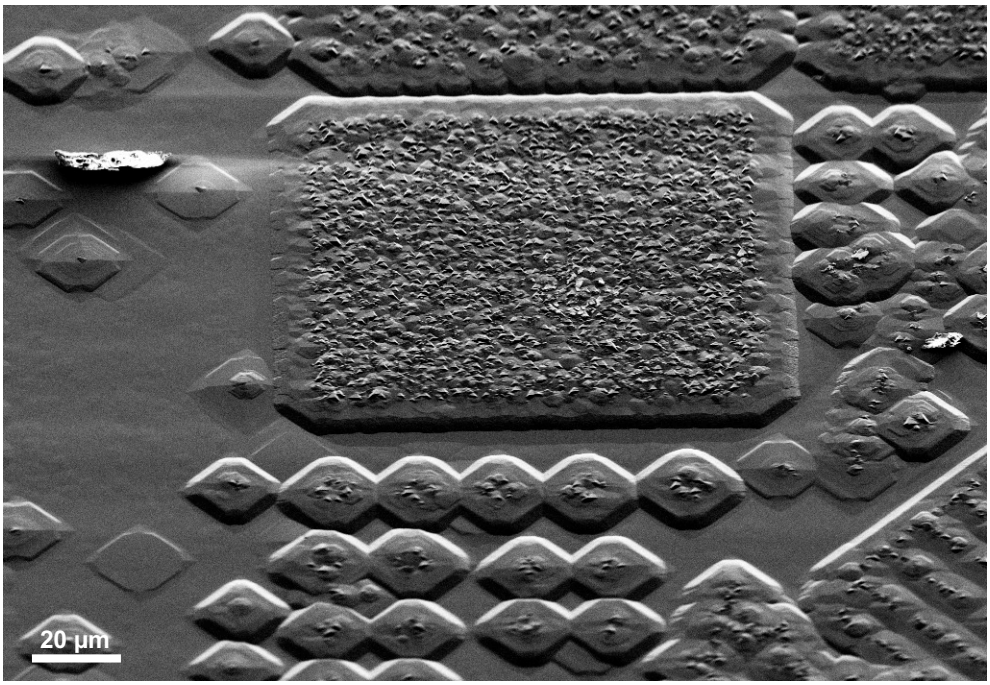

Fig.II.18. SEM micrograph of an array of overgrowth mesa disk and mesa rectangles of sample #4-HMCD.

In order to obtain results similar to sample #8-LMCU in a multilayer structure, sample #3-LMCD has been grown as a stack of 13 lightly boron-doped/undoped bilayers. Growth conditions for the undoped layers were the same than for sample #8-LMCU, CH_4/H_2=0.1 %, and 60 min of duration per layer. Doped layer required an increase of the methane concentration due to diborane reducing the sp^3 bonding formation during growth [Zou 2016]. For this reason, methane mixture in hydrogen was 0.25 % and diborane concentration relative to carbon was 10700 ppm. Duration of growth of doped layers was 2 min in order to have very thin structures. Fig.II.19 shows a SEM micrograph of sample #3-LMCD that looks very similar to sample #8-LMCU.

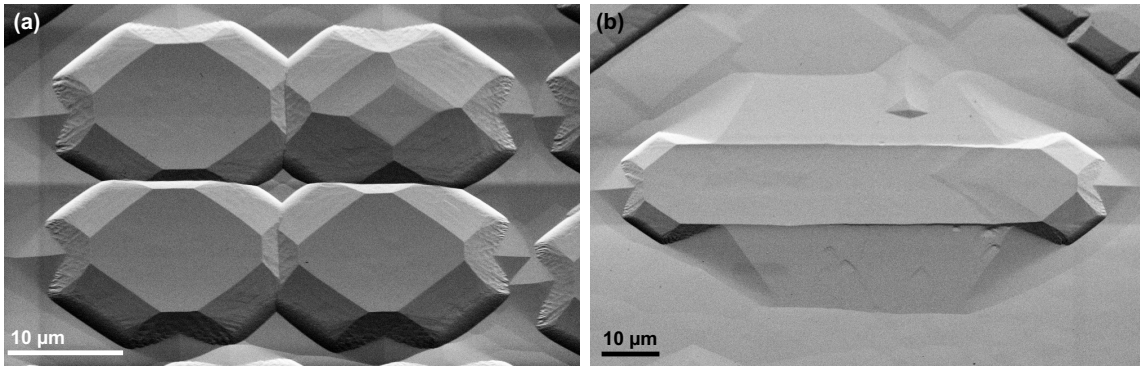

Fig.II.19. SEM micrograph of sample #3-LMCD of (a) an array of overgrowth mesa disks and (b) a mesa rectangle.

Based on the apparently good results on the growth of samples #8-LMCU and #3-LMCD, sample #10-LMCD has been grown with similar parameters, that is CH_4/H_2=0.1 % during the undoped layers growth and CH_4/H_2=0.25 % during the doped layers. In this case, only 6 doped-undoped bilayers were grown, with a duration of 1 hour for the undoped and 5 minutes for the doped ones. However, a low-quality HPHT diamond was used as substrate and it was etched with mesa structures up to a height of 2.7 μm instead of the 900nm value used for samples #3-LMCD and #8-LMCU. Diborane concentration was increased in order to have higher doping level and the ratio used was B/C=28000 ppm. As used in samples #8-LMCU and #3-LMCD, temperature and pressure were set at 900ºC and 33 Torr, however in this occasion power had to be reduced to 280 W to not overshoot such temperature. Fig.II.20 shows two SEM micrographs of the sample after growth. Fig.II.20 (a) shows a mesa structure with a squared shape. Surface of the sample looks clean of superficial defects. However, some roughness is observed mainly on the lateral sides of the mesa disk. These observations are also done on Fig.II.20 (b) that shows the same disk tilted 30º. The squared shape looks octahedral-like, similar to the shape observed for sample #1-F (see Fig.II.11). Nevertheless, growth conditions of sample #10-LMCD are very similar to the one of sample #3-LMCD but for a shorter time. It seems that the final shape of the mesa disk is strongly dependent of the growth time. In this way, the axes of the cross-like final shape of sample #3-LMCD would be formed after the first 3 hours of growth. A dashed white circle marks the initial shape of the disk.

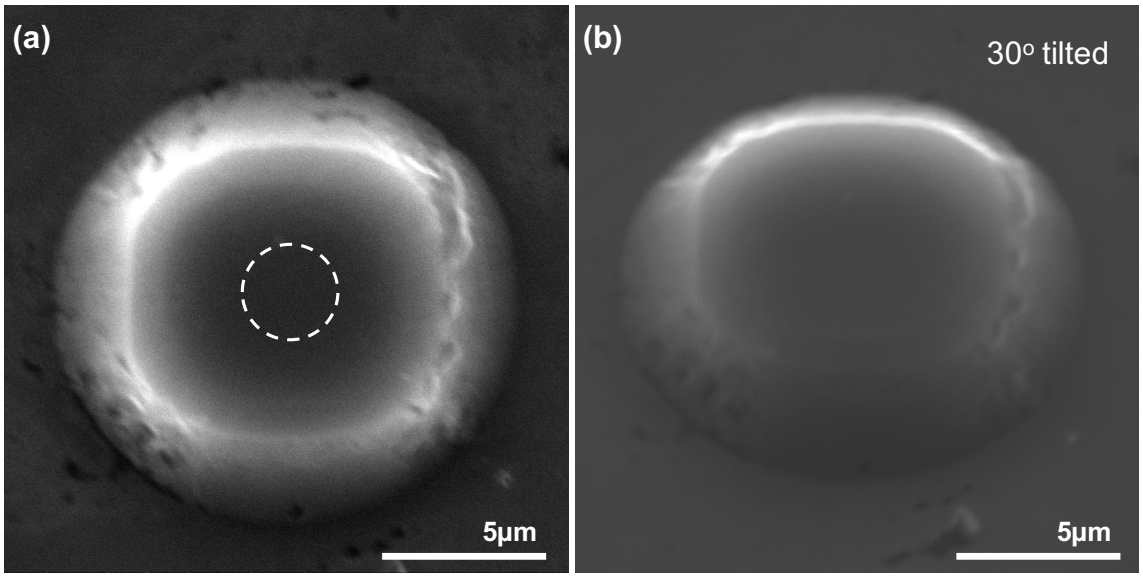

Fig.II.20. SEM micrographs of sample #10-LMCD with the sample (a) not tilted and (b) 30º tilted.

II.3.4. Sample #11-Disp

Originally intended to the device fabrication, sample #11-Disp is not englobed in any of the previously discussed groups. Substrate of this sample was also a {100}-oriented HPHT diamond. Over this substrate, and before any etching, a p^+ layer was growth during 15 minutes with a mixture of diborane of [C]/[B]=1200 ppm. On this layer, a thick undoped layer was growth using concentrations of methane and oxygen of 0.74% and 0.25% over hydrogen. The duration of this second growth was 3 hours and 36 minutes (216 min). Thickness were estimated by ellipsometry in 700 nm and 2175 nm, for doped and undoped layers, respectively. This is a classical recipe for p^{++} ohmic contacts at Institut Néel.

This sample was observed by optical microscopy (see Fig.II.21). It shows many superficial defects apparently randomly distributed over the surface of the sample.

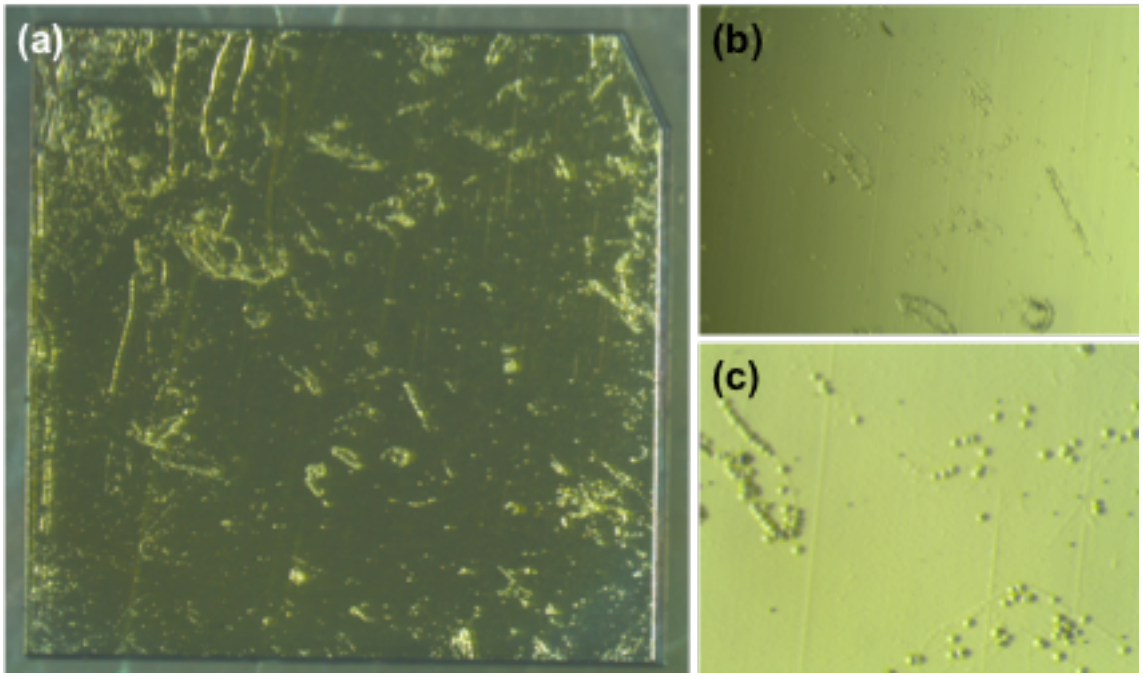

Fig.II.21. Optical microscope images of the sample surface after the first p^{++}/p^- bilayer growth. (a) corresponds to general view of sample #11-Disp. (b) and (c) are more magnified images, respectively.

The sample was then etched away by ICP-RIE, using the same conditions than previously but a different pattern only based in rectangles of 30μm x 1 mm, with their sides oriented along the {110} planes (full explanation about the mask configuration will be provided in *Chapter VI*).

The etched substrate was overgrown by an undoped layer during 3 hours using low methane concentration conditions (CH_4/H_2=0.1 %) and without oxygen, to favor lateral growth, i.e. growth along a different orientation than the one of the substrate (100). SEM micrograph of Fig.II.22 shows that defects observed before etching (see inset optical micrograph) still remain

after the last growth. Some of these defects have been marked by colored circles (red and black) and by arrows to help their identification.

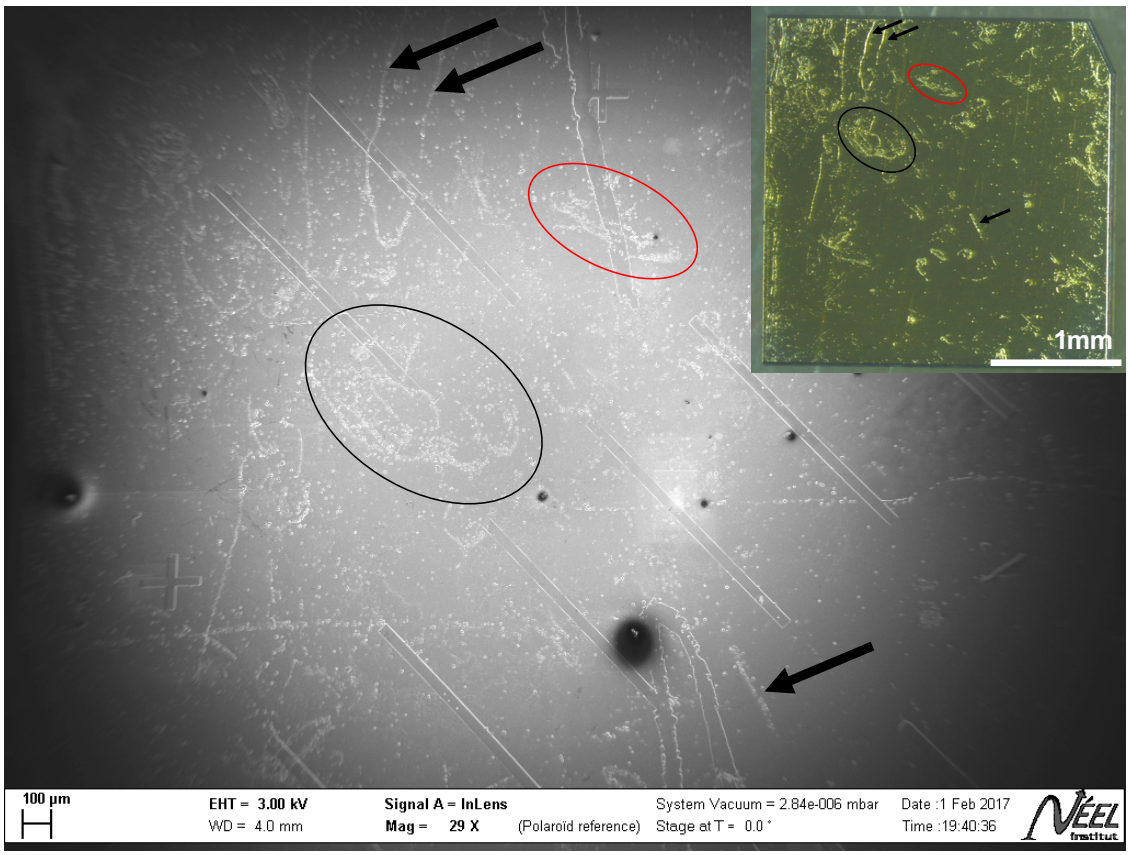

Fig.II.22. SEM micrograph of the surface of the sample after etching and growth. Superficial defects observed have been compared with the ones showed previously by optical microscopy. The optical micrograph is shown as an inset.

In addition to the superficial defects, aspects related to the faceting and growth are observed. Fig.II.23 shows additional SEM micrographs of sample #11-Disp. Fig.II.23 (a) is a low magnification view of the surface of the sample where many superficial defects are shown. Fig.II.23 (b) and (c) show the end of one of the mesa rectangles at higher magnification. Faceting is shown along the planes {011}. Contrast on the top of the overgrown structures seems to show the initial shape of such structures. To help in the identification of the contrast, thin dashed white lines have been drawn at the interface on Fig.II.23 (c) and (e). In fact, this contrast is more evident on Fig.II.23 (d) and (e), recorded with the sample tilted 33.5°. The width of the contrast coincides with the 30μm of the initial shape designed in the mask.

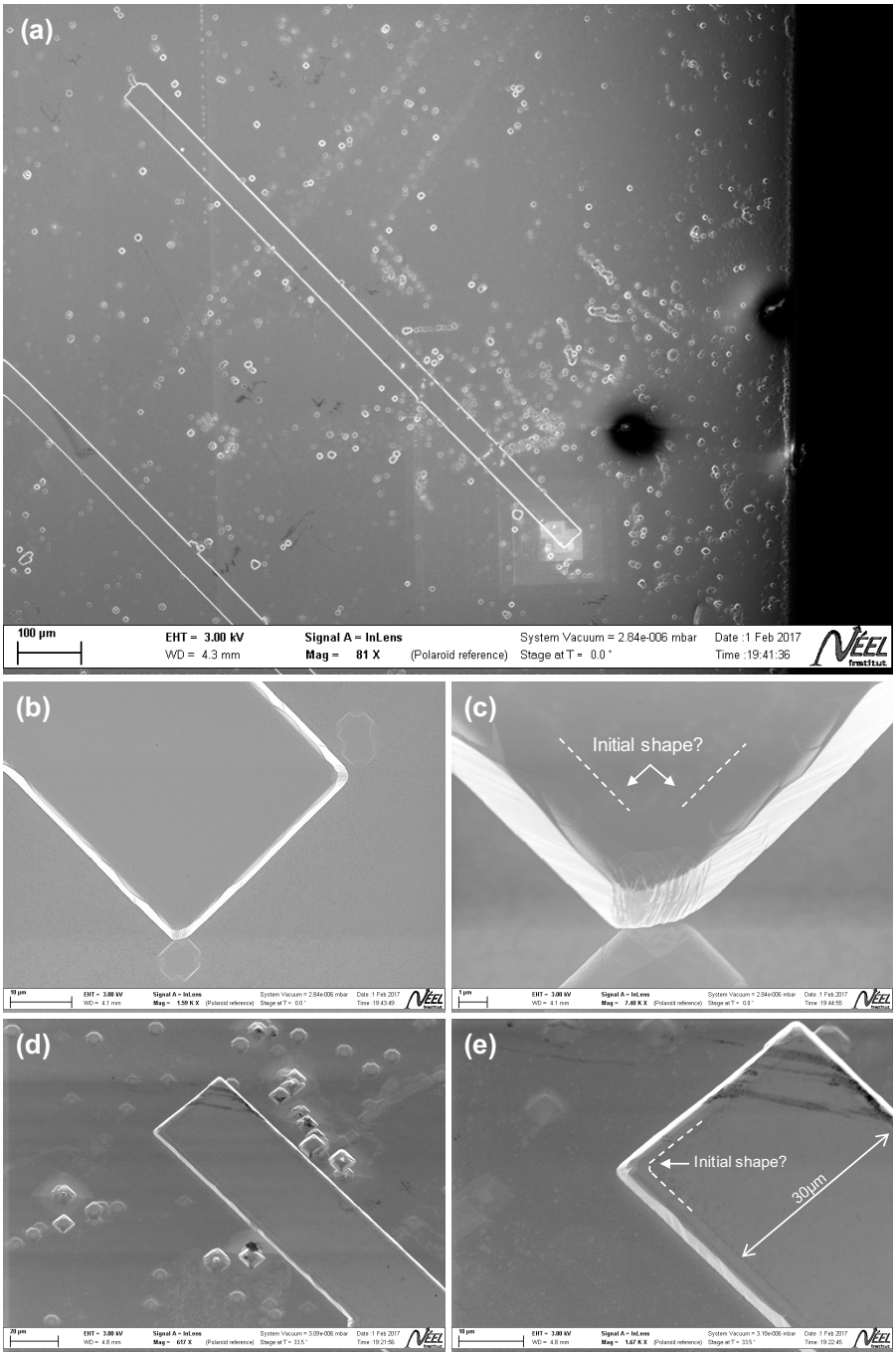

Fig.II.23. SEM micrographs of the sample after the first lateral growth (last p- layer). (a) A overgrown mesa rectangle is shown, surface of the sample exhibits many defects. (b) and (c) are SEM micrograph of one of the corners of the structure where initial shape seems to be shown by a contrast. (d) and (e) show similar SEM micrographs tilted 35°. Here, the contrast from the initial shape is more evident.

Finally, a last doped layer was overgrown on sample #11-Disp for a short duration (8 min). This layer was grown at low methane conditions (CH_4/H_2=0.25%) without oxygen and with a diborane concentration of [B]/[C]=28000ppm.

II.3.5. Summary of structures growth

For all further identifying purposes, table II.II summarizes the growth conditions of the samples studied in this thesis.

Table II.II. Growth conditions of samples used in the present thesis.

Sample	Power (W)	Temp (°C)	Pressure (Torr)	Layer	CH_4/H_2	O_2/H_2	B_2H_6/CH_4	Time (min)	
#1-F	300	910	33	Undoped	1%	0.25%	-	70	
#2-A	300	900	33	Doped	0.5%	-	14000	11	x10
				Undoped	0.75%	0.32%	-	12	x10
#3-LMCD	300	900	33	Doped	0.25%	-	10700	2	x13
				Undoped	0.1%	-	-	60	x13
#4-HMCD	300	900	33	Doped	0.5%	-	9600	1	x13
				Undoped	0.75%	0.32%	-	10	x13
#5-α16	310	910	50	Undoped	0.75%	0.25%	-	30	
#6-α10	280	830	33	Doped	4%	-	1200	10	
#7-β10	230	830	50	Doped	0.5%	-	6000	10	
#8-LMCU	300	900	33	Undoped	0.1%	-	-	840	
#9-HMCU	300	900	33	Undoped	0.75%	0.32%	-	140	
#10-LMCD	280	900	33	Doped	0.1%	-	28000	5	x6
				Undoped	0.25%	-	-	60	x6
#11-Disp	260	900	33	Doped	4%	-	1200	15	
				Undoped	0.75%	0.25%	-	216	
	280	920		Undoped	0.1%	-	-	180	
				Doped	0.25%	-	28000	8	

II.4. Conclusions

From the premises here exposed, we concluded that laser lithography and ICP-RIE etching are the most adequate techniques for patterning the substrate. Etching conditions have been optimized in order to obtain the best results with a relatively high etch rate.

The SEM micrographs showed in this chapter demonstrate the importance of the CH_4 concentration. Low concentration (0.1%) implies slower growth rate and more facetted structures, i.e. seems to improve the lateral growth quality. In addition, superficial defects seem to be highly

affected by the concentration of methane. The effect of the methane concentration on the CVD diamond growth is here also revealed by a fast survey of the bibliography. Many references used high pressure and low methane concentration for the growth into 111-oriented diamond substrates, whereas for growth on 001-oriented diamond, pressures used to be lower and methane concentrations higher [Hoshino 2012, Sato 2014, and Makino 2014]. Moreover, n^+ doped diamond grown on 001-oriented substrates at low methane concentrations has been reported to exhibit 111-facetted lateral growth [Hoshino 2012]. These parameters result from different optimization processes carried out on different machines. However, a clear tendency is here shown where 111- growth direction is optimum for low methane concentrations whereas high methane concentrations is more beneficial to 100- direction of growth. This implies that, even on 100-oriented substrates, 111 oriented faces can be promoted by using the favorable growth conditions. On the other hand, Hoshino *et al*. considered in their work continuous growth orientation throughout the whole process. The use of doped layers will test the reality of such an assumption.

Nevertheless, the CH_4/H_2 ratio is not the only parameter to take in account. Samples with the same methane concentration show very different final shapes. This is the case of samples #5-α16 and #9-HMCU. In this case, temperature is slightly different (10°C) but the main differences are in pressure, O_2/H_2 ratio and time. Moreover, samples #10-LMCD and #8-LMCD, both overgrown with quite similar conditions, show very different faceting. This difference is only attributed to the smaller growth time used during sample #10-LMCD.

In fact, all the above mentioned parameters play a role during the growth process. For example, the oxygen ratio was shown to influence the growth orientations and rates. Issaoui *et al*. studied the MPCVD diamond growth at a low boron concentration where the use of oxygen resulted in the inhibition of the {1 1 0} and {113} planes [Issaoui 2011]. Other authors also pointed out the effect of pressure on its growth [Johnston 1991]. In the current thesis, all these effects will be taken into account and discussed as far as possible.

Finally, the case of sample #11-Disp, whose contrast in SEM micrographs make out the anisotropic character of the growth, seems to confirm that low methane concentration favor the growth along the lateral sides of the structures and inhibits the growth along the {100}-orientation.

II.5. Summaries

II.5.I. Resumen

En el presente capítulo, se han expuesto las condiciones y técnicas utilizadas durante la realización de la tesis para el crecimiento de muestras de diamante.

El primer punto a considerar es la selección de un sustrato óptimo para el crecimiento. A este efecto, se han utilizado sustratos comerciales HPHT orientados en el plano (100) adquiridos en la empresa SUMITOMO. Dado que los sustratos serán grabados antes de proceder al crecimiento, su selección se simplifica. Así, de todos los factores que se suelen tener en cuenta para el crecimiento de diamante homoepitaxial masivo, solo será necesario considerar el ángulo de desorientación "miscut" y la densidad de defectos sub-superficial. Ambos parámetros se obtienen mediante técnicas no destructivas.

El ángulo Miscut, como se ha dicho, se define como la desorientación superficial cristalográfica de la muestra con respecto a una orientación cristalográfica principal. Tales medidas se llevan a cabo por difracción de rayos X donde se utilizan reflexiones simétricas de Bragg, en este caso se usó la [400]. El difractómetro de rayos X utilizado aquí fue un modelo CrysoTAX de la European Synchrotron Radiation Facility (ESRF), sito en Grenoble.

Los defectos sub-superficiales tales como las dislocaciones han sido revelados por topografía de haz blanco (White Beam Topography). En esta técnica, que se basa en procesos de difracción, un haz de rayos X blanco impacta sobre la muestra y escanea su superficie. Este haz es refractado proporcionando un mapa de intensidades de la señal refractada que refleja la cristalinidad de la muestra. De esta forma, la topografía de rayos X revela las irregularidades en una red cristalina no ideal. La información de defectos se obtiene de la modificación que

estos generan en la red de cristal. Los defectos se revelan como líneas negras en los mapas topográficos.

Una vez seleccionados los sustratos, se procede a su grabado. Si partimos de la base de que es necesaria una superficie vertical para la nucleación del diamante en estas orientaciones, este proceso resulta básico para lograr el crecimiento lateral. Hay que tener en cuenta que en esta tesis se referirá al crecimiento lateral como aquél que ocurre con orientaciones diferentes a la del sustrato. El proceso de grabado se ha llevado a cabo en los laboratorios del instituto Néel, el NANOFAB, y en los laboratorios compartidos por el CNRS y el CEA, el PTA-Grenoble).

La máscara utilizada para el grabado ha sido diseñada con el software KLayout, de libre distribución, y combina discos y rectángulos de diferentes tamaños y separaciones. Los discos permiten un estudio del facetado en orientaciones arbitrarias mientras que los rectángulos, que se han dispuesto en 4 orientaciones posibles (0^{o}, 45^{o}, 90^{o} y 135^{o}) dan información sobre el crecimiento y la coalescencia. Para incrementar las posibilidades de éxito, la máscara se ha cuadruplicado de forma que el grabado final ha consistido en la repetición de cuatro mascaras iguales sobre el sustrato.

Antes de llevar a cabo ninguna manipulación del sustrato estos deben ser limpiados. Para ello se emplea una solución de tres ácidos que elimina las contaminaciones metálicas y de oxidación, así como el carbono amorfo que se haya podido generar en la superficie. Dicha solución está formada por: una parte de ácido perclórico ($HClO_4$ 70%), cuatro partes de ácido nítrico (HNO_3 67%) y tres partes de ácido sulfúrico (H_2SO_4 98%). La muestra es introducida en esta solución durante dos horas a $450^{o}C$. Durante este tiempo, la solución se tornará amarilla y burbujeará. Tras estas dos horas, la solución habrá vuelto a su color transparente original, indicando que el proceso químico ha

terminado. Las muestras se limpiarán entonces en un baño de acetona y ultrasonidos y en etanol para después ser secadas con argón.

Con la muestra limpia y la máscara convenientemente diseñada, se lleva a cabo el proceso de litografía laser mediante un equipo Heidelberg DWL 66fs Laser Writer. La resistencia usada fue S1805. A la litografía le siguió la deposición metálica que se llevó a cabo en una evaporadora Plassys MEB550S. El metal empleado fue aluminio. Las muestras fueron chequeadas por microscopía óptica tras la litografía y metalización.

Para el grabado se hicieron pruebas en dos equipos diferentes. Primero en un reactor de grabado iónico reactivo (RIE) marca Plassys por su mayor accesibilidad y facilidad de uso. Por desgracia los resultados no fueron satisfactorios, con unas velocidades de grabado muy lentas y la superficie de la muestra con una muy mala definición, medida por perfilometría óptica.

Por ello se empleó finalmente un equipo de grabado iónico reactivo de plasma acoplado inducido (ICP-RIE) perteneciente al PTA-Grenoble. Se grabó con una profundidad aproximada de una micra y las muestras fueron chequeadas por SEM.

Tras una nueva limpieza como la indicada previamente, las muestras fuero introducidas en el reactor de crecimiento, un reactor MPCVD de fabricación propia basado en un reactor MPCVD japonés del NIMS. Las muestras crecidas y sus condiciones de crecimiento vienen resumidas en la tabla RES.II.1.

De las observaciones preliminares llevadas a cabo por SEM se ha llegado a las siguientes conclusiones: (i) la concentración de metano es clave para el crecimiento. Bajando su proporción se potencia el facetado y se reduce la densidad de defectos superficiales. Por el contrario, se reduce mucho la velocidad de crecimiento. (ii) La presión

y la duración del crecimiento, así como el uso de oxigeno también influye en la forma final de la estructura. Así, a pesar du utilizar la misma concentración de metano, si modificamos los parámetros anteriormente dichos, el facetado final de la muestra también variará.

RES.II.1.: *Tabla resumen de las condiciones de crecimiento empleadas durante la tesis.*

Muestra	Pot. (W)	Temp (°C)	Pres. (Torr)	Capa	CH_4/H_2	O_2/H_2	B_2H_6/CH_4	Tiempo (min)	
#1-F	300	910	33	No dop.	1%	0.25%	-	70	
#2-A	300	900	33	Dop.	0.5%	-	14000	11	x10
				No dop.	0.75%	0.32%	-	12	x10
#3-LMCD	300	900	33	Dop.	0.25%	-	10700	2	x13
				No dop.	0.1%	-	-	60	x13
#4-HMCD	300	900	33	Dop.	0.5%	-	9600	1	x13
				No dop.	0.75%	0.32%	-	10	x13
#5-α16	310	910	50	No dop.	0.75%	0.25%	-	30	
#6-α10	280	830	33	Dop.	4%	-	1200	10	
#7-β10	230	830	50	Dop.	0.5%	-	6000	10	
#8-LMCU	300	900	33	No dop.	0.1%	-	-	840	
#9-HMCU	300	900	33	No dop.	0.75%	0.32%	-	140	
#10-LMCD	280	900	33	Dop.	0.1%	-	28000	5	x6
				No dop.	0.25%	-	-	60	x6
#11-Disp	260	900	33	Dop.	4%	-	1200	15	
				No dop.	0.75%	0.25%	-	216	
	280	920		No dop.	0.1%	-	-	180	
				Dop.	0.25%	-	28000	8	

II.5.II. Résumé

Dans ce chapitre sont exposées les conditions de croissance et les techniques utilisées lors de la réalisation de la thèse.

Le premier point à considérer est la sélection du substrat optimal pour la croissance. Pour ce motif, ont été utilisés des substrats commerciaux HPHT SUMITOMO. En raison des conditions utilisées dans notre cas particulier, la sélection du substrat est simplifiée. De tous les facteurs qui sont généralement pris en considération pour la croissance massive du diamant homoépitaxial, seulement l'angle de désorientation "miscut" et la densité des défauts sous la surface sont considéré. Les deux paramètres sont obtenus par des techniques non destructives.

L'angle MISCUT, est défini comme la désorientation cristallographique de surface de l'échantillon par rapport à une orientation cristallographique principale. De telles mesures sont effectuées par diffraction des rayons X. Pour ce travail, nous avons utilisé la réflexion [400]. La largeur d'un pic de diffraction des rayons X est une fonction sensible de l'angle d'incidence lorsque l'angle d'incidence est inférieur à 1 °. Les mesures de la largeur des pics de l'angle de diffraction des rayons X pris avec une incidence variable peuvent être interprétées de manière à fournir des informations sur l'angle de désorientation des surfaces de verre de coupe par rapport aux plans de verre principal. Par conséquent, il est possible de mesurer des angles de coupe avec une precision de quelques minutes d'arc. Le diffractomètre à rayons X utilisé ici était un modèle CrysoTAX de l'European Synchrotron Radiation Facility (ESRF) sur le site de Grenoble.

Les défauts sous la surface, tels que des dislocations ont également été révélées par le faisceau blanc de topographie (White Beam Topography).

Une fois que les substrats sont sélectionnés, on peut alors procéder à la gravure. La gravure des substrats est nécessaire car pour obtenir

une « croissance latérale », nous devons l'initier sur une face verticale pour avoir une nucléation et une croissance horizontale. Ce procédé de gravure a été effectuée dans les laboratoires de l'Institut Néel, le Nanofab, et dans les laboratoires PTA-Grenoble, partagé par le CNRS et le CEA.

Le masque utilisé pour la gravure a été désigné avec le software KLayout, distribué gratuitement, et il combine des disques et des tranchées de différentes tailles et dispositions. Les disques permettent l'étude du facettage dans des orientations arbitraires alors que les tranchées, qui sont disposés en quatre orientations possibles (0°, 45°, 90° et 135°) fournissent des informations sur la croissance et la coalescence. Pour augmenter les chances de succès, le masque a été quadruplé de telle sorte que la gravure finale enregistrée se composait de la répétition de quatre masques identiques sur le substrat.

Avant toute manipulation des substrats, ceux-ci doivent être nettoyés. Pour ce faire, une solution de trois acides qui élimine la contamination du métal, l'oxydation ainsi que le carbone amorphe qui a été générées sur la surface, est utilisée. La dite solution est formée par : une partie d'acide perchlorique ($HClO_4$ à 70%), quatre parties d'acide nitrique (HNO_3 67%) et de trois parties d'acide sulfurique (98% H_2SO_4). L'échantillon est introduit dans cette solution pendant deux heures à 450 ° C. Pendant ce temps, la solution devient jaune et bouillonne. Après ces deux heures, la solution sera revenue à sa couleur transparente d'origine, indiquant que le processus est terminé. Les échantillons ont ensuite été nettoyés dans un mélange d'acétone dans ultrasons et d'éthanol et après ont été séché avec de l'argon.

Ensuite, un procédé de lithographie laser est effectué en utilisant un Heidelberg DWL 66fs Laser Writer. Le dépôt de métal aluminium a été effectué dans un évaporateur Plassys MEB550S. Les échantillons ont été

vérifiés par microscopie optique après la lithographie et la métallisation.

Pour les tests de gravure, deux différentes machines ont été utilisée. Le première est un réacteur gravure ionique réactive (RIE) marque Plassys pour sa plus facile accessibilité et utilisation. Malheureusement, les résultats ne sont pas satisfaisants, à cause des vitesses très lentes enregistrées.

Par conséquent, une deuxième machine de gravure ionique réactive de plasma à couplage inductif (ICP-RIE), de PTA-Grenoble a été utilisée. Les épaisseurs et rugosité du dépôt ont vérifiés par MEB.

Après un autre nettoyage identique à celui utilisé précédemment, les échantillons sont introduits dans le réacteur de croissance, un réacteur MPCVD de fabrication propre, basé sur un réacteur japonais MPCVD, habituellement nommé NIRIM. Les conditions de croissance utilisée pour chaque échantillon sont résumées dans le tableau RES.II.2.

RES.II.2. *Tableau récapitulatif des conditions de croissances employées pendant la thèse.*

Echant.	Puis. (W)	T (°C)	Press. (Torr)	Couche	CH_4/H_2	O_2/H_2	B_2H_6/CH_4	Temps (min)	
#1-F	300	910	33	No dop.	1%	0.25%	-	70	
#2-A	300	900	33	Dop.	0.5%	-	14000	11	x10
				No dop.	0.75%	0.32%	-	12	x10
#3-LMCD	300	900	33	Dop.	0.25%	-	10700	2	x13
				No dop.	0.1%	-	-	60	x13
#4-HMCD	300	900	33	Dop.	0.5%	-	9600	1	x13
				No dop.	0.75%	0.32%	-	10	x13
#5-α16	310	910	50	No dop.	0.75%	0.25%	-	30	
#6-α10	280	830	33	Dop.	4%	-	1200	10	
#7-β10	230	830	50	Dop.	0.5%	-	6000	10	
#8-LMCU	300	900	33	No dop.	0.1%	-	-	840	
#9-HMCU	300	900	33	No dop.	0.75%	0.32%	-	140	

#10-LMCD	280	900	33	Dop.	0.1%	-	28000	5	x6
				No dop.	0.25%	-	-	60	x6
#11-Disp	260	900	33	Dop.	4%	-	1200	15	
				No dop	0.75%	0.25%	-	216	
	280	920		No dop.	0.1%	-	-	180	
				Dop.	0.25%	-	28000	8	

Des observations préliminaires faites avec le MEB, nous déduisons que : (i) la concentration de méthane est la clé de la croissance. Avec la diminution de ce coefficient la croissance est plus facettée et la densité des défauts de surface est réduite. Donc la croissance est plus sélective dans certaines directions. D'autre part, la vitesse de croissance est fortement réduite. (ii) la pression et la durée de la croissance et l'utilisation d'oxygène influent également sur la forme finale de la structure. Ainsi, lorsque la même concentration de méthane est utilisée, le facettage final de l'échantillon peut également changer si pression, température et concentration d'oxygène sont modifiées.

III Homoepitaxial diamond lateral growth

Contents

Growth mechanisms involved in lateral overgrowth of mesa etched substrates were studied and discussed. A stratigraphic approach was introduced, based on the use of very thin doped layers to follow the growth orientations along the growth duration. Thanks to this approach, growth directions have been obtained and delimited resulting in a reproducible growth sequence, and the important role of methane concentration has been stressed. Another main role was played by the edges, corners and ridges of the mesa structures, resulting in a planarization trend which depended on the height of the mesa structures. Moreover, doped layers used for the stratigraphic approach were shown not to affect the growth.

III.1. Introduction

Homoepitaxial diamond 3D growth mechanisms by microwave plasma chemical vapor deposition (MPCVD) or at high-pressure and high-temperature (HPHT) have been largely studied [Wild 1994, Battaile 1998, Silva 2006, Silva 2008, Tallaire 2013 and Bogatskiy 2015] and the models developed are well known and accepted. These models are mainly based on the relative growth velocities of four low index crystal planes: {100}, {110}, {111} and {113}. The value of the velocity ratios (the so-called growth parameters) describing the global morphology of the crystal during the growth process allows to predict their final shape. This final shape is given by the slowest rate among facets sharing an edge that limits the growth. [Wild 1994, Silva 2006 and Silva 2008].

On a macroscopic scale, the overgrowth of 3D structures such as mesa structures obtained by etching from the flat surface of a diamond substrate can be looked upon as a liquid dropped on a 3D structured infinite surface with the same surface energy. The good wetting properties of this "liquid" are due to the fact that diamond is grown on diamond. Then, the additional diamond will tend to wet the whole surface, blurring out the 3D mesa structure in a planarized overgrowth. This implies different growth rates for the vertical and in-plane expansion of the overgrown material, generating additional strain at edges and corners. Moreover, lateral growth fronts originating in neighboring mesa patterns will coalesce at some point, leading to a planarization of the structure that may be the main objective of the overgrowth, but precludes a straightforward a posteriori domain shape analysis.

In order to study the intermediate stages of non-faceted or planarized overgrown diamond structures, in *Section III.2* we shall propose an approach that involves heavily doped nm-thick sublayers used as time markers in a stratigraphic configuration, similar to previous studies of stacks of SiGe alloys [Vescan 1994]. The boron-doped sublayers are easily distinguishable by transmission electron microscopy (TEM) in scanning TEM-high angle annular dark field (STEM-HAADF) and in the TEM conventional diffraction contrast mode [Araujo 2011], and act as milestones of the growth plane orientation as growth proceeds. This method was designed to address both the issue of defect generation induced by strong doping modulation, and that of progressive planarization of mesa structures upon epitaxial overgrowth.

With the aim to check the influence of growth conditions into the lateral growth process and based in the differences in the faceting observed on the SEM micrographs of samples grown with different methane concentrations (see *Chapter II*), parameters related to the growth along different orientation (111 and 100) have been evaluated. Along this line, *section III.3* is a

comparative study of lateral growth using two different methane concentrations, corresponding respectively to the standard conditions for 100 and 111-oriented substrates.

Section III.4 introduce the main reactions that take place during the growth process with a detailed discussion about the influence that on this process have the different parameters involved on homoepitaxial MPCVD diamond growth. As conclusion, an estimated expression of the expected growth velocity is obtained. Such expression is depending on the geometry of the patterned substrate. This influence, relative to the size and the geometrical singularities introduced by the mesa structures is analyzed in *Section III.5*. Finally, the reproducibility of growth is demonstrated to be independent of the boron doping. It proves the validity of the results obtained by the stratigraphic approach and neglecting any change in the growth due to its use.

III.2 The stratigraphic approach

For the present study, samples #1-F and #2-A have been used. As exposed in *Chapter II*, the overgrowth of sample #1-F yielded a single undoped layer while for sample #2-A a stack of nine periodic alternates of undoped and boron doped diamond layers were overgrown. Fig.III.1 shows a SEM micrograph of mesa-etched cylinders whose diameter was 4 microns, before (a) and after (b) being overgrown. The new contours of mesa-etched cylinders upon overgrowth have lost the circular geometry; the final shape is polyhedral (see Fig.III.1 (b)). A first observation suggested the existence of a (100) top facet accompanied by others such as {110} and {311} localized at the edges and corners of the overgrown cylinders. This suggest that the growth velocity vary with the orientation.

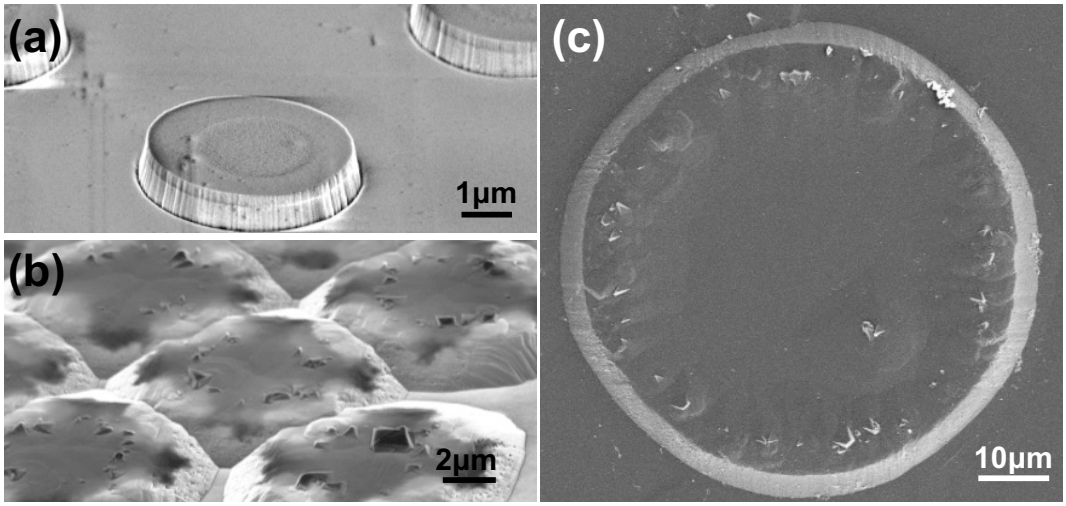

FIG. III.1. SEM images of sample #1-F taken before (a), after (b) a 70 min overgrowth by an undoped diamond layer and the superlattice overgrowth on the sample #2-A (c).

According to the Silva *et al*. method [Silva 2006], the crystallographic orientation of facets has been determined geometrically by measuring lengths, distances between edges, and tangent angles by assuming a (100) plane at the top of overgrown cylinders. Fig.III.2 (a) displays the crystallographic orientation of facets determined geometrically for sample #1-F. Facets along {311} and {110} planes were identified at borders. Cut edges with second order facets were found on {110} sides. These secondary facets could be tentatively ascribed to crystallographic planes {210} and {310}. The small size of these secondary facets does not allow to claim the exact plane orientation, and point out the limits of the geometrical determination for the present dimensions and spacing.

The height of overgrown cylinders was the same as before deposition. This confirmed that both the top of the overgrown cylinders and the etched surface away from the mesa patterns followed the initial (100) plane growth rate. This "vertical" growth rate (100) has been measured on the cross section of a 10-micron-thick layer grown under the same conditions [Chicot 2012]. Growth rates of facets have been estimated following a simple trigonometry method, illustrated in Fig.III.2 (b), and summarized in table III.1. In this method, we considered that the adjacent side was the facet altitude, and the opposite side was the growth rate. The distance separating the mesa-etched cylinder and the intersection of the facet with the original (100) plane gave an orthogonal projected length of the facet.

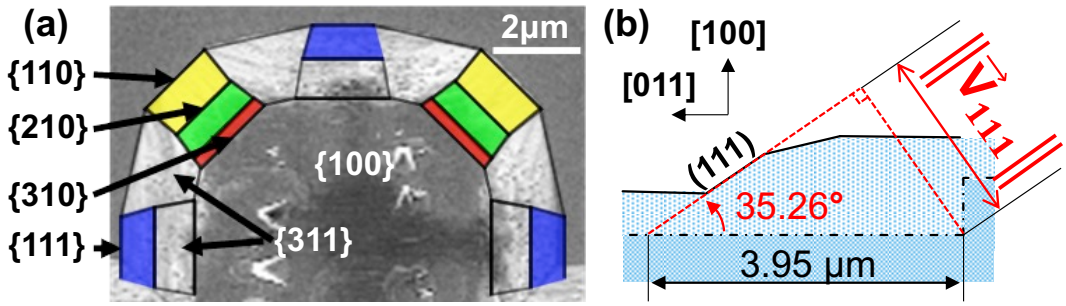

Fig.III.2.[*] (a) Top view of a half cylinder overgrown with indexed facets superimposed. Each color corresponds to a family of planes. (b) Schematic cross-section of an overgrown cylinder used to calculate the growth rate of the (111) plane. Solid and dash-dotted lines represent the final surface and the initial surface at the edge of the overgrown cylinders respectively.

Under the growth conditions of sample #1-F, the slowest family of planes to grow after the (100) was the {311}. These {311} types of planes in diamond were called stepped faces due to the large number of terrace edges, and were the most stable. However, the stability of such faces cannot be generalized in our case, because of the number of defects present at the walls of

[*]The author would like to thank to A. Fiori for the figure.

the mesa, and because of a typical trenching effect. Twinning may also arise on an edge of a face, or on the faces of a re-entrant etch pits, and emerge at the surface. This was observed on sample #1-F, where twinning hillocks are describing a circle following the top border of mesa-etched cylinders.

The method used above provides a simple way of estimating growth rates based on the shape of faceted overgrowth patterns. It does not require any cross-section analysis nor destructive characterization while providing valuable information about the growth. However, it has at least three limitations that should be kept in mind:

(i) as previously mentioned for the case of secondary faces, facets are not always easy to identify, especially for large disks diameters and short growth durations

(ii) the method assumes that the growth follows just one low index growth direction. It does not consider possible intermediate planes

(iii) it is not obvious to deduce the location of the intersection of the facet with the original plane, this is another source of error on the measured numerical values

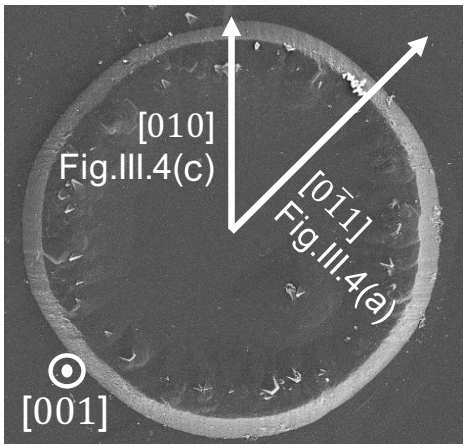

Fig.III.3. SEM top view micrograph of sample #2-A were orientation along the ones lamellas for TEM studies have been extracted are marked by arrows.

The first limitation was illustrated by the case of sample #2-A, where SEM observations showed cylinders with non-faceted lateral faces (Fig.III.1 (c)). In this case, there is no apparent faceting. This might be because the ratio of the overgrown thickness to the disk diameter is too small. Since the shape analysis of sample #2-A does not provide any quantitative clue about the growth mechanisms, an alternative method should be sought for. Thanks to the presence of doped layers, cross-section observations should allow to reveal internal growth features of the overgrown cylinders. To this end, two cross-section lamellas were extracted from the sample #2-A. The identification of growth features was guided by the contrast associated to the doping superlattice, which made the stratigraphy possible. Therefore, a first cross-section lamella has been cut

along [01$\bar{1}$], and a second one along [010] (see Fig.III.3). These lamellas have been analyzed by TEM in the bright field (BF) (Fig.III.4 (a)) and dark field (DF) modes (Fig.III.4 (c)), to reveal boron-doped layers and dislocations.

Fig.III.4 (a) shows a BF micrograph of the cross-section lamella made along the {011} plane. That TEM micrograph was recorded with the lamella oriented in the [011] zone axis, as shown in the diffraction pattern (see the corresponding inset). To guide the eyes, white dashed lines defined the position of the surface prior to overgrowth, highlighting the sidewall and top of the mesa-etched cylinder. In this BF image, boron-doped layers of the doping superlattice are revealed by dark contrasts. Fig.III.4 (c) shows a DF image of the cross-section lamella prepared along the {010} plane and recorded in the (001) zone axis (see the corresponding diffraction pattern in inset). On the DF micrograph, boron-doped layers are shown as pairs of white bright lines. The observation of two white lines for one boron-doped layer has been associated to interface strain as frequently reported in the literature. For example, the effect of strain on the contrast has been often observed on TEM micrographs for quantum dots [Gutierrez 2006]. The median position between such two white lines has been taken as a reference to measure the gap between two boron-doped layers. In the [100] direction, boron-doped layers were parallel with a constant spacing, which confirmed the periodic alternate deposition of the doping superlattice.

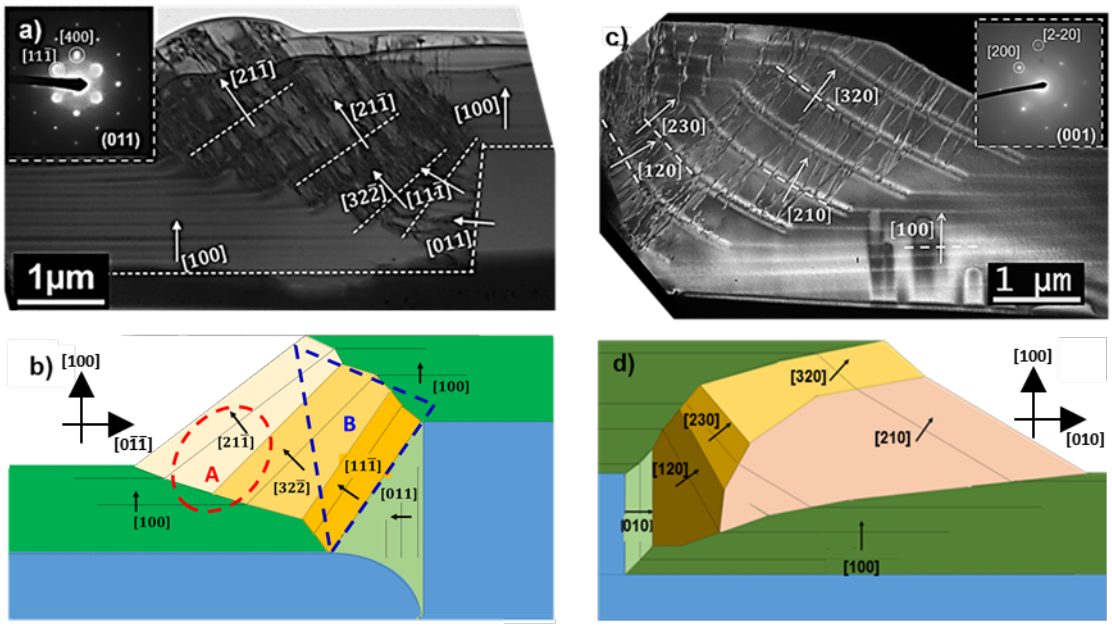

Fig.III.4. (a) Bright field micrograph of a cross-section made along the [01$\bar{1}$] direction in sample #2-A, observed at [011] pole. (c) Dark field micrograph of a cross-section made along the [010] direction observed at [001] pole same sample #2-A. In these micrographs, white dashed lines and arrows indicate the position of p^+ layers and growth directions respectively. (b) and (d) show schematic views of the groups of growth planes identified by color deduced from TEM observations of [01$\bar{1}$] and [010] direction respectively. In (b), the regions where A and B types of dislocations predominate are delimited by broken lines.

In both cross-sections, high densities of extended defects were present in the diamond located at the sidewall of the plasma-etched cylindrical mesa. At the opposite, almost none of such defects were located on the top surface, where growth followed the [100] direction. Three main factors could explain these defects: (i) the influence of the growth orientation on the defects generation resulting from high boron concentrations [Alegre 2014], (ii) the tension accumulated in boron-doped layers steps corners [Erasmus 2011], and (iii) defects generated by the ICP-RIE etching as etch-pits or trenching. Moreover, threading dislocations allowed to follow the growth direction of diamond at the sidewalls of the mesa-etched cylinder, because threading dislocations in diamond propagate along the growth direction [Zhang 2001]. White dashed lines have been drawn on the TEM images of Fig.III.4, with white arrows labelling these growth orientations. This pointed out an evolution of the growth direction, and a tendency to planarization. Schematic drawings of cross-sections made along [01$\bar{1}$] and [010] directions (Fig.III.4 (b) and Fig.III.4 (d) respectively) highlight the different orientations of growth planes. In these maps, colored regions correspond to successive growth directions. The boundaries between these regions are marked by dashed lines, and straight lines indicate the orientations of boron-doped layers. These maps exposed the progress of the growth from [011] to [211] direction, which was tilted at approximately 34° with respect to the (100) plane. In addition, the position of boron-doped layers acted as a time reference, allowing the calculation of growth rates for each direction. The growth rates summarized in Table III.I showed that the growth was faster for the terminal orientations: {210} (~ 35 nm/min), and {320} (~ 41 nm/min). But on top of the mesa, the growth rate goes through a maximum in fig III.4 (c) and (d), and not in fig III.4 (a) and (b) were the rates on top are the same as those in the bottom.

The evolution of growth orientation observed in sample #1-F was partially reproduced in sample #2-A. For example, the {311} facet in sample #1-F seemed to be replaced by {322} and {211} second order facets in sample #2-A, but with unchanged growth rate. Similarly, the {110} facet in sample #1-F was substituted by {120} and {210} in sample #2-A. One-step beyond, the {310} second order facet in sample #1-F could be viewed as {320} and {230} third order facets found in sample #2-A. These results confirm the validity of the first geometrical method for well facetted samples.

Table III.I. Growth rates (in nm/min) of facets estimated in sample #1-F (single undoped layer), and calculated #2-A (doping superlattice).

#	(120)	(110)	(210)	(230)	(310)	(320)	(100)	(31$\bar{1}$)	(21$\bar{1}$)	(32$\bar{2}$)	(11$\bar{1}$)	(01$\bar{1}$)
1-F	-	38.9	30.0	-	6.2	-	7.3	21.4	-	-	32.6	-
2-A	36.9	-	34.6	43.0	-	40.6	14.3	-	25.4	23.2	8.0	27.1

Moreover, the influence of boron-doped layers on the generation of dislocations is certain (boron inclusion, strain). Different types of defects have been identified in sample #2-A by applying the invisibility criterion on TEM micrographs [Scheel 2010]. Two kinds of Burger vectors have been found: $\mathbf{b_{112}} = \frac{1}{6}[112]$, and $\mathbf{b_{01\bar{1}}} = \frac{1}{2}[01\bar{1}]$ labelled here as *A* and *B*, respectively. These dislocations aggregated in different regions, marked by a red circle and a blue triangle in Fig.III.4 (b) for *A* and *B* defects, respectively. Depending on the Burger vectors, defects seemed to have different mechanism of generation. We observed that the *A* extended defects were located closer to the final surface, while *B* dislocations were generated in the region closer to the sidewall of the mesa-etched cylinder. Because of the region where they are shown, *B* dislocations seems to be enhanced by mechanism related with the substrate and the growth on mesa etched substrates. Whereas *A* defects may have been generated by the inclusion of the boron atoms following the mechanism proposed by Alegre *et al*. [Alegre 2014]. Dislocations and other defects will be studied in more detail in *Chapter IV*.

The overgrowth of mesa-etched diamond cylinders combined with a stratigraphic approach is a powerful tool to evaluate the growth rates along different crystallographic directions. In the first example provided here (sample #2-A), facetted overgrowth shows that the top face (100) was the slowest to grow. Faces {111} were visible only at twinning emergence, and {113} faces were presumed to border the sample at equilibrium. {110} faces appeared as ephemeral transition phases at the edges of mesa-etched structures. The difference in growth rate between those faces confirmed the tendency to obtain a flat top surface and the reduction of defects height.

Overgrowth realized with doping superlattices adds supplementary insights into the growth and defect generation mechanisms. The growth time sequences are in this way easily visualized by the stratigraphic structure of TEM cross-sections observation. A progressive change in the growth directions was observed at intermediate steps showing a tendency to planarization.

In addition, the use of embedded doped layers made possible to measure the ratio of growth rates with a high accuracy and to obtain the so-called growth parameters. The growth rate of {111}, {110}, and {311} faces normalized to the displacement of {100} surfaces gave three growth parameters as follows [Silva 2008]:

$$\alpha = \sqrt{3}\frac{V_{\{100\}}}{V_{\{111\}}} \qquad \text{eq.III.1}$$

$$\beta = \sqrt{2}\frac{V_{\{100\}}}{V_{\{110\}}} \qquad \text{eq.III.2}$$

$$\gamma = \sqrt{11}\frac{V_{\{001\}}}{V_{\{100\}}} \qquad \text{eq.III.3}$$

In our case, two of them can be obtained: $\alpha = 3.1$ and $\beta = 0.75$.

This method allows following step by step at a nm-scale the 2D and 3D growth dynamics. However, the presence of boron atoms may generate extra defects, which should affect standard growth mechanisms. These defects, in a high density concentration, may have influence on the growth plane orientation. In order to minimize the effect of the boron atom inclusion, the boron concentration should be reduced. However, the boron doping level must be high enough to introduce a compositional contrast on TEM micrographs [Araújo 2013]. In this work, plenty of threading dislocations have been observed. These defects will be studied in *Chapter IV*.

III.3 Influence of methane concentration

As previously exposed, the understanding of the growth mechanisms involved in the diamond lateral growth will open the door to the lateral diamond devices and improve substantially the diamond applications. With this aim, a tentative draft of the mechanism of lateral growth in diamond by MPCVD will be proposed in this section.

To reduce the possible effect of the high doping levels observed in the previous section, the samples under study (#3-LMCD and #4-HMCD) in this section were grown with a lower boron concentration in the doped layers. In order to determine the possible effect of the initial shape of the substrate, Fig.III.5 (a) shows SEM micrographs of a mesa-disk obtained by ICP RIE as described in *Chapter II* (full information about substrate preparation and growth conditions are shown in *Chapter II*). The sides of the disk look stretched and not perpendicular to the substrate but sloped after the etching. In addition, a few etch pits are shown on the smooth surface as well as the typical trenching effect (see arrows labelled A and B, respectively, in Fig.III.5 (a)).

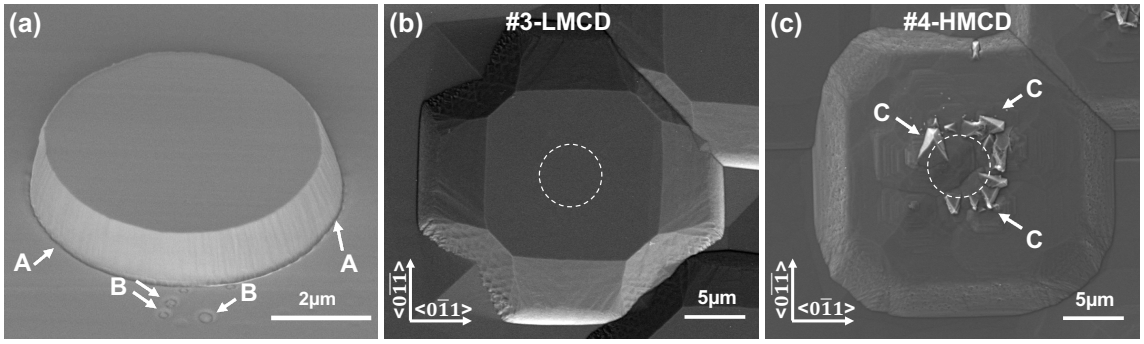

Fig.III.5. (a) SEM micrographs of an etched disk where arrows labelled A show the trenching effect and arrows labelled B show etch pits. (b) SEM micrographs of one of the disks overgrowth of sample #3-LMCD, the dashed white circle marks the position and diameter of the initial disk. (c) SEM micrographs of one of the disks overgrowth of sample #4-HMCD, dashed white circle marks the position and diameter of the initial disk and arrows labelled C show superficial defects. Note that magnification is different in micrograph (a) with respect to (b) and (c).

Fig.III.5 (b) corresponds to a SEM micrograph of one of the disks overgrown from the sample #3-LMCD, i.e. growth under low methane concentration. Faceting is observed along the (0 1 1) and (0 $\bar{1}$ 1) planes with a cross-like shape. In addition, no superficial defects were observed on the upper surface of the disk.

Fig.III.5 (c) shows a SEM micrograph of one of the disks overgrown from the sample #4-HMCD, i.e. growth under high methane concentration. The initial disk, marked by a dashed white circle, has evolved towards in a squared-shape structure where the sides are also facetted along the (0 1 1) and (0 $\bar{1}$ 1) planes. Some superficial twinning hillocks are observed describing a circle following the top border of etched disk; arrows and the letter C in the figure mark them.

From Fig.III.5 (b) and (c), epitaxial overgrowth seems to be more selective for sample #3-LMCD, i.e., for growth at lower methane concentrations (LMC). Note that selective growth is understood as the growth that mainly take place along the <011> directions. In addition, the specular symmetry of the facetted structures illustrates that there is no effect of the sloped side of the initial disk on the final shape.

Moreover, twinning defects are frequently generated by internal stacking faults. These stacking faults are usually created at {111} planes [Tallaire 2008]. Nevertheless, twins are only present in sample #4-HMCD and there are not evidences about differences in the {111} planes in both samples. The difference in the methane concentration between both samples inclines to think that lower concentrations being associated to low growth rates, provide a less stressed growth with lower number of atomic columns with free bonds [Delclos 1999] and this could be the reason because sample #3-LMCD does not exhibit twins. A detailed description of those defects is introduced in *Chapter IV (Section IV.4 page 133)*.

Fig.III.6 shows TEM cross sections micrographs of sample #3-LMCD. Doped layers used as markers are again apparent, thanks to the compositional contrast [Araujo 2013]. A dashed black line on Fig.III.6 (a) marks the initial shape of the substrate that is easy to find because the first grown layer was a doped one that delineated the profile (see Fig.III.6 (b)). Black contrast observed on the top of the samples corresponds to platinum deposited during the FIB lamella preparation. The misorientation angle of the different doped layers with respect to the [1 0 0] direction allows obtaining the growth orientation. It is, growth orientations are obtained by measuring the angle of the doped layers respect to the horizontal (corresponding to [1 0 0] orientation). Micrographs of Fig.III.6 (a) and (b) were recorded, in bright field mode, along the [0 0 $\bar{1}$] and [0 1 $\bar{1}$] zone axes, respectively. Regions with the same growth orientation have been identified and marked by colors. As it was expected from *section III.2*, growth orientations change along the growth process. Planes present on Fig.III.6 (a) seem to be projections of the planes shown in (b) on to the plane (001).

These planes correspond to the families of planes {3 $\bar{1}$ 1}, {2 $\bar{1}$ 1}, {1 1 $\bar{1}$} and {1 $\overline{11}$ 11}. In this way, (1 $\bar{1}$ 0), (2 $\bar{1}$ 0), (3 $\bar{1}$ 0) and (1 $\overline{11}$ 0) planes are the projections of (1 $\bar{1}$ 1), (2 $\bar{1}$ 1), (3 $\bar{1}$ 1) and (1 $\overline{11}$ 11), respectively. Note the presence of the (1 $\overline{11}$ 11) (h=1, l=$\overline{11}$, k=11) unusual plane.

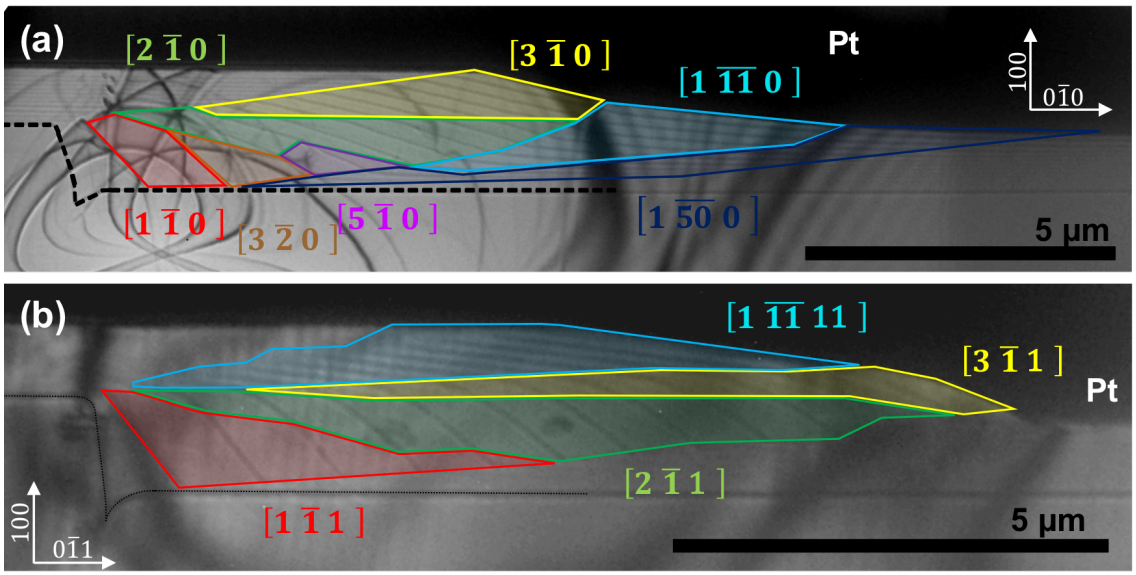

Fig.III.6. (a) TEM cross section micrograph of sample #3-LMCD oriented on the (001) pole. (b) TEM cross section micrograph of sample #3-LMCD oriented on the (011) pole. Doped layers are visible as dark contrast lines marking the regions of growth with the same orientations. These regions are highlighted by colors and labelled with the corresponding orientation using the same color. Platinum observed and marked by Pt is due to the FIB-lamella preparation.

In addition, from the SEM micrographs of Fig.III.7 (a) and (b), $(1\ \overline{50}\ 0)$ plane seems to be the projection of other two symmetrical planes. Indeed, in Fig.III.7 (b) four dashed lines mark four facet that coalesce on the plane of the lamella, (001). This situation encourages to think that orientations observed on Fig.III.6 (a) are the projections of the orientations observed on Fig.III.6 (b). Thus, only the projections of the planes (3 $\bar{2}$ 0) and (5 $\bar{1}$ 0) are actually contained on (0 0 1). The tendency of planarization, already reported [Issaoui 2011], is also noticeable. This tendency, which could also favor the generation of the unusual planes, is related to the macroscopic wetting mechanism already described. In this model, the planarization results from an expansion of the volume but also from a minimization of the surface energy.

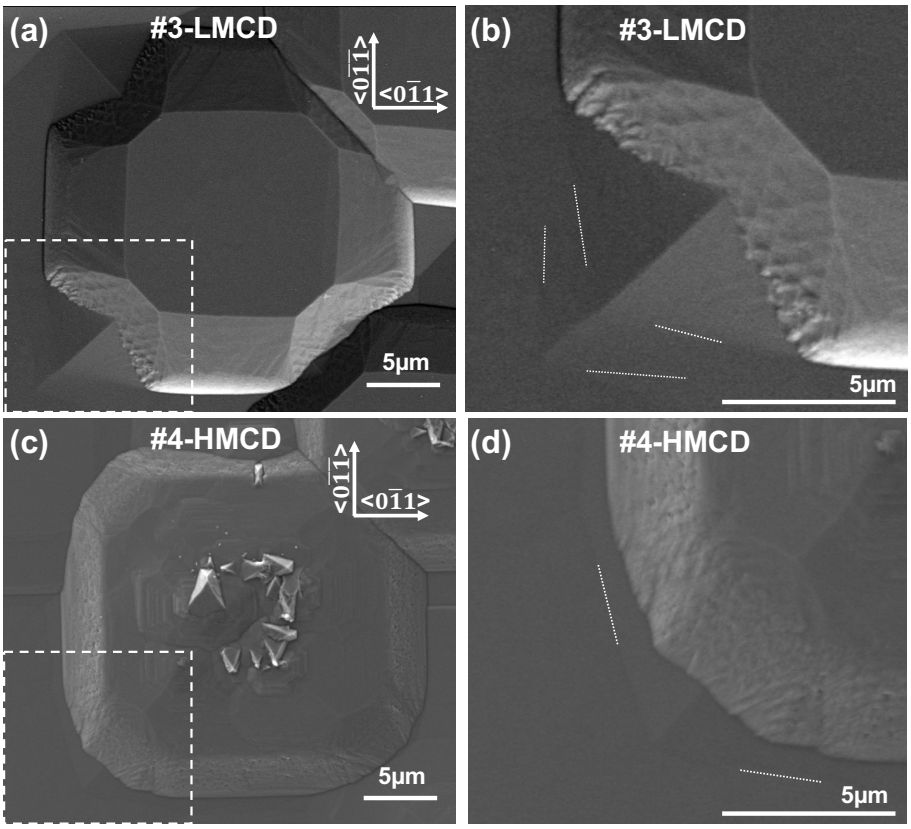

Fig.III.7. (a) SEM micrographs of one of the mesa disks overgrowth of sample #3-LMCD. (b) Detail of the overgrowth mesa disk framed in (a) by a dashed white rectangle. Dashed lines marks facets not easy to identify. (c) SEM micrographs of one of the mesa disks overgrowth of sample #4-HMCD, (b) Detail of the overgrowth mesa disk framed in (c) by a dashed white rectangle. Dashed lines marks facets not easy to identify.

Fig.III.8 shows similar micrographs for sample #4-HMCD. First difference observed from these micrographs in contrast to the previous one is the density of defects. The lamella of sample #4-HMCD is shown to be full of defects in the whole region grown above the initial disk. Defects are even observed on the {100}- orientation above the mesa. However, they seem to be generated on other growth planes and then extend to the (100) one. Actually, it is easy to observe how the defects lines are curving during their displacement to the surface following the growth orientation. It is also remarkable that most probably stacking faults generated on the region of the corners of the initial disk are the responsible of the twin defects observed on the top surface. In Chapter II, such kind of superficial defects were introduced as hillocks type (ii), here we can prove that their formations did not begin at the initial step of the growth. In this case, they started almost 1μm over the initial mesa structure. However, sample #3-LMCD does not show these superficial defects. The origin of these superficial defects is discussed in *Chapter IV*.

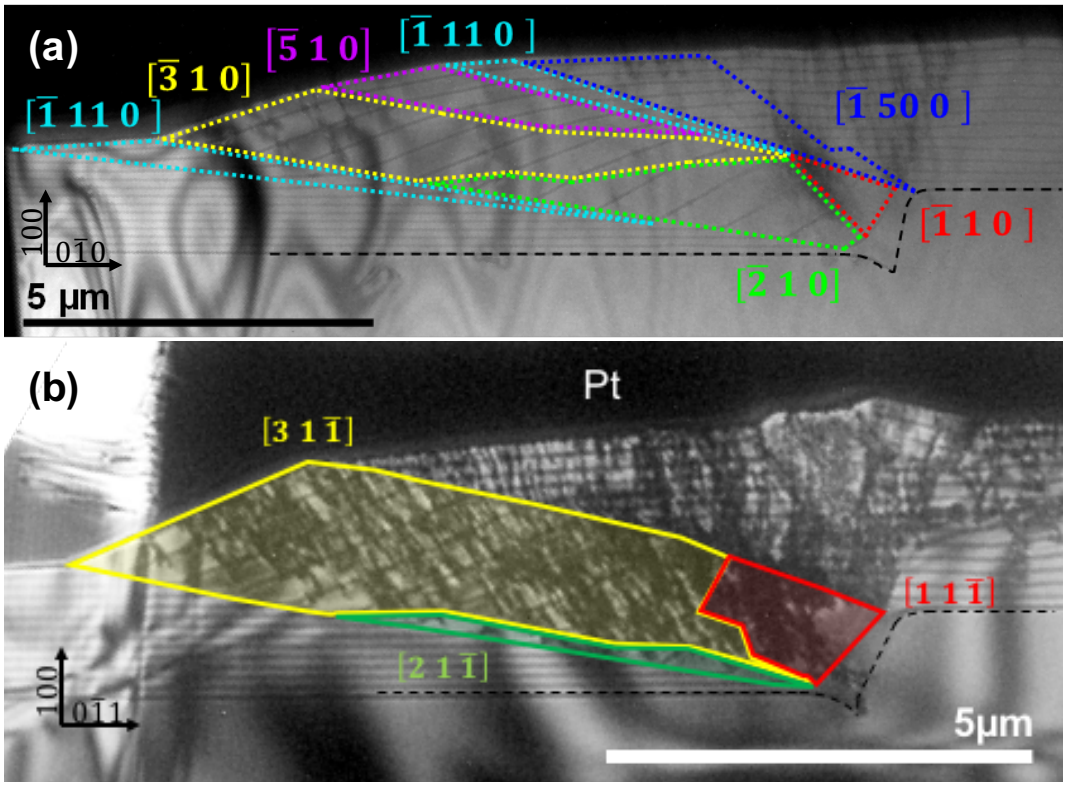

FIG.III.8. (a) TEM cross section micrograph of sample #4-HMCD oriented on the (001) pole. (b) TEM cross section micrograph of the same sample oriented on the (011) pole. Doped layers are visible as dark contrast lines marking the regions of growth with the same orientations. These regions are highlighted by colors and labelled with the corresponding orientation using the same color. Platinum observed and marked by Pt is due to the FIB-lamella preparation. Dashed black lines mark the initial shape of the mesa structures.

In terms of growth orientations, a similar number of growth sectors were observed in both samples. Orientations observed in sample #4-HMCD coincide with planes observed in sample #3-LMCD but the size of the growth sectors and the times of generations differ. Unusual planes ($\bar{1}$ 11 0) and ($\bar{1}$ 50 0), that in sample #3-LMCD appeared at the bottom side of the structures, appears in sample #4-HMCD also at the top side. This unusual planes arise then sharing edge with the {100}-orientation in a kind of buffer-like intermediate plane in the planarization tendency.

In addition, most of the planes observed on the lamella oriented on the (0 0 1) pole are projections of the ones obtained for the lamella oriented on the (0 1 1) pole. Planes {1 1 0}, {2 1 0} and {3 1 0} seems to correspond to the projection of the planes {1 1 1}, {2 1 1} and {3 1 1}, respectively, on the (0 0 1) plane (see Fig.III.7 (c) and (d)).

From these results, it was deduced that, in both cases, the growth is mainly happening along the two equivalent [1 $\bar{1}$ 0] and [1 1 0] directions. In this way, the main difference in the lateral growth mechanism between both samples is that sample #3-LMCD growth moving forward its growth planes as a front, and sample #4-HMCD increased the size of this front at the same time

that the forward motion was happening. This is the reason why Fig.III.5 (b) shows a final cross-like shape and Fig.III.5 (c) shows a quadrangular final shape.

The stratigraphic approach allows to measure the growth rates for the different planes. Obtaining intensity profiles, distance between doped layers can be measured with high accuracy and the growth ratios for each sample can be calculated. The values of these velocities are given in table III.II. As expected from the growth conditions, growth rates were ten times slower for sample #3-LMCD than for #4-HMCD. In addition, equivalent growth orientations showed similar velocities.

Table III.II. Growth rates (in nm/min) of facets calculated from the spacings of doping superlattices. Equivalent growth orientations are grouped by shaded/unshaded columns. Sample named #3 corresponds to sample #3-LMCD and sample named #4 is corresponding to #4-HMCD.

#	[3 1 $\bar{1}$]	[3 $\bar{1}$ 0]	[2 1 $\bar{1}$]	[2 $\bar{1}$ 0]	[1 1 $\bar{1}$]	[1 $\bar{1}$ 0]	[1 $\overline{11}$ 11]	[1 $\overline{11}$ 0]	[0 0 1]	[3 $\bar{2}$ 0]	[5 $\bar{1}$ 0]	[1 $\overline{50}$ 0]
3	6	3	8	10	12	14	2	2	1	13	7	2
4	36	33	63	41	59	-	-	12	11	-	27	15

As reported in the literature [Issaoui 2011], the lateral faces of the disk tend to disappear during the overgrowth, for the benefit of the top (1 0 0) face that expands. However, this tendency seems to be different between #3-LMCD and #4-HMCD samples. Final growth planes of sample #4-HMCD are [3 $\bar{1}$ 1] and [0 0 1]. [3 $\bar{1}$ 1] shows a growth velocity 3.3 times faster than [0 0 1]. This result predicts that sample #4-HMCD will lose the lateral faces to favor the [0 0 1]. On the other hand, the final shape of #3 is formed by 3 coexistent planes: (3 $\bar{1}$ 1), (0 0 1) and (1 $\overline{11}$ 11). (3 $\bar{1}$ 1) is disappearing to favor the (1 $\overline{11}$ 11) plane which is 3 times slower. However, velocities of (0 0 1) and (1 $\overline{11}$ 11) are quite similar and it is not as easy as in the case of the growth conditions of sample #4-HMCD to predict what will happen with these (1 $\overline{11}$ 11) planes.

If we consider the eq.III.1 and eq.III.3, previously defined, α and γ parameters can be obtained. The values obtained for each sample are: α_3=0.2, γ_3=0.6, α_4=0.3 and γ_4 =1.0, respectively. Both cases show similar α parameter which is lower than 1. On the other hand, γ parameters also remain small but higher than 11 α/5. According to the bibliography [Silva 2008], this indicates that {1 0 0} is the slowest faces (α<1). However, it is also reported that in growth process in which γ>11 α/5, {1 1 3} constitute the crystal steady shape for an infinitely long growth time. This is clearly the case of sample #4-HMCD whose γ parameter is equal to one. Nevertheless, even if {1 1 3} seems to be the dominant face in both cases, a planarization tendency is also observed. Such planarization is more evident in the case of sample #3-LMCD, where γ<1. For this case (γ<1), the model mentioned [Silva 2008] predicts that facets (100) will dominate over the {1 1 3} ones that is in contradiction to the {1 1 3} domain. This contradiction could explain the

presence of unusual intermediate planes (between {1 1 3} and {0 0 1}) that were previously mentioned.

Another remark about the growth rates reported in table III.II is that the growth velocity increase for the crystalline growth directions which make a higher angle with the normal [100] direction. In others words, growth is faster for the orientations that make higher angels respect to the [100]. This apparent anisotropy might be related to a lower efficiency of carbon etching by hydrogen (see below) on tilted growing surfaces, and/or to the overwhelming influence of wetting effects on lateral growth.

III.4. Chemical mechanism of lateral growth

The current section introduces a description of the growth carried out in the samples. The main chemical reactions have been analyzed to provide a law governing the behavior of growth rates.

III.4.1. First Stage: Activation of the surface

Already introduced in Chapter I, diamond growth is carried out by plasma in a hydrogen based gas. Plasma induces the generation of hydrogen radicals by dissociating H_2 into H atoms. These hydrogen radicals have been shown to be the main actors during the growth since they produce methyl radicals from methane [Banholzer 1992, Liu 1995, Gicquel 2001, Netto 2005, Richley 2012 and Schwander 2011]. The recombination of those methyl radicals induces the formation of C_2H_y radicals responsible for the growth. Such reactions are schematized in Fig.III.9 [Yang 2015].

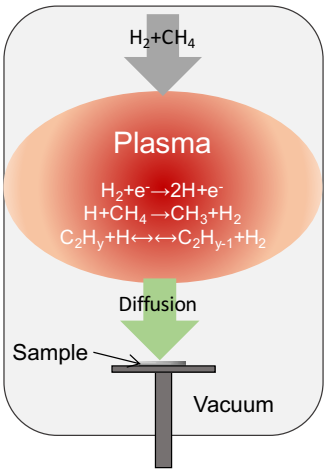

Fig.III.9. Schema of the plasma reactions and radicals generation during MPCVD diamond growth.

Those generated radicals reach the surface interacting with the superficial atoms, ideally carbon atoms. However, most of diamond surface is hydrogen terminated and most of radical precursors cannot react with the diamond surface to form sp^3 bonding. Instead of it, radicals impact against hydrogen atoms and are sent back to the plasma [Harris 1990, Butler 1993, Netto 2005 and May 2010]. In this way, the growth requires of the activation of the superficial carbon atoms. It takes place by a first step that consists into the H abstraction (C_d-H+H→C_d^*+H_2) followed by a second one through in which CH_3 are adsorpted at the active site (C_d^*+CH_3→C_d-CH_3) [Lee 1999, Banholzer 1992, Frauenheim 1993, Richley 2012 and Lai 2016]. Here, asterisk marks actives atoms and *d* subscript identifies diamond carbon atoms, i.e. C_d-H are hydrogen passivated carbon atoms from the diamond lattice, and C_d^* are active carbon atoms from the diamond lattice. Once the first gas reactions take place in the plasma and methane has been discomposed in (among others) H and CH_3, such atoms and radicals react with the surface of the sample. Fig.III.10 (a) shows the hydrogen terminated diamond surface, because of this H-terminated surface, CH_3 radicals are sent back to the plasma whereas hydrogen atoms react with the ones from the substrate forming H_2 and leaving behind a surface radical (dangling bond). The carbon atom is then activated to react with a radical. The likely case is that another H atom binds to this site, as Fig.III.10 (b) shows. It results in a hydrogen terminated surface again and the extra energy resulted from the deactivation of this site is dissipated as heat through the substrate.

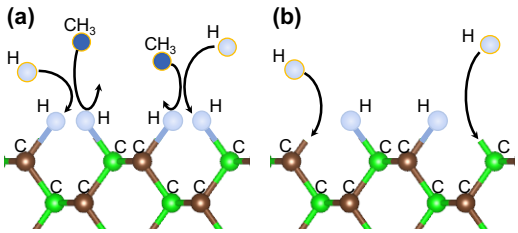

FigIII.10. Schematics of the first steps of diamond growth by CVD. (a) shows the activation of two sites by the abstraction of the H atoms. It occurs when a hydrogen radical react with it and form H_2. The case of the impinging of CH_3 instead of H is also showed without result. (b) shows the likely reaction of H radicals into the active site. It results in the passivation (deactivation) of the surface.

Hence, the number of dangling bonds at the diamond surface at any time, i.e. the fraction of surface carbon atoms, results from the equilibrium between the hydrogen abstraction and the hydrogen addition reaction at the surface:

$$F = \frac{[C_d^*]}{([C_d^*]+[C_dH])}, \qquad \text{eq.III.4}$$

where C_d refers to sp^3 carbon in the diamond structure at the surface, and $[C_d^*]$ and $[C_dH]$ are the respective densities of open and hydrogen-terminated surface sites. The three main chemical reactions which govern this equilibrium are [Frenklach 1997]:

$$H + C_dH \leftrightharpoons H_2 + C_d^* \quad \text{eq.III.5}$$

$$H + C_d^* \leftrightharpoons C_dH \quad \text{eq.III.6}$$

$$C_d^* + C_xH_y \leftrightharpoons C_dC_xC_y \quad \text{eq.III.7}$$

As the flux is constant, these expressions can be written as [May 2010]:

$$k_1[H][C_dH] \leftrightharpoons k_{-1}[H_2][C_d^*] \quad \text{eq.III.8}$$

$$k_2[H][C_d^*] \leftrightharpoons k_{-2}[C_dH] \quad \text{eq.III.9}$$

The forward rate constant, k_{-1}, is only important for high substrate temperatures (T_s>1000°C) which is not our case. The constant k_2, thermal desorption, as well as eq.III.7, can be ignored as C_xH_y effects are too small [May 2010]. In this way, the following equation of equilibrium is obtained:

$$F = \frac{1}{\left\{1+\frac{k_2}{k_1}+\frac{k_{-1}[H_2]}{k_1[H]}\right\}} \xrightarrow{T_s<1000°C,\text{then } k_{-1}\sim 0} F = \frac{1}{\left\{1+\frac{k_2}{k_1}\right\}} \xrightarrow{k_2 \gg k_1} F = \frac{k_1}{k_2} \quad \text{eq.III.10}$$

Under typical CVD growth conditions, that is CH_4/H_2~1% and T_s~900°C, F~0.1 [May 2010], it means that there will be around 10% of the diamond surface with these dangling bonds. Such conditions match perfectly with the conditions of sample #4-HMCD and, as a first approximation, can be extrapolated to the growth conditions of Sample #3-LMCD.

Activation and deactivation radical sites are then governed by the reactions carried out between the gas and the surface:

$$Activation\ rate = (k_1[H]_s + k_{-2})U \quad \text{eq.III.11}$$

$$Deactivation\ rate = (k_2[H]_s + k_{-1}[H_2])A \quad \text{eq.III.12}$$

where A and U are the activated and deactivated surface sites respectively, while constants are the same as in eq.III.8, eq.III.9 and eq.III.10.

III.4.2. Second stage: Carbon atom sticking

Fortunately, in some occasions the radicals attached to the surface dangling bonds are CH_3. It will depend on the probability of such species to hit the substrate surface. The gas concentration of the different chemical species in the MPCVD reactor can be obtained by mass

spectrometry and used to estimate the number of CH_3 species existing on the surface of the sample. Knowing this value, the aeral frequency of CH_3 impacts in $cm^{-2}{\cdot}s^{-1}$ is given by:

$$[CH_3]_s \times \frac{v}{4} \qquad \text{eq.III.13}$$

where $v = 3757 \times T_{ns}^{0.5}$ ($cm{\cdot}s^{-1}$) is the thermal velocity of CH_3 and T_{ns} is the temperature of the gas near to the surface. In addition, as shown in Fig.III.10 (a), most of CH_3 radicals will impact into H-terminated sites, thus bouncing off without reacting.

The CH_3 bonding to the surface is, however, quite vulnerable, and can easily be etched or desorbed back into the gas phase. In fact, diamond growth can be viewed as resulting from the competition between etching and deposition processes, with the carbon atoms being added to and removed from the diamond surface on an atom-by-atom basis. However, if the process of H abstraction, dangling bond creation, and CH_3 addition, were to occur again, on a site adjacent to the pendant CH_3, then there's the possibility that the new carbons can link up, and finally be locked into the lattice. This would expand the diamond lattice, as shown in Fig.III.11.

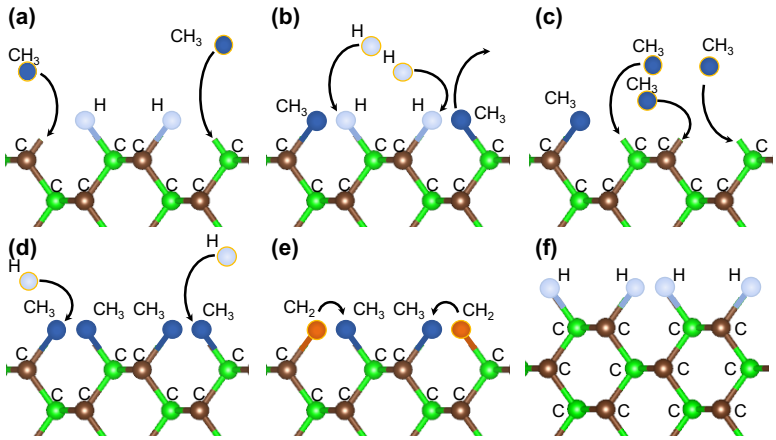

FigIII.11. Schematics of the first steps of diamond growth by CVD. (a) shows the reaction of two CH_3 radicals with two activated sites. (b) shows the sites occupied by the CH_3 and how two others H atoms activate sites in the surface. In addition, one of the CH_3 is desorb back into the gas phase, that is quite probably, leaving the site activated. (c) shows the reaction of CH_3 species on those activates sites. (d) shows the reaction of H with them, forming CH_2 H_2. (e) shows the reaction between CH_3-CH_2 neighbors that results in the stabilization of the carbons at the site with sp^3 showed in (f).

Considering that $T_s = T_{ns}$ and that over 1 cm^2 of (100) diamond there are $\sim 1.56 \times 10^{15}$ carbon atoms, the ratio of CH_3 species adsorbed ($C_d^* + CH_3 \rightarrow C_d\text{-}CH_3$) per superficial radical sites ($site^{-1}{\cdot}s^{-1}$) is:

$$CH_3^{abs\ rate} = \frac{\left\{P \times [CH_3]_s \times \frac{3757 \times \sqrt{Tns}}{4}\right\}}{1.56 \times 10^{15}} \qquad \text{eq.III.14}$$

where P is the probability of adsorption onto a radical site (sticking probability). It results from the combination of factors that reduce the probability of reaction, such as geometry factors (g) due to unfavorable collision orientation and a steric-electronic factor (s). In this way, $P=g$ x s. The factor s has been estimated to be $s\sim0.15$ [Klippenstein 2006].

III.4.3. Third stage: Carbon migration

The here referred migration process was introduced by Frenklach *et al.* [Frenklach 1997] and it is displayed in Fig.III.12. From a stable bridging structure, for example the one shown in Fig.III.10, further hydrogen abstraction reactions allow the CH_2 groups to migrate across the dimer chain until they meet another CH_2 bridge group, or a step-edge, at which point they will lock into place, extending the diamond lattice, and leading to large regular crystals. For this to happen, a neighbor active site is needed (Fig.III.12 (a)). The CH_2 will move to form a double bond with the neighbor active carbon (Fig.III.12 (b)). Then, CH_2 will finish its migration by forming a new stable bridging structure (Fig.III.12 (c)).

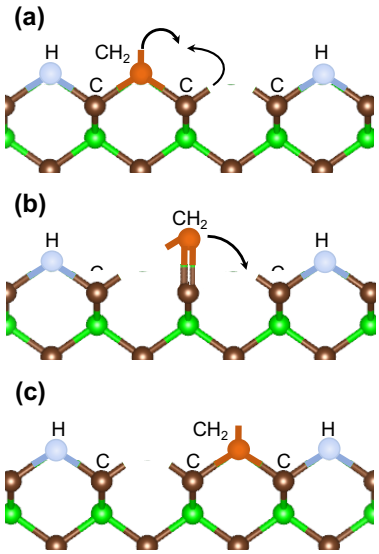

FigIII.12. Schematics of the CH_2 group migrations across a dimmer chain.

At such temperatures (T_s>700°C), there is a probability of migration of the adsorbed carbon species across the surface until they meet a step-edge where they are added to the diamond lattice. The migration rate to be considered is that for an activated CH_2 bridging group to move along or across a dimer row. It will depend on the probability of diffusion by hopping which is given by:

$$k_{hop} = 6.13\times10^{13} e^{-\frac{128400}{RT_s}} \qquad \text{eq.III.15}$$

multiplied by the probability of finding a suitable radical site in a neighboring position. Such probability typically responds to an equation type $\{1-(1-C)^4\}$ and has an estimated value of 0.1 [May 2010].

Surface migration of lone CH_2 groups has been reported to be fast and nearly isotropic in both directions, along dimer chains and along dimer rows. Nevertheless, the diamond bridge migration is conditional to the formation of surface biradicals. Consequently, the 3D shape of our samples as well as the coexistence of different planes during the growth process give to the migration an important role in the chemical vapor deposition of our samples.

III.4.4. Fourth stage: Carbon etching

During single crystal diamond growth, T_s and the superficial hydrogen atom concentration are high. Thus, sp^2 graphitic carbon ratio etching rate is about 20 times higher than carbon sp^3 [May 2010]. In this way, most of the graphitic carbon is considered etched away. In contrast, diamond etched is highly depending of the total flux rate [Bousquet 2015] but can be considered as constant:

$$k_{etch} = A_{etch} e^{-\frac{E_q}{RT_s}} \qquad \text{eq.III.16}$$

where A_{etch} is the frequency of collision ($10^{13} s^{-1}$) and E_a is the activation energy (equivalent to the C bonding energy, 348 $kJ \cdot mol^{-1}$).

III.4.5. Estimate of the growth velocity

By considering all these expressions as well as the simplification applicable to the cases described in section III.2, growth velocity should be governed by an equation such as:

$$V_{growth} \propto \frac{k_1}{k_2} \times \frac{\left\{ g \times s \times [CH_3]_s \times \frac{(3757 \times \sqrt{T_{ns}})}{4} \right\}}{1.56 \times 10^{15}} \times A_{etch} e^{-\frac{E_a}{RT_s}} \times C(g) \times 6.13 \times 10^{13} e^{-\frac{128400}{RT_s}} \qquad \text{eq.III.17}$$

For samples #3-LMCD and #4-HMCD, all parameters can be considered constant with the exception of CH_3 and the geometry. The term geometry includes the surface concentration of carbon atoms since free bonds will depend of the plane. In the other hand, the terms CH_3 will be a function of the CH_4. It means that will be smaller for the low methane concentration (LMC) growth than for the high methane concentration ones (HMC). In this way, velocity of growth will be done by an expression as follow:

$$V_{growth} = K \times f(g) \times [CH_3]_s \qquad \text{eq.III.18}$$

$$K = \frac{k_1}{k_2} \times s \times \frac{\left(3757 \times \sqrt{T_{ns}}\right)}{4} \times \frac{1}{1.56 \times 10^{15} \times N_A} \times A_{etch} e^{-\frac{E_a}{RT_s}} \times 6.13 \times 10^{13} e^{-\frac{128400}{RT_s}} \quad \text{eq.III.19}$$

Considering now $T_s=T_{ns}=1173.15$ K, $\frac{k_1}{k_2}=0.1$, s=0.15, $A_{etch}=10^{13}$ s^{-1}, $E_a=348$ kJ/mol, $N_A=6.023x10^{23}$ mol^{-1}, M=0.1 and R=8.314477 J/mol·K the value of the constant, *K*, is:

$$K = 5.25 \times 10^{-20} \frac{cm \times mol}{s^2} = 1.89 \times 10^{-9} \frac{nm \times mol}{min^2} \quad \text{eq.III.20}$$

III.5. Influence of the geometry of mesa

In addition to the growth conditions, geometry of the substrate surface influences the growth. In fact, local growth effects are shown to take place on the overgrowth on patterned substrates, where the proximity of different growth orientation interact. It makes strong difference respect to massive planar growth models making very difficult to extrapolate massive phenomenon and predictions to nanometer scale [Biasol 2002]. The existence of different initial orientations affects the molecular affinity of hydrocarbons in a similar way that for the nanodiamond particles growth [Lai 2016]. The presence of structures with different sizes of surfaces and orientations result in a different chemical reactivity and affinity to specific adsorbates. Growth on (100) orientations, where adsorption is favored and with it 2x1 reconstruction, is different than on (111) orientations where graphitization is promoted resulting in a less active facet, or than the rough (110) facet, both with tilted-chain reconstruction [Frauenheim 1993, Richley 2012, Lai 2016]. In the case of nanodiamond, this results in a different shape of the nanoparticles. In the case of nanostructures overgrowth, consequences on the final shape of the overgrown pattern can be anticipated.

Previous section explained such growth behaviors at a nanometric scale, pointing out the main factors involved in those growth process and providing an expression for estimating the growth velocities along different orientations. However, such an analysis left unknown the factor coming from the substrate geometry. This section begins explaining the reason of the formation of the different growth fronts and evaluating the outcome of their progress and continues assessing the role that geometry factors such as height and corners play.

III.5.1. Influence of the plane of growth

The 3D configuration of the substrate used for growth, brings additional possibilities of sticking to the carbon atoms. In fact, the substrate used for the growth was 100-oriented, however, the presence of corners and (011) faces, because of it is very rough [Sutcu 1992], will be the

preferential sites to occupy by the carbon atoms. This situation is encouraged by the biradical sites existing in such planes that has been shown as essential into the sticking probability. As a consequence of the multiplanar configuration generated by the mesa, i.e. due to the different initial orientation in a mesa patterned substrate, the growth itself is not homogeneous and it will start from the corner and along the 111 direction. In the following, the first steps of this growth are presented on the basis of two main principles: (i) carbon atoms will preferably stick at biradical sites, (ii) carbon atoms will migrate (as was previously exposed) to the corner of the structure. In this simplified schema, surface after etching has been considered atomically flat and all the sites actives. Both suppositions can be assumed in a first approximation because: at the atomic scale, surface can be considered flat, and growth was performed with high flux of hydrogen (the exceptional case of HMC will be introduced at the end of the section). Monoradical sites (these are bonding to one carbon) are drawn as orange lines whereas biradical sites (these are bonding to two carbons) are drawn as red lines. Note that there are sites formed by a mono plus a double bonding.

As shown in *Section III.2* (page 67), in the inner corner, at the foot of the mesa structure, the first lateral orientation of growth observed in the sample was along 111. Fig.III.13 schematizes its formation according to the premises previously exposed.

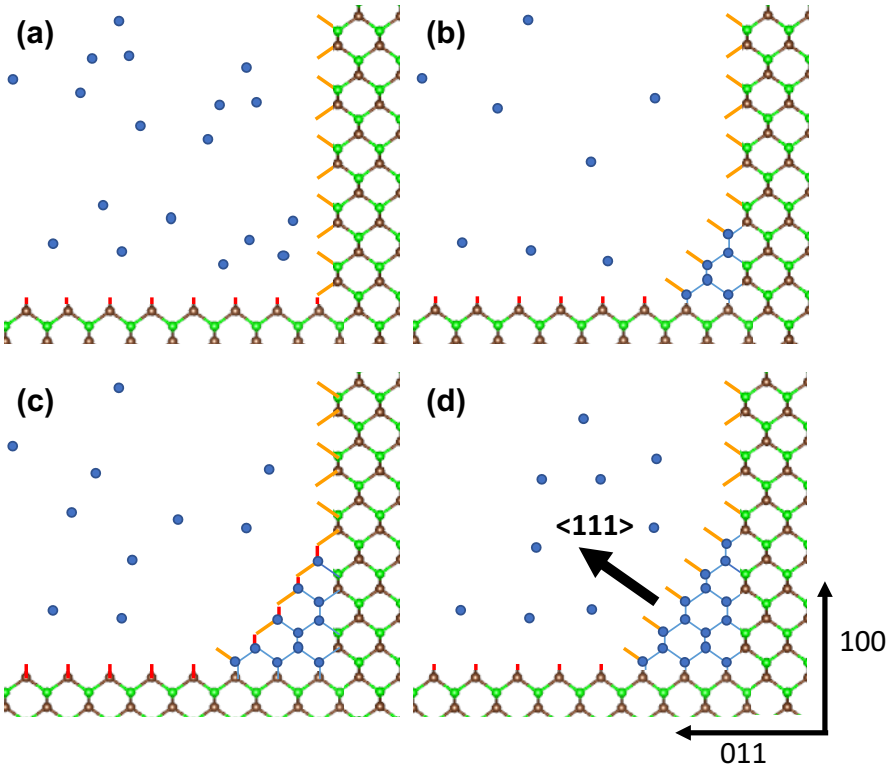

FigIII.13. Simplified schematics of the first steps of growth. Free carbon atoms (radicals) are shown as blue balls, orange lines are the monoradical sites whereas red lines correspond to biradical sites. (a) shows the

bottom corner of the structure at the beginning of the growth. (b) shows the same region after the stacking of the first atoms. (c) shows situation in which the 111-surface is high reactive and (d) the corner when a number of atoms enough to identify the (111) plane have been deposited.

(111) plane is formed in a very first step by the attraction of the atoms to the bi(tri)radical site placed on the corner (Fig.III.13 (a)). First atoms are stacked in the surrounding (Fig.III.13 (b)) and, rapidly, they generate a high reactive plane (Fig.III.13 (c)). In fact, the growth along the 111 orientation combines a situation with many high reactive sites (Fig.III.13 (c)) with others where all the sites are monoradicals (Fig.III.13 (d)).

Now, let's suppose that, in the situation showed in Fig.III.13 (d), the new carbon atom is sticking in a biradical site instead of a monoradical one. Let's also suppose that such biradical site is the closely neighbor to the first monoradical. This situation can be easily promoted by the carbon migration and favored by the fact that border between (100) and (111) surfaces are singularities where carbon atoms sticking is more probable. This is displayed in Fig.III.14 (a), where the double monoradical site (it is biradical) is rapidly occupied by a carbon atom. This inclusion changes the process by generating additional biradical sites combining two monoradicals (see Fig.III.14 (b)). As a consequence, stacking preferences are modified and sample starts to growth along the <211> orientation.

In the case of growth along the 111 orientation, there is a situation in which all the bonding are monoradicals. In this second step, in which growth is along the <211> direction, the growth front is formed by the recurrence of the system "monoradical-monoradical-biradical" (Fig.III.14 (c)).

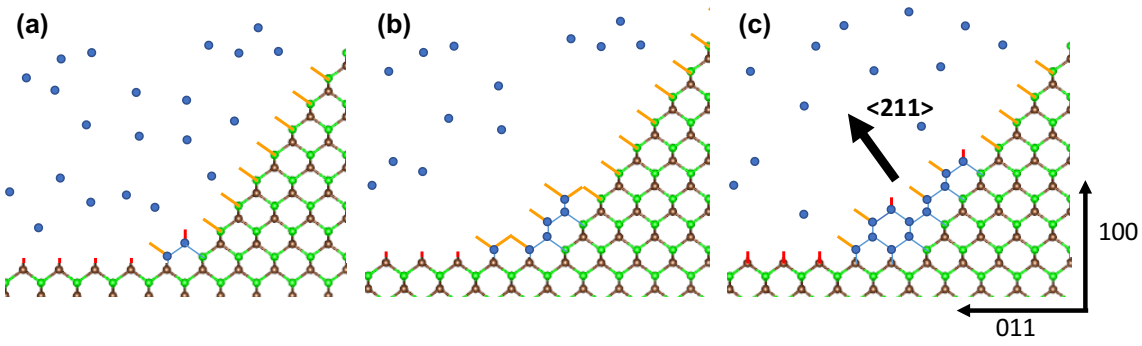

FigIII.14. Simplified schema of the transformation of the (a) (111)-front of growth to the (c) (211)-front of growth.

Fig.III.15 (a) shows the case in which another additional atom is stacked on the (100) surface. In the same way as previously, it changes the distribution of free bonding and, then, the plane of growth. Fig.III.15 (b) shows an intermediate state whereas Fig.III.15 (c) shows the plane

(311) formed. The growth front in this case, is formed by recurrences of the system "monoradical-biradical", that tentatively induce a higher stability due to the higher density of biradical sites.

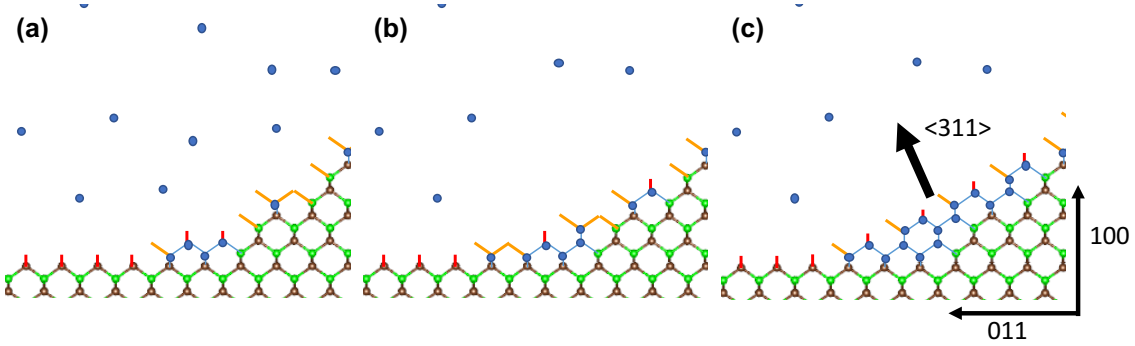

FigIII.15. Simplified schema of the transformation of the (a) (211)-front of growth into the (c) (311)-front of growth.

As was exposed as a premise of this reasoning, methane concentration plays an important role. This is the reason of the differences in growth between the two recipes used for the samples studied. Higher concentrations of methane probably do not influence the sites activation because the atomic H concentration is still high enough. However, it results in a larger number of C radicals that will stack in a faster and *disorganized* way. The hopping probability (defined in the previous section) remains equal, however, the migration is radically reduced due to the minor probability to have a free neighbor bonding, because of the higher number of C radicals that will rapidly stack into the surrounding active sites, blocking surface diffusion. Moreover, the probability of a C atom to stack in an additional biradical site from the 100 face (that is the origin of the change of growth front as has been exposed) will increase and, therefore, the change of the growth front will be faster and more abrupt. These situations favor the generation of dislocations as TEM micrographs showed.

Furthermore, when the atomic H concentration is low, other fates for the reactive surface adducts become possible, such as reaction with other gas-phase hydrocarbon radicals (such as CH_x and more complex species C_yH_z, $y>1$) which may lead to restructuring of the surface, or even re-nucleation of a new, misoriented crystallite. These processes have been proposed to be one route by which the size of crystallites is prevented from becoming larger in polycrystalline diamond. They might be here at the origin of of the twins and crystallites observed on the top of the HMC samples that will be discussed in *Chapter IV*.

III.5.2. Influence of the corner

There are two critical regions into the structures studied. They are the inner or lower (A) and outer or upper (B) corners. In these two position, growth is limited in a different way and it is necessary to be studied independently.

When growth takes place nearby A, see Fig.III.16 (a), the driving force controlling the shape of the surface is the minimization of the surface energy by growing a new surface making at an inner open corner an obtuse angle with the lateral and bottom surface respectively. The important point is that the edges of the growing facet are inner obtuse angles with surfaces that thanks to the wettability associated with homoepitaxial growth provide instantly the possibility for a lateral expansion of the facet at the edges as the perpendicular growth proceeds.

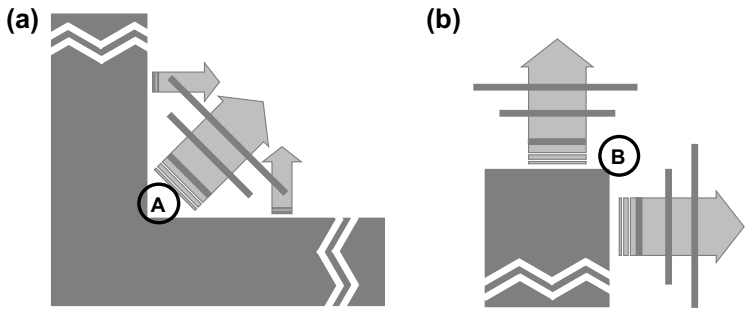

Fig.III.16. Schematics of the growth restrictions at the (a) inner corner, called A, and (b) upper corner, called B due to the adjacent faces to both positions.

However, when growth takes place in B (Fig.V.16 (b)), the situation is completely different. In this case the facets cannot enlarge laterally if adjacent facets are not growing fast enough: the growth is limited by the slowest facets. This situation explains the fact that, at *B* slower growth rates give the final facet of the structure, as has been classically reported [Silva, Tallaire, …], whereas for *A* are the fast growth planes those that give the final facet. In fact, growth at B cannot be faster than in A because it requires support from the lateral growth to continue in this direction.

These two positions introduce then geometric limitation into the growth. Such restrictions are displayed together in Fig.III.17. Fig.III.17 (a) shows the first step of the growth in a two-dimensional perspective. In this interpretation, four growth orientations are considered: (i) in red color are orientations along (1 0) and (0 1) following the shape of the initial structure, (ii) in green is drawn a fast and tilted orientation along (1 1) that comes from the corners and (iii) in blue is

drawn a less tilted and, consequently, slower orientation along (2 1) that also comes from the corners.

As has been mentioned, green orientation can only take place at the inner corner. Obviously, growth velocity along this orientation is different than along the (1 0)-direction (and its equivalent (0 1)). For simplification reason, v_{11} has been considered three times faster than v_{10} and $v_{21}=v_{10}$. After a Δt period of growth, these differences of growth velocity results in the change of the shape of the structure.

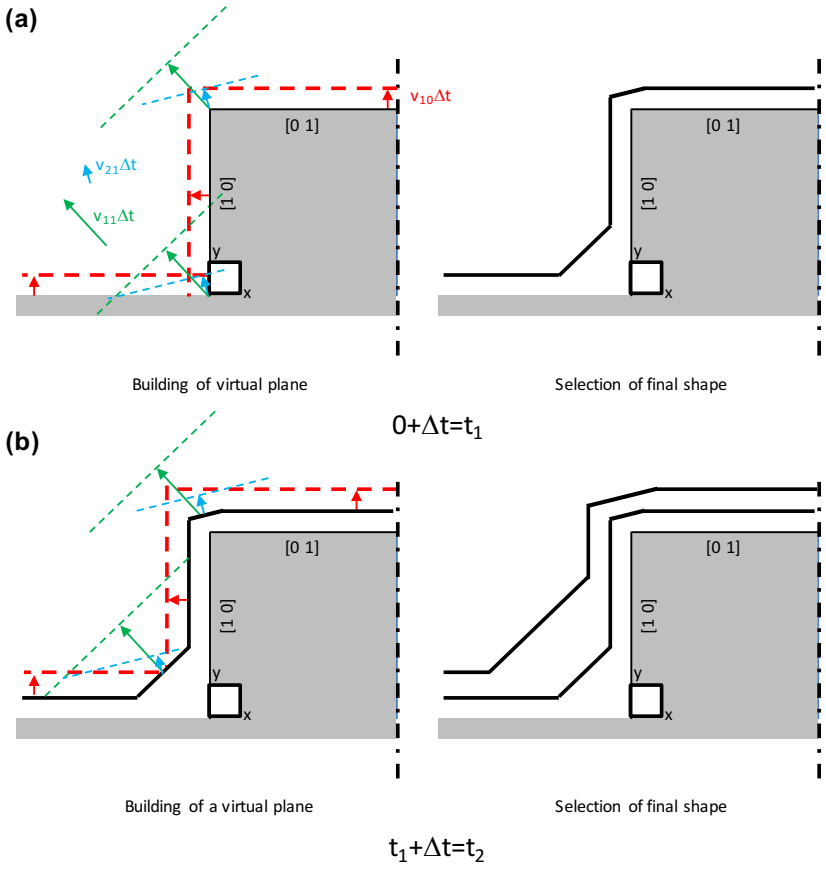

Fig.III.17. Schematics of the growth along the corners at the first stage of growth. Corners acts as generators of virtual planes. Geometry restriction at those places will determine the final shape.

However, the upper corner cannot grow along the green orientation. In this region, slow velocities govern the growth. In fact, Fig.III.7 (a) shows that tilted growth orientations with growth rates in the range of the (10) will limit the growth at those positions.

This behavior continues during the growth process and each Δt results in an increasing of the new facets appeared in the inner and upper corner. Fig.III.17 (b) shows this system in a time $t_1+\Delta t$.

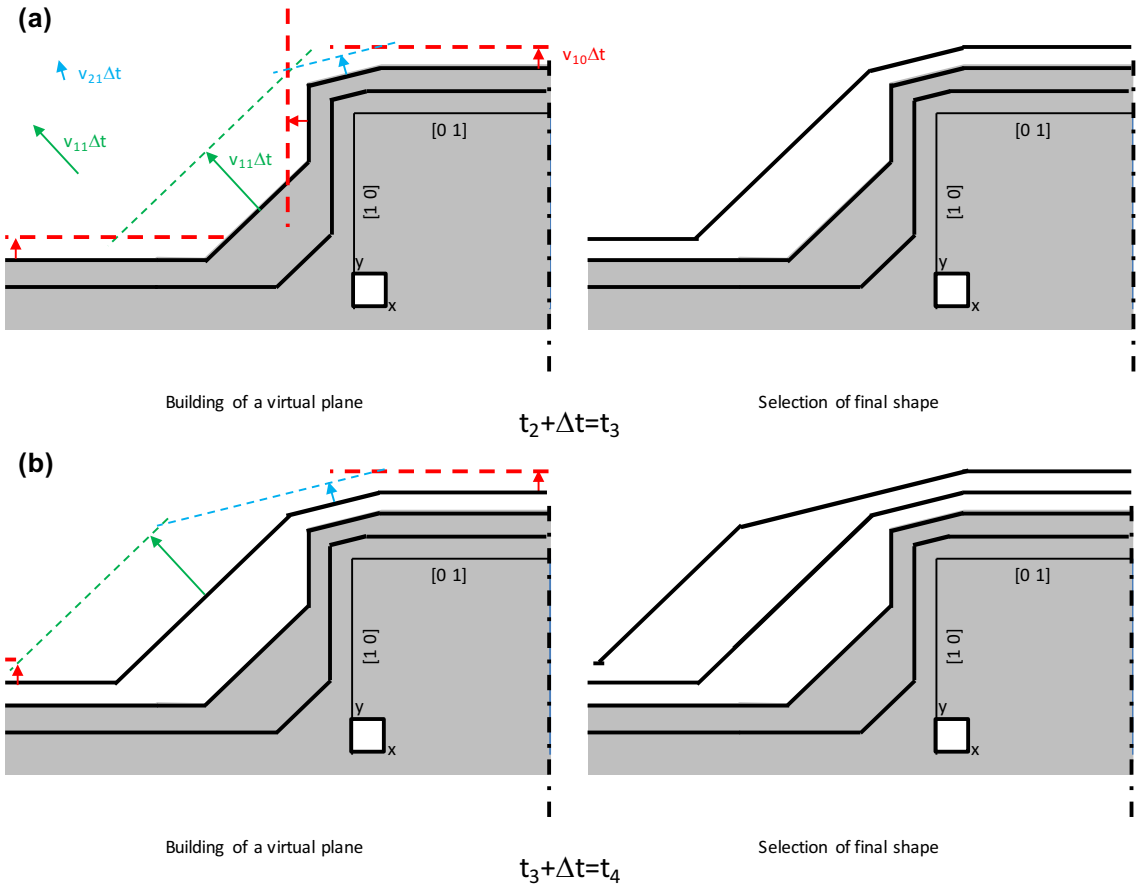

Fig.III.18. Schematics of the growth restrictions at the (a) inner corner, called A, and (b) upper corner, called B due to the adjacent faces to both positions.

Fig.III.18 (a) shows the Δt in which (11) and (21) converge. At such position (11) will be limited by the growth rate along (21). Posterior growth stage shows that this limitation results in the reduction of the (11) growth sector (Fig.III.18).

This mechanism explains TEM observations in which the same doped layers growth along different orientations (see as example Fig.III.6), i.e. the coexistence of different growth sectors at the same moment of the growth process. Moreover, the changes on the growth sectors can be related to this growth orientation convergence. These changes should be induced by the planarization trend, that is a minimization of the surface energy. However, mesa geometries such as corners, have a strong influence on the time sequence and interplay of the growth sectors.

III.5.3. Influence of the mesa height

One of the geometrical parameters that can be easily controlled by varying the etching time is the height of the mesa structure. Height is a key parameter since it regulates the distance between the two main singularities, corners A and B, and, consequently, the final shape of the nanostructures growth depends on it. In order to evaluate the influence of such a parameter, a comparative study of samples #3-LMCD, #11-Disp and #10-LMCD, all of them grown at the same low methane concentration, is here presented. Growth conditions of the samples were exposed in *Chapter II*. Lateral growth on sample #11-Disp was carried out with similar conditions to samples #3-LMCD and #10-LMCD. However, the substrate used for the mesa etching was previously overgrown with standard (HMC) conditions. In any case, these previous treatments should not have a strong influence into the lateral growth orientations. The main growth parameters are summarized for each sample in table.III.IV. It is shown that the main differences are doping (thirteen low doped layers, a thick non-intentionally doped layer with a very thin highly doped layer, and six highly doped layers, respectively), growth time (~13hours, ~3 hours and ~6 hours) and height (900nm, 1700nm and 2700nm).

Table III.IV. Growth conditions of samples #3-LMCD, #10-LMCD and #11-Disp.

Sample	Layer	CH_4/H_2	B_2H_6/CH_4	Time (min)		Total Height (nm)
#3-LMCD	Doped	0.25%	10700	2	x13	~900
	Undoped	0.1%	-	60	x13	
#11-Disp	Doped	0.25%	28000	5	x6	~1700
	Undoped	0.1%	-	5	x6	
#10-LMCD	Undoped	0.1%	-	180	x1	~2700
	Doped	0.25%	28000	8	x1	

Fig.III.19 show TEM micrographs of samples (a) #3-LMCD, (b) #11-Disp and (c) #10-LMCD. Sample #3-LMCD has been studied in the previous sections. The growth orientations followed during its growth wereas obtained by stratigraphic approach. Because sample #11-Disp was not grown with a multilayered configuration, from Fig.III.19 (b) it is not possible to determine intermediate growth planes. Nevertheless, the orientation of growth at the last step of the process is deduced from its final shape. It shows a lateral growth oriented along the <111> and <211> directions. Fig.III.19 (c) shows the lateral growth of sample #10-LMCD with the electron diffraction pattern indexed as inset in the figure. With the exception of the first doped layer, growth is shown parallel to the 111- orientation. The first doped layer shows a growth along two different orientations: 111- near the corners, and 110 in the middle part. Growth rate measured by the thickness of the undoped layers shows that the rate along the 111-orientation at the top region,

was about half of the rate respect to that of the bottom region (5.7nm/min and 10.5nm/min, respectively). This is in accordance to the premises exposed in the previous section: lateral growth is required in order to perform the growth at the upper corner.

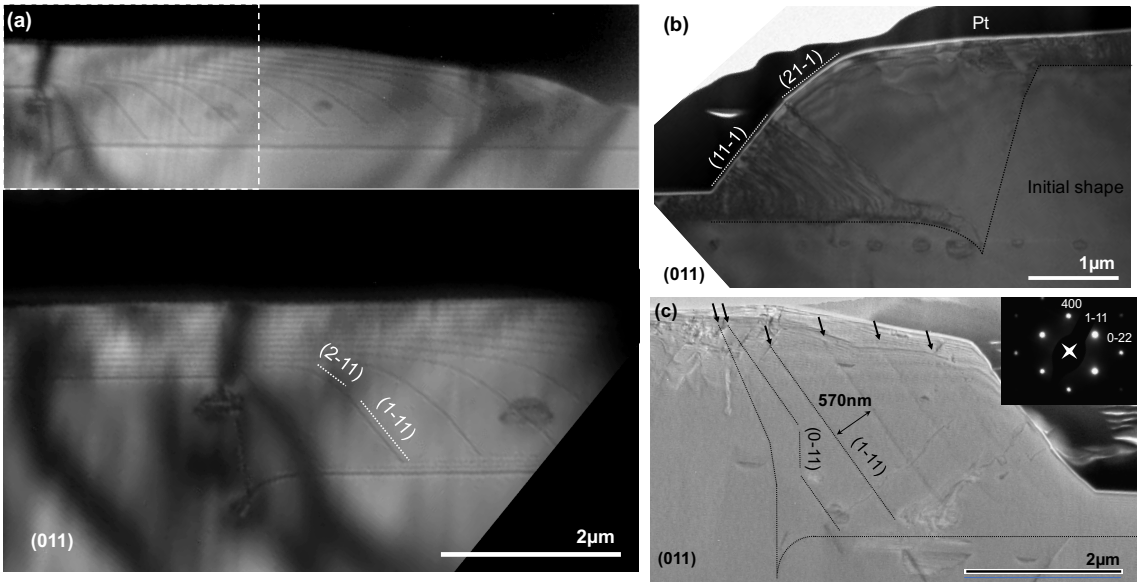

Fig.19. (a) TEM micrographs of sample #3-LMCD with a general view of the lamella on the top and the region of the initial shape magnified. (b) TEM micrograph of sample #11-Disp, and (c) TEM micrograph of sample #10-LMCD with its diffraction patterns indexed as inset. All the micrographs have the main plane of growth marked by dashed lines and identified with labels.

In sample #3-LMCD, growth sectors can be well identified using the stratigraphic approach. The obtained pattern is then extrapolated to Sample #11-Disp by superimposing and elongating to superimpose the corners of the mesa structure (Fig.III.20 (b)). It matches perfectly. It has been repeated with sample #10-LMCD where it also matches (Fig.III.20 (c)). Because of change times on this sample are larger, i.e. growth sectors required longer times to change, has been possible to enlarge the growth sector along [111] and to include a small initial region growth along the [110] direction that was not identified on the others samples. Fig.III.20 (d) summarizes then the regions of growth for mesa structures from 900nm to 2700nm of height.

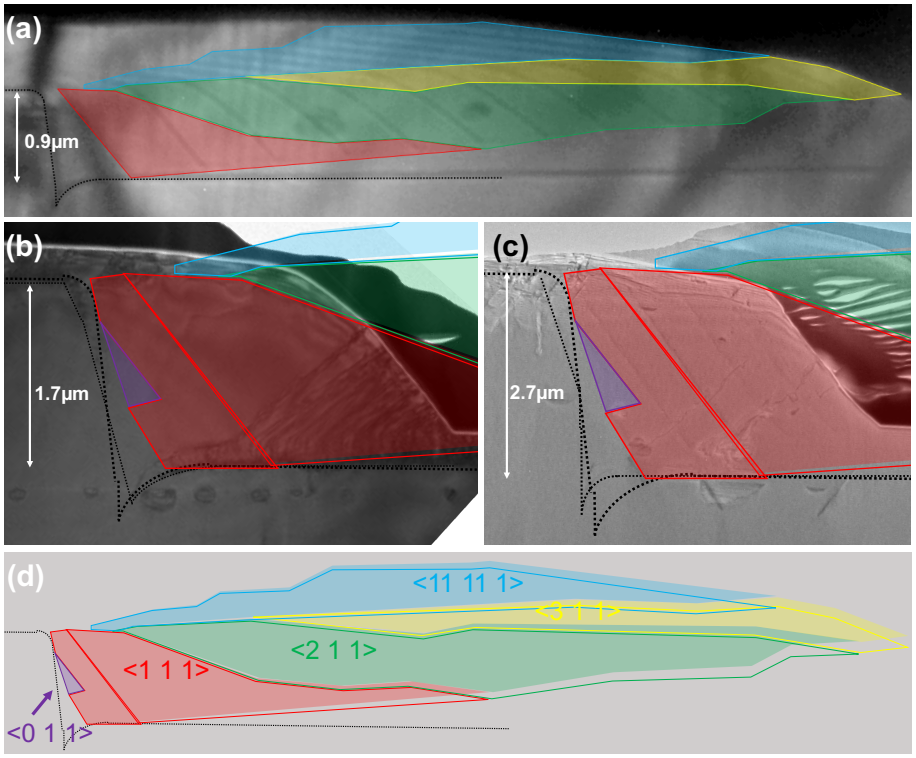

Fig.III.20. (a) TEM micrograph of sample #3-LMCD with the growth sectors marked by colors. Such sectors have been elongated keeping the proportion to be adapted to the height of sample (b) #11-Disp and (c) #10-LMCD. It matches perfectly in both cases. (d) shows then the growth sectors for micrometric diamond mesa structures overgrowth.

From this study, it can be concluded that, keeping the growth conditions, growth sectors will be the same, i.e. the process is reproducible. Moreover, the height of the mesa structure will define the time sequence of the growth sector, being then possible to select patterns that lead to a specific orientation during a longer time.

III.6. Reproducibility of the process

The results obtained from the height study confirm the reproducibility of the growth process. However, one of the main aspects of the stratigraphy approach, the use of boron during the growth, even if it was in a very low proportion and just for very-thin layers, must be evaluated. On principle, boron doping is mainly substitutional, meaning that boron atoms are incorporated into the diamond lattice substituting carbon atoms. A first idea about the weak influence of such incorporation on the faceting of the nanostructures after growth was given in Fig.III.20 where 3 hours of undoped low methane concentration growth resulted to be the same as using boron doped layers. In order to confirm this indication, doped and undoped high methane concentration

samples were also compared. In this way, growth results of sample #4-HMCD, exposed in this chapter, are compared with the undoped sample #1-F, whose growth conditions where very similar. However, sample #1-F was grown for 70 minutes whereas sample #4-HMCD was grown for 130 minutes. Fig.III.21 (c) shows a SEM micrograph of the sample #1-F, where facets were obtained by optical profilometer. These facets have been compared with that of sample #4-HMCD (see Fig.III.21 (a) along the <010> direction, and Fig.III.21 (b) along the <110> direction) at the same thickness, i.e. corresponds with the space in between doped layer number 6 and 7. This result shows the exact equivalence between both samples and illustrates the reproducibility of the growth for both recipes (LMC and HMC).

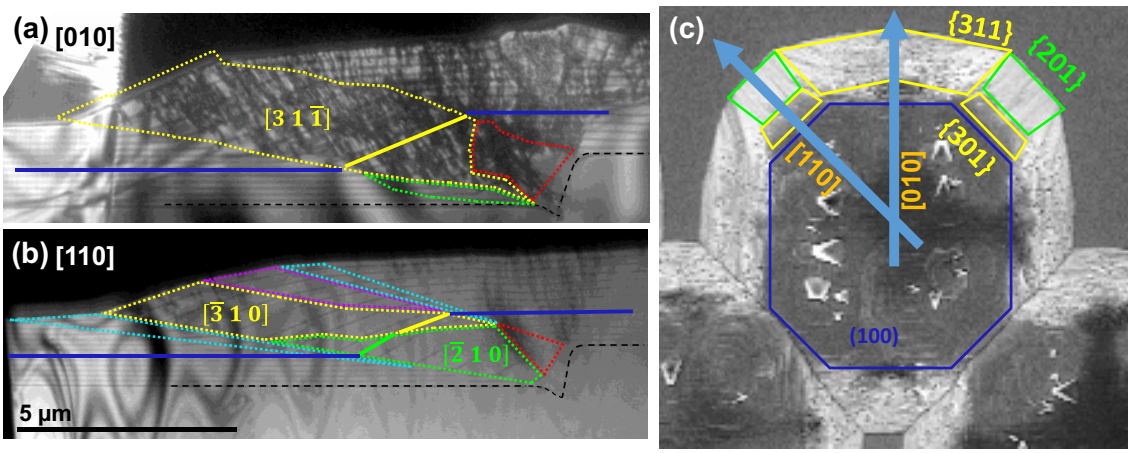

Fig.III.21. Comparative of the growth orientation of sample #4-HMCD, (a) and (b), corresponded to 130min growth, and sample #1-F (c), corresponded to 70 min growth. Region of sample #4-HMCD growth between the minutes 66 and 77 corresponds to the space between doped layers 6th and 7th. Growth orientations coincide as show solid lines in (a) and (b).

Even though we demonstrate here that the incorporation of highly doped thin layer do not affect the growth orientation pattern (growth sectors). An increase of the doping level could change this assertion. Indeed, Zou *et al*. [Zou 2016] reported that boron atoms positioned within the second atomic carbon layer cause an enhancement in the growth rate. On the other hand, the effect of B positioned in the other atomic carbon layers showed a decreased growth. Moreover, high boron concentrations can induce the formation of dislocations that can modify growth velocities [Alegre 2014].

III.7. Conclusions

The overgrowth of patterned substrates leads to the coexistence of different growth planes at the same time. A stratigraphic study showed that these planes change along the growth thickness, leading to a planarization favored by both the minimization of the total surface energy

and the high wettability associated to homoepitaxial growth. The microscopic chemical process has been described at an atomic scale. The repetition of the growth without supperlattice structure but with the same results shows the weak to nonexistent influence of the boron atoms at those levels on the growth process, and highlight the reproducibility of the growth.

In this way, it is possible to predict the growth orientation at different times of the growth process and for different mesa sizes. Consequently, it is possible to choose particular orientations and growth durations to obtain a particular final shape. Moreover, low methane concentration growth has been shown as an optimal condition for mesa overgrowth. It exhibits a better crystal quality and favors the lateral character of the growth.

III.8. Summaries

III.8.1. Resumen

El crecimiento de diamante en tres dimensiones por CVD ha sido objeto de estudio desde finales del siglo pasado. Gracias a dichos estudios, se desarrolló un modelo capaz de prever la forma final del facetado en función de las velocidades de crecimiento a lo largo de las orientaciones {110}, {111} y {113} respecto a la {100}. Basados en este modelo, en este capítulo hemos abordado el crecimiento lateral de nuestras muestras mesa.

Para el cálculo de las velocidades de crecimiento en diferentes orientaciones, así como la obtención de dichas orientaciones, se ha empleado un modelo estratigráfico. Para ello, las muestras han sido crecidas con multicapas finas dopadas con boro. Este dopado genera un contraste cuando son observadas por microscopía electrónica de transmisión evidenciando así la orientación seguida durante el crecimiento. Primero se han estudiado las muestras #1-F y #2-A. La muestra #1-F fue crecida sin capas dopadas y su facetado se obtuvo por perfilometría óptica. Las velocidades de crecimiento fueron deducidas haciendo uso de simples relaciones trigonométricas.

A pesar de la utilidad de la técnica, ésta tienes al menos tres limitaciones: (i) las caras del facetado no son fáciles de identificar y en muchas ocasiones existen facetados secundarios que pasan desapercibidos. Esto es especialmente acuciante en discos de gran diámetro y corto crecimiento. (ii) El método asume que el crecimiento es siempre a lo largo de una misma dirección. No se tienen en cuenta posibles planos de crecimiento intermedios. (iii) No es fácilmente estimable el punto de intersección entre la faceta a medir y el plano original, siendo por tanto una fuente de error no desdeñable.

Todas estas limitaciones son salvables utilizando la aproximación estratigráfica previamente introducida. Las observaciones TEM realizadas sobre esta muestra mediante dicha técnica mostraron planos intermedios y facetados secundarios poniendo de manifiesto las carencias detectadas en el método trigonométrico. De hecho, la muestra #2-A presenta un gran número de orientaciones diferentes con diferentes velocidades de crecimiento. Dichas velocidades están recogidas en la tabla III.I y de ellas se obtienen los parámetros de crecimiento siguientes: α=3.1 y β=0.75. Ésta técnica estratigráfica permite seguir paso a paso el crecimiento dinámico 2D y 3D en escala nanométrica.

Con ese objetivo, la aproximación estratigráfica ha sido utilizada para el estudio de las muestras #3-LMCD y #4-HMCD. Estas muestras fueron crecidas con las mismas condiciones exceptuando la concentración de metano en hidrogeno que fue de 0.1% y 0.75% respectivamente (las condiciones de crecimiento de todas las muestras vienen detalladas en el capítulo II). Las diferencias entre ambos crecimientos son claras desde la primera observación. Mientras que la muestra #3-LMCD presenta un aspecto final con forma de cruz, la muestra #4-HMCD exhibe una forma cuadrada. Ambos casos muestran

un facetado principal a lo largo de las direcciones <0 1 1> y <0 -1 1>. Además, las estructuras mesa de la muestra #4-HMCD están coronadas por defectos superficiales tipo montículo (hillocks) que no están presentes en la muestra #3-LMCD.

Las orientaciones de crecimiento han sido obtenidas para ambas muestras utilizando para ello la aproximación estratigráfica. Las dos muestran los mismos planos de crecimiento, pero con diferente momento de aparición. Las velocidades de crecimiento han sido calculadas para cada muestra obteniéndose unos parámetros de crecimiento: α=0.2 y β=0.6 para la muestra #3-LMCD y α=0.3 y β=1.0 para la muestra #4-HMCD. De estos parámetros de crecimiento se deduce los planos {1 0 0} son los más lentos y que estos serán dominantes frente a los planos {1 1 3} en el caso de la muestra #3-LMCD. Para la muestra #4-HMCD sin embargo, estos planos serán los que marquen la forma final. En cualquier caso, una tendencia a la planarización de las estructuras es observada en ambas muestras.

Tomando estas cuatro muestras como ejemplo, puede realizarse una primera aproximación al mecanismo de crecimiento lateral de diamante homoepitaxial. Desde un punto de vista fisicoquímico, se ha publicado en numerosas ocasiones que son los radicales hidrogenados los principales actores durante el crecimiento de diamante por MPCVD. Esto se debe a que son estos radicales los que producen metilo-radicales a partir del metano. La recombinación de éstos últimos en la superficie del diamante induce la formación de sitios activos C_2H_y, responsables del crecimiento.

Debido a que la mayor parte de la superficie del diamante es hidrogeno-terminada, el crecimiento requiere de un primer paso consistente en la activación de esta superficie que puede ser por abstracción de hidrógeno o adsorción de CH_3. La fracción de átomos de

carbono activos vendrá dada por tanto por el equilibrio entre el hidrogeno abstraído y el adicionado por la reacción. Teniendo en cuenta nuestras condiciones de crecimiento, esta proporción puede ser estimada en un valor próximo a 0.1.

Otro proceso clave en el crecimiento de diamante es su erosión durante el proceso. Muchos de los átomos de carbonos adsorbidos migran desde su posición inicial a otros puntos de la superficie. La distancia de migración está estimada en unos 10Å y existen tres procesos por los que puede darse: (i) simples saltos de una posición más alta a otra cerca de una esquina o borde; (ii) vuelta del átomo al gas; y (iii) vuelta desde una esquina o borde a otra posición. Este proceso de migración puede ser deducido a partir de las condiciones particulares del crecimiento.

Por otra parte, la probabilidad de erosión en diamante monocristalino es considerada bastante baja y la mayoría del carbono que se elimina es grafito.

La activación y desactivación de sitios radicales estará gobernada por las reacciones químicas que se lleven a cabo entre el gas y la superficie de la muestra. Sin embargo, la probabilidad de salto de un átomo de un sitio activo a otro dependerá de su probabilidad de movimiento, así como de la geometría de la superficie.

Por último, el coeficiente de escisión puede obviarse debido a que es un proceso menor que elimina menos del 2% de las especies adsorbidas.

Teniendo en cuenta todos estos parámetros se obtiene una estimación para la velocidad de crecimiento que vendrá dominado por la concentración de CH_3 y un parámetro geométrico.

Dentro de este factor geométrico, las esquinas juegan un papel clave. La esquina inferior tiene una superficie inferior y lateral para sustentarse. De esta forma son las orientaciones de crecimiento más rápidas las que marcan el crecimiento. El caso de la esquina superior, sin embargo, es el opuesto. La ausencia de planos sobre los que sustentarse hace que sean las orientaciones con velocidades de crecimiento más lentas las que marquen el facetado.

Un estudio en muestras recrecidas sobre sustratos grabados con discos de diferente altura (#3-LMCD, #10-LMCD y #11-Disp) muestra que el crecimiento es análogo en todos los casos. Es decir, los sectores de crecimiento son los mismos y las regiones donde estos aparecen son proporcionales a la altura del disco.

La reproducibilidad de este proceso de crecimiento se ha evaluado. Las muestras #1-F y #4-HMCD fueron crecidas con condiciones muy similares exceptuando el hecho de que para la muestra #4-HMCD se hizo uso de líneas de dopado para la aproximación estratigráfica y su tiempo de crecimiento fue muy superior. Precisamente estas líneas de dopado nos permiten comprobar que el crecimiento en #4-HMCD a tiempos correspondientes con los del facetado final de #1-F sigue la misma orientación que la de éste último. Se pone así de manifiesto no solo que el crecimiento es reproducible, sino que además las capas de dopado usadas para marcarlo no influyen en las orientaciones que este sigue.

III.8.2 Résumé

La croissance du diamant en trois dimensions par CVD a été étudiée depuis la fin du siècle dernier. Grâce à ces études, un modèle a été développé que peut prédire la forme finale du facettage en fonction des taux de croissance selon des directions {110}, {111} et {113} par

rapport à la {100}. Sur la base de ce modèle, dans ce chapitre, nous avons abordé la croissance latérale sur des échantillons prégravé avec une surface en mesa. En utilisant le facettage mesuré en profilométrie optique, les vitesse de croissance ont été calculés à l'aide des relations trigonométriques simples.

En dépit de l'utilité de la technique, au moins trois limitations ont été identifiées : (i) les facettes ne sont pas faciles à identifier et souvent il y a des facettes secondaires qui passent inaperçues. Ceci est particulièrement fréquent pour les disques de grand diamètre et de croissance courte. (ii) La méthode suppose que la croissance est toujours dans la même direction. Les éventuels niveaux intermédiaires de croissance ne sont pas pris en compte. (iii) Il est difficile d'estimer le point d'intersection entre la facette à mesurer et le plan d'origine, ce qui constitue une source d'erreur non négligeable.

Toutes ces limitations peuvent être ignorées en utilisant l'approche stratigraphique. En effet, pour la mesure des vitesse de croissance selon différentes orientations, une méthode stratigraphique a été mise en œuvre. Pour ce faire, la croissance des échantillons a été faite avec des multicouches minces dopées avec du bore. Ce dopage permet d'obtenir un contraste en microscopie électronique à transmission et indique l'orientation suivie au cours de la croissance. Cette technique a montré des niveaux intermédiaires et facettes secondaires, mettant en évidence les faiblesses identifiées dans la méthode trigonométrique. En fait, l'échantillon #2-A présente un grand nombre d'orientations différentes avec différents vitesse de croissance. Ces vitesses ont été mesurées et les paramètres de croissance α=3,1 et β=0,7 ont été obtenus. Cette technique stratigraphique permet de suivre étape par étape la croissance dynamique 2D et 3D à l'échelle nanométrique.

À cette fin, l'approche stratigraphique a été utilisée pour étudier les échantillons #3-LMCD et #4-HMCD. La croissance de ces échantillons a été réalisée dans les mêmes conditions sauf que la concentration de méthane dans l'hydrogène était de 0,1% et 0,75%, respectivement (les conditions de croissance de tous les échantillons sont décrites dans le chapitre II). Les différences structurales entre les deux croissances sont immédiates. Tandis que l'échantillon #3-LMCD présente un aspect final cruxiforme, l'échantillon #4-HMCD présente une forme carrée. Les deux cas montrent une facette principale le long des directions <0 1 1> et <0 -1 1>. En outre, les structures mesa de l'échantillon #4-HMCD sont couronnése de défauts de surface de type « hillocks » (buttes, ou pyramides tronquées) qui ne sont pas présents dans l'échantillon #3-LMCD.

Les orientations de croissance des deux échantillons ont été obtenues en utilisant cette approche stratigraphique. Les deux échantillons montrent les mêmes orientations de croissance, mais avec différentes durées pour chaque étape. Les taux de croissance ont été calculés pour chaque échantillon, les paramètres de croissance obtenu sont : α = 0,2 et β = 0,6 pour l'échantillon #3-LMCD et α = 0,3 et β = 1,0 pour l'échantillon #4-HMCD. Ces paramètres de croissance, indiquent que les plans {1 0 0} sont les plus lents à croître, et que ceux-ci sont dominants par rapport aux plans {1 1 3} dans le cas de l'échantillon #3-LMCD. Alors que pour l'échantillon #4-HMCD, ces plans sont ceux qui marquent la forme finale. En tout état de cause, une tendance à l'aplanissement (on parle de « planarisation ») des structures est observée dans les deux échantillons.

Compte tenu des résultats obtenus sur ces quatre échantillons, une première approche du mécanisme de croissance latérale de diamant homoépitaxial a été proposée. D'un point de vue physico-chimique, il a

été signalé à plusieurs reprises que les radicaux hydrogénés sont les acteurs majeurs de la croissance du diamant par MPCVD. En effet, ces radicaux sont des radicaux méthyle produits à partir du méthane. La recombinaison de ce dernier sur la surface du diamant induit la formation de sites actifs C_2H_y responsables de la croissance.

Étant donné que dans le réacteur,la majeure partie de la surface du diamant est à terminaison hydrogène, la croissance nécessite une première étape consistant à activer la surface, soit par abstraction d'hydrogène ou par adsorption de CH_3. La fraction d'atomes de carbone actif est donnée à la fois par l'équilibre entre l'hydrogène ajouté et retiré par réaction. Compte tenu de nos conditions de croissance, ce rapport peut être estimé à une valeur proche de 0,1.

Un autre processus clé de la croissance du diamant est la gravure résultant de la gravure par hydrogène au cours du procédé assisté par plasma. Un grand nombre d'atomes de carbone adsorbés migrent depuis leur position initiale vers d'autres points de la surface. Il y a trois processus qui peuvent se produire (i) des sauts simples à partir d'une position plus centrale vers une autre à proximité d'un coin ou un bord; (ii) le retour de l'atome au gaz; et (iii) des déplacements de l'atome d'un coin ou un bord vers une autre position. Les caractéristiques de ce processus de diffusion peuvent être déduites des conditions particulières de croissance.

En outre, le risque d'érosion de la phase monocristalline du diamant est considéré comme assez faible et la plupart du carbone éliminé est du graphite.

L'activation et la désactivation des sites de radicaux seront régis par les réactions chimiques qui ont lieu entre le gaz et la surface de l'échantillon. Cependant, la probabilité d'un atome de sauter d'un site actif un autre dépend de la probabilité de migration ainsi que de la

géométrie de la surface. Dans cette dernière, les angles des structures mesa sont très importantes. L'angle inférieur a une surface au fond et sur les côtés pour la « soutenir ». Ainsi, l'orientation de la croissance à ces endroits est la plus rapide. Pour l'angle supérieur, c'est l'inverse. L'absence de plans sur lesquels les faces puissent s'appuyer limite les taux de croissance et les faces les plus lentes déterminent le facettage.

Une étude de la reprise de croissance sur des disques gravés des différentes hauteurs (# 3-LMCD, # 10-LMCD et #11-DISP) montre que la croissance était similaire dans tous les cas. On retrouve les mêmes configurations et les mêmes étapes à différents moments. Autrement dit, les plans de croissance sont les mêmes et les régions où elles apparaissent sont homothétiques, de dimensions proportionnelles à la hauteur du disque.

La reproductibilité de ce processus de croissance peut être évaluée. Les conditions de croissance des échantillons #1-F et #4-HMCD ont été très similaires, sauf le temps de croissance a été plus élevé pour cet échantillon. Ce sont précisément les lignes de dopage qui nous permettent de vérifier que la croissance du #4-HMCD correspond, à certains moments, au facettage final du #1-F. Il est donc démontré non seulement que la croissance est reproductible, mais aussi que des couches dopées utilisées pour marquer les lignes directrices n'affectent pas la généralité des observations.

IV Defects

Contents

Defects generated during the lateral growth were analyzed. Two factors have been investigated, the growth orientations and the growth conditions. From this analysis, particular crystallographic planes, for example {111}, have been shown to favor the generation of dislocations. Moreover, high methane concentration growths have generated a higher density of dislocations. Nevertheless, lateral growth has been shown as a technique able to reduce the overall density of those threading dislocations, and to deviate them far away from the initial mesa. In addition, the coalescence of mesa growth favor their recombination, a feature that may lead to defect-free areas. Finally, hillocks observed on the top of the mesa structures, and reported in previous chapters, have been studied. Their origin and the shape of the crystallite responsible for the occurrence of the hillock have been determined.

IV.1 Introduction

Crystallographic defects are interruptions in the regular pattern of a perfect crystal. Such interruptions can take place at an individual lattice point (point defects), along a line of atoms (dislocations) or affecting a whole atomic plane (planar defect). These defects have different influence on the mechanical and electrical properties of diamond. The exceptional properties of synthetic diamond will make it a material suitable for high power electronics only if a good crystallographic quality (i.e. a low density of such defects) is ensured.

Diamond, being an insulator when undoped, and more precisely a wide bandgap semiconductor, requires doping for electronic applications. There are two main dopants in diamond technology: boron (*p* doping) and phosphor (*n* doping). In the case of boron, when the concentration in diamond increases up to $5x10^{20}atm/cm^3$, properties change drastically from an insulating behavior to a metallic one [Bustarret 2008-a]. Metallic diamond is a key element of the future diamond based electronics and metallic diamond substrates can be the structure on which the future commercial electronic devices will be designed. Unfortunately, homoepitaxial boron doped layers usually contain planar and point defects [Araujo 2010 and Prokhorov 2013]. The origin of these defects is not well understood yet, but they have an undesirable impact on the resulting diamond based devices [Alvarez 2014 and Siegert 2015]. The understanding of the mechanism of defects generation during the boron doped diamond growth and its relationship to boron incorporation will help to understand and improve the boron-doped diamond growth. This is one of the required technological steps to develop commercial electronic devices based on diamond.

In fact, defects have become one of the main restrictions for the development of commercial diamond substrates [Siegart 2015]. Many works reported this topic in 2D diamond growth [Liang 2014, Lodes 2015 and Xie 2015] contributing to improve significantly the growth of diamond films and the control of the doping level to the point where the fabrication of δ-doped diamond layers could be contemplated. [Chicot 2012, Alvarez 2014, Makino 2014, Chicot 2014, Fiori 2014 and Bousquet 2014]. Thanks to these progresses, the first successful diamond electronic devices were reported [Traoré 2014, Alvarez 2014, Makino 2014, Takeuchi 2014, Muret 2015 and Xie 2015] and additional designs such as vertical-type devices have been envisioned [Jiang 2015].

The study of the lateral diamond growth has pointed out many lattice related defects on the studied samples. Lattice strain at the corners of trenches and mesa rectangle structures as well as additional surface effects are common generator of defects [Steeds 1998]. In addition, it is known that doping can also induce the generation of dislocations by boron atom proximity effects even in nm-thick layers [Long 2008, Alegre 2014 and Lodes 2015]. Then, the suppression of all

these factors that acts as defect generators is basic for the success on the fabrication of the final devices. To understand the defect generation mechanism is critically needed to be able to grow defect free lateral microstructures.

IV.2. Defects generation upon lateral growth

During growth on patterned substrate the coexistence of different growth orientation is achieve. It allows the separate study of the growth orientation and the growth conditions into the generation of defect. The following sections are the results of both studies.

IV.2.1 Defects generation depending on the growth orientation

Aiming to improve the boron doped diamond quality, Alegre *et al.* [Alegre 2014] reported a mechanism of dislocation generation that established a critical boron-doping level in diamond. They determined the existence of a relationship between the growth orientation and the defect generation in boron doped diamond. In this section, an extensive study of defects in heavily boron-doped layers on different growth planes orientations is presented.

In order to determine where defects occur, within the heavily doped layers, or at interfaces with the substrate or with a layer of different doping level, as well as its relationship with the layer thickness, sample #2-A has been studied. Fig.IV.1 shows weak beam (WB) micrographs for two different reflections (g=022 and g=111) recorded at the {011} pole. This region presents a high density of defects. Arrows with p^{++} labels have been included in figure for an easier identification of the doped layers. First observation is that the <111> facets of the triangular shaped pit defects on the substrate (probably coming from etching before CVD-growth) induce the <111> growth orientation of the first p^{++} layers and also for first nanometers of the underneath direction undoped buffer layer, instead of the expected <100> growth. That is, growth direction is clearly conditioned by the existence of superficial defects on the substrate. As shown in the micrographs, extended defects are generated in the first doped layer. These defects glide firstly in the {111} planes changing after some nanometers to the {100} ones.

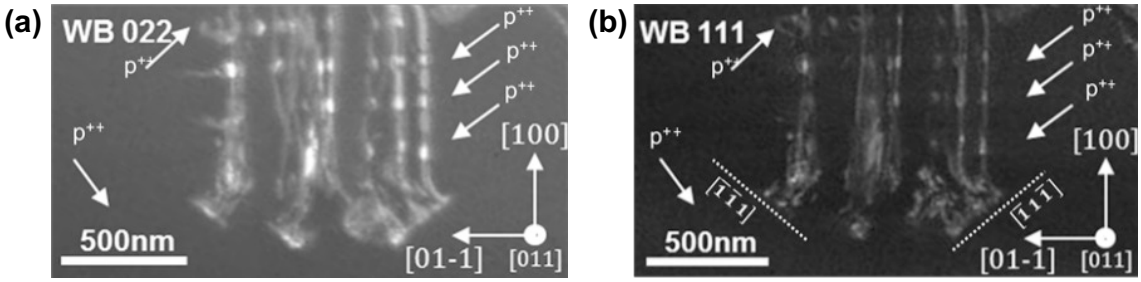

Fig.IV.1. Weak beam micrographs in two beam conditions of sample #2-A for the (a) 022 and (b) 111 reflections. Doped layers are marked by arrows and p^{++} label. Growth plane, where the defects are generated, are marked by dashed lines in (b) and corresponds with $(\bar{1}\bar{1}1)$ and $(\bar{1}1\bar{1})$ planes.

Dislocations generated by strain related or lattice mismatch usually occur at the interface between doped and undoped layers [Kitagoh 2010]. However, Fig.IV.2 shows an annular dark field (ADF) micrograph, recorded at 20 cm camera length, where dislocations are generated at different positions with respect to the doped layers.

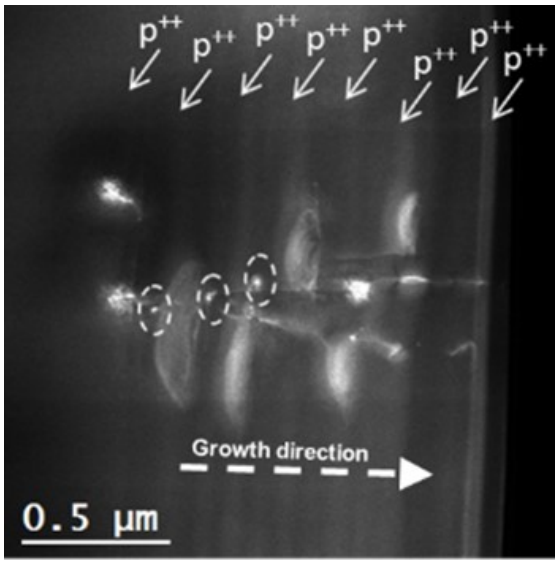

Fig.IV.2. Anular dark field (ADF) micrograph of sample #2-A recorded at 20cm camera length where defects marked by white dashed circles are placed at diferent position of the boron-doped layers marked by p^{++} labels.

By 3D-superficial defects generated during the growth process, different orientations have been compared. Growth defects such as pyramidal hillocks (PH) or flat hillocks (FH) are commonly placed on the surface of epitaxial diamond samples growth by CVD [Sawada 2001]. The formation of these defects has been thoroughly studied by authors as Tallaire *et al.* [Tallaire 2008]. Here, the TEM study of a 3D facetted surface defect that randomly appears on the surface of most of the samples growth at high methane concentration conditions, is presented. These surface defects ar

named in *Chapter II* as hillocks type (i). The origin of the PHs is identified to be related to substrate defects.

Fig.IV.3 shows dark field (DF) micrographs of the PH in two beam conditions for (a) g=400, (b) g=022 and (c) g=111 reflections of the {011} pole. PH had a squared shaped base with their side parallel to the ⟨011⟩ and ⟨0$\bar{1}$1⟩ directions. As expected, each face of the hillock shows different growth direction at the surface of the sample. They have been identified and marked in the bright field (BF) micrograph presented in Fig.IV.3 (d).

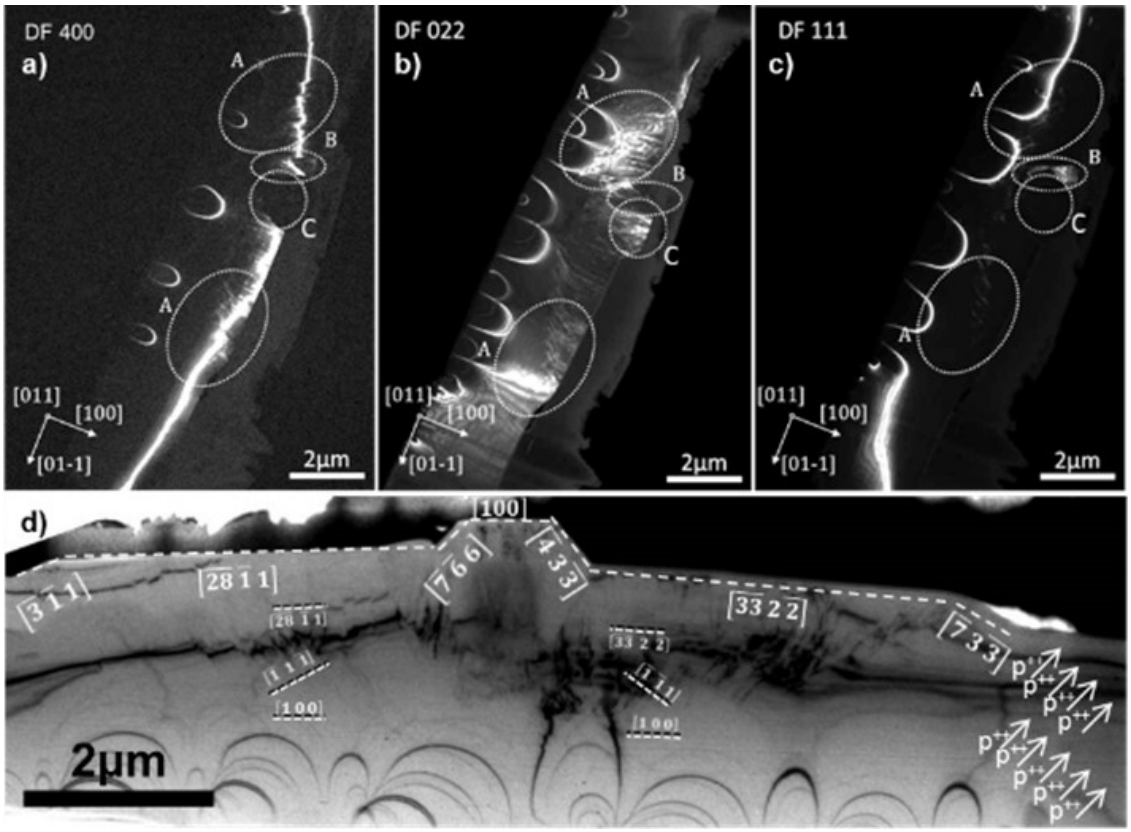

Fig.IV.3. DF micrographs of a cross section of a pyramidal hillock (PH) of sample #2-A in two beam conditions for (a) g=400, (b) g=022 and (c) g=111 reflections. Groups of defects are encircled and labeled in figures (a), (b) and (c) according with their Burger vectors. "A" defects correspond to $\boldsymbol{b} = \pm\frac{1}{6}[11\bar{2}]$ and "B" ones to $\boldsymbol{b} = \pm\frac{1}{2}[1\bar{1}0]$. (d) Bright field micrograph of the PH whose different growth orientations are marked by white dashed lines and identified by labels. Doped layers are marked by arrows and p++ labels. They show different orientations during growth. Six of these intermediate growth directions are indicated by white/black dashed lines where they are revealed by the doped layers and planes and identified by labels. Black and white arcs are artifact generated by thickness changes.

Doped layer thickness have been measured by TEM allowing to estimate the growth ratio for each orientation. The values obtained for the thickness of the doped layer and the growth ratio

are 40 nm and 212.4 nm/h, 57 nm and 302.6 nm/h, 37 nm and 196.5 nm/h, 52 nm and 278.8 nm/h, 40 nm and 212.4 nm/h, 26 nm and 139.6 nm/h and 39 nm and 205.0 nm/h in the [$\overline{33}$ 2 $\overline{2}$], [$\overline{1}$ $\overline{1}$ 1], [100], [$\overline{3}$ $\overline{1}$ 1], [$\overline{28}$ $\overline{1}$ 1], [$\overline{7}$ $\overline{6}$ 6] and [$\overline{4}$ 3 $\overline{3}$] orientation respectively and they are displayed on table IV.I.

Table IV.I. Thickness (nm) and growth velocities (nm/h) per orientation.

	[$\overline{33}$ 2 $\overline{2}$]	[$\overline{1}$ $\overline{1}$ 1]	[100]	[$\overline{3}$ $\overline{1}$ 1]	[$\overline{28}$ $\overline{1}$ 1]	[$\overline{7}$ $\overline{6}$ 6]	[$\overline{4}$ 3 $\overline{3}$]
Thickness	40	57	37	52	40	26	39
Growth rate	212.4	302.6	196.5	278.8	212.4	139.6	205.0

The high density of defects, generated at initial growth planes, is shown in DF micrographs (Fig.IV.3 (a), (b) and (c)). Three different regions of defects have been identified and they have been marked by white dashed circles. Doped layers show different growth orientations during PH formation. These changes in the growth directions curved the dislocation lines. Fig.IV.3 (d) shows that growth orientation changed at least twice during the PH generation. Final ($\overline{28}$ $\overline{1}$ 1) and ($\overline{33}$ 2 $\overline{2}$) planes started from a (100) orientation. After around 400nm, such orientation changed to the ($\overline{1}$ $\overline{1}$ 1) and ($\overline{1}$ 1 $\overline{1}$), respectively.

In fact, the dislocations density, defined as sum of the dislocations length per volume:

$$\rho = \frac{\sum \text{dislocation length}}{volume}, \qquad \text{eq.IV.1}$$

has been calculated for each one of the growth planes identified in the sample. The higher density of dislocations was obtained for the {111} planes since these form the glide system.

In order to determine the Burger's vectors, invisibility criterion has been employed [Williams 1996]. Complete invisibility of dislocations is only achieved under conditions of:

$$\vec{g} \cdot \vec{b} = 0 \qquad \text{eq.IV.2}$$

where ***g*** is the reflection to take the TEM micrograph and **b** is the dislocation Burger's vector. *Table IV.II* shows the result of applying this criterion for the reflections of the [011] zone axis, g=220, g=111 and g=400. Micrographs taken with all these three reflection families allow to determine that the Burger's vector are in the <011> directions.

Table IV.II. $\boldsymbol{g}\cdot\boldsymbol{b}$ invisibility criterion for the most common Burger vectors, $\boldsymbol{b}$, and reflections, $\boldsymbol{g}$, of the {110} pole in a fcc crystal.

$\boldsymbol{g}$ \ $\boldsymbol{b}$	$\pm\frac{1}{6}[11\bar{2}]$	$\pm\frac{1}{6}[121]$	$\pm\frac{1}{6}[211]$	$\pm\frac{1}{3}[111]$	$\pm\frac{1}{2}[101]$	$\pm\frac{1}{2}[10\bar{1}]$	$\pm\frac{1}{2}[011]$	$\pm\frac{1}{2}[01\bar{1}]$	$\pm\frac{1}{2}[110]$	$\pm\frac{1}{2}[1\bar{1}0]$
(400)	$\pm 2/3$	$\pm 2/3$	$\pm 4/3$	$\pm 4/3$	± 2	± 2	0	0	± 2	± 2
$(0\bar{2}2)$	± 1	$\pm 1/3$	0	0	± 1	± 1	0	± 2	± 1	± 1
$(11\bar{1})$	$\pm 2/3$	$\pm 1/3$	$\pm 1/3$	$\pm 1/3$	*0*	± 1	0	± 1	± 1	0

This criterion has been also used for dislocations of Fig.IV.3 where the same Burger's vectors were observed and marked with labels "A" and "B". However, a third region of defects, marked with the label "C" is shown in this figure. Head *et al.* [Head 1973] included the term "$\boldsymbol{g}\cdot\boldsymbol{b}$*=-2/3*" as invisible for partial dislocations depending of the deviation from the Bragg angle. This invisibility criterion is in agreement with $b=-\frac{1}{6}[11\bar{2}]$ dislocations. In this way, defects marked by the "C" label correspond to edge dislocations with the same Burger vector than the "A" group.

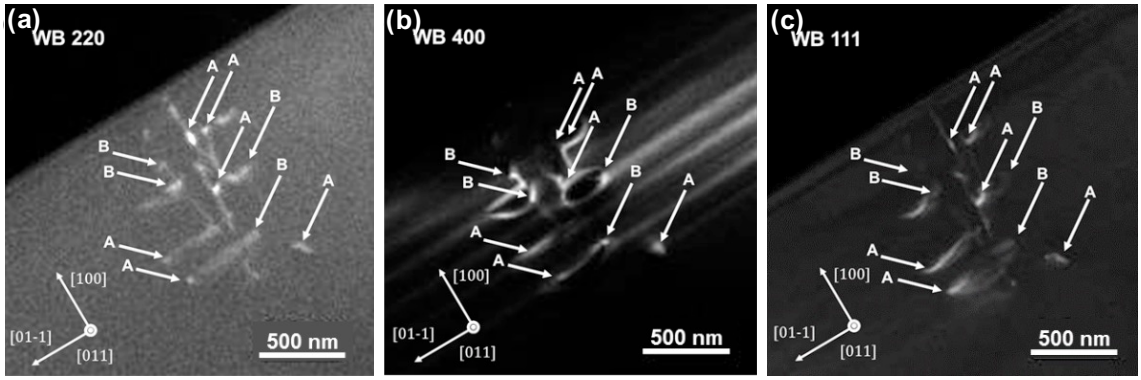

Fig.IV.4. Weak beam micrographs under two beam conditions for the (a) 220, (b) 400 and (c) 111 reflections. Arrows and labels are used to identify the defects. "A" corresponds to a $1/6\left[11\bar{2}\right]$ Burger's vector and "B" to $1/2\,[1\bar{1}0]$ one. Doped layers are clearly visible for 400 reflexion.

Fig.IV.4 shows weak beam (WB) micrographs in two beam conditions in the same region that the sample recorded at Fig.IV.2. Micrographs were recorded at the (011) pole for the three reflections: g=220 (Fig.IV.4 (a)), g=111 (Fig.IV.4 (b)) and g=400 (Fig.IV.4 (c)). Defects with $\boldsymbol{b}=\pm\frac{1}{6}[11\bar{2}]$, marked with label "A", and $\boldsymbol{b}=\pm\frac{1}{2}[1\bar{1}0]$, marked with label "B", have been observed. Similar dislocations have been previously reported on HPHT [Mussi 2013] and MPCVD [Alegre 2015] diamonds.

Fig.IV.5 shows a high-resolution transmission electron microscopy (HREM) micrograph of a doped region of the sample recorded at the {011} pole. Stacking faults are observed forming an

angle of 70.53°. These planar defects correspond with the ∑3 coincident-size-lattice structure [Zhang 1999]. In addition, the Fourier transforms performed on the defects (white dashed square on Fig.IV.5 (a)) showed that they correspond to the {111} type. These structures are twin boundary-like and they have been observed in polycrystalline diamonds [Sawada 2001 and Lu 2012]. Preferred grain boundary planes are the closest packed planes of the corresponding CSL that is, {111} planes. Here, an additional observation of the preferential planes for extended defects generation is shown. Edge dislocations were also observed by HREM, as shown in Fig.IV.5 (a) and (b) at higher magnification. In this case, they correspond to threading edge dislocations with $1/2\,[1\bar{1}0]$ Burger's vectors.

In correspondence with the dislocation generation model published by Alegre *et al*. [Alegre 2014], the following aspects are studied: (i) in tipped dislocations (Fig.IV.4 (b) and Fig.IV.5) are generated insight the heavily doped layer, (ii) such dislocations (observed as points) changes then their orientation to follows the growth directions.

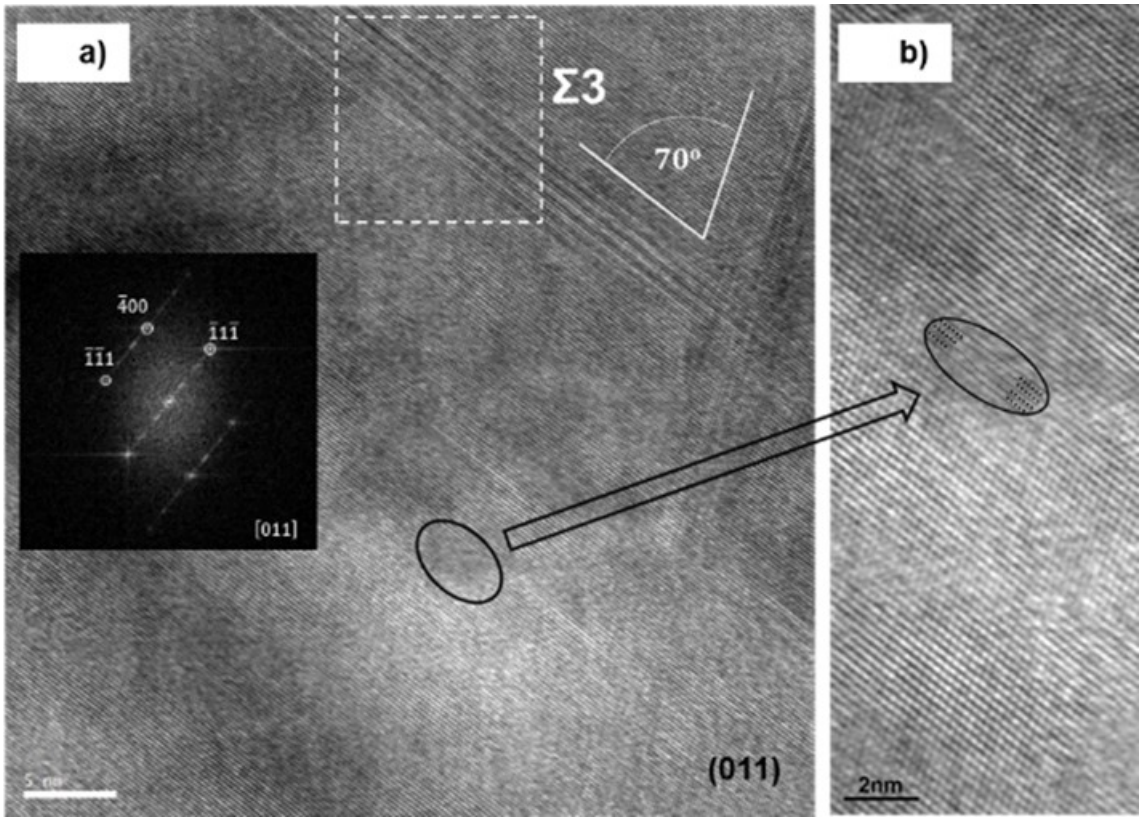

Fig.IV.5. HREM micrographs recorded at the (011) pole for sample #2-A. Planar defects such as stacking faults (SFs) as well as dislocations are observed. SFs form an angle close to 70° consistent with the ∑3 type in the CSL model. Inset of (a) is the Fourier transform, corresponding to the white dashed square, demonstrated that SFs are {111} type. Some dislocations were also observed being (b) enlarged of (a) where a threading dislocation (TD) is identified.

In general, regions of the sample, where the growth plane is the (100) one, are almost free of defects. Therefore, for heavily boron doped layers, there is a tendency to propagate defects at {111} planes in opposition to {100} ones under exactly the same growth conditions. This behavior is in accordance with the mechanism reported by Alegre *et al*. [Alegre 2014]. Neighboring effects between boron atoms might be higher for {111} family planes than for {100} ones since firsts have smaller planar distance. Local strains due to the distance between the substitutional boron pairs and their neighbors have a higher influence on the generation of dislocations than interface stress related effects [Matthews 1974 and Alegre 2014].

Additional growth directions have being studied thanks to local changes in the growth directions due the presence of etch-pits, at the initial stage of growth, and pyramidal hillock, formed during the growth. A large number of defects have been obtained along the <111> growth direction, in contrast with other directions that use the same growth conditions. In this way, it has been observed a dependence of the dislocation generation on the growth orientation. TDs observed had $\frac{1}{6}[\,11\bar{2}]$ and $\frac{1}{2}[1\bar{1}0]$ Burger's vectors and stacking faults with the structure Σ3 {111} coincident-site-lattice (CSL) have been identified [Zhang 1999]. All these results are consistent with the model proposed by Alegre *et al*. [Alegre 2014].

IV.2.2 Defects generation versus growth conditions

During MPCVD there are many growth parameters that can lead to the generation of defects. To obtain a general overview of such defect generation, this section presents a TEM study on eight diamond samples (samples #2-A, #3-LMCD, #4-HMCD, #5-α16, #6-α10, #7-β10, #8-LMCU and #9-HMCU) grown under different conditions of pressure, power, doping and/or methane concentration. These conditions were described in *Chapter II*.

Fig. IV.6 shows dark field micrographs of sample #2-A recorded at $\bar{2}20$ ((a) and (b)) and 220 (c) reflections of the {001} pole which pattern is also shown in Fig.IV.6 (d). The different growth directions generated during the overgrowth were discussed in *Chapter III*. Micrographs have been recorded in diffraction-contrast mode and two beam conditions considering three different reflections to determine the Burger's vectors. Point shaped defects, only shown with the [$\bar{2}20$] reflection (see Fig.IV.6 (b)), are marked by white arrows. They correspond to dislocations that usually are observed at the p^{++}/NID interface. These dislocations were generated in the growth plane probably induced by boron proximity effects as already reported for heavily doped layers [Alegre 2014]. Thus, first the dislocation lies in the growth plane and, at some point, it can

bend to follow the growth direction. Tipped defects are shown to be located inside the layers. Some of them have been also marked by white arrows in Fig.IV.6 (a) for clarity.

In the micrographs, doped layers appear as pairs of white bright lines. As explained in *Chapter III*, this is due to the in-plane strain induced by the boron atoms [Gutierrez 2006]. In addition, doped layers are shown brighter in the corners region (see Fig.IV.6 (c)). This is attributed to an increase of actives sites at the corners of the structures. *Chapter III* described such regions as singularities with a larger number of dangling bonds.

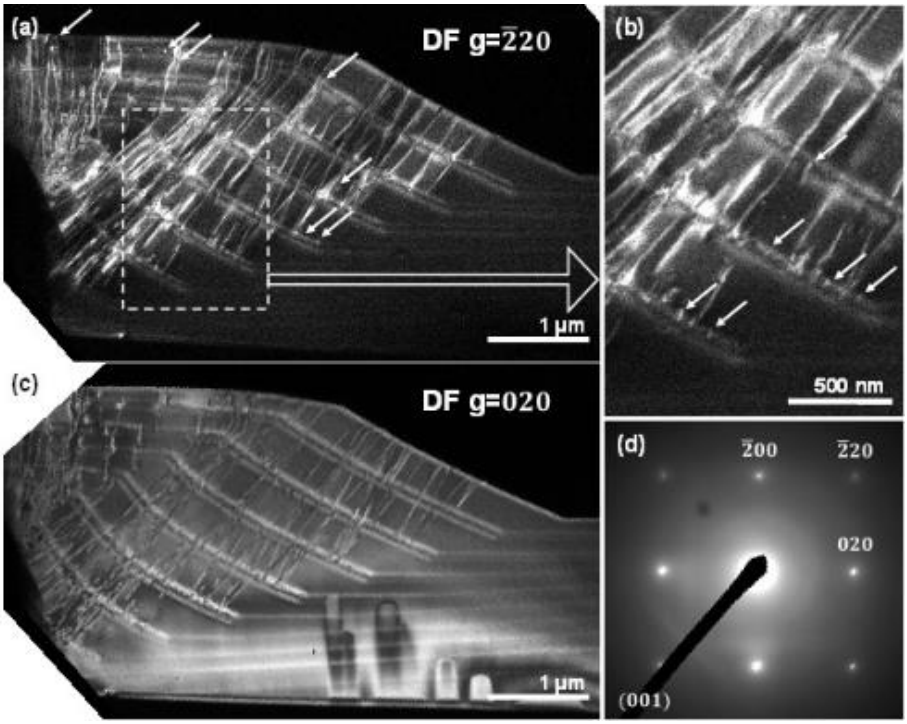

Fig.IV.6. DF micrographs of the sample #2-A in the (001) pole of a lamella made in the $(00\bar{1})$ plane taking with the $[\bar{2}20]$ ((a) and (b)) and [020] (c) reflections, and the diffraction pattern (d). Arrows point out tipped dislocations in (a) and enlarged in (b).

Fig.IV.7 shows weak beam micrographs under two beams conditions of sample #2-A recorded at the {011} pole using $[02\bar{2}]$ (Fig.IV.7 (a)), $[\bar{1}1\bar{1}]$ (Fig.IV.7 (b)) and [200] (Fig.IV.7 (b) inset) reflections. As was seen in Fig.IV.6, sample is shown to be full of defects. These defects are clearly visible at $02\bar{2}$ and $\bar{1}1\bar{1}$ reflections but not revealed by the 400 reflection (just residually). It corresponds to $\mathbf{b} = \frac{1}{2}[01\bar{1}]$ and $\mathbf{b} = \frac{1}{2}[0\bar{1}1]$ Burger's vectors according with the invisibility criterion (eq.IV.2). These Burger vectors are included in the same family as the one called B in previous section. From these micrographs, it can be determined three types of defects in sample #2-A: (i) Superficial defects existing prior the overgrowth. They could be generated during the etch process or be inherent to the substrate; (ii) Corners of the mesa structure. Bottom and top

corners seem to be generators of large number of dislocations (mainly top corner); And (iii) doped layers. It is observed most of the contrast produced by the dislocations in the micrographs have their beginning at these doped layers.

Note the absence of defects with Burger's vector $\boldsymbol{b} = \pm\frac{1}{6}[11\bar{2}]$ in these micrographs. This fact suggests that the presence of such defects in the previous sections was induced by the pyramidal hillocks.

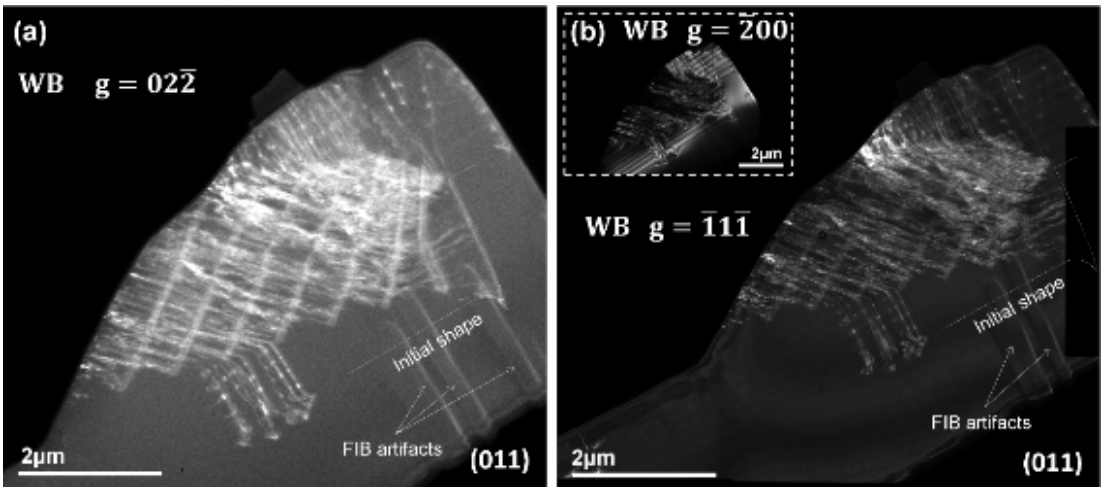

Fig.IV.7. WB micrographs of the sample #2-A at the (011) pole recorded using the (a) [02$\bar{2}$], (b) [$\bar{1}1\bar{1}$] and [200] reflections (see the inset).

Fig.IV.8 shows dark field micrographs of sample #3-LMCD taken with two beam conditions oriented along the {011} pole. As was anticipated in *Chapter III*, the density of defects is much smaller than in the previous studied sample. Fig.IV.8 (a) shows a dark field micrograph of half side of one of the overgrown disk recorded using the [0$\bar{2}$2] reflection. Initial shape of the disk is marked by a dashed white line. Doped layers are visible by a soft white contrast and residual contrast is obtained from three planar defects. Fig.IV.8 (b) shows a dark field micrograph of the same region recorded using the [$\bar{1}\bar{1}$1] reflection. Initial shape has been also marked here in the same way and doped layers are also visible but with dark contrast. Planar defects are more intense at these TEM conditions and four of them are visible at the region recorded (one of them was practically not visible using the [0$\bar{2}$2] reflection). They are generated near or into the doped layers. Note that two of these planar defects lie in the substrate and one of them (the one invisible in Fig.IV.8 (a)) in the bottom corner of the initial disk. Inset of Fig.IV.8 (b) shows one of these planar defects at higher magnification. Taking with the same [$\bar{1}\bar{1}$1] reflection. Doped layers are also marked in this inset. Despite planar defects are near or into doped layers we cannot conclude that doping is the source of its generation.

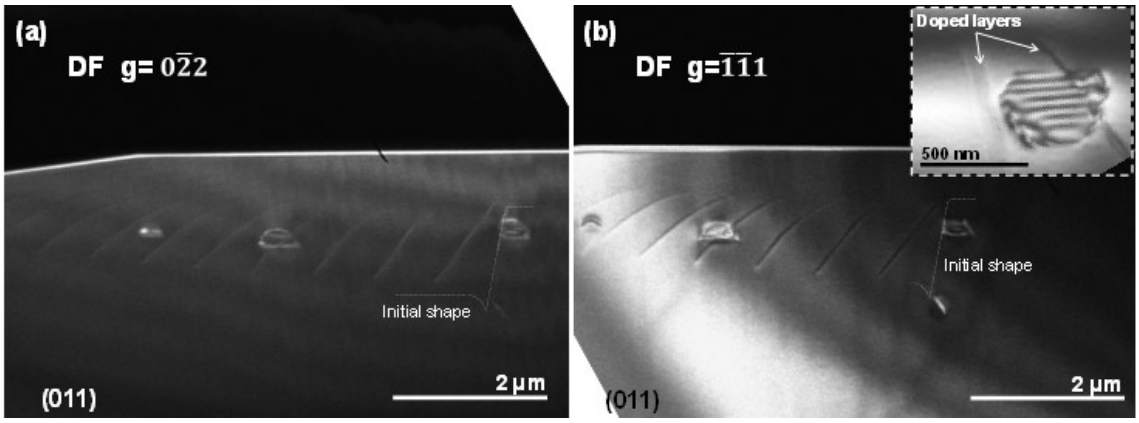

Fig.IV.8. Dark field micrographs of sample #3-LMCD recorded under two beam conditions oriented at the {011} pole using the (a) [0$\bar{2}$2] and (b) [$\bar{1}\bar{1}$1] reflections. Inset shows one of the planar defects in detail.

Fig.IV.9 shows a bright field micrograph of a general view of sample #4-HMCD ((a)) and two dark field micrographs of the same region of this sample ((b) and (c)). Micrographs have been recorded in two beam conditions along the {011} pole. The FIB lamella is plenty of defects as it was also observed for sample #2-A. However, from Fig.IV.9 (a), the origin of the defects seems to be now different. Most of defects on sample #4-HMCD come from the corners of the initial disk (see white dashed line that marks the initial disk shape), and, in contrast to sample #2-A, there is not any evidence of boron doped layers to act as defect sources.

The invisibility criterion has been also used for this sample in order to determine the Burger's vector of the observed dislocations. Because dislocations are visible by using reflections (a) $\mathbf{g} = \bar{2}00$ and (c) $\mathbf{g} = \bar{1}\bar{1}1$ and remains invisible with the reflection (b) $\mathbf{g} = 0\bar{2}2$, a Burger's vector $\mathbf{b} = \frac{1}{6}[211]$ has been determined. Note that dislocations are not fully invisible at $\mathbf{g} = 0\bar{2}2$ since the lamella is a bit tilted. This is also the reason why additional white contrasts are shown. When large lamellas are polished at very thin thickness, inner tensions bend it. Due to this fact, it is not possible to have the whole lamella oriented along the same zone axis, generating the mentioned contrast artifact.

In addition to the dislocations, there is on the top of the upper corner an inhomogeneity shown with a dark contrast in Fig.IV.9 (b) and (c) that reveals its different orientation respect to the rest of the sample. This corresponds to a crystallite, already mentioned in *Chapter II* and *III* when they were observed by SEM on the top of the overgrown disk of samples #1-F, #2-A, #4-HMCD and #9-HMCU. They were classified as type (ii) hillocks because of their shape and place of generation. Their analysis and study will be carried out in a further section of the current chapter.

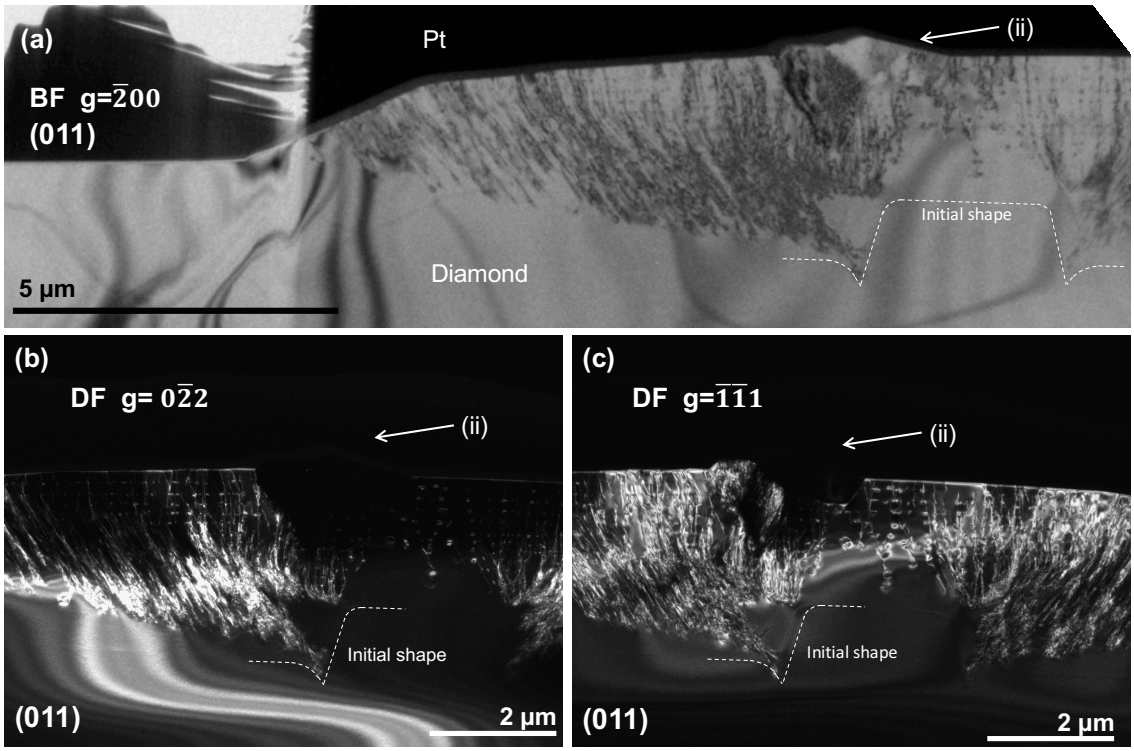

Fig.IV.9. Micrographs of sample #4-HMCD recorded in two beam conditions along the (011) pole. White dashed lines mark the initial shape of the etched substrate in each. (a) Bright field micrograph recorded using the $\bar{2}00$ reflection. Platinum marked by Pt is due to the FIB-lamella preparation. Superficial defect observed on the top of the samples seems to come from the upper corner of the initial disk. It is marked by the label (ii). Dislocations are clearly visible by dark contrasts. (b) Dark field micrograph recorded using the $0\bar{2}2$ reflection. Most dislocations are not visible, due to lamella is tilted. (c) Dark field micrograph recorded using the $\bar{1}\bar{1}1$ reflection. Dislocations are shown as white contrasts.

Fig.IV.10 shows dark field micrographs of sample #9-HMCU taking with two beam conditions oriented along the (001) pole using the (a) $\bar{2}00$, (b) $\bar{2}20$ and (c) 020 reflections. Dislocations are in similar configuration to those of sample #4-HMCD. Most of them are coming from the corners of the initial profile of the disk estimated from the doped layers. The same $\mathbf{b} = \frac{1}{6}[211]$ Burger's vector observed in sample #4-HMCD is attributed to these dislocations. Crystallites previously anticipated are marked in Fig.IV.10. They are clearly shown by a different contrast in micrographs (b) and (c).

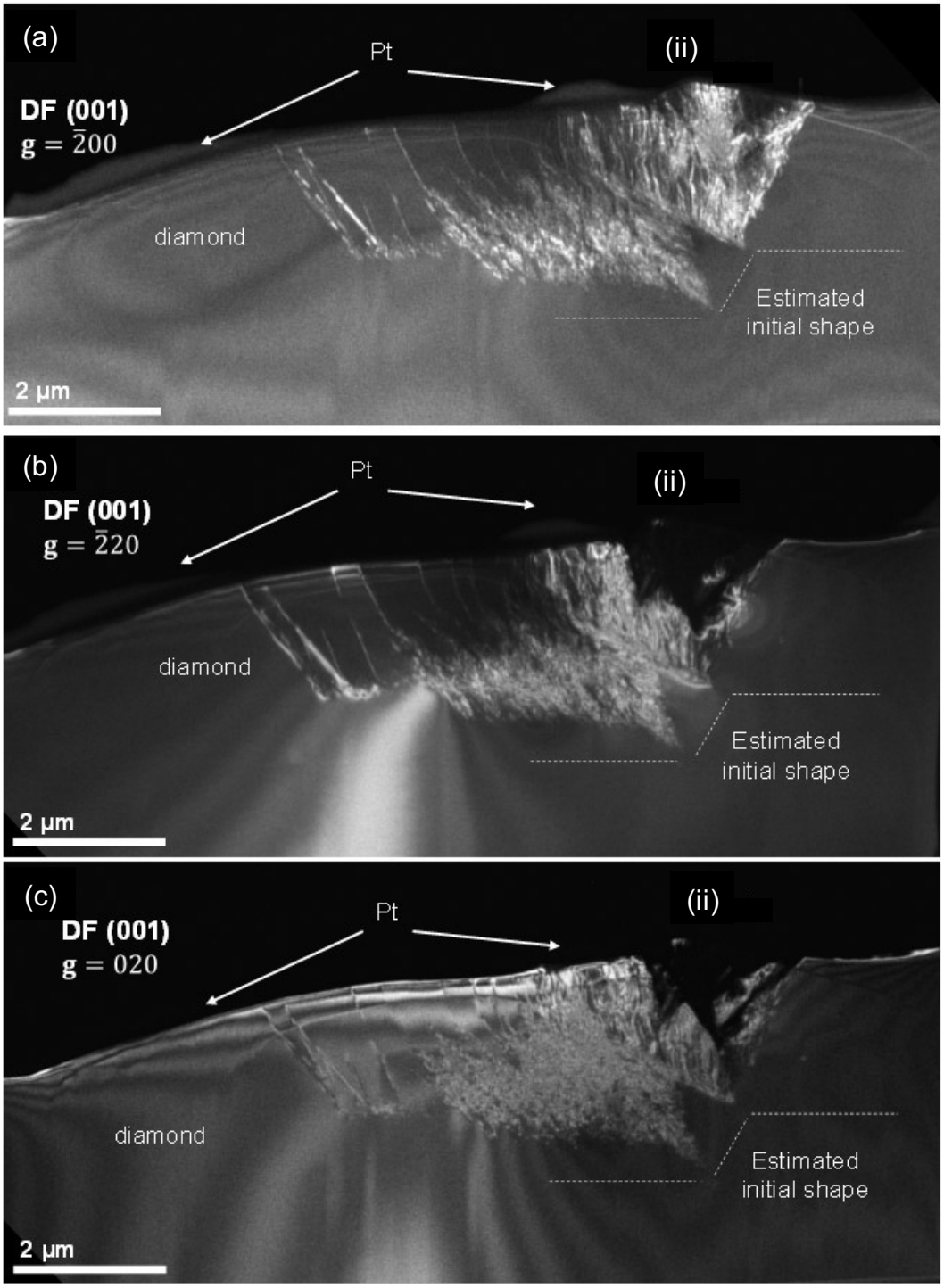

Fig.IV.10. DF micrograph of sample #9-HMCU in two beam conditions oriented along the (001) pole recorded using the (a) $\bar{2}$00, (b) $\bar{2}$20 and (c) 020 reflections. Platinum coming from the sample preparation as well as the superficial defect observed on the SEM micrographs are labelled. Dashed white line marks the location of the initial disk. Dislocations are observed to come from both corners of the initial disk in the same way as was observed for sample #9-HMCU.

Fig. IV.11 shows micrographs of sample #5-α16 recorded in two beam conditions with the sample oriented along the (011) pole. Fig. IV.11 (a) and (c) correspond to dark field micrographs of one half side of one disk using $\mathbf{g} = \bar{2}00$ and $\mathbf{g} = 02\bar{2}$ reflections, respectively. Fig. IV.11 (b) and (d) show the other half side using the $\mathbf{g} = \bar{2}00$ reflection in bright field mode and $\mathbf{g} = 02\bar{2}$ reflection in weak beam mode. There is not compositional contrast between substrate and overgrowth region due to sample #5-α16 was growth as a single undoped layer. However, defects mark the shape of the initial disk facilitating the identification of the top and bottom corners. In addition, dislocation lines are observed to be curved during the growth process. Invisibility criterion has been employed determining $\mathbf{b} = \frac{1}{6}[21\bar{1}]$ Burger's vector.

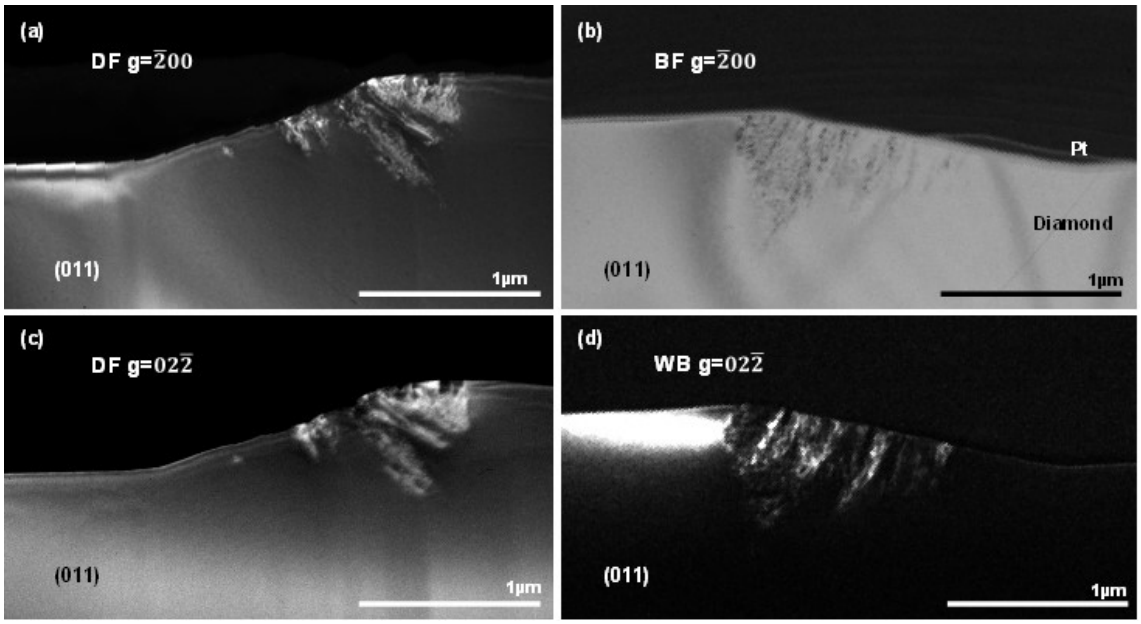

Fig.IV.11. Micrographs of both sides of a disk of sample #5-α16 oriented along the <011> direction recorded under two beam conditions using (a) dark field mode and $\mathbf{g} = \bar{2}00$ reflection, (b) bright field mode and $\mathbf{g} = \bar{2}00$ reflection, (c) dark field mode and $\mathbf{g} = 02\bar{2}$ reflection and (d) weak beam mode and $\mathbf{g} = 02\bar{2}$ reflection. Dislocations appear as white contrast except in bright field micrographs where they show up black.

Fig.IV.12 shows two weak beam micrographs of sample #6-α10. They were recorded in two beam conditions on the {011} pole using reflections (a) $[\bar{2}00]$ and (b) $[\bar{1}1\bar{1}]$. This sample shows sides parallel to the {111} planes in the micrographs. The overgrown layer is shown to be full of defects that are visible using $\mathbf{g}=[\bar{2}00]$ and $\mathbf{g}=[02\bar{2}]$ reflections. Such dislocations correspond to $\mathbf{b} = \frac{1}{6}[21\bar{1}]$. Additionally, some defects marked by arrows in Fig.IV.12 (b) remain invisible in (a). These defects, that are also visible for $\mathbf{g}=[02\bar{2}]$, have $\mathbf{b} = \frac{1}{2}[01\bar{1}]$ Burger's vector.

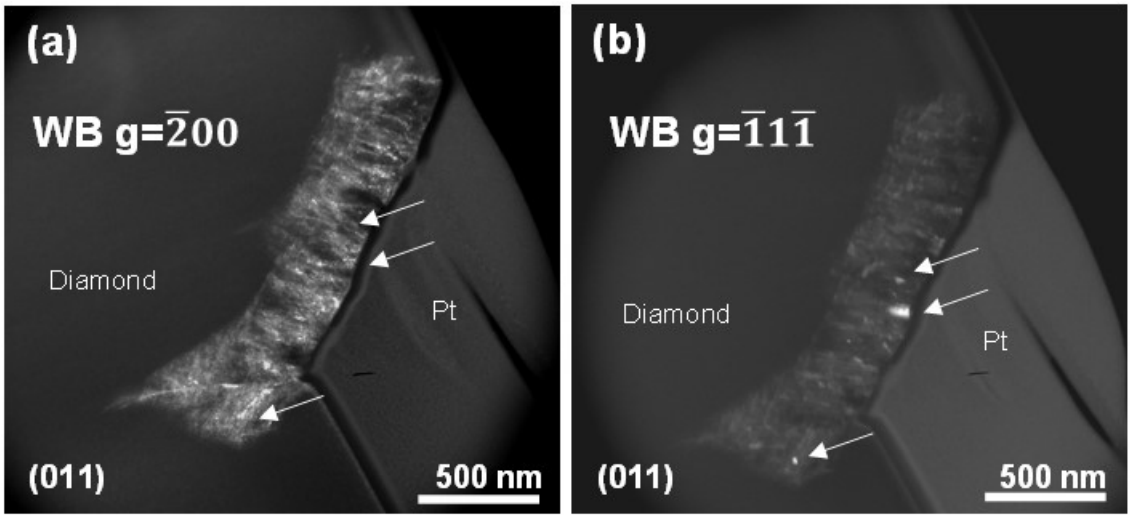

Fig.IV.12. Weak beam micrographs of one side of a disk of sample #6-α10 at two different reflections: (a) $\mathbf{g}=\bar{2}00$ and (b) $\mathbf{g}=\bar{1}1\bar{1}$. Arrows show defects with $\mathbf{b}=\frac{1}{2}[01\bar{1}]$ Burger's vector.

Fig.IV.13 shows micrographs of sample #7-ß10 corresponding to a overgrown boron doped diamond layer. Similar to sample #6-α10, this sample also shows {111} lateral growth direction in the micrographs. However, in this case dislocations are not observed with the $\mathbf{g}=\bar{2}00$ reflection. By using the invisibility criterion, the assigned Burger's vector is $\mathbf{b}=\frac{1}{2}[01\bar{1}]$. Defects are not generated in specific positions of the disk, as corners, but they seem to be originated at different places and to cover the whole epilayer.

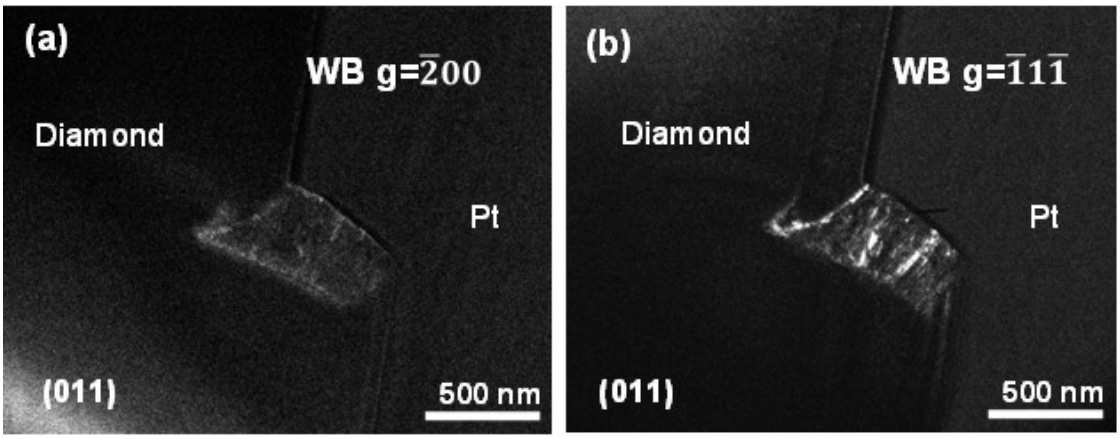

FIG.IV.13. Weak beam micrographs of one side of a disk of sample #7-ß10 using (a) $\mathbf{g}=\bar{2}00$ and (b) $\mathbf{g}=\bar{1}1\bar{1}$ reflections.

Table IV.III summarizes the results presented so far. The first evidence is that, in terms of defects, sample #3-LMCD and #4-HMCD have the same behaviour as #8-LMCU and #9-HMCU samples, respectively. This implies that very thin and low boron doped layers do not have any

influence in the defects behavior and that the four samples are undoped-like. In addition, samples #3-LMCD and #8-LMCU are free of linear defects and involve only a few planar defects.

Table IV.III. Summary of Burger's vectors of the dislocations present in each sample. Growth conditions are also included.

Sample	Layer	CH_4/H_2	O_2/H_2	B_2H_6/CH_4	Time (min)	Defects
#2-A	Doped	0.5%	-	14000	11x10	$\mathbf{b} = \frac{1}{2}\langle 011 \rangle$
	Undoped	0.75%	0.32%	-	12x10	
#3-LMCD	Doped	0.25%	-	10700	2x13	Planar defects
	Undoped	0.1%	-	-	60x13	
#4-HMCD	Doped	0.5%	-	9600	1x13	$\mathbf{b} = \frac{1}{6}\langle 211 \rangle$
	Undoped	0.75%	0.32%	-	10x13	
#5-α16	Undoped	0.75%	0.25%	-	30	$\mathbf{b} = \frac{1}{6}\langle 211 \rangle$
#6-α10	Doped	4%	-	1200	10	$\mathbf{b} = \frac{1}{6}\langle 211 \rangle$ and $\mathbf{b} = \frac{1}{2}\langle 011 \rangle$
#7-β10	Doped	0.5%	-	6000	10	$\mathbf{b} = \frac{1}{2}\langle 011 \rangle$
#8-LMCU	Undoped	0.1%	-	-	840	Planar defects
#9-HMCU	Undoped	0.75%	0.32%	-	140	$\mathbf{b} = \frac{1}{6}\langle 211 \rangle$

According to this, undoped samples are characterized by the presence of dislocations with $\mathbf{b} = \frac{1}{6}\langle 211 \rangle$ Burger's vector, whereas dislocations in doped samples have dislocations defined by $\mathbf{b} = \frac{1}{2}\langle 011 \rangle$ Burger's vector. However, there is one sample which breaks this general rule, it is sample #6-α10. To understand this fact, it is necessary to come back to the growth conditions exposed in Chapter II and included in Table IV.III. This sample was grown with the highest methane concentration of the whole set of samples. From *Chapter III,* it is known that such conditions imply a faster and less ordered growth. So, even if doping inclusion generated some dislocations ($\mathbf{b} = \frac{1}{2}\langle 011 \rangle$), in that case the generation of additional $\mathbf{b} = \frac{1}{6}\langle 211 \rangle$ dislocations were necessary.

Density of dislocations have been estimated in function of their Burger's vector on samples #5-α16, #6-α10 and #7-ß10 based in the formula eq.IV.1.. The results obtained after this comparative analysis showed that defects belonging to the [112] Burger's vector family have a higher concentration in the non-intentionally doped sample #5-α16, with a density of $\rho_{[211]=}57x10^4$ cm^{-3}, while sample #6-α10 has a density of $\rho_{[211]}=1x10^4$ cm^{-3}. In the case of defects belonging the [011] Burger's vector family, a density of $\rho_{\{011\}}=4x10^4$ cm^{-3} and $\rho_{[011]}=25x10^4$ cm^{-3} were obtained for samples #6-α10 and #7-ß10, respectively.

Being assigned dislocations with $\mathbf{b} = \frac{1}{2}\langle 011 \rangle$ Burger's vector to the inclusions of doping atoms, it seems reasonable to quantify such influence into the defects generation. From the study of Alegre *et al*. [Alegre 2014], the critical boron doping level, CBL, for a percentage of methane similar to the used for sample #2-F, (0.5%), is $6.5x10^{20}$ atm/cm^3 and $3.2x10^{21}$ atm/cm^3 for <111> and <100> growth directions, respectively. Considering an homogenous distribution of boron atoms independently of the growth direction, these levels are smaller than the doping level of the sample #2-F, which is $1.2x10^{21}$ atm/cm^3, for the <111> growth direction and very close to the limit for <100>. This is consistent with the fact that a lot of TDs were generated along the lateral (111) growth plane and that the density of dislocations was almost zero for (100) one. In the case of sample #6-α10, the doping level is $\sim 2x10^{20}$ atm/cm^3, which is much smaller than the CBL on the <100> orientation (estimated at $2.5x10^{21}$ atm/cm^3) while for the <111> direction there are not measurements. However, similar to the case of samples grown with 0.5% of CH_4/H_2, it seems reasonable to assume that the CBL will be smaller for <111> orientation and close to 10^{20} atm/cm^3. This last assumption would explain the fact that we don't observe any defect due to doping in the <100> growth orientation, and that their density in the {111} lateral growth sector is too small.

Planar defects where also found in the samples. Fig.IV.14 shows a HREM micrograph of sample #4-HMCD in which stacking faults are present. Stacking faults observed on samples #2-A, #4-HMCD and #9-HMCU corresponds to the ∑3 coincident-size-lattice (CSL) structure and {111} type.

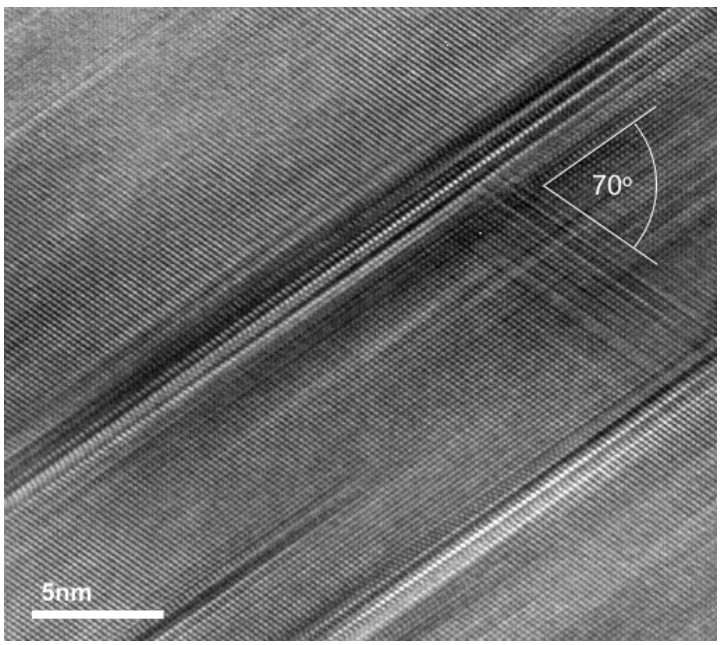

Fig.IV.14. High Resolution TEM micrograph of sample #4-HMCD where stacking faults are observed. Their analysis shows that they correspond to {111} type ∑3 CSL.

This study proves the existence of two mechanisms for generating dislocations. The first is related to the inclusion of high boron doping levels. This doping induces the generation of $\mathbf{b} = \frac{1}{2}\langle 011 \rangle$ dislocations. On the other hand, growth parameters logically play an important role. High growth rates (i.e. high methane concentrations) induce the generation of dislocations with $\mathbf{b} = \frac{1}{6}\langle 211 \rangle$ Burger's vectors. The $\mathbf{b} = \frac{1}{2}\langle 011 \rangle$ Burger's vector corresponds to perfect dislocations which move the atoms to identical sites on the crystal. $\mathbf{b} = \frac{1}{6}\langle 211 \rangle$ Burger's vector, in contrast, corresponds to partial dislocations that generate additional stacking faults. This explains the fact that SFs are observed in the samples together with $\mathbf{b} = \frac{1}{6}\langle 211 \rangle$ dislocations. Moreover, perfect dislocations can be dissociated into partial ones when such division is energetically favorable. This is the case of $\mathbf{b} = \frac{1}{2}\langle 011 \rangle$ dislocations, that can be divided in two $\mathbf{b} = \frac{1}{6}\langle 211 \rangle$ ones in the so-called Shockley partial dislocations. We can conclude that boron inclusion does not generate planar defect but perfect dislocations. On the other hand, undoped growth with high methane concentration generates partial dislocations. When such samples are slightly doped, all the perfect dislocations are dissociated by the Shockley process. When doping is too high, some perfect dislocations remains.

IV.3. Lateral growth to reduce TD density

Recently, Tallaire *et al*. proposed techniques based on lateral growth using macro terrace etching to reach defects-free surfaces [Tallaire 2017]. Terrace overgrowth has been also used by other authors to obtain smooth diamond surface. Earlier on, Tokuda *et al*. reported nanometric flattened surface by the use of mesa etched 111-oriented substrates [Tokuda 2010 and Tokuda 2012].

In the current section, micrometric terraces are used to study the propagation of TDs. To follow the growth direction at all times and evaluate its effect on the trajectory of the dislocations, samples of study (#10-LMCD, #3-LMCD and 4-HMCD) were grown with very thin boron doped layers in a superlattice structure. This method, introduced in the previous chapter III as stratigraphic approach, provides the growth orientation every 100 nm. Moreover, overgrowth coalescence of such terraces was also studied to determine the viability of its use for the annihilation of TDs. It is well known that in some cases the interaction of dislocations results in their annihilation or creation of another dislocation to low the energy of the system.

The main goal of the current work was to answer to questions: 1. Could micro-lateral growth be used to achieve large defect-free areas? and 2. Could terrace coalescence reduce the dislocation density? The first question corresponds to the investigation of the behaviour of dislocations coming from the terraces of etched substrates when they are overgrown. Once this

question is solved, it will be investigated the effect of the overgrown terrace coalescence in the distribution of the TDs. The three samples used to answer both questions are sample #10-LMCD for question 1, and samples #4-HMCD and #3-LMCD for the second question.

IV.3.1 Can micro-lateral growth reach large defect free areas?

Fig.IV.15 shows a bright field (BF) TEM micrograph of sample #10-LMCD recorded along the 011 zone axis. Micrograph shows the first steps of growth thanks to the stratigraphic approach. Initial shape of the terrace is marked by a dashed white line for clarity. Doped layers are shown as dark contrast lines and three of them are marked by arrows in Fig.IV.15. A TD coming from the substrate is marked by black arrows. It is observed that this TD changes its trajectory when overgrowth starts. Lateral growth pushes the dislocation away from the initial shape terrace. Growth plane has been determined from the doped layers as the {111} one. This dislocation suffers a drift parallel to such direction. Black arrows mark the initial and the final orientation of the dislocation in the micrograph.

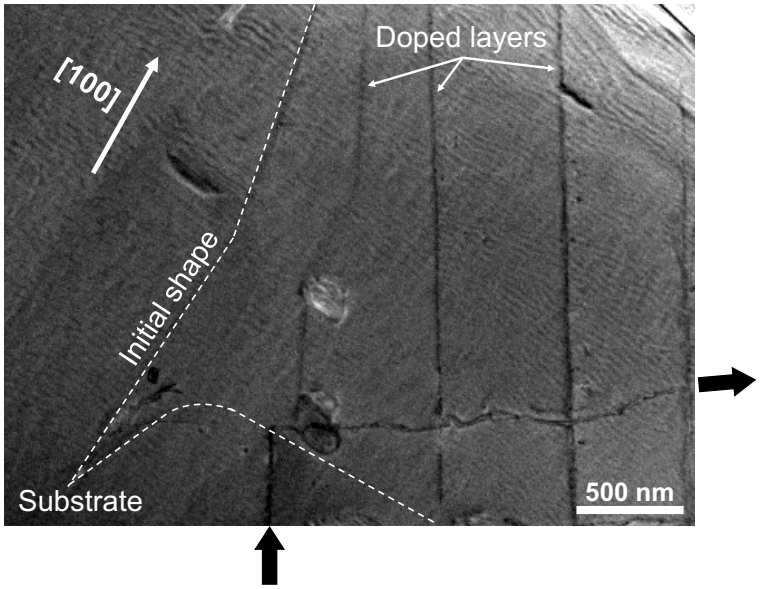

Fig.IV.15. TEM micrograph of sample #10-LMCD, recorded along the 110 zone axis. Doped layers are identified as dark contrast lines and marked by white arrows. The initial shape of the terrace is marked by a dashed white line. Dislocation modified its trajectory during the lateral growth (see black arrows showing its directions).

Thus, the situation observed and reported in macro-scaled terraces [Tallaire 2017], takes also place in the overgrowth of micro-scaled terraces. Therefore, overgrowth on micro-terraces can be proposed for achieving defect-free regions where terraces are designed in order to redirect the TDs away of the initial profile since the growth follows the 111-direction. In this way, the nearest

dislocations, i.e. dislocations coming from the inner corner of the terraces, will be displaced a distance equal to 1.4 times the terrace height. It is equivalent to the tangent of the 54.7° angle between <100> and <111> directions.

IV.3.2 Does terrace coalescence reduce dislocation density?

To answer this question, samples were overgrown until the TDs coalescence. Fig.IV.16 shows one of the lamellas made by FIB for this study. It corresponds to a HR-SEM micrograph where the initial terraces shape is shown as the dark contrast region at the bottom of the lamella and the doped layers as thin dark contrast lines. These doped layers have been identified with arrows in the figure. This lamella corresponds to the 2μm inter-terrace distance region of sample #3-LMCD.

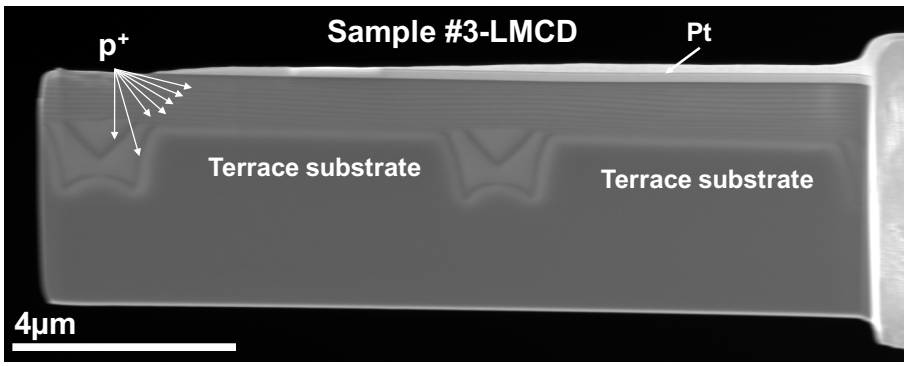

Fig.IV.16. HR-SEM micrograph of a FIB lamella extracted from the 2 μm inter-terrace distance region of sample #3-LMCD. Initial mesa/terraces are marked by white label "Terrace substrate" and some of the doped layers are identified by arrows. Platinum deposited during the FIB procedure is identified as the white contrast on the top.

As mentioned in *Chapter III*, the growth conditions of sample #4-HMCD generates a high density of dislocations, Fig.IV.17. This TEM DF micrograph was recorded using the [022] reflection in two beam conditions along the [011] zone axis. The initial shape of the terrace is marked by a dashed white line. Etching resulted in a non-planar bottom trench whose unplanarity probably contributes to the generation of dislocations. In fact, the trench bottom surfaces are not shown as the 1μm smooth planar surface as desired, but as a deep etch pit. Using the invisibility criterion, many TD appeared upon overgrowth, with all the variety of Burger vectors expected for a FCC crystal due to the countless interactions of these dislocations that come from the lateral sides of the terraces. Nevertheless, as was previously exposed, they are redirected to coalesce between terraces. This region is shown at higher magnification in the inset of Fig.IV.17. Dislocations coming from the substrate tend to follow the <111> orientation of the lateral growth. They merge in the

middle and some of them change their direction to glide to the surface following the <100> orientation. In fact, in this area marked with a dashed white rectangle in Fig. IV.17, the density of dislocations is drastically reduced by the recombination of TDs with different Burger's vector. This image confirms that dislocations can be annihilated, at least partially, by their recombination at the midpoint of the micro-terraces.

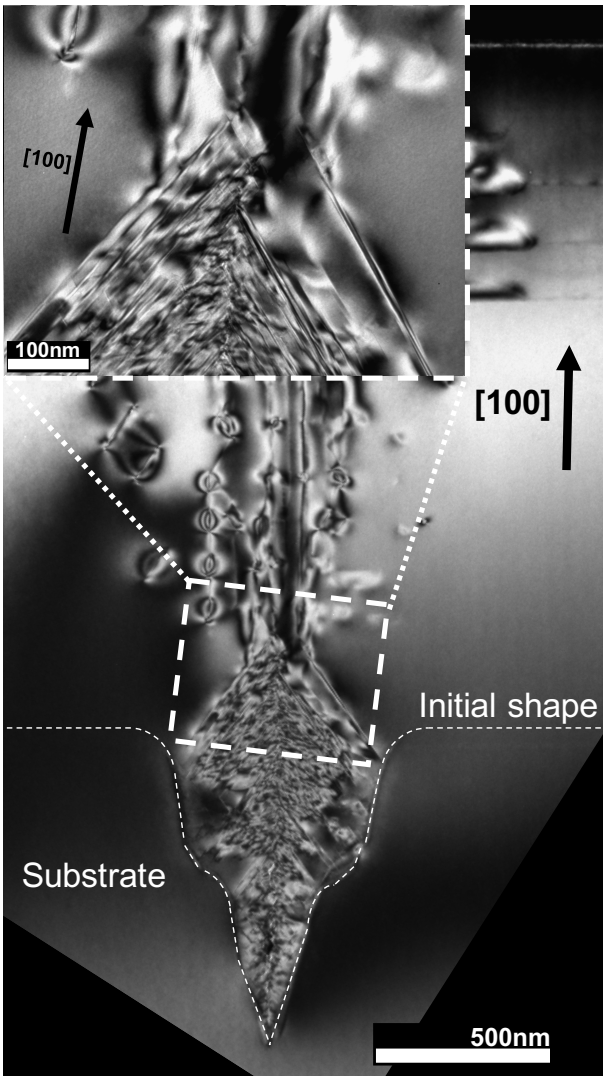

Fig.IV.17. Dark field TEM micrograph of a 1μm inter-terrace distance region of sample #4-HMCD. The initial profile of both terraces is marked by a dashed white line. Region of dislocations coalescence, marked by a dashed white rectangle, is shown at higher magnification as an inset.

TEM micrographs of the terrace coalescence in sample #3-LMCD are shown in Fig. IV.18. The lower growth rate of this sample, reported in *Chapter III*, results in a lower density of threading dislocations. However, the use of doped layers has been observed to induce additional dislocations in the places where growth directions change abruptly. These points act as sharp corners adding extra strain and generating additional defects [Alegre 2014].

Fig.IV.18(a) shows the overgrowth coalescence of two terraces separated 1 μm. As it was observed in sample #3-LMCD, the quality of the etching was poor for low inter-mesa distances. In this case, the abrupt surface together with the boron doping result in the generation of dislocations in the two small bottom corners. Nevertheless, such dislocations are annihilated by their recombination.

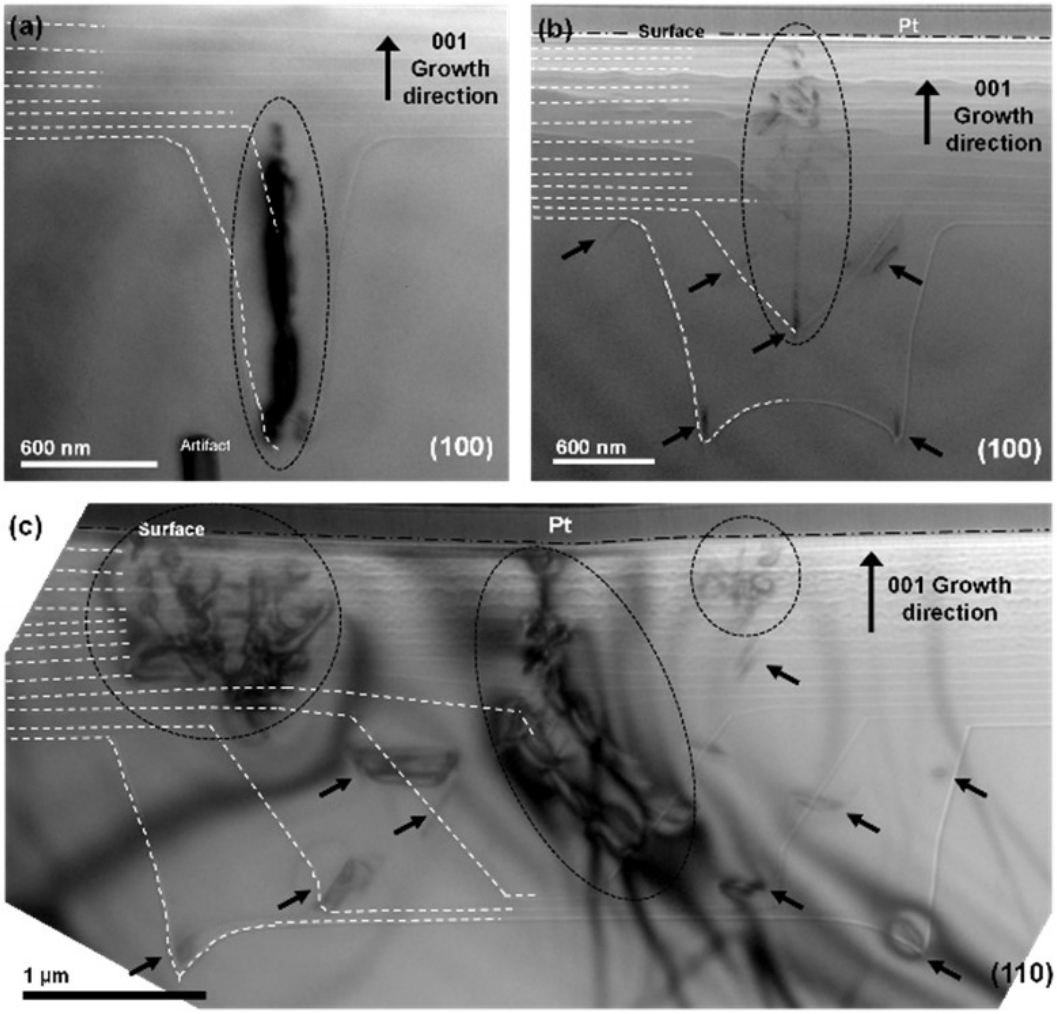

Fig.IV.18. Bright field TEM micrographs recorded along the 011 zone axis of (a) 1μm, (b) 2μm and (c) 5μm terrace distances in sample #3-LMCD. Initial shape of terraces as well as doped layers are partially marked by dashed white lines. Planar defects are marked by black arrows whereas TD are identified by dashed black circles.

Fig.IV.18(b) and (c) show the overgrowth coalescence of two terrace separated by 2 μm and 5 μm, respectively. Doping layers, as well as the initial shape of the terraces, are partially marked by dashed white lines. It is observed that growth orientation was mainly along [111] in the region between terraces. Doping layers are revealed as defects generators since, in all cases,

planar defects are shown to appear in the doped layers. These defects are marked by black arrows in the micrographs of Fig.IV.18. In addition to these planar defects, threading dislocations, marked by dashed black circles, are observed. They are also generated in the doped layers but mainly in the region where these doped layers are abruptly blended forming a sharp corner, due to the overgrowth coalescence.

Consequently, terrace overgrowth coalescence has been shown to reduce threading dislocations density but the heavily doped thin layers, have been shown to generate additional extended defects.

In this way, it has been proved that TD can be redirected far away from the terraces thanks to the lateral growth. It can provide large free defects regions depending on the size of the terraces. For the ones here studied, where the growth direction was [111], the free defect areas were, at least, as big as 1.4 times the height of the terrace, i.e. the height of the terrace multiplied by the tangent of 54.74º.

Moreover, free defect surfaces may be further enlarged by the coalescence of terraces. Along the coalescence line, threading dislocations recombine and, in most of the cases, result in their annihilation. To optimize this technique, the distance between terraces should corresponds to 2.8 times the height of such mesa structures.

IV.4. Superficial hillocks

Hillocks-like superficial defects are commonly obtained by CVD diamond growth. In the literature, there are two reason to which their generation is attributed: screw dislocations ([Tsuno 1994, Kreutz 1995, Tokuda 2010 and Tokuda 2012]) and penetration twins ([Wild 1994, Tamor 1994 and Bogatskiy 2015]). However, most of these studies were performed by techniques as atomic force microscopy (AFM) or photoluminescence (PL) whereby not clear evidences of their generation could be provided.

Thus, in order to study the origin of the formation and generation of such hillocks, transmission electron microscopy (TEM) studies are required [Tallaire 2016]. In the following, a cross sectional TEM study is proposed, first of sample #4-HMCD (equivalent to #9-HMCU), which has been shown many defects in its surface, and then #3-LMCD, which does not exhibit any superficial defect. The subject of study are the so-called hillocks type (ii) defects already mentioned in the previous sections.

Fig.IV.19 shows SEM micrographs of samples (a) #4-HMCD and (b) #3-LMCD. Among of others differences in facetting already reported in *Chapter III*, sample #3-LMCD (Fig.IV.19 (b)),

that was grown at low rate, resulted free of superficial defects. In fact, authors who reached atomically step-free surface always used methane concentration lower than 0.05% [Watanabe 1999, Tokuda 2009, Tokuda 2010 and Tokuda 2012]. The present results show that on 100-oriented diamond substrates, surfaces free of superficial defects can be achieved by growing at slightly higher methane concentrations, such as CH_4/H_2=0.1%.

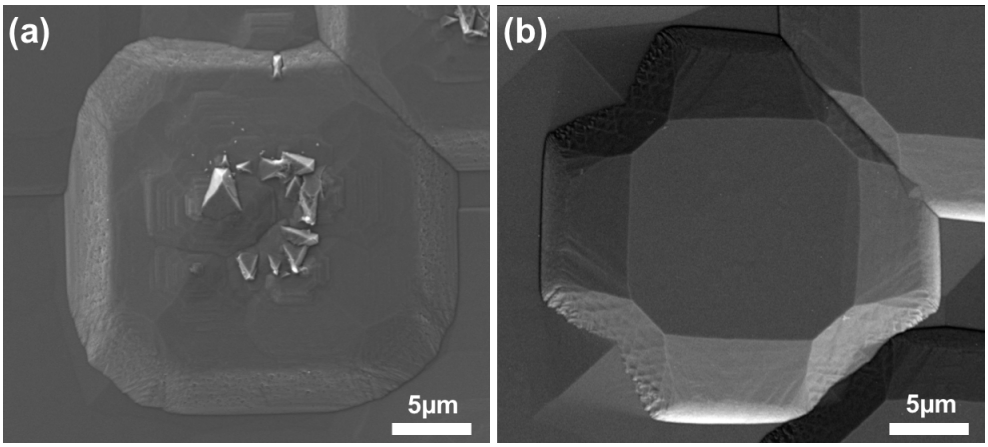

Fig.IV.19. SEM micrographs of one mesa structure of (a) #4-HMCD, where pyramidal shaped hillocks are visible on the top; and (b) sample #3-LMCD, whose surface is shown to be free of superficial defects.

Fig.IV.19(a) shows a mesa structures of samples #4-HMCD crowned by triangular shaped hillocks. These hillocks look to be grown mainly on the corners of the initial structures since they are aligned forming a circle with a diameter similar to that of the initial mesa structure. Moreover, hillocks show well faceted sides and they seem to follow four equivalent configurations, all of them symmetric respect to the <011> direction. Hillocks have then two lateral faces parallel and the other two forming an angle of 18° respect to the <011> direction. All of them are identical except for the four possible orientations. They form a pyramidal shape with the apex leaned toward one of the sides. Hillocks with similar triangular geometry have been also reported [Takami 1999, Teraji 2003, Teraji 2004 and Tokuda 2012], being an open topic. Takami *et al*. [Takami 1999] attributed the formation of those hillocks to twins. However, this explanation was rejected by Teraji [Teraji 2004] who found the geometry of defects observed inconsistent with the twin theory. TEM analysis is therefore essential to determine the origin of these defects. Tokuda *et al*. [Tokuda 2012] also overgrew on etched substrates by MPCVD, obtaining roughs surfaces. They grew over {111}- oriented HPHT substrates at 0.5% of methane concentration and concluded that the roughness appeared because diamond growth at higher methane concentration is dominated by multi-nucleation on terraces. This idea was already anticipated in *Chapter III* were the nucleation of additional grains was proposed to be due to the growth parameters.

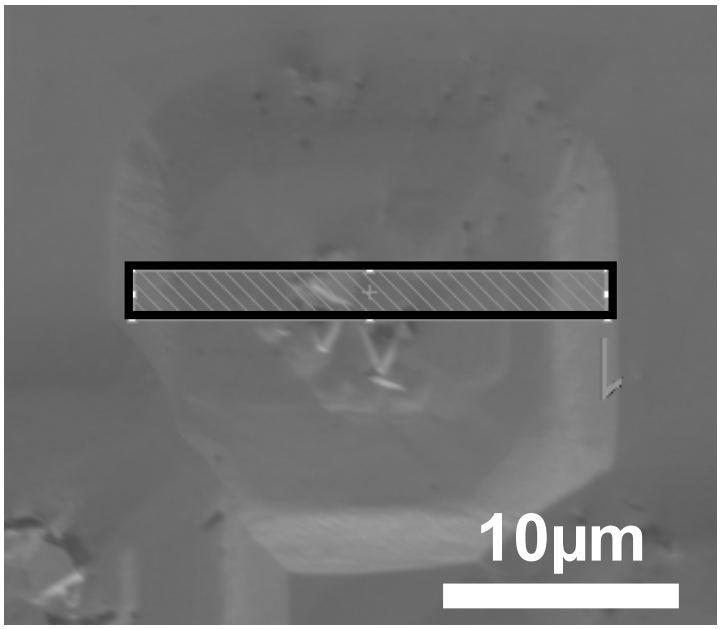

Fig.IV.20. SEM micrograph of sample #4-HMCD with the region from where the lamella was extracted marked by a black rectangle.

A SEM micrograph with the region where the lamella was extracted marked by a black rectangle is shown in Fig.IV.20. The irrregular shape of the observed grain is mainly due to its being composed of two merging crystallites. The challenge of extracting the lamella from the exact centre of the hillock could not be met. TEM micrograph corresponds then to a cross section shifted by about 300 nm from the centre of the hillock. All this explains why the shape of the crystallite was not symmetric.

Fig.IV.21 shows TEM micrographs of a region of sample #4-HMCD crowned by a hillock. Fig.IV.21 (a) corresponds to a dark field micrograph recorded by exciting the $[\bar{4}00]$ reflection with the sample oriented along the (011) zone axis. Hillock and the region where the hillock is coming from have a dark contrast revealing a different orientation than the rest of the lamella. High density of dislocations is also pointed out under the hillock and coming from the corners of the initial disk. They are shown as white contrast in the micrograph. The Burger vector of the observed dislocations was deduced from the invisibility criterion. On the basis of such a criterion, when $\mathbf{g}\cdot\mathbf{b}=0$, the contrast from dislocations won't be visible. In the same way, reflections for which $\mathbf{g}\cdot\mathbf{b}\neq 0$ will show the dislocations. In our observations, the contrast associated to the dislocations was visible for $\mathbf{g} = \bar{4}00$ and $\mathbf{g} = \bar{1}\bar{1}1$ reflections, and remained invisible for reflection $\mathbf{g} = 0\bar{2}2$. From these observations, the Burger vector is shown to correspond to one of the following: $\mathbf{b} = \frac{1}{6}[211]$, $\mathbf{b} = \frac{1}{6}[\bar{2}11]$, $\mathbf{b} = \frac{1}{6}[2\bar{1}\bar{1}]$ or $\mathbf{b} = \frac{1}{6}[\bar{2}\bar{1}\bar{1}]$.

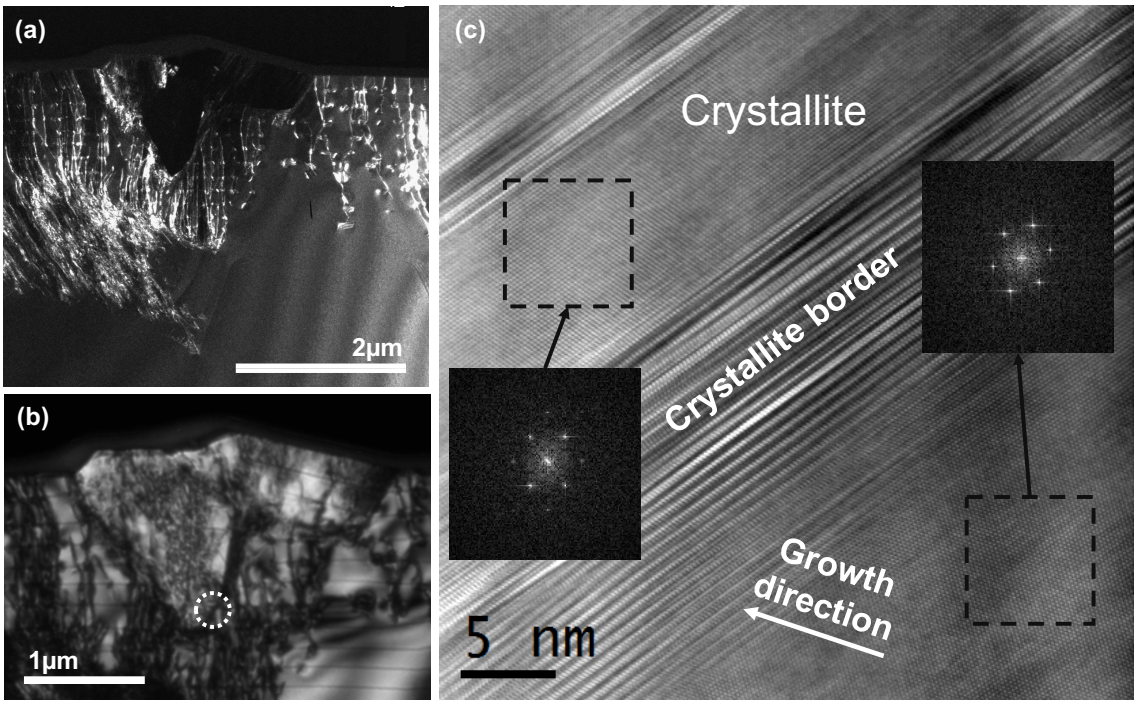

Fig.IV.21. (a) TEM dark field micrograph of sample #4-HMCD recorded under two beam conditions with the sample oriented along the [011] zone axis using the $\mathbf{g} = \bar{4}00$ reflection. Dislocations are shown as white contrast. Crystallite under the hillock exhibits a different dark contrast than the rest of the sample evidencing a different orientation. (b) TEM bright field micrograph of the region of the crystallite at higher magnification. Horizontal black contrasts, due to the thin doped layers, show changes into the growth orientation in and out the crystallite. Dashed white circle marks the region where HREM micrograph was obtained. (c) High resolution TEM micrograph of this region of the crystallite boundary. Fourier transforms have been obtained at both sides of the border evidencing the different orientations.

Fig.IV.21 (b) shows a TEM bright field micrograph recorded at higher magnification with the sample oriented along the (011) pole. Doped layers evidence the different growth orientation and rates inside and outside the crystallite. Dashed white circle marks on this image the region where Fig.IV.21 (c) was recorded. Fig. IV.21 (c) is a high resolution TEM micrograph that reveals the epitaxial character of the growth. This image also highlights the presence of staking faults and twins together with the dislocations. In fact, partial dislocations and twining structures have been reported previously as the origin of the hillocks [Tsuno 1994 and Sawada 2001]. The observed twins form an angle of 70.53°. These planar defects correspond with the $\sum 3$ coincident-size-lattice structure [Zhang 1999]. In addition, a Fourier transform performed on this defects showed that they correspond to {111} type (not shown here). These structures are twin boundaries-like and they have been observed in monocrystalline diamond in the previous section already (see figure IV.14) and were frequently reported for polycrystalline diamond [Sawada 2001 and Lu 2012]. This is consistent with the fact that twins act as borders of the crystallites.

The insets in Fig.IV.21 (c) display two patterns obtained by Fourier transforms at the regions enclosed by white dashed squares. They are situated at the two sides of the border of the crystallite and reveal orientations along the same [011] zone axis but tilted by 73°. On such FFT, the [111] directions coincided, while the [022] direction of the crystallite formed a 18 degrees angle with the [400] direction of the rest of the sample, which was the substrate orientation.

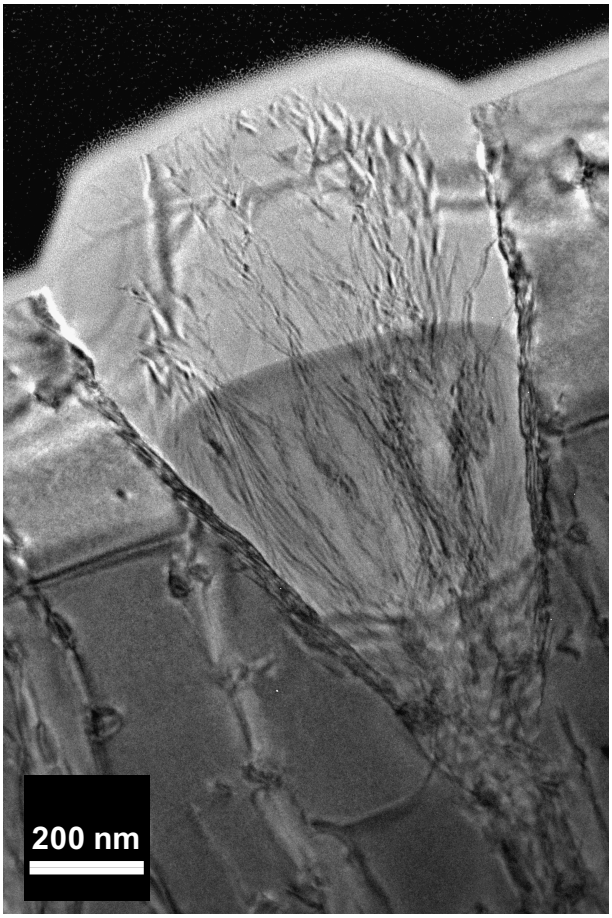

Fig.IV.22. TEM bright field micrograph recorded in two beam conditions along the 011 zone axis of a crystallite formed on sample #4-HMCD. Many dislocations seem to merge at the beginning of the crystallite.

Fig.IV.22 shows TEM micrograph of another crystallite showing up on top of sample #4-HMCD. In this case, the hillock was oriented perpendicular to that observed in Fig.IV.21. It was formed by an individual crystallite and allows to have a better image of the shape. Thanks to the doped layer is also possible to follow the growth orientation at each position. In this way, contrast due to the looping of the dislocations in the doped layers shows planar growth under the crystallite. As was expected because of the hillock formation, the growth rate is shown to be higher in the crystallite respect to the regular region of the diamond and the last doped layer is shown to be above its reference height outside the crystallite. This contributes also to the asymmetric shape of the cross section of the crystallite.

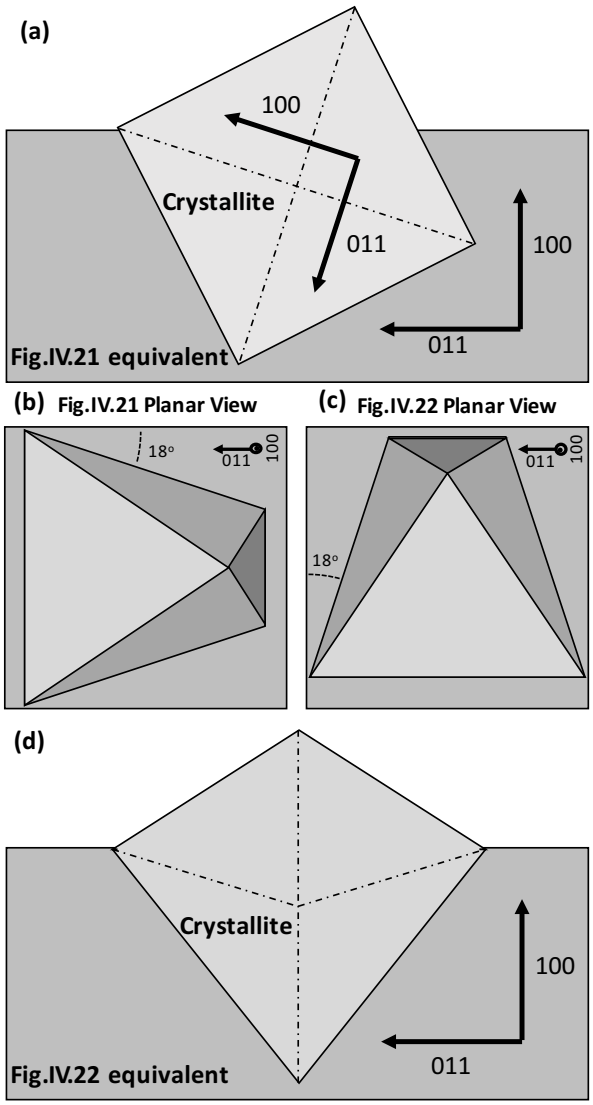

Fig.IV.23. Schematics of the crystallite for the two proposed configurations assuming that the lamella was obtained at the centre of the crystallite. (a) and (b) correspond to the situation shown in Fig.IV.21 as cross section and planar view, respectively. (c) and (d) are the equivalent for Fig.IV.22.

From this analysis, it is concluded that pyramidal hillocks are formed by nanoscopic crystallites with planes {111} as faces. Such crystallites are tilted 18º with respect to the rest of the sample, coinciding with the orientations ⟨122⟩ of the substrate, and seems to be generated by TD with a Burger vector perpendicular to those orientations, $\mathbf{b} = \frac{1}{6}\langle 211\rangle$. The reason to have 4 different cases of hillocks corresponds to each equivalent Burger vector, $\mathbf{b} = \frac{1}{6}[211]$, $\mathbf{b} = \frac{1}{6}[\bar{2}11]$, $\mathbf{b} = \frac{1}{6}[2\bar{1}\bar{1}]$ or $\mathbf{b} = \frac{1}{6}[\bar{2}\bar{1}\bar{1}]$.

Fig.IV.23 shows a schematical representation of the situation, where (a) and (b) sketch the situation studied in Fig.IV.21; and (c) and (d) the case shown in Fig.IV.22. The analogy

between the four cases observed in the surface of samples #9-HMCU and #4-HMCD is here displayed.

This work has confirmed that hillocks formation was highly correlated to the growth rate used. In fact, it was already proposed in *Chapter III* that high methane concentrations can favour the secondary nucleation of extra crystals. Tentatively, the increase of bonding possibilities and the particular geometry of the substrate due to the corners of the mesa structure favoured this possibility. Nevertheless, sample #3-LMCD proved that under the same conditions of pressure, temperature and plasma power, it was possible to obtain smooth surfaces without any pyramidal hillock simply by reducing the methane concentration and, consequently, the growth rate.

On the other hand, TEM micrographs have shown that hillocks observed on the surface hide crystallites under them. That is, hillocks are the superficial exponent of a crystallite embedded in the sample. These crystallites, generated during growth at high velocities, are caused by partial dislocations $\mathbf{b} = \frac{1}{6}\langle 211\rangle$, and form twins at their boundaries. These twins have been determined as $\sum 3$ coincident-size-lattice structure and {111} type. Crystallites grow perpendicularly to the Burger vector generator and have {111} boundaries. There are four different configurations of crystallites, one for each $\mathbf{b} = \frac{1}{6}\langle 211\rangle$ Burger vector.

Thanks to the use of very thin doped layers, growth orientation has been determined at nanometric scale. Under the crystallite, planar growth was observed. In contrast, inside the crystallite, growth followed a different orientation with a faster growth velocity. This explains that crystallites are shown as pyramidal hillocks on the surface. HREM proved the epitaxial character of the growth of the crystallite on the sample and reject the theory of twins as origin of the hillock. Finally, because results for sample #9-HMCU and #4-HMCD were the same, it is concluded that boron doping has not any significant influence on the formation of these defects.

IV.5. Summaries

IV.5.1. Resumen

Los defectos cristalinos son uno de los principales impedimentos en el desarrollo de dispositivos electrónicos basados en diamante. En la presente tesis se ha realizado un completo estudio de defectos aparecidos durante el crecimiento lateral. En el estudio de un defecto superficial de la muestra #2-A se han observado dislocaciones en las capas de dopado. Históricamente, este tipo de defectos han estado asociados a la

deformación inducida por el dopado y, por tanto, se ha asumido que su origen estaba en la intercara entre la capa dopada y la no dopada. Sin embargo, observaciones en campo oscuro anular (ADF por sus siglas en inglés) han demostrado que las dislocaciones aparecen en diferentes posiciones de la capa dopada atribuyéndosele como origen una deformación de la red cristalina más local.

El estudio del defecto superficial, correspondiente a un montículo piramidal (PH), ha mostrado la curvatura de las capas dopadas y, por lo tanto, del crecimiento, así como su velocidad que ha resultado ser más alta para la orientación (111), como era de esperar. Una alta densidad de defectos ha sido también observada que ha resultado ser mayor en estos mismos planos de crecimiento. Esto confirma la afinidad particular de las dislocaciones a ser generadas en estos planos más compactos frente a otros.

Haciendo uso del criterio de invisibilidad se han obtenido los vectores de Burger de las dislocaciones observadas que resultaron ser $\boldsymbol{b} = \pm\frac{1}{6}[11\bar{2}]$ *y* $\boldsymbol{b} = \pm\frac{1}{2}[1\bar{1}0]$.

Gracias a las imágenes de alta resolución pudieron observarse defectos planares como fallos de apilamiento que forman un ángulo de 70.53° *y corresponden con* $\Sigma 3$ *en la estructura red-tamaño-coincidente (CSL por sus siglas en inglés). También se han identificado dislocaciones de borde en estas micrografías correspondientes al vector de Burger anteriormente mencionado* $\boldsymbol{b} = \pm\frac{1}{2}[1\bar{1}0]$.

En general, las regiones de la muestra donde el crecimiento fue según la dirección [100] no mostró dislocaciones ni defectos, evidenciando el hecho de que con las mismas condiciones de crecimiento los planos (111) favorecen la generación de defectos.

Como continuación a este trabajo, se han estudiado el resto de muestras con el objetivo de obtener claves del crecimiento en la generación de defectos. Este extenso estudio ha mostrado: (i) la existencia de defectos superficiales en el sustrato, quizás generados durante el grabado, que se extienden como dislocaciones en la capa crecida. (ii) Las esquinas de las estructuras mesa como principales generadores de defectos. (iii) Alta densidad de defectos en las capas altamente dopadas. Estos resultados no son extrapolables al caso de las muestras #3-LMCD ni #8-LMCU, ambas crecidas a bajo metano, que no mostraron dislocaciones y únicamente mostraron fallos de apilamiento como defectos en las micrografías TEM.

De esta forma, las muestras #2-A y #7-ß10 presentaron dislocaciones con vector de Burger de la familia $\boldsymbol{b} = \pm\frac{1}{2}\langle 011\rangle$, las dislocaciones de las muestras #4-HMCD, #5-α16 y #9-HMCU tenían un vector de Burger de la familia $\boldsymbol{b} = \pm\frac{1}{6}\langle 211\rangle$ y la muestra #6-α10 presenta ambas familias de vectores de Burger. Por su parte, y como se dijo anteriormente, las muestras #3-LMCD y #8-LMCU no presentan dislocaciones y defectos planares fueron observados.

El estudio mostró que las dislocaciones con vector de Burger $\boldsymbol{b} = \pm\frac{1}{2}\langle 011\rangle$ son principalmente favorecidas por el dopado mientras que las dislocaciones pertenecientes a la familia de vectores de Burger $\boldsymbol{b} = \pm\frac{1}{6}\langle 211\rangle$ tienen un origen diferente. De esta forma, cuando la muestra es dopada, la deformación del plano (ésta deformación es debida a efectos de proximidad de los átomos de boro) tiende a generar dislocaciones del tipo $\boldsymbol{b} = \pm\frac{1}{2}\langle 011\rangle$, exceptuando para el caso de la muestra #6-α10 que combina ambas familias de dislocaciones.

El uso del crecimiento lateral como técnica para la reducción de dislocaciones ha sido evaluado. Se ha comprobado como el crecimiento

lateral empuja a las dislocaciones hacia fuera, haciendo posible conseguir zonas libres de ellas. Además, se ha probado que la interacción entre dislocaciones, favorecida por la coalescencia de dislocaciones en los puntos medios de las terrazas, permite la aniquilación de estas mediante su recombinación. El uso de ambas técnicas puede ser utilizado en la mejora de la calidad cristalina e implementado en el diseño de dispositivos electrónicos y otras aplicaciones en las cuales los defectos cristalinos son, a día de hoy, escollos insalvables.

Un defecto común que aparece durante el crecimiento de diamante para dispositivos electrónicos son los defectos superficiales con forma de montículos (hillocks en inglés). La aparición de estos defectos ocurre, además de arbitrariamente en la superficie de las muestras, coronando los discos y trincheras alineados siguiendo el contorno de la estructura original (antes del crecimiento). Para estudiar su origen se han observado las muestras #4-HMCD y #9-HMCU. Ambas mostraron estos defectos como granos independientes del resto de la muestra. Estos granos provienen de zonas de alta densidad de dislocaciones llegándose incluso a identificar en una de las micrografías la dislocación responsable de su generación. Las imágenes de alta resolución mostraron igualmente una gran densidad de defectos planares (fallos de apilamiento) en las fronteras de grano.

IV.5.2. Résumé

Les défauts cristallins sont l'un des principaux obstacles au développement de dispositifs électroniques à base de diamant. Dans cette thèse, nous proposons une première étude des défauts apparus au cours de la croissance latérale. Dans l'étude d'un défaut de surface de l'échantillon #2-A, des dislocations ont été observées dans les couches dopées. Historiquement, ces défauts sont associés à la déformation

induite par le dopage et il est donc supposé que leur origine est situé à l'interface entre la couche dopée et non dopée. Cependant, les observations STEM en mode champ sombre annulaire (STEM-ADF) ont montré que les dislocations apparaissent dans des positions différentes de la couche dopée, ce qui atteste que d'autres mécanismes sont responsables de la génération de dislocations.

L'étude du défaut de surface correspondant à une butte pyramidale (PH) a montré que sa croissance et sa vitesse étaient plus élevée et de par son orientation des planes {111} de croissance. Une densité élevée de défauts a également été observée dans ces mêmes plans. Ceci confirme l'affinité particulière des dislocations à être générées dans ces plans plus compacts. En utilisant le critère de l'invisibilité les vecteurs de Burger sont identifiés comme étant $\boldsymbol{b} = \pm\frac{1}{6}[11\bar{2}]$ et $\boldsymbol{b} = \pm\frac{1}{2}[1\bar{1}0]$.

Grâce aux observations en mode haute résolution (HREM) des défauts planaires tels que les fautes d'empilement ont pu être mise en évidence. Celles-ci forment un angle de 70.53° et correspondent à des $\Sigma 3$ dans la structure « coincident-site-lattice ». Des dislocations de coin ont également été identifiées dans ces micrographies, qui correspondent au vecteur de Burger, $\boldsymbol{b} = \pm\frac{1}{2}[1\bar{1}0]$.

D'une manière générale, les régions de l'échantillon où la croissance était dans la direction <1 0 0> n'ont montré aucune dislocation ni défaut. Ceci démontre qu'avec les mêmes conditions de croissance, ce sont les plans {1 1 1} qui favorisent la formation de défauts.

Suite à ce travail, nous avons étudié les échantillons restants afin de déterminer le rôle de la croissance dans la génération de défauts. Cette étude a montré (i) l'existence de défauts de surface dans le substrat, peut-être générés ou révélés lors de la gravure, qui prolongent les dislocations dans la couche ; (ii) les coins de la structure mesa

comme les principaux générateurs de défauts ; (iii) une haute densité de défauts dans des couches fortement dopées. Ces résultats ne sont pas extrapolables aux cas des échantillons #3-LMCD ou #8-LMCU, tous deux avec des conditions de croissance à bas dopage, qui n'ont pas montré de dislocations mais seulement des fautes d'empilement dans les micrographies MET.

Ainsi, les échantillons #2-A et #7-ß10 ont présenté des dislocations avec un vecteur de Burger de la famille $\boldsymbol{b} = \pm\frac{1}{2}\langle 011\rangle$, alors que les échantillons #4-HMCD, #5-α16 et #9-HMCU ont des dislocations avec un vecteur Burgers de la famille $\boldsymbol{b} = \pm\frac{1}{6}\langle 211\rangle$. L'échantillon #6-α10 présente à la fois les deux familles de vecteurs de Burger. De plus, comme indiqué ci-dessus, les échantillons #3-LMCD et #8-LMCU ont seulement quelques défauts planaires et les dislocations n'y ont pas été observées.

L'étude a montré que les dislocations avec un vecteur de Burger $\boldsymbol{b} = \pm\frac{1}{2}\langle 011\rangle$ sont principalement générées par dopage tandis que les dislocations appartenant à la famille de vecteurs de Burger $\boldsymbol{b} = \pm\frac{1}{6}\langle 211\rangle$ ont une origine différente. Ainsi, lorsque l'échantillon est dopé la déformation dans le plan (par effets de proximités et non par un effet d'énergie de la déformation) a tendance à générer des dislocations de type $\boldsymbol{b} = \pm\frac{1}{2}\langle 011\rangle$, sauf pour le cas de l'échantillon #6-α10, qui combine les deux familles de dislocation.

L'utilisation de la croissance latérale comme technique pour réduire les dislocations a été également évaluée. Il a été constaté que les dislocations dans le diamant suivent la direction de croissance et donc sont « déviées » par la croissance latérale autour des terrasses. Ceci permet de libérer de dislocation ces zones. En outre, il a été prouvé que l'interaction entre dislocations, favorisée par la coalescence des dislocations sur les lignes médianes entre les terrasses, permet

l'annihilation partielle de celles-ci par leur recombinaison. Les deux techniques peuvent être utilisées pour améliorer le cristal et pourraient être mis en œuvre dans la conception de nouveaux substrat de diamant libre de dislocation.

Un défaut commun qui se produit pendant la croissance du diamant pour les applications électroniques sont des défauts de surface en forme de buttes (hillocks en anglais). L'apparition de ces défauts se produit d'une part de façon arbitraire sur la surface des échantillons, et d'autre part au-dessus des arêtes des disques et des tranchées, et semblent alignées suivant le contour de la structure d'origine (avant la croissance). Pour étudier leur origine les échantillons #4-HMCD et #9-HMCU ont été observés. Les deux ont montré que ces défauts correspondaient à des grains séparés du reste de l'échantillon. Ces grains proviennent de zones avec une haut densité de dislocations. Des images en haute résolution ont également montré une forte densité de défauts planaires (défauts d'empilement) à la frontière de ces grains.

V Boron doped layers

Contents

Boron content has been estimated in four different samples (#3-LMCD, #10-LMCD, #11 Disp and #4-HMCD) using two different techniques. First, CL measurements have been carried out on FIB-lamellas obtaining doping averages of ~1.5x10^{19} cm^{-3}. However, these results are not highly accurate due to the low signal (high noise level) as well as the effects related to the quasi-delta doped layers that acts as quantum dots and whose recombination time is too small. CL studies on sample #11-Disp was carried out on plan view (not on a lamella). They show, by monochromatic CL maps, selective growth on the lateral sides of the mesa-rectangles. Moreover, an alternative method was used to estimate the [B] content on samples with dislocations. It is based on solid solution strengthening of the doped layers.

V.1. Introduction

Doping diamond is a well studied topic due to its numerous applications (see *Chapter I)*. It is performed by the inclusion of doping entities (here boron atoms) in the crystal lattice that replace the carbon atoms in the lattice network. Quite generally, the cell parameter of the host network varies systematically with the concentration of the foreign atoms. For isoelectronic substitutional atoms, i.e. impurities that have the same valence electronic structure as the substituted atom, the simplest geometrical model proposed initially by Vegard [Vegard 1921] is sufficient to explain these variations [Scheffler 1987]. However, in the case of heterovalent substitutional atoms, even if there is only a valence shift of one between the foreign and host atom, the situation is not clear. Due to the larger covalent radius of boron (r_B=0.88 Å) compared to that of carbon (r_C=0.77 Å), the introduction of substitutional boron into diamond leads to an expansion $\partial a/a$ of the lattice parameter [Brunet 1998a, Brazhkin 2006, Wojewoda 2008 and Kawano 2010]. These variations of the cell parameters are significant mainly for very high doping levels ([B]>10^{19} cm^{-3}) [Brunet 1998a] and result in a shift of the lattice parameter of 0.3% (0.011Å) for the maximum [B] concentration achieved, [B]~$7x10^{21}$ cm^{-3} [Brazhkin 2006]. As a consequence of such expansions, strain and/or defects can be introduced which would be detrimental for the characteristics of the device [Alegre 2014]. Fig.V.1 shows two HRTEM micrographs of sample #3-LMCD of a region, that includes the interface doped/undoped, grown along (a) {111} and (b) {311}.

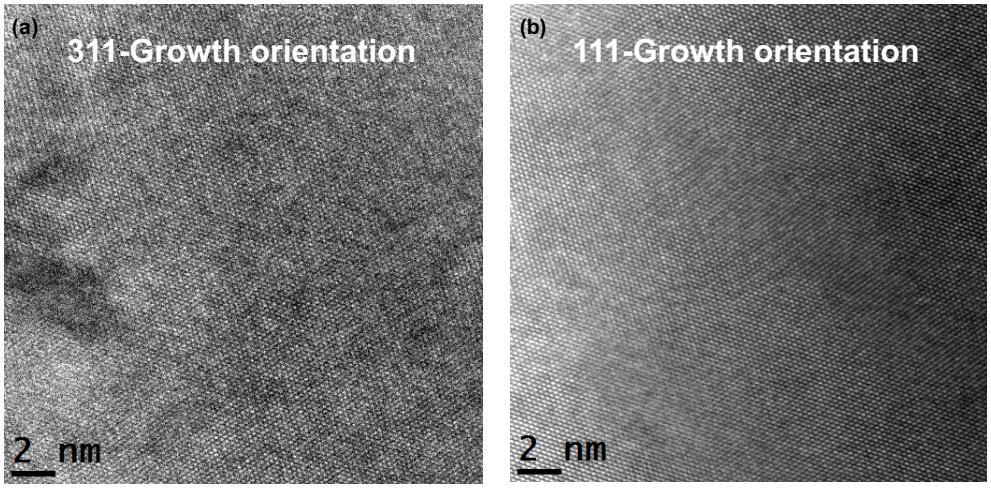

FIG.V.1 HREM micrographs in a region with a doped layer growth along (a) {311}- orientation and (b) {111}- direction.

Due to the different atomic number Z of boron respect to the carbon, doped diamond films modify their atomic scattering factor, $f(\theta)$, respect to the intrinsic diamond one [Williams 1996]. This induces a difference in the scattered beams intensity which can be used, either in STEM-

HAADF or in CTEM, to visualize the doped layers. A quantification of this contrast can be used to determine [B] concentrations for high [B] content ($>10^{20}$ cm^{-3}). Another possibility is to use STEM-EDS but here again, only doping above 10^{20} cm^{-3} can be detected. Indeed, the low Z number of B makes really difficult (up to now, not reports found) to detect it in diamond.

Nevertheless, an alternative spectroscopy technique is cathodoluminescence (CL). This technique collects the photon generated by the interaction of the incident electrons with the electrons of the sample. The consecutive radiative recombination signal depends on the electronic properties of the sample. In particular, at low temperature, excitons bound to boron impurities have specific spectral signatures that make it possible to determine the boron levels. One of the main restriction in the use of this technique is the presence of dislocations. The strain generated around the dislocation bend the valence and conductions bands trapping all the carriers. Their mobility is then strongly reduced and electrons and holes recombine generally through non-radiative channels. In some materials as diamond, a relatively weak large band (labelled A-band in diamond) can result from the radiative carrier recombination at the dislocation. When the density of defects is high enough (as in some cases presented in chapter IV), the evaluation of the doping levels by CL is no more possible.

Thus, the presence of dislocations means also a challenge for the quantification of boron (dopant) in diamond by CL. In this chapter, the dislocation behavior at undoped/doped interface is used as a new technique to assess the doping level. Solid solution strengthening is usually used in metallurgy to increase the hardness of alloys like aluminum or steel, i.e. to modify the dislocation mobility behavior. The inclusion of impurity atoms in a network modify the primary structure by deforming the lattice. Such deformation results into an increase of the hardness, i.e. reduces the dislocation mobility. For a threading dislocation, solid solution strengthening means a higher resistance to its lateral shift. By measuring the additional energy required of the dislocations to pass through the doped layer it should be possible to determine the boron concentration.

In this line, the current Chapter presents two different methods for the study and estimation of the [B] concentration according to the particular characteristics of each sample.

V.2. [B] estimate by CL

Cathodoluminescence is a technique commonly used to evaluate the boron incorporation and the presence of crystalline defects [Yan 2002, Sauer 2003, Kasu 2004, Araujo 2004, Araujo 2005, Baron 2006, Ghodbane 2010, Araujo 2011a, Araujo 2011b, Omnès 2011 and Fernandez-

Lorenzo 2012,]. Doping by boron modify the electronic properties of diamond, pinning the Fermi level and incorporating acceptor levels in the bandgap, that can form an impurity band merging with the valence band above the metallic transition.

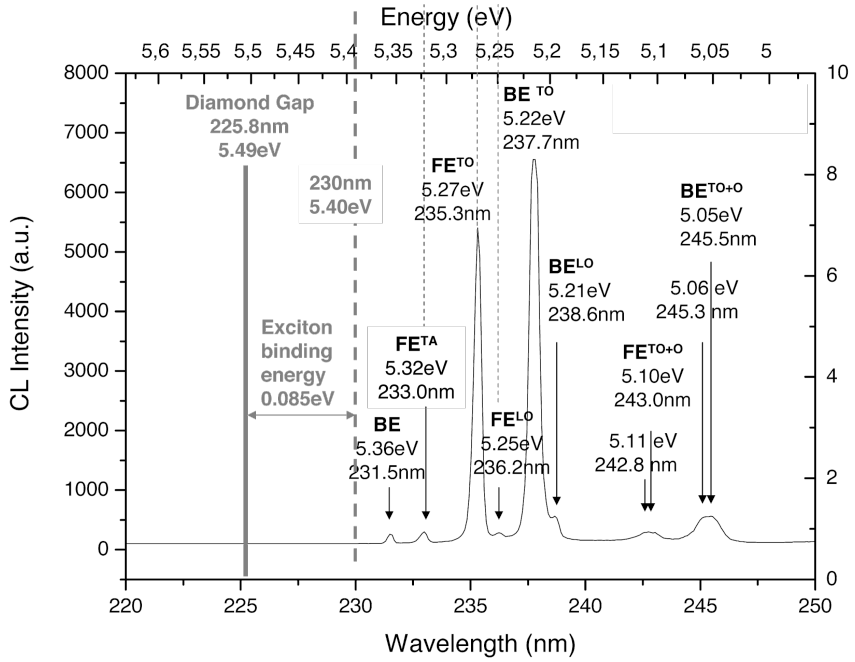

Fig.V.2. CL spectra recorded at 5 K temperature in the excitonic range of a CVD boron doped diamond sample [Fernández-Lorenzo 2012]

CL measurements can be performed to evaluate the boron incorporation. In Fig.V.2, a CL spectrum of boron doped CVD diamond is shown in the excitonic recombination energy range. Peak related transitions are indicated on the spectrum at helium temperature (T=5 K) [Fernández-Lorenzo 2012]. Because the bandgap is not direct, phonons are involved in the radiative recombination process and transverse acoustic (TA), transverse optic (TO) and longitudinal optic (LO) modes of phonon energy 0.087 eV ($\hbar\omega_{TA}$), 0.141 eV ($\hbar\omega_{TO}$) and 0.163 eV ($\hbar\omega_{LO}$) respectively, are associated to the different exciton replicas [Tanabe 2001, Koizumi 2001 and Kadri 2004] as shown on the spectrum. The diamond bandgap is 5.49 eV and the exciton binding energy is 0.085 eV. Then according to the phonon energies the FE^{TA}, FE^{TO} and FE^{LO} are observed at 233 nm (5.32 eV), 235.3 nm (5.27 eV) and 236.2 nm (5.25 eV), respectively. As the binding energy of the exciton to the boron dopant is 0.055 eV [Tanabe 2001 and Koizumi 2001], the respective BE (bound exciton) related energies are shifted by these values, i.e. BE^{TA}=231.5 nm (5.36 eV), BE^{TO}=237.7 nm (5.22 eV) and BE^{LO}=238.6 nm (5.20 eV) as indicated on the spectrum. The first is usually not observed as the peak overlaps the FE^{TO} one. However, as the intensity of the TO replica is much higher (more than 30 times), the 5.27 eV peak is fully attributed to FE^{TO} recombinations.

High [B] content

Authors showed that the energy of the main signal decreased from 5.220 eV, down to 5.04 eV when $[B]>10^{20}cm^{-3}$, then remained constant when $[B]>10^{21}\ cm^{-3}$ [Sauer 2003]. They ascribed the main signal in the low and high [B] ranges to the boron bound exciton recombination assisted by the TO phonon (BE^{TO}) and its decreasing energy to band gap shrinkage. It is largely accepted that the shift of this peak towards lower energies is caused by the narrowing of the gap due to the boron incorporation in the diamond lattice. For (100) homoepitaxial film with high $[B]=2x10^{19}$ cm^{-3}, a decrease of the BE^{TO} energy down to 5.195 eV was shown [Baron 2005]. These studies have been repeated for a large number of cases and doping values, generating a graph (see dashed blue line in Fig.V.4) that can be used as reference for the evaluation of doping levels in polycrystalline and homoepitaxial diamond.

An empirical relationship between boron levels and energy values of BE^{TO} peaks for [B] ranges of $1.5x10^{19}\ cm^{-3}<[B]<6x10^{20}\ cm^{-3}$ in diamond homoepitaxy is therefore:

$$E(eV) = 5.211 - 0.112\log([B]/1.5x10^{19}) \qquad \text{eq.V.1}$$

Low [B] content

Total incorporation in the lattice of low boron doping diamond includes three main components [Omnès 2011]:

First, the substitutional single atom boron concentration, $[B]_s$. Such boron atoms correspond to the electrically active shallow acceptors, with the expected ionization energy level of 0.37 eV above the valence band [Thonke 2003].

Second, the boron passivated by hydrogen concentration, [BH]. Such single substitutional boron atoms bound to hydrogen atoms are known to behave as non electrically active species, with deep energy levels in the gap [Barjon 2006 and Habka 2010].

Third, the boron complexed to punctual defects, mainly vacancies, [BV complex]. Such boron atoms also give deep energy levels in the gap [Muret 2010] and therefore are not electrically active.

Low temperature CL (<13 K) measurements can provide then [B] concentrations in the {100}-oriented diamond in the full 10^{14}-$10^{18}\ cm^{-3}$ from the free and bound excitons optical features [Omnès 2011].

The shape of the peaks has also been shown to change with the concentration of boron on the layers. The full width at half maximum (FWHM) of the BE^{TO} peak for homoepitaxial films, remains constant around 10meV for low [B], increases with [B] across the high [B] range up to ≈

90 meV, remains around ≈ 110 meV with dispersion according to the preparation conditions for heavy [B].

Additionally, Omnès *et al*. [Omnès 2011] performed cathodoluminescence studies at low temperature in order to determine low to moderate boron concentrations. As the probability of exciton binding to one impurity depends linearly on its density, the relative intensity ratio between FE^{TO} and BE^{TO} allows to determine the boron content [Kawarada 1993 and Fernandez-Lorenzo 2012]. By comparing SIMS with I_{BETO}/I_{FETO} CL ratios on (100) oriented homoepitaxial diamond samples with boron concentrations from 10^{16} cm^{-3} to $6x10^{18}$ cm^{-3} was defined the following expression:

$$[B] = 3.5\times10^{16}\frac{I^{BE_{TO}}}{I^{FE_{TO}}}. \qquad \text{eq.V.2}$$

This linear relationship was observed for doping values in the 10^{16}-$3x10^{17}$ cm^{-3} range, and for measurements performed at 10 kV acceleration voltage and 5 K temperature. For values of boron doping concentration higher than $3x10^{17}$ cm^{-3}, results do not match with the linear expression.

The expressions and graphs mentioned above are used in the current thesis to determine the boron concentration and the expected variation into the doping by the different planes of growth. Experiments have been carried out at low temperature (5K) and using an electron beam accelerated by 10kV of voltage. Originally, samples studied were #3-LMCD, #4-HMCD, #10-Disk and #11-disp. However, the high density of dislocations of sample #4-HMCD promotes the non-radiative recombinations of electrons and holes decreasing the signal under the noise level. For this reason, in the following sections are introduced only the results corresponding to samples #3-LMCD, #10-LMCD and #11-Disp.

V.2.1. CL measurements on sample #3-LMCD

Sample #3-LMCD was grown with 10700 ppm of B_2CH_6 relative to CH_4 (conditions are given in Chapter II). However, the incorporation of boron atoms into the lattice also depends on the methane concentration during the growth. The doped layers of this sample were grown at low methane concentration of CH_4/H_2=0.1%.

Doped layers of the sample are ~6nm thickness and they are not visible under thermo-ionic emission gun SEM. Moreover, the contrast observed on field emission gun SEM (see Fig.IV.16), is drastically weakened by the thickness of the samples required for CL experiments (600nm-1μm thick). For this reason, cathodoluminescence are “blind experiments”. SEM probe

has been placed on the lamellas using as reference the TEM micrographs already shown in the previous chapters. In this line, doped layers have been found by trial and error.

Nevertheless, when CL study was performed in this sample, a peak characteristic of boron doping (BE^{TO}) was always obtained.

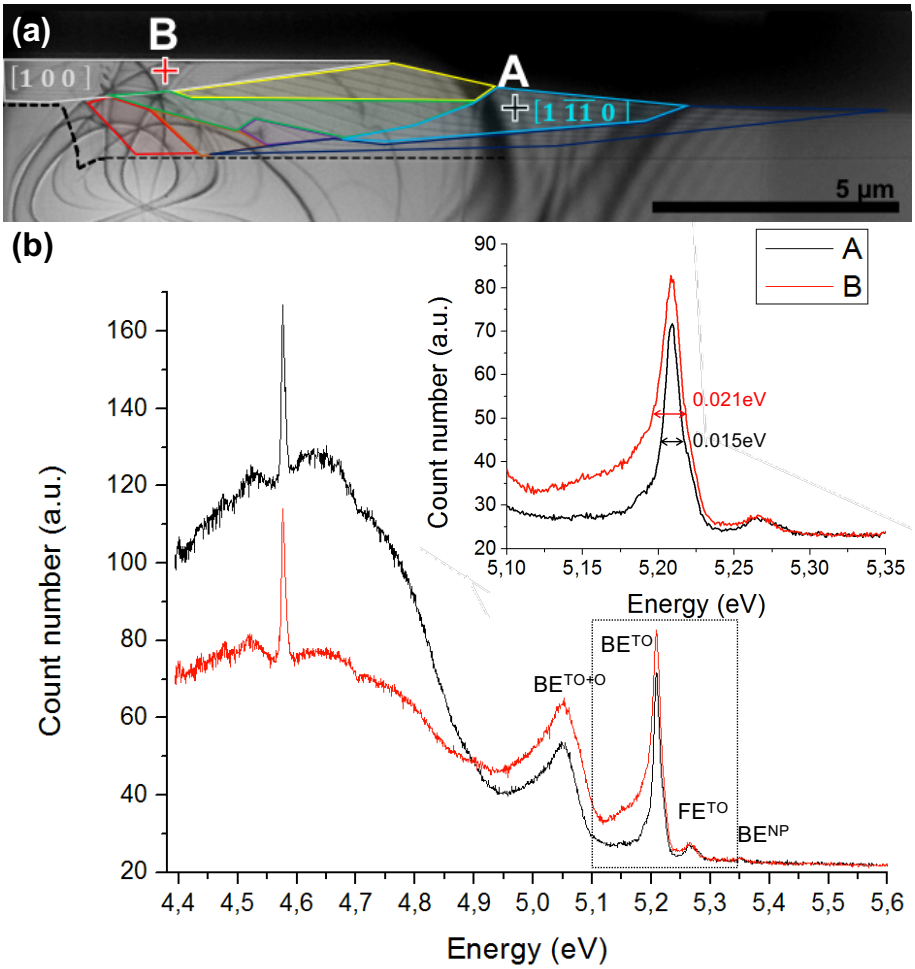

Fig.V.3. (a) TEM micrograph of sample #3-LMCD with the different growth orientation marked. Crosses A and B mark the position where CL spectra were recorded. (b) A (black) and B (red) CL spectra with the main excitons marked. Inset is shown at higher detail the region from 5.1 eV to 5,35 eV.

Fig.V.3 (a) shows TEM micrographs of a lamella equivalent to the one on which the CL measurement were performed. Positions where the spectra were recorded are marked by black and red crosses and the letter A and B, respectively. They correspond to growth orientations along the $(1\ \overline{1}1\ 0)$ and $(1\ 0\ 0)$ planes.

Fig.V.3 (b) displays both superimposed spectra to help in the comparative analysis. BE^{NP}, FE^{TO}, BE^{TO} and BE^{TO+O} excitons peaks are clearly shown at 5.35 eV, 5.26 eV, 5.20 eV and 5.05 eV, respectively. This fact anticipates a low boron concentration in the layers [Dean 1965]. In fact, the

values of the BE^{TO} energies, ~5.209 eV and 5.208 eV, both higher than 5.195 eV, indicates $[B]<2x10^{19}$ cm^{-3} [Baron 2005]. Based on that, sample is out or in the border of the first low doping range. This means at the beginning of the high doping range which stand between $1.5x10^{19}<[B]<6x10^{20}$ cm^{-3} and ruled by eq.V.1. The values of BE^{TO} excitons for each position are practically the same, 5.209 eV in A and 5.208 eV in B, it is also an indicative of boron concentration is about $2x10^{19}$ cm^{-3} [Baron 2006]. From these values, and if it is considered that they are in the range of validity of eq.V.1, boron concentration results in $1.5x10^{19}$ cm^{-3} for both positions. Fig.V.4 shows the extrapolation of these BE^{TO} energies in the graph shown in the bibliography [Baron 2006].

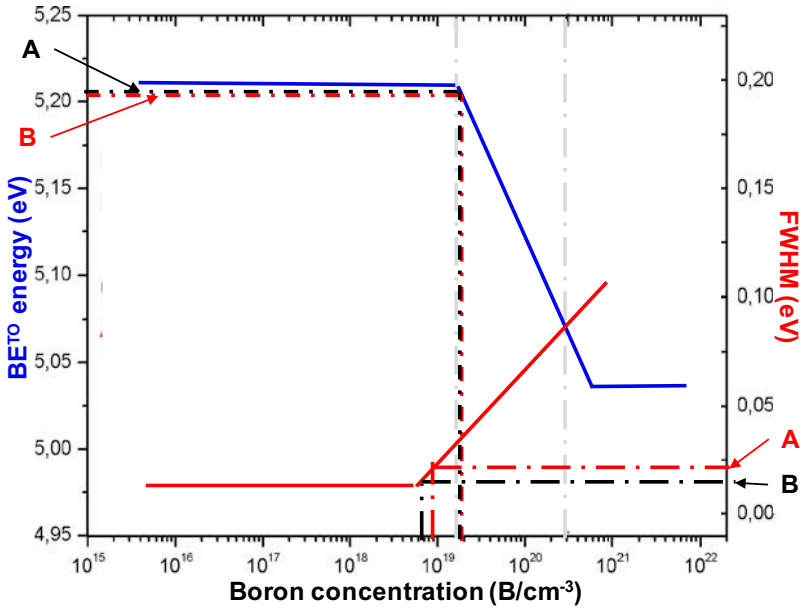

Fig.V.4. Tendency of energy and full width at half maximum of the BE^{TO} exciton versus the boron content in homoepitaxial films [Baron 2006], with the values obtained in sample #3-LMCD for position A, in black color, and for position B, in red color.

Authors also used values of FWHM of the BE^{TO} peak to estimate the [B] concentrations. For our sample, unlike the value of the BE^{TO} energy is almost the same, FWHM is clearly different for both position. It is easily to determine in the inset of Fig.V.3 (b). There is shown the region of the spectrum corresponding to BE^{TO} and FE^{TO} energies (framed in the full spectrum). FWHM obtained are 0.015 eV position A and 0.021 eV for B. Fig.V.4. shows FHWM values extrapolated and they result in concentrations of ~$9x10^{18}$ cm^{-3} for position A and ~$7x10^{18}$ cm^{-3} for position B.

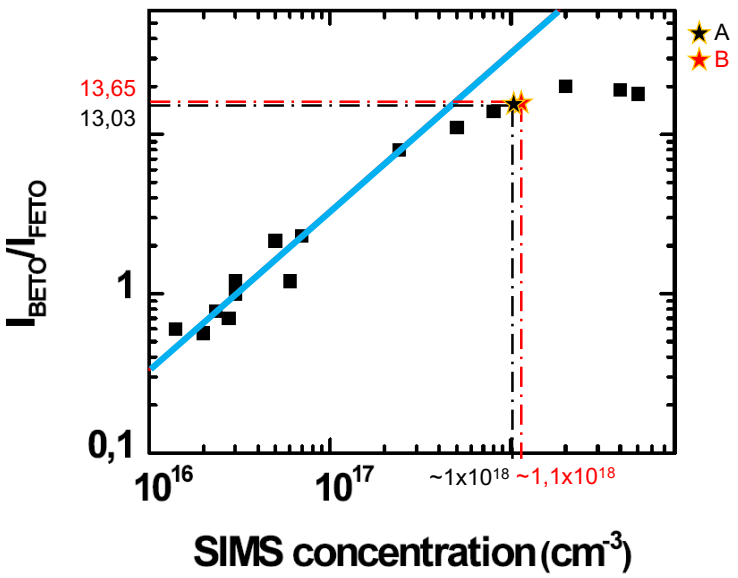

Fig.V.5. BE^{TO} to FE^{TO} peak intensity ratios as function of the boron SIMS determined absolute concentration [Omnès 2011], with the values obtained in sample #3-LMCD.

Considering low boron doping values, the intensities of the BE^{TO} and FE^{TO} peaks is evaluated. Their resulted ratios are used in the second approximation, showed in Fig.V.5. This approximation is valid for concentration ranges of 10^{16} to $6x10^{18}$ cm^{-3}. These ratios are out of the line of tendency (blue line in Fig.V.5), but they have been enlarged to follow the bibliography results. Boron concentration for these ratios results in [B]~$1x10^{18}$ cm^{-3}, for A, and [B]~$1.1x10^{18}$ cm^{-3}, for B. This estimation is highly sensitive to intensity of the FE^{TO} peak. Here, these peaks are in a range near to the noise of the signal. Thus, most probably the [B] content is underestimated by this approximation.

Moreover, note that, despite the boron layers are about 6 nm thickness, BE^{TO} peak was always obtained into the spectra. Spectra where obtained from small scanning windows. Considering that undoped layers are 100nm thickness and, likely on average, two doped layer and one undoped are scanned, it would be expected to obtain a 10% of BE^{TO} intensities over 90% of FE^{TO} ones. Nevertheless, results showed ratio intensities FE^{TO}/BE^{TO} of 0.1, i.e. carrier are trapped at the doped layer. This implies two possible effects:

- First, the quasi-∂ doped layer acts as a quantum well (QW). Charge fall inside and recombine.
- Second, recombination time into the quasi-∂ layer is much lower than in the undoped diamond: $\tau_{rec,\delta} \ll \tau_{rec,undop}$.

V.2.2. CL measurements on sample #10-LMCD

As described in *Chapter II*, growth conditions of sample #10-LMCD only differs from the one of sample #3-LMC in the boron concentration used (B/C=28000ppm). The same procedure as previously was followed for CL characterization. However, in contrast with sample #3-LMCD where a BE^{TO} peak was always obtained, here, carrier do not recombine in the doped layer and spectra from the undoped region were the most common recorded. This points out the worse transport in this sample which is due to dislocations (see *Chapter IV*). In addition, because of such bad crystal quality, the CL signal was very low and it was necessary to use large slits to have enough signal. Spectra have been recorded trying to characterize the maximum number of possible orientations.

SEM micrograph of the region analyzed by CL has been compared with TEM micrographs. Fig.V.6 (a) shows the SEM micrographs with two positions where the spectra were recorded marked with white crosses. TEM micrograph of the same region, where the doped layers are marked with thin black dashed lines, is shown as inset. From this micrograph, doped layers have been drawn on the SEM figure. They are overpainted with white dashed lines. Spectrum A was recorded on one of those doped layers. Spectrum B, in contrast, was recorded on non-intentionally-doped diamond. Fig.V.6 (b) shows superimposed the spectra recorded in both positions. To help in the identification of the peaks observed, spectrum A was displaced along the vertical axes. Moreover, peaks marked are pierced by dashed gray lines.

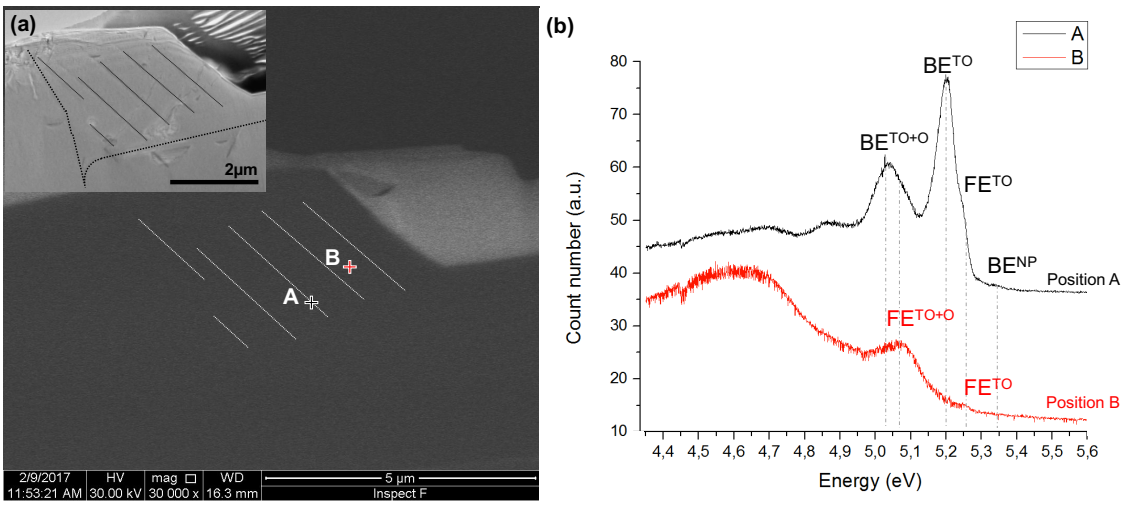

Fig.V.6. (a) SEM image of the lamella of sample #10-LMCD where the CL study was performed with the positions where spectra were recorded marked by crosses. White dashed lines mark the doped layers, based on the TEM image shows as inset where these doped layers are marked by dashed black lines. (b) Spectra of both positions with the main peaks marked.

As anticipated, position B does not show BE^{TO} peak. Instead of that, two peaks are observed. Because of their dissymmetry, their FWHM and the energy that separates both peaks they are identify as FE^{TO} and FE^{TO+O} excitations, with energies of ~5.265 eV and ~5.05 eV.

On the other hand, spectrum in position A shows FE^{TO} and FE^{TO+O} peaks overlapped by the BE^{TO} (at 5.201 eV) and BE^{TO+O} (at 5.044 eV) excitation, respectively. This overlapping is attributed to the use of large slits. B^{NP} peak is also observed at an energy of 5.352 eV. Baron *et al*. [Baron 2006] reported this range of energies and excitations in low boron content films (samples with $5x10^{18}$ cm^{-3} and $1.8x10^{19}$ cm^{-3} of [B]). BE^{TO} energy is compared with the ones reported in the bibliography to estimate the boron concentration. As shown in *Chapter III*, doped layers follow the {111}- orientation, and thus BE^{TO} energy obtained will be first compared with results obtained for this orientation in the bibliography [Ghodbane 2010]. A [B] of $1.7x10^{19}$ cm^{-3} is deduced.

Cathodoluminescence spectra have been recorded in additional position of the sample. Fig.V.7 (a) shows these four positions (D, E, F and G) marked by crosses. The corresponding spectra are displayed superimposed in Fig.V.7 (b). Position D, that lies outside of the doped layer, shows a spectrum similar to B (see Fig.V.6). It corresponds to a NID region.

Position E, in contrast, was recorded on a doped layer. It is not easy to claim the plane of growth but it seems to be the {100}. BE^{TO} peak at such position has an energy of 5.217 eV which is higher than the energy found in A and, presumably, implies at lower boron content. BE^{NP}, FE^{TO}, FE^{TO+O} and BE^{TO+O} have been also identified with energies of 5.359 eV, 5.265 eV, 5.163 eV and 5.060 eV, respectively.

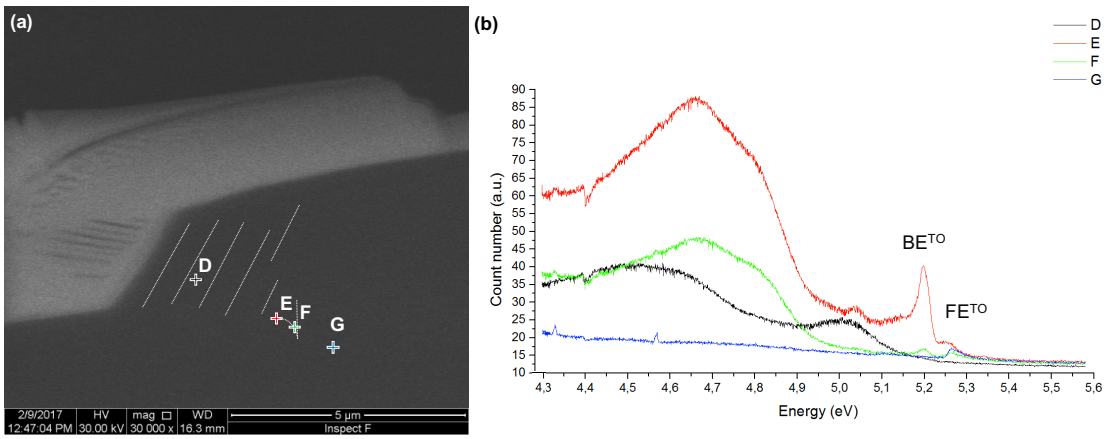

Fig.V.7. (a) SEM image of the lamella of sample #10-LMCD where the CL study was performed with the positions where spectra were recorded marked by crosses. White dashed lines mark the doped layers. (b) Spectra of the four positions.

Position F also corresponds to a doped region. In this case, it seems to match with the corner of the initial mesa shape. From its spectrum, energies of its BE^{TO} and FE^{TO} peaks are 5.207 eV and 5.265 eV.

Positions E and F are both doped. However, energies of BE^{TO} peaks show different boron concentrations. These concentrations have been estimated comparing with bibliography [Baron 2006]. Boron concentrations resulted in $1.4x10^{19}$ cm^{-3} and $1.6x10^{19}$ cm^{-3}, respectively.

The [B] is shown to vary depending the growth orientation. However, the variation for the present exposed condition is around $1\text{-}2x10^{19}$ cm^{-3}.

V.4.3. CL measurements on sample #11-Disp

Sample #11-Disp has been studied by cathodoluminescence at ~5K and 10kV acceleration voltage. This sample was laterally overgrowth undoped. Doped layer was only grown for a few minutes (8 min) at the end of the growth. Diborane ratio used was the same as for sample #10-LMCD, 28000 ppm with CH_4/H_2=1%. Study was performed in plan-view (not on a lamella) knowing the existence of two main growth orientations, (211) and (111) (see *Chapter III*).

Fig.V.8 (a) shows a SEM micrographs of the sample with the four different positions where spectra were recorded: A, at the bottom surface of the sample, B, on the {111}-lateral planes, C, on the {211}- lateral planes and D, on the top surface. The corresponding spectra are shown in Fig.V.8 (b). A and D positions show spectra of non-doped diamond with a few and low emitter peaks, typical from bad quality substrates. In contrast, B and C shows clearly the peaks BE^{NP}, FE^{TO} and FE^{TO+O} at the energies 5.354 eV, 5.265 eV and 5.106 eV, respectively. BE^{TO} and BE^{TO+O} peaks are shown at 5.207 eV and 5.042 eV, respectively, for B, and 5.208 eV and 5.043 eV, respectively, for C. FE^{TO+2O} are also observed in both spectra at around 4.898 eV.

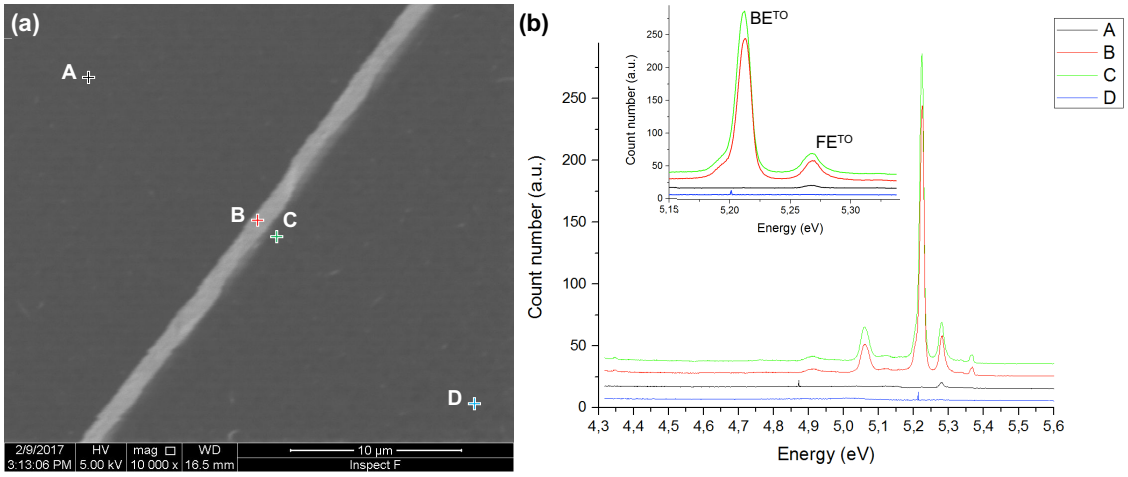

Fig.V.8. (a) SEM micrograph of sample #11-Disp with the location where CL spectra were recorded. (b) CL spectra at these locations. In the inset, the energies are expanded to point out the excitonic recombination behavior changing the e-beam location.

These spectra show doping in only some regions of the sample that was grown without any mask. In order to check if this is due to the fact that bad quality of substrate blocked any emission, Fig.V.9 shows spectra of two other positions, E and F, with the position where they recorded marked in SEM micrographs show as inset. Position E, Fig.V.9 (a), shows a spectrum with a very high FE^{TO} emission at 5.265 eV. BE^{NP}, BE^{TO} and FE^{TO+O} are also identified with lower emission at the 5.317 eV, 5.210 eV, and 5.101 eV energies, respectively. Whereas, position F, Fig.V.9 (b) shows a spectrum where BE^{TO} peak is the dominant exciton, with an energy of 5.208 eV. BE^{NP} (5.352 eV), FE^{TO} (5.265 eV) and BE^{TO+O} (5.046 eV) are also registered.

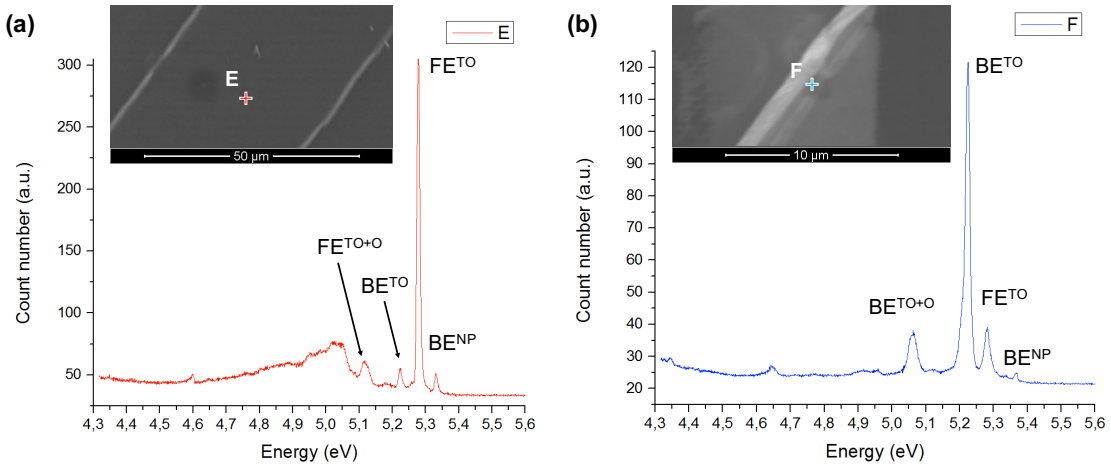

Fig.V.9. CL spectrum at the positions marked with a cross in the SEM micrographs SE mode showed as inset. Main peaks are identified.

The spectral results show a doping level in A, D and E positions of this sample around $2x10^{15}$ cm^{-3}. In addition, it demonstrates that selective growth is possible. To further study this intriguing growth behavior, monochromatic CL mapping at the BE^{TO} energy has been carried out.

In Fig.V.10, monochromatic CL micrographs, at this energy, at different locations around a rectangular shaped mesa are shown. The micrograph (a) and (c) are the SE (secondary electron mode) recorded micrograph corresponding to the CL-mode shown in (b) an (d) respectively. The white signal in SE corresponds to the lateral {111}-shaped of the mesa. Fig.V.10 (b) and (d) demonstrate that only at these locations, a boron-doped material was deposited.

More in detail, Fig.V.10 (c) shows a SEM micrograph of the corner of rectangle. The different contrast on the top is due to a previous scanning. Surface of the sample looks dirty due to the cooling-heating process for the CL measurements. (d) shows the BE^{TO} CL map of the same region. Image is similar to (b) but the corner seems less doped than the lateral sides of the structure.

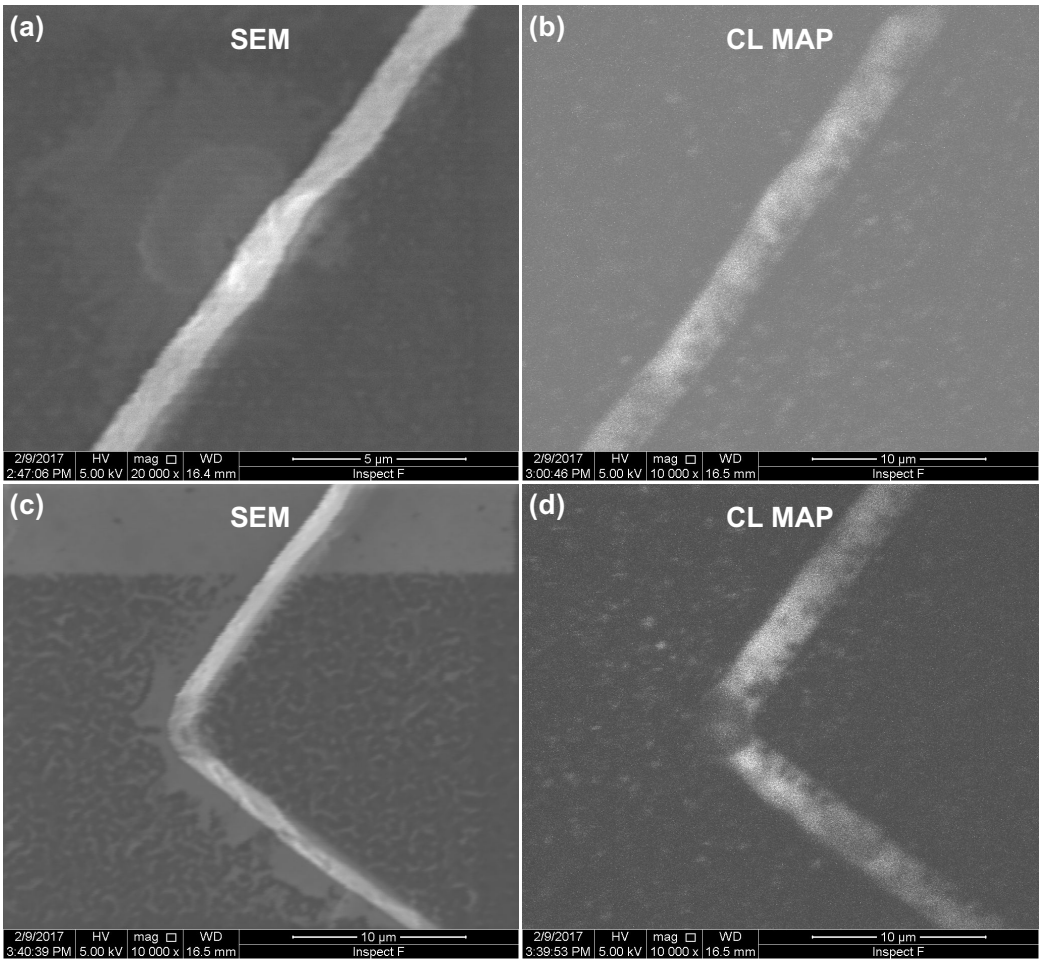

Fig.V.10. (a) and (c), SE-SEM of two different regions of sample #11-Disp. (b) and (d), BE^{TO} peak (5.210 eV) CL-maps corresponding to the same region.

V.3. [B] estimate by Solid Solution Strengthening.

Chapter IV demonstrated that lateral growth pushes dislocations out. These dislocations vary their trajectories when they pass through a doped layer. Such variations result from the strengthening of the doped layers that makes easier for the dislocation to glide in the undoped layers than in the doped ones.

As has been introduced, doping in diamond is achieved by the substitutional inclusion of doped atoms in the crystal lattice of diamond. Such atomic substitution generates a deformation of the lattice network that, in the case of boron atom and doping level of [B]<2.7x10^{20} cm^{-3}, can be estimated by eq.V.3 [Brunet 1998b].

$$\varepsilon = \gamma_{hkl}\frac{\delta a}{a} = \gamma_{hkl}7.8\times10^{-25}[B] \qquad \text{eq.V.3}$$

Alternatively, boron inclusions at the diamond lattice network can be seen as allowing elements into the crystalline lattice forming a solid solution. The non-uniformity generated by boron atoms makes plastic deformation more difficult by impeding dislocation motion and creating an increase in the yield stress of the material. As has been said, because of the small size of the boron atoms (but bigger than the C ones), solid solution (here resulting in a boron-doping) is substitutional. The inclusion of such atoms into the network distorts it generating an isostatic stress field (spherically symmetric). This field interacts with the dislocations hampering their expansion (see Fig.V.11). Nevertheless, boron doped layers are permeable to the dislocation's crossing and, if their energy is high enough, those dislocations propagate through the layer.

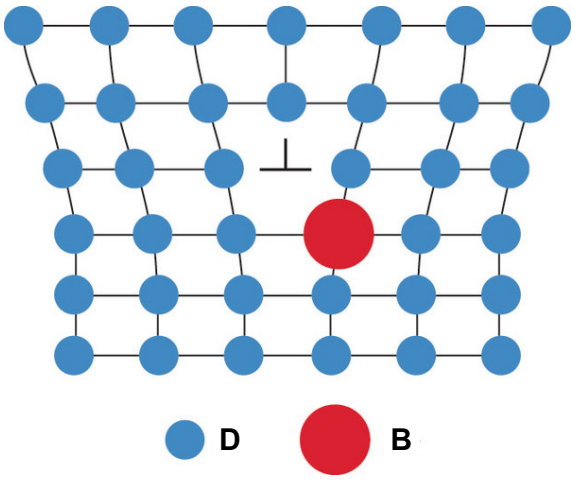

Fig.V.11. Diagram that shows how solid solution strengthening works. The larger B atoms are forced into the crystal structure of the diamond. If the atom B, which expand the lattice, is below the dislocation, then the dislocation is attracted by B. But if it is above, the dislocation suffers a repulsion. This places an outward compressive stress on the local diamond lattice, and also helps block dislocation motion. The dislocation symbol is that upside down "T" shown to the above left of the red B atom.

When a dislocation is pushed by any strain a displacement of the dislocation takes place. However, if some "object" (i.e. dislocation, other atoms as here boron, …) is in the way of the dislocation, a stop/brake can occur. This effect is labelled strengthening or hardening. Therefore, due to the strengthening into the doped layer, an increasing of tension is needed for the dislocation to continue its advance. This stopping point that must be overpassed or won over by the strain depends on the distance to the impurity and is expressed by Frank-Read [Frank 1950] as:

$$\Delta\tau_c \propto \frac{Gb}{L} \qquad \text{eq.V.4}$$

where the subscript *c* mains critical, G is the shear modulus, b is the modulus of the Burger's vector, L is the distance in between solutes atoms and the proportionality constant depends on the deformation generated by the boron atoms.

If we consider a regular squared distribution of solute in the gliding plane and that only the atoms placed just above and below the gliding plane are considered to affect the dislocation, we have $[B] = {2\sqrt{3}}/{L^2 a}$, boron atoms per unit volume, being *[B]* the boron concentrations and a the lattice parameter. Thus, $L = \sqrt{{2\sqrt{3}}/{a[B]}}$. Moreover, the dislocation is propagating along the {hkl}-planes. Those planes are not necessarily those of stress. Thus, the projection of the stress over the gliding planes and the gliding direction (slip system) of the dislocation is the Schmid factor, M. The resulting additional stress per unit length of the dislocation will then be:

$$\Delta\tau_c = \alpha G b \sqrt{{[B]a}/{\sqrt{12}}} \cdot M \qquad \text{eq.V.5}$$

Taking into account the size effect and anisotropy of the boron atoms, α can be expressed as distortion or plastic deformation induced: $\alpha = \varepsilon^{3/2}$, where ε is the strain induced by the stress in the diamond crystal. Considering the previous discussion about the network distortion by the boron inclusion, it can be argued that such inclusion implies an increase of the critical tension that is given by:

$$\Delta\tau_c = \left(\gamma_{hkl}\frac{\Delta\epsilon^{\perp}}{\epsilon^{\perp}}\right)^{3/2} Gb\sqrt{{[B]a}/{\sqrt{12}}}M \qquad \text{eq.V.6}$$

Lateral growth has been shown to push dislocations away (see *Chapter IV*). However, the strengthening of the doped layer results in that dislocations are moved more easily in the undoped region than in the doped ones. In the instant when the dislocation stopped slipping, the material is just at the yield strength in the doped and in the undoped material. Thus, as the yield strength increases by a factor $\Delta\tau_c$ in the doped region, the increase of elastic energy in this layer becomes:

$$E_{\Delta solid\ solution} = \frac{1}{2}\tau_c \varepsilon_c = \frac{1}{2}\frac{\tau_c^2}{G} = \frac{\left(\gamma_{hkl}\frac{\Delta\epsilon^{\perp}}{\epsilon^{\perp}}\right)^3 G^2 b^2 M^2 a[B] Vol}{2\sqrt{12}G} \qquad \text{eq.V.7}$$

In multilayered doped/undoped samples, as is our case, this results in a modification of the trajectory of the dislocation. Instead to move straight, the line becomes curved, enlarging its length by routing a lengthened half-moon-like trajectory. This is sketched in Fig.V.12. This addition in length implies an increase of the elastic energy of the dislocation that has to be equal to the increase of the critical tension by the boron impurities in the doped layer:

$$E_{\Delta dislocation\ lenght} = E_{\Delta solid\ solution} \qquad \text{eq.V.8}$$

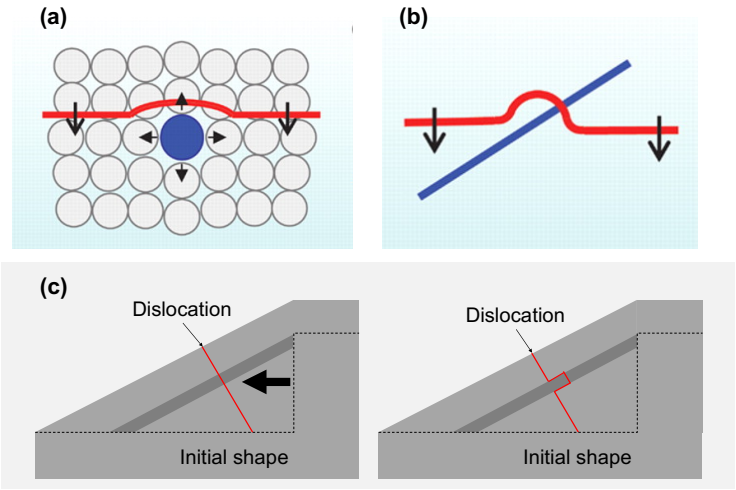

Fig.V.12. Sketch of the situation observed on the samples. (a) Boron solute atom (blue circle) strain the matrix to impede the motion of a dislocation (red line) through the lattice. (b) Doped layer (blue line) deviate the motion of the dislocation (red line). (c) Situation in our particular case, dislocations generated during the overgrowth or coming from the substrate climb to the surface. The mesa structure pushes the growth laterally, as identified by a black arrow, resulting in the displacement of the dislocation. However, due to the doping, this displacement is not the same all along the TD and the section of it that passes through the doped layer remains stacked.

The elastic energy stored by a dislocation per unit length is defined as the line tension [Hirth 1965] and it is given by the expression:

$$T \cong \frac{Gb^2}{2(1-\nu)} \qquad \text{eq.V.9}$$

where ν is the Poisson coefficient. Poisson coefficient is the ratio of transverse contraction strain to longitudinal extension strain along the direction of stretching force, $\nu = \frac{\epsilon^{\perp}}{\epsilon^{\parallel}}$. Such value depends on the Young and the shear modulus of diamond, G and E respectively, $\nu = \frac{E}{2G} - 1$. Being such

modulus, at room temperature, 1050 GPa and 478.0 GPa respectively [McSkimin 1972 and Spear 1994], Poisson's ratio for diamond is calculated to be equal to 0.098.

We observe that the dislocation length increase by taking a looped shape instead of a rectilinear. In this way, the extra elastic energy stored by the dislocation along the additional itinerary shown in Fig.V.12 will be [Hirth 1965]:

$$\Delta E_{dislocation\ length} \cong \frac{Gb^2}{2(1-\nu)}\Delta l \qquad \text{eq.V.10}$$

being Δl the extra distance covered by the dislocation in the loop drawn on the doped layer. As was anticipated, such energy must coincide with the additional elastic energy of the doped layer.

Finally, equalizing eq. (V.6) to (V10), we obtain:

$$\Delta E_e = \frac{\left(\gamma_{hkl}\frac{\Delta\epsilon^{\perp}}{\epsilon^{\perp}}\right)^3 G^2 b^2 M^2 a[B] Vol}{2\sqrt{12}G} = \frac{Gb^2}{2(1-\nu)}\Delta l \qquad \text{eq.V.11}$$

In order to determine the area, it was considered as the region encircled by the dislocation, it is the region enclosed by the loop. Moreover, from our CL studies, it is known that [B] content is under 2.7x10^{20} cm^{-3}. So, based on eq.V.3, $\frac{\Delta\epsilon^{\perp}}{\epsilon^{\perp}} = 7.8\times10^{-25}[B]$ [Brunet 1998b], eq.V.11 can be written as follows:

$$\Delta E_e = \frac{\left(\gamma_{hkl}7.8\times10^{-25}\right)^3 G^2 b^2 M^2 a[B]^4 Vol}{2\sqrt{12}G} = \frac{Gb^2}{2(1-\nu)}\Delta l \qquad \text{eq.V.12}$$

From this expression, it is possible to obtain the boron concentration into the doped layer:

$$[B] = \sqrt[4]{\frac{\sqrt{12}\Delta l}{(7.8\times10^{-25})^3 Vol M^2 a(1-\nu)\gamma_{hkl}{}^3}} \qquad \text{eq.V.13}$$

V.3.1. Strengthening study on sample #10-LMCD

As was previously explained, sample #10-LMCD was overgrown on a low-quality substrate. This is demonstrated by the observed dislocations coming from this substrate and threading throughout the layer. Fig.V.13 shows a DF TEM micrograph of a FIB lamella of the sample where some dislocations are coming from the substrate and deviated due to the overgrowth. One of these dislocations, far enough from the others to avoid dislocation-dislocation interactions (see white arrow), has been used for the study.

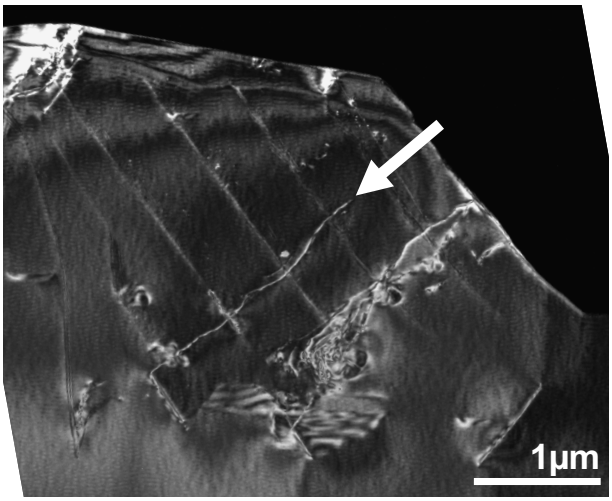

Fig.V.13. DF TEM micrograph recorded in two beam conditions with the sample oriented along the (011) pole using the [200] reflection.

Fig.V.14 (a) shows one of these threading dislocations (TD). The micrograph has been recorded in a region featuring a doped layer. When dislocations traverse the doped layer, they follow a semicircle, as was predicted. Note that, Due to dislocation is shown by TEM because of the strain induced, it depends on the conditions with which the micrograph is recorded. For this reason, dislocation is shown displaced respect to the doped layer.

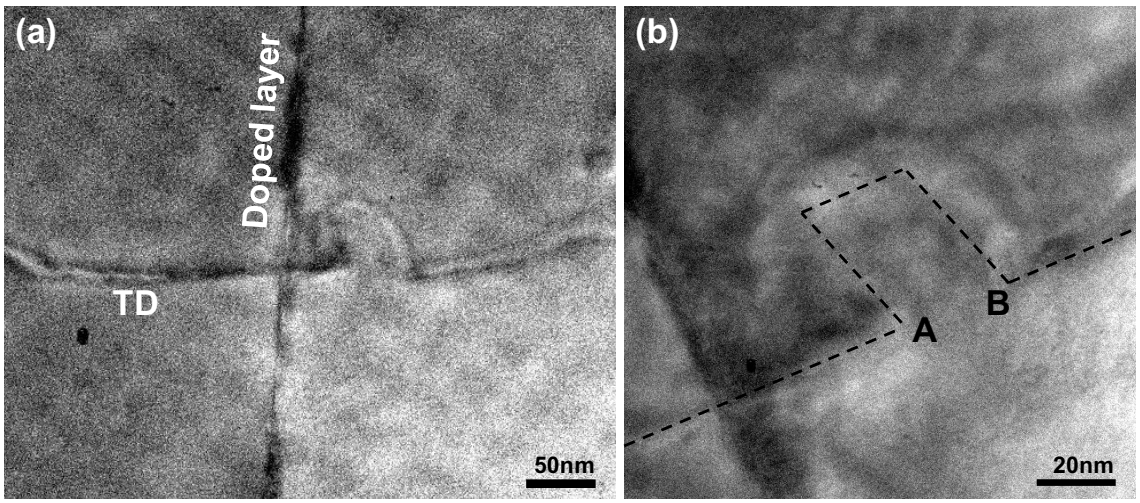

Fig.V.14. (a) TEM micrograph recorded on the [011] zone axis of a region of sample #10-LMCD where a dislocation form a loop around the doped layer. (b) Dislocation loop at higher magnification. An approximate trajectory of the dislocation is marked by a black dashed line. A and B mark the points where the dislocation is deviated.

Fig.V.14 (b) shows the semicircle formed by the dislocation at higher magnification. Two positions, A and B, have been marked on the micrograph. Each one of these positions marks the place where dislocation is curved and, consequently, where it starts to feel the strengthening due

doping. The dislocation length from A to B is marked by a dashed black line in the figure, and its value is L=109 nm against a direct A to B distance of d=30 nm. In this way, Δl=L-d=79 nm and Vol = 46807 nm^3.

From the analysis of this sample reported in Chapter III, it is known that growth around this position was along the {111}-plane. So, γ_{hkl}=γ_{111}=0.9136 and $H \approx 0.3$. Introducing these values into eq.V.13, a boron concentration in the doped layer of [B]=4.9x10^{19} cm^{-3} is derived.

V.3.2. Strengthening study on sample #4-HMCD

The same rationale has been used to estimate doping levels in sample #4-HMCD, which was grown under different conditions. The methane concentration was 0.75 % (0.5 % during the undoped layer) and the boron concentration was 9600 ppm (see Table II.III). Due to the high density of dislocations in this sample, it has been necessary to look for one far enough from the other to be able to neglect the interaction between TD. This dislocation is shown in Fig.V.15 (a). The region where micrographs were recorded is shown as inset, it corresponds to {133} growth orientation. Unfortunately, the value of γ_{311} is unknown, for this reason, [B] will be estimated considering γ_{111}.

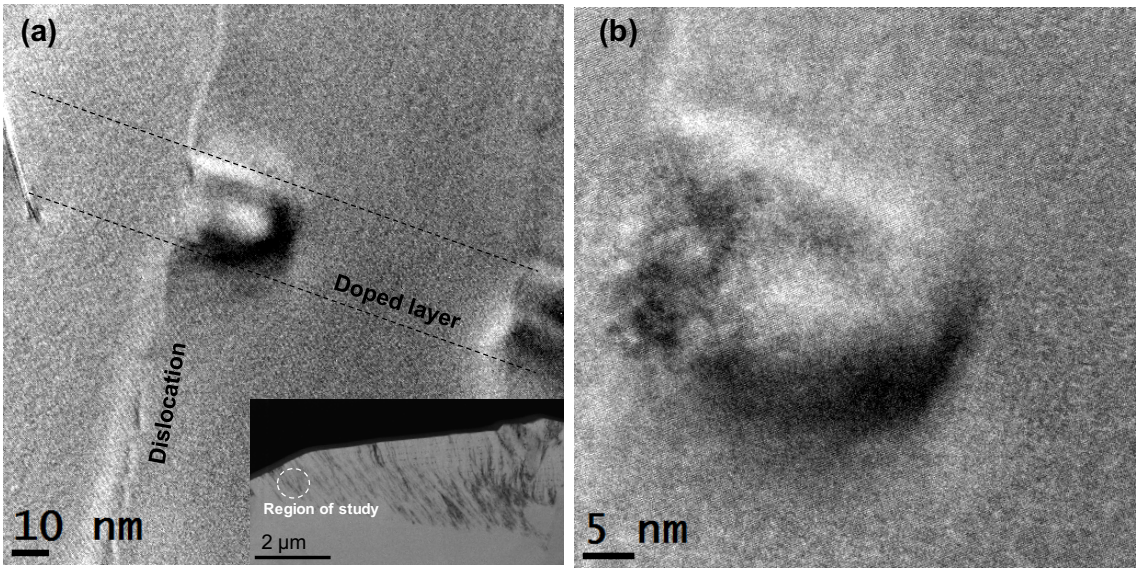

Fig.IV.15. (a) TEM micrographs of a dislocation deviated when it passes through a doped layer. The inset shows the sector where the micrograph was taken. (b) HRTEM micrograph of the deviation of the dislocation.

Fig.V.15 (b) shows at higher magnification that the deviation of the dislocations result from the strengthening. From this micrograph, L=65.2 nm, d=49.6 nm, Δl=15.4 nm and Vol = 2933.4 nm^3 are obtained. From eq.V.13, a [B] content of [B]=6.5x10^{19} cm^{-3} was determined.

V.4. Conclusions

In the present chapter, the boron content in the layers grown along different orientations have been estimated by different techniques. First CL was used to determine the [B] content. Two ranges of concentrations can be assessed by this technique, either low [B] in the range of 10^{15}-10^{18} cm^{-3}, or high [B] in the range 10^{19}-10^{21} cm^{-3}. Unfortunately, the grown samples are just at the beginning of the second range. Another limitation of this technique is the presence of dislocations which offer new recombination radiative and non radiative channels. In consequence, the exciton emission disappears and another approach is necessary. In summary, variation of the doping level respect to the growth plane orientation was demonstrated, with [B] contents in the 10^{19} cm^{-3} range for all facets.

For the dislocation-rich region where CL cannot be used, a novel method was proposed. It is based on the solid solution strengthening of the doped layers. The obtained boron-content values obtained are in the range of that obtained by CL. From this study, we obtained [B]=$4.9x10^{19}$ cm^{-3} along the {111} plane for sample #10-LMCD and [B]=$6.5x10^{19}$ cm^{-3} along the {311} of sample #4-HMCD.

Using the growth behavior versus orientation learned in the previous chapter, a fully selective growth of highly B-doped layer exclusively on the (111)-oriented facets has been demonstrated. This result has obvious important implications on further electronic device designs where photolithography steps can be avoided.

More in detail, this selective growth was demonstrated by monochromatic mapping at the BE^{TO} peak energy on sample #10-LMCD. From *Chapter III*, it is known that samples grown with low methane concentrations have a quite low growth rate. Extrapolating results from #3-LMCD to #10-LMCD, during the 8 minutes that the layers were grown, a 96 nm-thick NID layer is expected on the {111} planes, against only 8 nm along the {100}-direction. Considering now that layer grown was doped with boron, these thicknesses are expected to be much thinner [Zou 2016] but with a similar contrast.

V.5. Summaries

V.5.1. Resumen

Debido a sus numerosas aplicaciones, el uso de dopantes en diamante es un tema muy estudiado. El diamante dopado se logra mediante la introducción de átomos externos en la red cristalina del

diamante. Éstos átomos sustituyen a los átomos de carbono deformando de esta forma la red. A pesar de que los radios del boro (r_B=0.88 Å) y del carbono (r_C=0.77 Å) difieren en más de un 14%, la deformación que el dopado de boro introduce en la red cristalina a niveles de dopado de 10^{20} cm^{-3} es de tan solo el 0.006%. Esto hace que su cálculo directo sea muy difícil.

Una técnica alternativa para la obtención del dopado es el uso de catodoluminescencia. La técnica fue introducida en el Capítulo I y estima la concentración de boro en las capas a partir de las excitaciones BE^{TO} que se detectan. Esta técnica se ha empleado para la estimación del dopado de las muestras #3-LMCD, #10-Dk y #11-Disp. Se emplearon lamelas-FIB de espesores entre 0.5 µm y 1 µm que permitieron el análisis por CL de la recombinación de excitones en sección trasversal. De esta forma se pudo estimar el dopado sobre diferentes planos.

Sobre la tercera de las muestras se tomaron medidas en sección planar. La intensidad de las señales se vio perjudicada por las dislocaciones existentes en la muestra, sin embargo se pudo comprobar un dopado selectivo, detectando el pico BE^{TO} a en los planos crecidos {111}.

Todos los dopados obtenidos por CL en estas muestras fueron del orden de $1-5x10^{19}cm^{-3}$.

Como alternativa a la CL en la estimación del dopado, se han utilizad las dislocaciones. El diamante dopado con boro puede también ser visto como una aleación en la cual el boro endurece por solución sólida. Considerando esto, las capas dopadas tendrán una tensión crítica de diferirá de las no dopadas en proporción a la cantidad de boro existente en las mismas. Al haber crecido las muestras sobre sustratos escalonados (estructuras mesa), se vio en el Capítulo IV que las estructuras empujan las dislocaciones hacia fuera. Debido a la diferencia de dureza, la trayectoria de la dislocación varía en la capa no dopada y en la dopada. La diferencia

de longitud existente equivale a una energía que debe ser igual a la diferencia de tensión crítica introducida por dopado.

Considerando esta argumentación, el dopado se ha calculado en las muestras #10-Dk y #4-HMCD obteniendo valores de $4.9x10^{19} cm^{-3}$ y $6.5x10^{19} cm^{-3}$ respectivamente.

V.5.2. Résumé

L'utilisation de dopants dans le diamant est bien documentée en raison de ses nombreuses applications. Le diamant est dopé par l'introduction d'atomes qui ont une valence 5 (dopage n) ou 3 (dopage p) dans le réseau du diamant. Ces éléments remplacent des atomes de carbone déformant ainsi le réseau. Bien que les rayons covalents du bore (r_B = 0,88 Å) et du carbone (r_C = 0,77 Å) soient différents de plus de 14%, le dopage de bore a un niveau de 10^{20} cm^{-3} introduit une déformation du réseau cristallin de seulement de 0,006% qui rend la mesure directe difficile.

Une autre technique pour mesurer le dopage est l'utilisation de la cathodoluminescence. Elle a été introduite dans le Chapitre I et permet d'estimer la concentration du bore dans les couches par la détection des recombinaisons radiative des excitons liés au dopant, recombinaisons BE^{TO}. Cette technique a été utilisée pour estimer les échantillons dopés #3-LMCD, #10-LMCD et #11-Disp. Des lamelles-FIB d'épaisseur entre 0,5 µm et 1 µm ont permis une analyse CL des recombinaisons excitonique en section transversale. Les résultats ont permis de évaluer le dopage sur différentes facettes.

Un autre échantillon a été mesuré en section planaire par CL. L'intensité est réduite par des dislocations existantes dans l'échantillon, mais on a pu démontrer un dopage sélectif sur certaine face verticale. Le pic BE^{TO} n'est observable que sur les plans {111}.

En prenant compte du rapport entre les intensités FE^{TO} et BE^{TO}, les dopages obtenus sont certainement légèrement sous-évalué car une partie des recombinaisons peuvent avoir lien dans le couche non-dopée. Cependant, pour le cas présent, c'est la position du pic BE^{TO} qu'a été utilisée et donc les valeurs sont assez fiables. Les variations de dopage, suivant la direction de croissance obtenus sont assez faibles et reste dans la même décade. Toute les couches sont dans une fourchette de 1-5 x $10^{19}cm^{-3}$

Pour les couches avec de forte densité de dislocations, l'émission excitonique est assez faible et il est difficile de déterminer le dopage. Afin de surmonter cette difficulté, une nouvelle méthode basée sur le durcissement par solution solide (des dopants) a été mise en œuvre. En raison de la différence de dureté entre la couche non dopée et dopée, la dislocation a une mobilité différente et, sous la contrainte générée par la croissance latérale, elle prend une forme de demi-cercle. Le modèle permet de remonter au taux de dopage. Celui-ci, a été calculé pour les échantillons #10-LMCD et #4-HMCD. Des valeurs de 4.9x$10^{19}cm^{-3}$ et 6.5x$10^{19}cm^{-3}$ ont été obtenu.

VI Perspective for the design of future electronic devices

Contents

Based on the previous results, this chapter envisions a future Schottky diode device. The design drastically reduces the engineering steps usually required and reduces then the risk of failure during the fabrication process. Indeed, such structure has as main advantages: (i) filter of dislocations, (ii) allow an arbitrary large field region as it is a lateral structure (iii) Improve ohmic contact as the p+ layer is grown on a {111} facet. (iii) Spare photolithography steps..

VI.1. Introduction

Previous chapters are composed all oriented to the design and future fabrication of a diamond-based power device. The interrelation of those sections is evidenced in this chapter where all the aspect come together to design a new device architecture. In this line, the substrate selection, shape of the structures etched and growth conditions will be selected according to the knowledge learned in *Chapter III*. Also in the results obtained in the studies of defect generation, *Chapter IV*, and doping, *Chapter V*. This situation will be repeated for the rest of the steps considered in the fabrication of a Schottky diode (doping, contacts, …).

The use of the results previously obtained opens new path for different solutions in the design devices. Thus, the present chapter presents some alternative designs that simplify and reduce the number of steps required in their fabrication. Many lithography steps are required in usual Schottky device fabrication. This chapter introduces a new option that reduces them and, consequently, reduces cost, time and risks of failed during the processing.

Among all the different opportunities that open the previous results (for example, new MOS alternative), this chapter proposes the design for different diamond-based Schottky diode with a three-dimensional architecture from its very beginning. In order to illustrate the project, the proposition will be accompanied by experimental results obtained on sample #11-Disp.

As a first step in the device architectures, here a Schottky diode is proposed taking advantage of the selective growth, i.e. highly doped {111}-facets.

VI.2. The architecture

Most of the benefits into the use three dimensional architectures for the devices fabrications were introduced in *Chapter I*. Here, however, additional practical benefits are provided.

Fig.V.1. (a) shows the most usual pseudo-lateral Schottky punch through geometry currently used [Traoré 2015]. It has a p^{++} layer over the substrate as first layer growth (or just after a buffer layer). In 100-oriented diamond, (the only oriented substrates here considered), this layer is usually growth at high methane concentrations (4% CH_4/H_2). It has been shown to generate high density of dislocations and superficial defects (hillocks). This layer is used as ohmic contact. It means that the posteriors layer overgrowth must be etched away to fabricate those electrodes. The use of a different architecture that will not require this first doped layer will

therefore reduce an etching process (that require lift-off lithography), as well as the possible defects induced by this p^{++} layer growth.

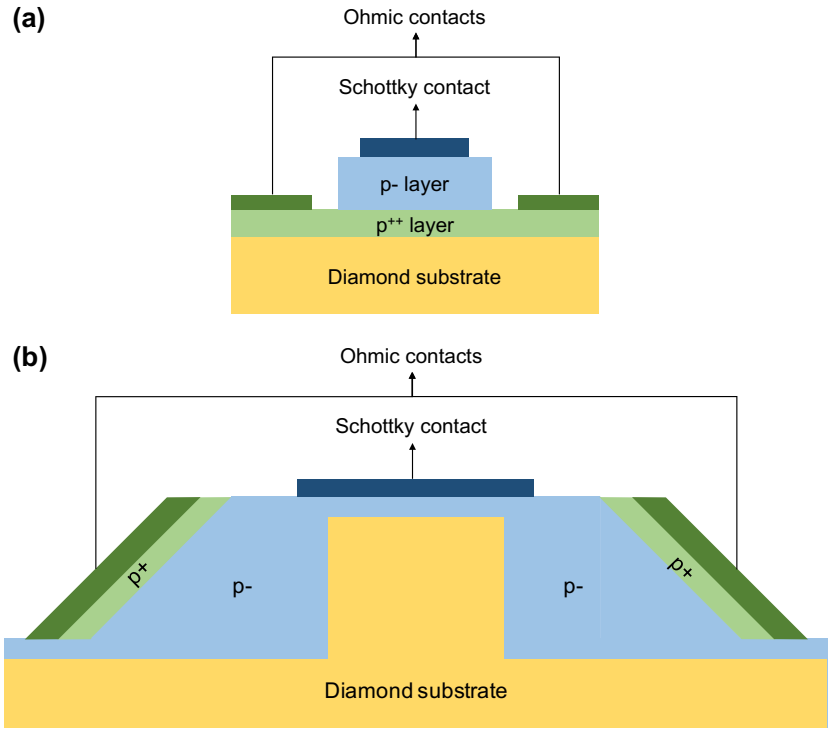

Fig.VI.1. (a) Typical pseudo-vertical Schottky diode architecture used up to now by the authors [Traoré 2015]. (b) Pseudo-vertical Schottky diode architecture proposed.

Here a lateral configuration is proposed (see Fig.VI.1 (b)). Because it is lateral, the electrical field is expected to be less uniform with some weak points but, in contrast, it will allow enhancing the field region. In the design, has been taken into account the minimization of defects (etch pits from etching process as well as dislocations from the substrate) as will be following described. In this line, {100}-oriented diamond substrate with the lower dislocations density would be selected.

VI.2.1. Substrate three-dimensional shaped

This substrate should be etched by ICP-RIE to get the desired structure. *Chapter II* has shown undesirable effects during etching by ICP-RIE as etch-pits or trenching effect. Conditions of ICP-RIE should be carefully selected to reduce them, mainly the trenching effect. The architecture will be configured to have the active region on the top and the lateral side of the etched structure. In this way, they will be covered by the mask during the etching process avoiding the generation of etch pits at those regions.

Chapters II and *III* show mesa structures facetted as squared that, in the case of low methane concentration conditions (LMC), become in cross-like structures. For the device architecture, faceted planes want to be maximized and mesa structures are then not useful. From *Chapter III* it is proved that rectangles designed correctly oriented with the substrate results in well full facetted structures. Moreover, this design can provide larger surfaces.

Fig.VI.2 schematizes the mask to use for the etching process. It is based in the repetition of rectangle with 30μm x 1000μm. Such mask will allow to fabricate contacts on the top at least high enough for electrical measurement with conventional probes. As was seen, orientation is the key in order to obtain a good faceting after overgrowth. For this reason, rectangles have their side parallel to the {110} planes.

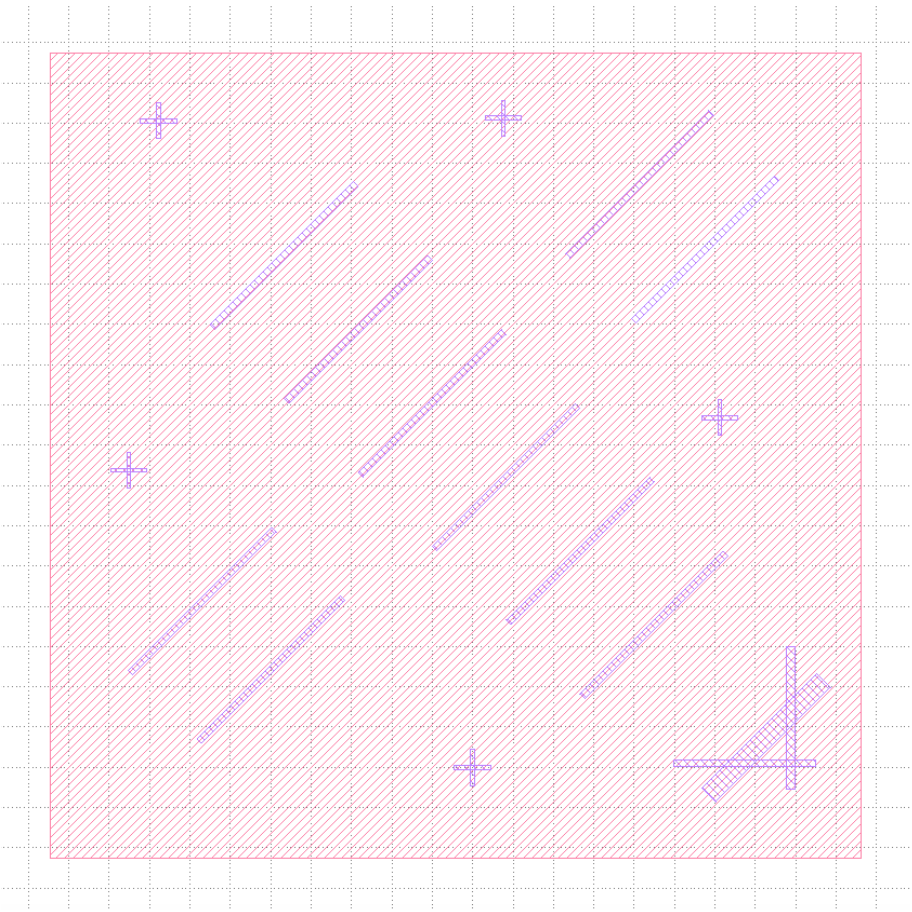

Fig.VI.2. Mask used to achieve the three-dimensional structures in the substrate. Crosses and triangle-like motif are designed to help in the match during the different lithography process required.

Height of the structures can be defined in base of *Chapter III* results. Indeed, faceting orientation and mesa size can be selected according to the height of the structures and the times of growth. Fig.VI.3 shows a schematic of the growth sectors based on the results from Chapter III. It is known that B doping is more effective, i.e. boron atoms incorporate easily the crystal sites

when growth is oriented in {111} planes [Zou 2016]. Therefore, 1.7μm depth was etched away by ICP RIE to obtain large {111}-oriented surfaces.

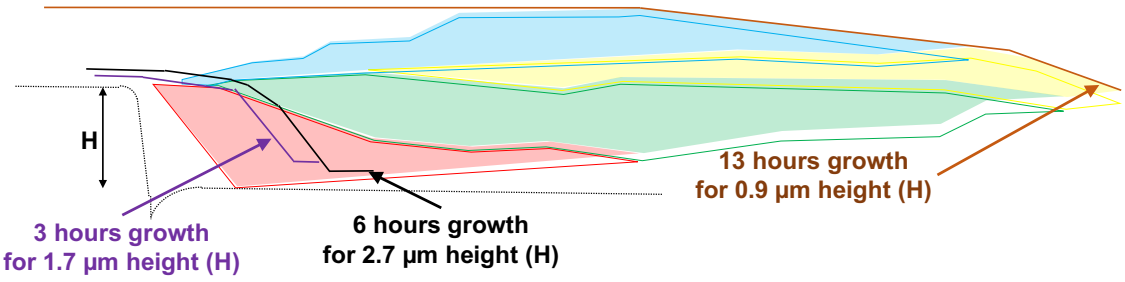

Fig.VI.3. Schematic of the growth sectors and the final shape for three different mesa heights (0.9 μm, 1.7 μm and 2.7 μm) and three different times (3, 6 and 13 hours).

VI.2.2. Growth

Low methane concentration will be obviously selected as recipe of growth. It is based in: (i) Not generation of killer defects, and (ii) maximization of the {111}-orientation. Recipe to use is the one defined for *#8-LMCU*. Under those conditions, it was shown in Chapter IV that only few planar defects are generated.

Thus, growth should be carried out at 0.1 % of CH_4/H_2, 33 Torr and temperature of about 900 ºC to reproduce the same conditions. Moreover, total flux must remain constant during the full growth process (700 sccm in our case). Not oxygen, neither diborane is used in this first growth step.

Growth duration is selected according to the height of the etched structures. *Chapter III* showed the proportionality of the region with the same orientations respect to the height. Taking into account the growth velocity (v_{111}=12nm/min) obtained in the same *Chapter III*, sample #11-Dispt was p^- growth for three hours (see Fig.VI.4 (a)).

Fig.VI.4 (b) displays the three main advantages that are associated to such growth. They correspond to:

(i) It generates a thick (thicker than 2μm) and good quality {111}-oriented lateral layer with a surface of about 3.3μm.
(ii) It generates a good-quality layer of about 200nm over the structure.
(iii) It increases the top size of the etched structure.

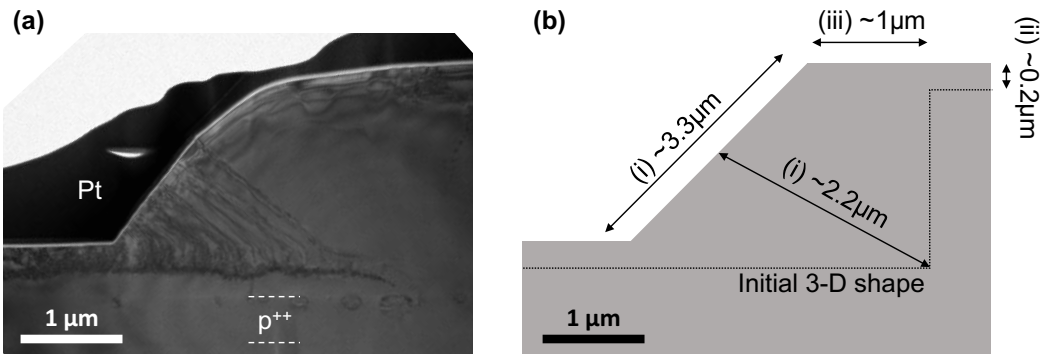

Fig.VI.4. (a) BF TEM micrograph of sample #11-Disp recorded after overgrowth. Many defects are observed due to the first doped layer (marked) and because of a bad procedure during ICP-RIE etching. (b) Schema of the expected structure obtained under the procedure described in the current chapter. Distance marked highlight the advantages enumerated on the text.

VI.4.3. Doping

As it was already introduced, the project proposed has not the initial p^{++} layer which with the one conventional diamond-based devices are fabricated. Instead to this p^{++} layer all under the device, the metal diamond for the ohmic contact will be achieved in the lateral sides of the structure. Fig.VI.5 draws the structure looked for.

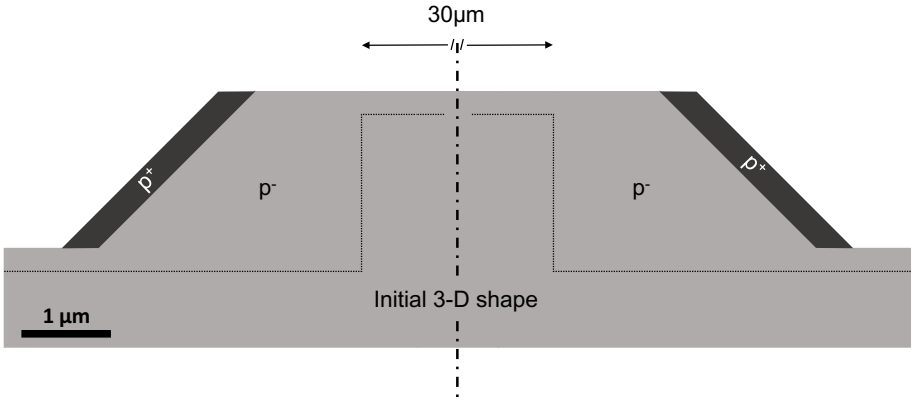

Fig.VI.5. Cross sectional view of the structure looked by the growth and etching procedures.

Chapter V shows this selective doping that is based on the different growth velocities versus surface orientation. The conditions of growth used will be the same than the used for the p^+ layer on sample #10-Disk. From Chapter V, [B] content is estimated on about 10^{20} cm^{-3}.

Duration of growth is chosen as short as possible to avoid doping on the {100}-orientations but large enough for the design of the ohmic contact. For the case here exposed, 8 minutes of growth was employed. Results exposed in *Chapter V* showed selective growth.

After this doping, a very short etching (≤10 nm) on the same reactor is suggested. It can be done by stopping the fluxes of CH_4 and H_2 and adding O_2 for a few minutes. By this etching, the undoping of the {100}-orientations guaranteed. Moreover, etching will affect less to the {111}-planes due to more compact structure. This etching has not been carried out here and a prior experimental study of it is recommended, since this kind of etching often generates etch-pits defects.

VI.3. Electrical contacts

By following the instructions exposed, arrays of three-dimensional structures are obtained. Every structure has two different regions, NID and p^+, easily identifiable by their different orientations ({100} and {111}, respectively). Over such structure contacts must be deposited.

The same lift-off lithography used during the masking for etching can be employed for the contact fabrication. This fabrication is following discussed.

VI.3.1. Ohmic contact

The band structure of an ohmic metal-semiconductor junction is shown in Fig.VI.6. For a *p*-type, semiconductor, when $\phi_m > \phi_s$, the band alignment at thermal equilibrium leads to an upward semiconductor band bending at the interface related to a hole accumulation (Fig.VI.6 (b)). If such junction is biased (V) so that holes flow from the semiconductor to the metal, they encounter no barrier. Moreover, in reverse direction, the upward band bending to holes accumulation at the interface, behaves like an anode (holes source), which will provides a copious supply of holes [Rhoderick 1978]. The resistance (R) of the semiconductor will therefore determine the electrical current (I) via the ohmic law $V = I \times R$.

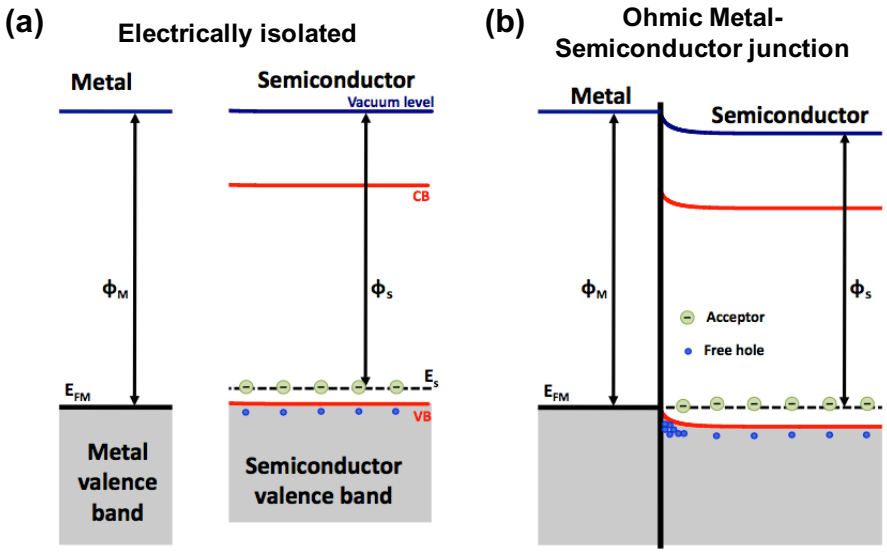

Fig.VI.6. Band structure of ohmic metal/*p*-type semiconductor junction at thermal equilibrium. (a) Isolated metal and *p*-type semiconcutor, (b) band alignment at thermal equilibrium.

Ohmic contact are fabricated on the top of the metallic diamond. It corresponds to the orientation {111}. These planes are small (in our case about 3 μm thick) and the metal deposition will not be perpendicular to them. Fig.VI.7 shows the geometry used. In green color is shown the metal deposited. To have larger area for contacting, metal can excess to the {111}-planes. In this case, is preferable to cover the top side of the structure than the bottom because of the crystal quality is expected to be better there (Fig.VI.7 (a)). Contacts are designed as rectangles that cover all the lateral sides of the structure. They are not designed as a unique contact but a repetition of rectangles. In this way, in the case of short-circuit in one of them it is possible to use another consequently increasing the probability of success (Fig.VI.7 (b)).

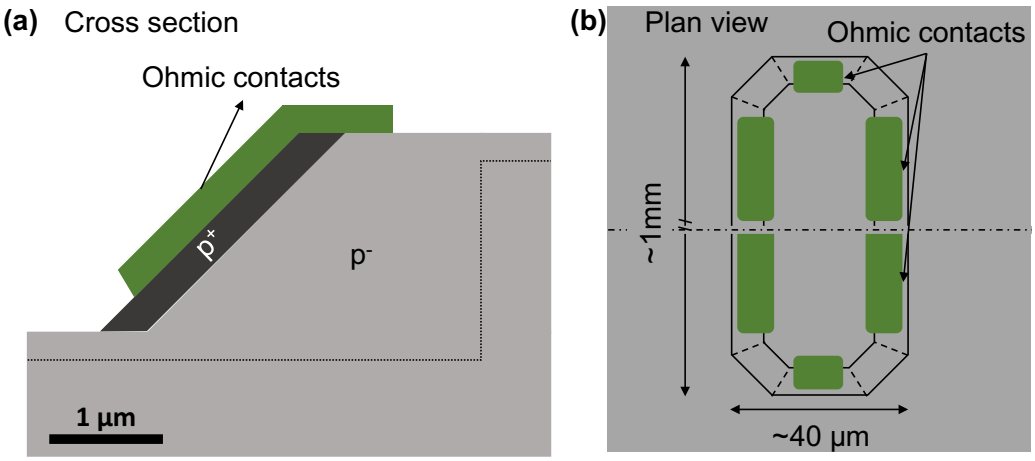

Fig.VI.7. Schema of the metal deposition (green) for the ohmic contact fabrication. (a) Cross section of half structure and (b) plan view.

Based on Traoré thesis [Traoré 2015], ohmic contacts are formed by a fist 30 nm thickness of titanium layer. It is due to its good adhesion to TiC interfacial layer formation. On this layer, 50 nm of platinum to avoid gold diffusion towards the contact and 40 nm gold are deposited that provide good thermal stability (above 600°C) and further a lower contact resistivity. Layers were annealed for 30 minutes at 500°C to ensure titanium carbide interfacial layer formation.

VI.3.2. Schottky contact

When the metal work function is lower than that of the semiconductor (see Fig.VI.8 (a)), the band alignment gives rise to a built-in potential barrier the so-called Schottky barrier ϕ_b at the interface (Fig.IV.8 (b)) and a downward semiconductor band bending.

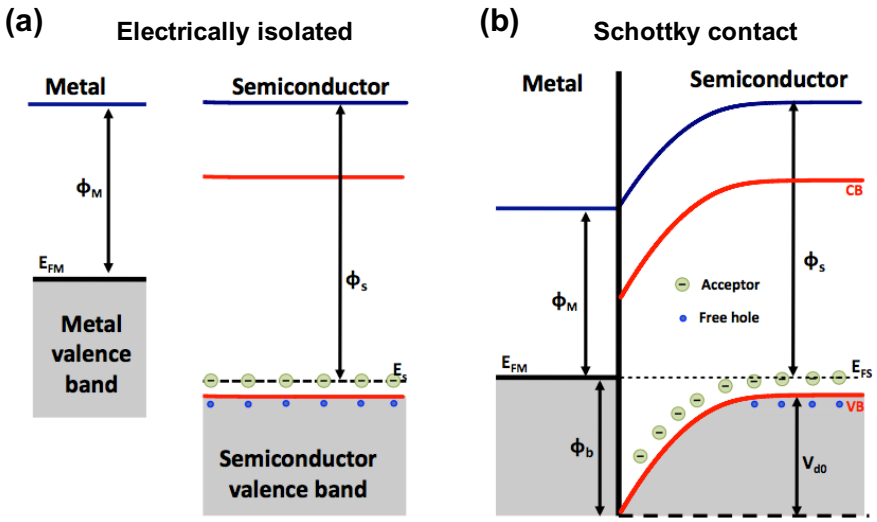

Fig.VI.8. Band structure of metal/p-type semiconductor Schottky junction at thermal equilibrium. (a) Electrically isolated and p-type semiconductor and (b) band alignment at thermal equilibrium.

As stated by the Schottky-Mott theory, the potential barrier arises because of a charge transfer from the semiconductor (higher Fermi level) to the metal. The charges transferred, here holes, leave behind uncompensated acceptor atoms and furthermore a positive charges accumulation on the surface of the metal (extra conduction carrier contained within a Thomas-Fermi screening distance ~0.1 Å [Rhoderick 1978]). At thermal equilibrium as shown Fig.VI.8 (b), the band alignment involves a downward semiconductor band bending (diffusion potential V_{d0}) related to the negatively charged acceptor atoms the depletion region and an abrupt barrier in the metal side (ϕ_b). V_{d0} is the potential barrier that encounters free carrier diffusing towards the metal whereas ϕ_b inhibits carrier injection from the metal to the semiconductor. The ideal Schottky Barrier Height (SBH) is defined by the Mott equation:

$$\phi_b = {}^{E_g}/_{q} - (\phi_m - X_s) \qquad \text{eq.VI.1}$$

Where X_s is the Electron Affinity (ES) of semiconductor and q the elementary charge. Under zeros bias and for a slightly doped semiconductor (Fermi level close to acceptor level), V_{d0} can be approximated as followed $qV_{d0} \approx q\phi_b - E_a$, where E_a is the acceptor ionization energy. Under applied bias V, this potential becomes $qV_d = qV_{d0} - qV$.

Accordingly, the barrier V_d is lower under forward bias (Fig.VI.8 (a)) thus favoring a carrier injection from the semiconductor to the metal (Jsm). Fig.VI.8 (b) shows the reverse situation where the diffusion potential increases versus reverse bias V_r. The electrical current (J_{ms}) in this latter case is induced by a carrier injection from the metal to the semiconductor.

To fabricate the Schottky contact, first diamond sample surface is oxygenated by ozone treatment [Teraji 2009, Traoré 2015]. Oxygenation for sample #11-Disp consisted in expose the diamond surface to a vacuum deep ultraviolet (VUV) light irradiation in an oxygen atmosphere. The VUV light source is a xenon Excimer lamp center at 172 nm. It was carried out at 500 mbar of pressure for two hours.

Then, Schottky electrodes were defined by laser lithography, as for the ohmic contact. The design used is displayed in Fig.VI.9. It consists in $25\mu m \times 300\ \mu m$ size rounded corner rectangles on the top of the etched structures. This design ensures the not overlapping of both contacts (ohmic and Schottky) and, as for ohmic contact, increase the probability of success by repetition.

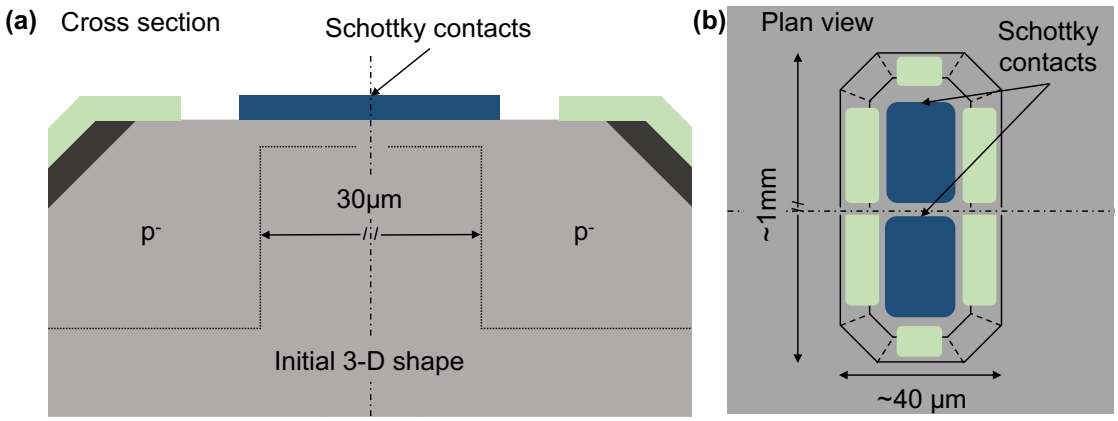

Fig.VI.9. Schema of the metal deposition (blue) for the Schottky contact fabrication. (a) Cross section and (b) plan view.

Again, results from Traoré thesis [Traoré 2014 and Traoré 2015], encourage the use of zirconium (20 nm) as first layer of the electrode fabrication. Investigation proved a good chemical reactivity with oxygen from the diamond surface, ensuring the good adhesion [Piñero 2016].

Moreover, electrical characterization exhibited an extremely good rectification behavior with a high current density about 10^3 A·cm^{-2} at 6 V, a very low reverse current density (10^{-8} A·cm^{-2}) up to maximum voltage ($|V_{max}| = 1000\,V$) and the highest Baliga's Power Figure Of Merit (BFOM), 244 MW·cm^{-2}, reported for diamond Schottky diodes [Traoré 2015].

Over the Zr layer, 30 nm of platinum and 10 nm of gold are deposited to improve the contact with the probes and reduce its resistivity.

Fig.VI.10 shows an optical microscopy micrograph of the Schottky diode designed where some of the contacts are marked to help in their identification. As *Chapter II* anticipated, surface of the sample is shown full of defects. Electrical characterization was carried out on it even though such defective surface predicts a probably ohmic character of the contact [Ohmagari 2011 and Kato 2015]. Once measured, this prediction was confirmed. Thus, results are not worthy to be showed. The dislocations (see Fig.VI.4 (a)) on the substrate acts as short-circuit and killed the device.

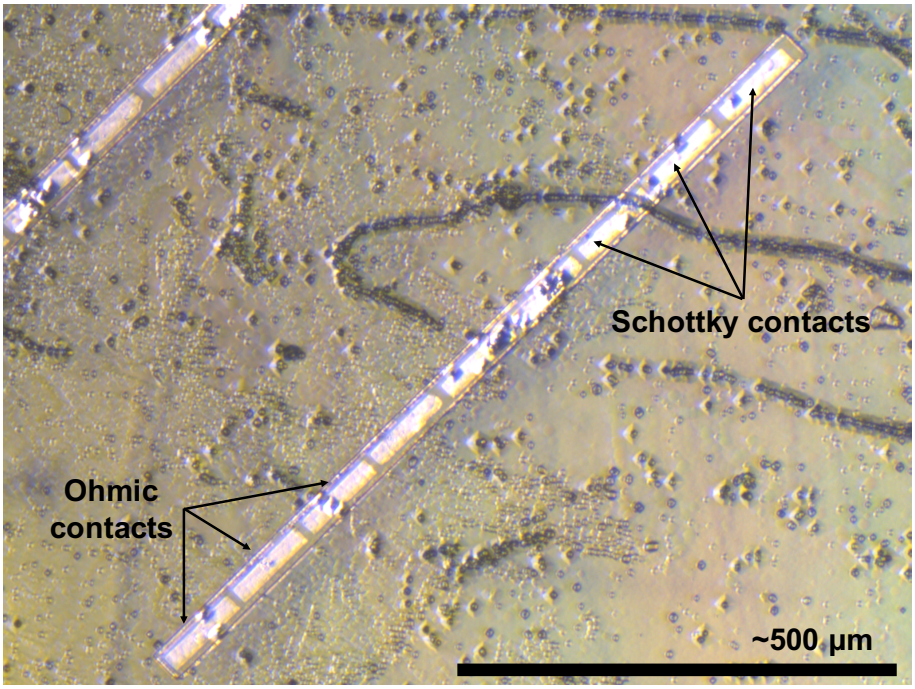

Fig.VI.10. Optical micrograph of the surface of the sample where an attempt of Schottky diode was fabricated. As *Chapter II* anticipated, surface of the sample is shown full of superficial defects. Some of the ohmic and Schottky contact have been marked by arrows to help in their identification. Scale has been estimated by the size of the contacts.

Fig.VI.11 shows (a) the usual pseudo-vertical Schottky diode and (b) the model here proposed and. In this figure is easy to understand why high density of dislocation acts at short-circuit. Dislocations coming from the substrate (red line in Fig.VI.11 marked by arrows) cross the

p^{++} layer in their climbing to the surface. The probability to have dislocations under the ohmic and Schottky electrodes is quite high. Thus, such dislocations contact the electrodes to the doped layer and, consequently, ohmic and Schottky electrodes are contacted by a metallic layer. Nevertheless, dislocations in our model should not have the same consequences since there is not p^{++}.

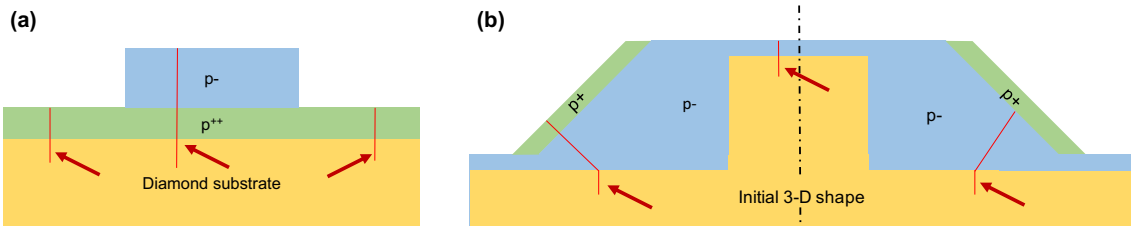

Fig.VI.11. (a) Common pseudo-vertical Schottky diode. (b) New Schottky diode here proposed. Red lines highlight possible dislocations.

VI.4. Conclusions

This last *Chapter VI* concludes the experimental work presented in the thesis with the proposition of a vertical Schottky diode whose fabrication steps are exposed in detailed. Such device avoids two critical steps due to its influence in the generation of defects: the p^{++} initial layer and the etching.

In addition, the design is proposed to minimize the likely presence of dislocations coming from the commercial substrate basing its work in good quality overgrowth layers. Moreover, because there is not a p++ layer that contact the dislocations, they will not act as short-circuit.

In summary, such structures have as advantages:

- Filter dislocations.
- Allow an arbitrary large field region as it is a lateral structure.
- Spare photolithography steps.
- Improve ohmic contact as the p+ layer is grown on a {111} facet.

This architecture can be used not just for Schottky diodes but for MOS-FET by modifying the Schottky terminal by a MOS one (by substituting Zr by Al_2O_3 layer).

VI.6. Summaries

VI.6.1. Resumen

Este capítulo aúna los resultados obtenidos en los anteriores para la optimización en el diseño y fabricación de un diodo Schottky. En dicho diseño se ha tratado no solo de mejorar sus prestaciones (como fue introducido en el Capítulo I), sino de simplificar su fabricación reduciendo sus pasos tecnológicos y haciendo así más fácil la consecución del mismo.

El diodo Schottky propuesto se basa en el crecimiento a bajo metano sobre sustratos grabados con forma tridimensional. En este caso, los sustratos deben grabarse con forma rectangular, mejor que mediante estructuras mesa, pues se ha comprobado que el facetado es similar y con estas estructuras las caras orientadas en el plano {111} son mayores. Por lo tanto, se grabará el sustrato de forma que tengamos rectángulos de unos 2.7 µm de altura, con sus caras paralelas a los planos {011} y de dimensiones 1mm x 30µm aproximadamente.

Dichos sustratos se recrecerán con condiciones iguales a las utilizadas para la muestra #8-LMCU pero por una duración de tan solo 3 horas (para esta altura se ha calculado que es el tiempo óptimo). Este crecimiento proporciona unos 200 nm de capa {100} de calidad además de unas caras de más de 3 µm en la dirección {111}.

Tras el crecimiento de la capa no dopada, se crecerá durante 8 minutos una fina capa dopada con las condiciones utilizadas para la muestra #10-Dk. Esto proporciona una capa de unos 50 nm de diamante metálico.

En el mismo reactor, utilizando el plasma únicamente con oxígeno, se debe hacer un muy corto grabado (inferior a 10 nm) que nos asegure que en la orientación{100} no tendremos capa dopada.

Una vez hemos crecido sobre nuestro sustrato grabado, realizaremos los contactos Ohmicos y Schottkys. Los primeros los diseñaremos como

rectángulos de unas 3 µm de ancho de forma que queden restringido a la capa lateral {111} de la muestra (puede sobre salir algunos nanómetros por la parte superior siempre que lo tengamos en cuenta en el diseño de los contactos Schottky). Para la fabricación de los contactors utilizaremos litografía lift-off como la empleada para las máscaras en el grabado. Los contactos consistirán en una capa de 30 nm de titanio sobre la que se depositarán 50 nm de platino y, sobre estos, 40 nm de oro. Los contactos se recocerán para lograr tener una fina capa de carburo de titanio en la intercara con el diamante.

Los diodos Schottky se fabricarán sobre la estructura grabada. Tendrán un tamaño de 25 µm x 300 µm. Antes de la deposición, se someterá al sustrato a una oxidación mediante la exposición a radiación ultravioleta en atmosfera de ozono. Para los contactos Schottky se usará zirconio (20 nm) sobre los que se deposita 30 nm de platino y 10 de oro para mejorar el contacto eléctrico y reducir la resistencia.

Este diseño, además de las mejoras esperadas de los dispositivos verticales, tendrá menos dependencia de la calidad cristalina puesto que, al no existir capa metálica bajo los contactos no hay riesgo de que las dislocaciones puedan cortocircuitarlos.

Además, dicha geometría es extrapolable a otros dispositivos. Por ejemplo, tan solo variando el Zr del contacto Schottky por Al_2O_3 podríamos fabricar un MOSFET.

VI.6.2. Résumé

Ce chapitre combine les résultats obtenus dans ce travail de thèse afin d'optimiser la conception et la fabrication d'une diode Schottky. Nous avons essayé non seulement d'améliorer leur performance (tel que présenté dans le chapitre I), mais de simplifier les étapes de fabrication et de réduire leur technologie en facilitant sa réalisation.

La diode Schottky proposée est basée sur une faible croissance du méthane sur des substrats avec une forme rectangulaire pour favoriser une croissance latérale sur des planes {111}.

Concernant les conditions de croissance, nous préconisons celle de l'échantillon #8-LMCU. Cette croissance fournirait une couche de 200 nm {100} de bonne qualité ainsi que certaines faces de plus de 3 microns d'épaisseur dans la direction {111}.

Ensuite, une croissance de la couche non dopée, pendant 8 minutes, il pousse une mince couche dopée, avec les conditions utilisées pour l'échantillon #10-LMCD. Ceci fournirait une couche d'environ 50 nm d'épaisseur à caractère métallique.

Dans le même réacteur, en utilisant uniquement un plasma d'oxygène, une gravure très courte (moins de 10 nm) est préconisée pour garanti l'absence de couche dopée sur les faces {100}.

C'est seulement après que les étapes de technologie permettront de terminer le dispositif. Par lithographie, les contacts ohmique sur les faces {111} fortement dopée et des contacts Schottky sur les {100} non-dopées. Les contacts ohmique sont constitués d'une couche de 30 nm de titane sur lequel 50 nm et de platine déposés sur ceux-ci, 40 nm d'or. Les contacts nécessitent un recuit pour obtenir une couche mince ayant le carbure de titane à l'interface avec le diamant.

Concernant les contacts Schottky, avant le dépôt du Zr, le substrat subira une oxydation par exposition à un rayonnement ultraviolet dans une atmosphère d'ozone. Les contacts de Schottky nécessitent ensuit un dépôt de zirconium (20 nm) sur lequel est déposé 30 nm de platine et 10 d'or pour améliorer le contact électrique et de réduire sa résistance.

Cette conception, en plus des améliorations attendues des dispositifs verticaux, sera moins dépendante de la qualité cristalline car, avec l'absence de couche de contacts métalliques (diamant fortement dopée) les

risques de générer des dislocations est moindre donc avec moins de risque de court-circuit.

En outre, cette géométrie est applicable à d'autres dispositifs. Par exemple, remplacer le contact Schottky de Zr par de Al_2O_3 nous obtenons un transistor MOS.

VII General conclusions

The present thesis is dedicated to the achievement of lateral growth, which can project the diamond technology towards 3D device architectures, and the main general conclusion is that the manufacturing of a 3D electronic device based on diamond is possible and feasible using lateral growth onto patterned substrates. A stratigraphic-related method allowed to stand the control of such lateral growth where growing parameters are shown govern growth direction and defect generation.

The achievement of lateral growth of diamond has involved the development, optimization, deep knowledge and control of several tools of the growing process. This lets to establish methodologies to allow the fabrication of 3D structures. All these aspects lead to some partial conclusions that will be set out below:

- First aspect was deduced from bibliography and experimentally confirmed: methane content is a key factor into the homoepitaxial MPCVD diamond growth along different orientations. These observations were confirmed by TEM, using the mentioned stratigraphic approach, which demonstrated a faster lateral oriented growth at low methane concentration.
- The latter approach is shown to be a powerful technique to study the growth mechanism. In addition to the influence of the methane concentration, the use of this method has shown that, in analogy to HPHT growth of diamond, overgrowth on patterned substrate is carried out along growth sectors that change during the process. TEM analysis has shown that the orientations of such growth sectors depend on the growth conditions but their thicknesses? are conditioned by the height of the mesa pattern. In this way, the growth sector can be reduced by reducing the height, or enlarged by making the mesa structure taller, *i.e.*, the height of the mesa structure determines the size of the growth sectors. This conclusion allows preselecting the height of the mesa structure according to the overgrowth surface orientation and size looked for. Actually, this is one of the three mesa geometry factors that play an important role on the growth process. The other two factors are the growth plane and the corners of the mesa structures. The growth plane is crucial since parameters as roughness and density of double bonding depend on it. However, its influence is strongly related to the growth conditions used, for example total flux and/or methane concentration that will define, among others, the free bonding density as well as the migration probability. On the other hand, corners are geometric limitations to the growth restricting the shape of the structure, i.e. the faceting and, consequently, the growth sectors. Both corners mark borders between vertical and horizontal surfaces that limit the growth. In this way, on

the upper corner the growth shape is defined by the slowest growth ratios whereas in the inner corner the faster ones define it.

These are the main conclusions concerning the growing process of 3D diamond structures for electronic devices. However, some other items with cross-linked character have arised and must be also remarked:

- All former conclusions were obtained thanks to the stratigraphic approach. It has been shown to be a powerful tool of traceability of the growing process, and also proves the reproducibility of the growth and that the use of thin boron doped layers does not affect to the growth orientations.
- However, those doped layers can generate extended defects as threading dislocations, and a full description of them has been provided. Indeed, it has been concluded that highly boron doped levels on thin or thick layer overgrown on patterned substrates generates TDs with Burgers vector $\mathbf{b} = {}^{1}/_{2}\langle 011\rangle$. High methane concentration growth results to furnish in a TD generation. In this case, for undoped or lightly boron doped layers overgrown on patterned substrates, TDs with $\mathbf{b} = {}^{1}/_{6}\langle 211\rangle$ are generated. Usually, highly boron doped layers overgrown at high methane concentration generates only dislocations with $\mathbf{b} = {}^{1}/_{2}\langle 011\rangle$ Burgers vector. Nevertheless, when methane concentration is very high (~4%) also the presence of dislocations with $\mathbf{b} = {}^{1}/_{6}\langle 211\rangle$ are evidenced. Lightly boron doped layers grown on patterned substrate at low methane concentration result free of TD. Moreover, TEM micrographs showed that in these cases, TD coming from the substrate are shifted due to the lateral growth. It can be used to shift the TDs far away from the mesa. This can promote their interaction to get their annihilation and obtain TDs free regions even on low substrate quality. Moreover, superficial defects, usually observed as triangular-hillocks-like, frequently appear on high methane concentration grown samples, are demonstrated to correspond to {111}-faceted crystallites generated by high density of TDs with Burgers vector $\mathbf{b} = {}^{1}/_{6}\langle 211\rangle$.
- TDs usually complicate, or even make impossible, to determine material properties as the doping level, i.e. the boron content. A new method, based on the fact that dopant induces mechanical strengthening, has been developed to determine the doping level in highly defective regions.
- Finally, selective growth, i.e. growing exclusively on lateral facets without any deposition in the vertical axis, is demonstrated to be produced using low methane concentrations. In particular, a selective highly doped lateral growth has been obtained as demonstrated by CL mapping on lateral facets.

In summary, this work has established the influence of the main geometrical and chemical parameters involved on homoepitaxial diamond growth over patterned substrates. Selective growth and, consequently, selective doping has been successfully achieved. Moreover, defects generated under different growth conditions have been identified demonstrating that lateral growth is also a useful technique to filter TDs.

These conclusions have applications in, among others, defect engineering, electronics and power electronics, structural characterization of semiconductors materials and three-dimensional diamond overgrowth.

Resumen

En resumen, este trabajo ha establecido la influencia de los principales parámetros geométricos y químicos en el crecimiento homoepitaxial de diamante sobre sustratos grabados. Se ha logrado de forma satisfactoria el crecimiento selectivo lateral y, consecuentemente, el dopado selectivo. Además, los defectos que se generan debido a las diferentes condiciones de crecimiento han sido identificados demostrando que el crecimiento lateral puede ser una técnica útil en el filtrado de dislocaciones.

Estas conclusiones tienen aplicaciones en ingeniería de defectos, electrónica y electrónica de alta potencia, caracterización estructural de semiconductores y crecimiento de diamante tridimensional, entre otras.

Résumé

En résumé, ce travail a établi l'influence des principaux paramètres géométriques et chimiques impliqués dans la croissance des diamants en homoépitaxie sur des substrats gravés. La croissance sélective et, par conséquent, le dopage sélectif a été atteint avec succès. De plus, des défauts générés dans différentes conditions de croissance ont été identifiés démontrant que la croissance latérale est également une technique utile pour filtrer les TD.

Ces conclusions ont des applications dans, entre autres, l'ingénierie des défauts, l'électronique et l'électronique de puissance, la caractérisation structurale des matériaux semi-conducteurs et la croissance tridimensionnelle des diamants.

Bibliography

Achard 2007	J. Achard, F. Silva, A. Tallaire, X. Bonnin, G. Lomvardi, K. Hassouni, and A. Gicquel, J. Phys. D, **40**, 6175 (2007).
Achard 2011	J. Achard, F. Silva, R. Issaoui, O. Brinza, A. Tallaire, H. Schneider, K. Isoird, H. Ding, S. Koné, M.A. Pinault, F. Jomard, and A. Gicquel, Diam. Relat. Mater., **20,** 145 (2011)
Alegre 2014	M.P. Alegre, D. Araujo, A. Fiori, J.C. Pinero, F. Lloret, M.P. Villar, P. Achatz, G. Chicot, E. Bustarret, and F. Jomard, Appl. Phys. Lett., **105**, 173103 (2014)
Alvarez 2006	J. Alvarez, F. Houzé, J.P. Kleider, M.Y. Liao, and Y. Koide, Superlattices and Microsctructures, **40**, 343 (2006)
Alvarez 2014	J. Alvarez, M. Boutchich, J.P. Kleider, T. Teraji, and Y. Koide, J. Phys. D: Appl. Phys., **47**, 55102 (2014)
Ando 2012	Y. Ando, T. Kamano, K. Suzuki, and A. Sawabe, Jap. J. Appl. Phys., **51**, 090101 (2012)
Araujo 2004	D. Araujo, A. Tajani, E. Gheeraert, and E. Bustarret, J. Phys. Cond. Mater., **16**, S287 (2004)
Araujo 2005	D. Araujo, M. Kadri, M. Wade, E. Bustarret, and A. Deneuville, Phys. Status solidi C, **2**, 1336 (2005)
Araujo 2010	D. Araújo, P. Achatz, R. El Bouayadi, A.J. García, M.P. Alegre, M.P. Villar, F. Jomard, and E. Bustarret, Diam. Relat. Mater., **19**, 972 (2010)
Araujo 2011-a	D. Araújo, M.P. Alegre, A.J. García, M.P. Villar, E. Bustarret, P. Achatz, P.N. Volpe, and F. Omnès, Phys, Status Solidi C, **8**, 1366 (2011)
Araujo 2011-b	D. Araújo, P. Achatz, R. El Bouayadi, A.J. García, M.P. Alegre, M.P. Villar, F. Jomard, and E. Bustarret, Diam. Relat. Mater., **19**, 972 (2010)
Araujo 2013	D. Araújo, M.P. Alegre, J.C. Piñero, A. Fiori, E. Bustarret, and F. Jomard, Appl. Phys. Lett., **103**, 042104 (2013)
Aubry 2004	O. Aubry, J.-L. Delfau, C. Met, L. Vandenbulcke, and C. Vovelle, Diam. Relat. Mater., **13**, 116 (2004).
Balasubramanian 2009	G. Balasubramanian, P. Neumann, D. Twitchen, M. Markham, R. Kolesov, N. Mizuochi, J. Isoya, J. Achard, J. Beck, J. Tissler, V. Jacques, P.R. Hemmer, F. Jelezko, and J. Wrachtrup, Nat. Mater., **8**, 383 (2009)
Baliga 1982	B.J. Baliga, J. Appl. Phys., **53**, 1759 (1982)
Baliga 1989	B.J, Baliga Elec. Dev. Lett., **10**, 455 (1989)

Banholzer 1992	W. Banholzer, Surf. Coat. Technol., **53**, 1 (1992)
Baron 2005	C. Baron, M. Wade, A. Deneuville,T, E. Bustarret, T. Kocinievski, J. Chevalier, C. Uzan-Saguy, R. Kalish, J. Butler, Diam. Relat. Mater., **14**, 350 (2005)
Baron 2006	C. Baron, M. Wade, A. Deneuville, F. Jomard, J. Chevallier, Diam. Relat. Mater., **15**, 597 (2006)
Battaile 1998	C.C. Battaile, D.J. Srolovitz, and J.E. Butler, J.Cryst. Growth, **194**, 353 (1998).
Bauer 2005	T. Bauer, M. Schreck, H. Sternschulte, and B. Stritzker, Diam. Relat. Mater., **14**, 266 (2005)
Benndorf 1994	C. Benndorf, . Joeris, and R. Kroger, Pure Appl. Chem., **66**, 1195 (1994)
Bergonzo 2001	P. Bergonzo, A Brambilla, D. Tromson, C. Mer, B. Guizard, F. Foulon, and V. Amosov, Diam. Relat. Mater., **10**, 631 (2001)
Bergonzo 2006	P. Bergonzo, D. Tromson, and C. Mer, J. Syncrotron Rad., **13**, 151 (2006)
Biasol 2002	G. Biasol, A. Gustafsson, K. Leifer, and E. Kapon, Phys. Rev. B, **65**, 205306 (2002)
Bogatskiy 2015	A. Bogatskiy, and J.E. Butler, Diam. Relat. Mater., **53**, 58 (2015)
Bou 1992	P. Bou, J.C. Boettner, and L. Vandenbulcke, Jpn. J. Appl. Phys., **31**, 1505 (1992)
Bousquet 2014	J. Bousquet, G. Chicot, D. Eon, and E. Bustarret, Appl. Phys. Lett., **104**, 021905 (2014)
Bousquet 2015	J. Bousquet, PhD Thesis, Université Grenoble, 2015
Brazhkin 2006	V. V. Brazhkin, E. A. Ekimov, A. G. Lyapin, S. V. Popova, A. V. Rakhmanina, S. M. Stishov, V. M. Lebedev, Y. Katayama, and K. Kato, Phys. Rev. B **74**, 140502(R) (2006)
Brenner 1990	D.W. Brenner, Phys. Rev. B: Condens. Matter., **42** (15), 9458 (1990)
Brunet 1998-a	F. Brunet, P. Germi, M. Pernet, Thin Solid Films, **322**, 143 (1998)
Brunet 1998-b	F. Brunet, P. Germi, M. Pernet, A. Deneuville, E. Gheeraert, F. Laugier, M. Burdin, and G. Rolland, J. Appl. Phys. **83**, 181 (1998)
Buckley 2010	B.B. Buckley, G.D. Fuchs, L.C. Basselt, and D.D. Awschalom, Science, **330**, 1212 (2010)

Bundy 1955	F.P. Bundy, H.T. Hall, H.M. Strong, and R.H. Wentorf, Nature, **176,** 51 (1955)
Bustarret 2008-a	E. Bustarret, Phys. Stat. Sol. A, **205**, 997 (2008)
Bustarret 2008-b	E. Bustarret, P. Achatz, B. Sacepe, C. Chapelier, C. Marcenat, L. Ortega, and T. Klein, Phil. Trans. R. Soc. A, **366**, 267 (2008)
Butler 1993	J.E. Butler, R.L. Woodin, Phil. Trans. R. Soc. A, **342**, 209 (1993)
Cheesman 2005	A. Cheesman, J.N. Harvey, and M.N.R. Ashfold, Phys. Chem. Chem. Phys., **7**, 1121 (2005)
Chen 2013	Y. Chen, L.B. An, and X.X. Yang, Mater. Proc.Manufacturing, **753**, 2578 (2013)
Chicot 2012	G. Chicot, T.N.T. Thi, A. Fiori, F. Jomard, E. Gheeraert, E. Bustarret, and J. Pernot, Appl. Phys. Lett., **101**, 162101 (2012)
Chicot 2014	G. Chicot, A. Fiori, P. N. Volpe, T. N. Tran Thi, J. C. Gerbedoen, J. Bousquet, M. P. Alegre, J. C. Piñero, D. Araújo, F. Jomard, A. Soltani, J. C. De Jaeger, J. Morse, J. Härtwig, N. Tranchant, C. Mer-Calfati, J. C. Arnault, J. Delahaye, T. Grenet, D. Eon, F. Omnès, J. Pernot, and E. Bustarret, J. Appl. Phys., **116**, 083702 (2014)
Childress 2006	L. Childress, M.V.Gurudev Dutt, J.M. Taylor, A.S. Zibrov, F. Jelezko, J. Wrachtrup, P.R. Hemmer, and M.D. Lukin, Science, **314**, 281 (2006)
Conte 2010	G. Conte, G. Ricciotti, P. Calvani, and E. Giovine, Electronics Letters, **24**, 46 (2010)
Danker 2009	M. Danker, S. Eick, B. Hofmann, M. Hauf, S. Ingebrandt, A. Offenhäusser, M. Stutzmann, and J.A. Garrido, Adv. Funct. Mater., **19**, 2915 (2009)
Deák 2007	P. Deák, A. Kováts, P. Csíkváry, I. Maros, G and. Hárs, Appl. Phys. Lett,. **90**, 051503 (2007)
Dean 1965	P.J. Dean, E.C. Lightlowlers, D.R .Wight, Phys. Rev. A, 140, 352 (1965)
Delclos 1999	S. Delclos, D. Dorignac, F. Phillipp, S. Moulin, and A. M. Bonnot, Diam. Relat. Mater., **8**, 682 (1999)
Ehrlich 1966	G. Ehrlich and F.H. Hudda. J. Chem. Phys., **44**, 1039 (1966)
Ekimov 2004	E.A. Ekimov, V.A. Sidrov, E.D. Bauer, N.N. Mel'nki, N.J. Curro, J.D. Thompson, and S.M. Stishov, Nature, **428**, 542 (2004).
El-Hajj 2008	H. El-Hajj, A. Denisenko, A. Kaiser, R.S. Balmer, and E. Kohn, Diam. Relat. Mater., **17**, 1259 (2008)

Erasmus 2011	R.M. Erasmus, R.D. Daniel, and J.D. Comins, J. Appl. Phys., **109**, 013527 (2011)
Fernandez-Lorenzo 2012	C. Fernández-Lorenzo, D. Araújo, M. González-Mañas, J. Martín, J. Navas, R. Alcántara, M.P. Villar, D. Bagriantsev, J. Cryst. Growth, **353**, 115 (2012)
Fillon 2012	R. Fillon, Rapport de stage, Grenoble INP PHELMA, 2012
Fiori 2012	A. Fiori, PhD Thesis, Université Grenoble, 2012
Fiori 2014	A. Fiori, F. Jomard, T. Teraji, G. Chicot and E. Bustarret, Thin Solid Film, **557**, 222 (014)
Frauenheim 1993	Th. Frauenheim, U. Stephan, P. Blaudeck, and D. Porezag, Phys. Rev. B, **48 (**24), 18189 (1993)
Frenklach 1997	M. Frenklach, and S. Skokov, J. Phys. Chem. B, **101**, 3025, 1997
Friel 2009	I. Friel, S.L. Clewes, H.K. Dhillon, N. Perkins, D.J. Twitchen, and G.A. Scarsbrook, Diam. Relat. Mater., **18**, 808, (2009).
Fujii 2007	T. Fujii, and M. Kareev, J. Appl. Phys., **89**, 2543 (2001)
Gaowei 2012	M. Gaowei, E. M. Muller, A. K. Rumaiz, C. Weiland, E. Cockayne, J. Jordan-Sweet, J. Smedley, and J. Woicik, Appl. Phys. Lett., **100,** 201606, (2012)
Ghodbane 2010	S. Ghodbane, F. Omnès, C. Agnès, Diam. Relat. Mater., **19**, 273 (2010)
Giannuzzi 1999	L.A. Giaunnuzzi, B.I. Prenitzer, J.L. Drown-MacDonald, S.R. Brown, R.B. Irwin, F.A. Stevie, and T.L. Shofner, Analysis of in service failures and advances in microstructural characterization, **26**, 249 (1999)
Gicquel 1994	A. Gicquel, K. Hassouni, S. Farhat, Y. Breton, C.d. Scott, M. Lefebvre, and M. Pealat, Diam. Relat. Mater., **3**, 581 (1994)
Gicquel 2001	A. Gicquel, K. Hassouni, F. Silva and J. Achard, **1,**479, (2001)
Gicquel 2012	A. Gicquel, N. Derkaoui, C. Rond, F. Benedic, G. Cicala, D. Moneger, and K. Hassouni, Chem. Phys., 398, 239 (2012)
Goldstein 1981	Goldstein, G. I.; Newbury, D. E.; Echlin, P.; Joy, D. C.; Fiori, C.; Lifshin, E. (1981). Scanning electron microscopy and x-ray microanalysis. New York: Plenum Press. ISBN 0-306-40768-X
Gurudev 2007	M.V. Gurudev Dutt, L. Childress, L. Jiang, E. Togan, J. Maze, F. Jelezko, A.S. Zibrov, P.R. Hemmer, and M.D. Lukin, Science, **316**, 1312 (2007)
Gutierrez 2006	M. Gutirrez, M. Herrera, D. Gonzalez, R. Garcia, and M. Hopkinson, Appl. Phys. Lett., **88**, 193118 (2006)

Habka 2010	N. Habka, J. Barjon, F. Jomard, and J. Chevallier, Phys. Rev. B, **81**, 045207 (2010)
Harris 1990	S.J. Harris and D.G Goodwin, J. Phys. Chem. **97**, 23 (1993)
Hassouni 2010	K. Hassouni, F. Silva, and A. Gicquel, J. Phys. D, **43**, 153001 (2010)
Head 1973	A.K. Head, P. Humble, L.M. Clarebrough, A.J. Morton, and T.C. Forwood, Computer Electron Micrographs and Defects Identification (North-Holland Publiching Company, Amsterdam, 1973)
Hei 2016	L.F. Hei, Y. Zhao, J.J. Wei, J.L. Liu, C.M. Li, W.Z. Tang, and F.X. Lu, Diam. Relat. Mater., **69**, 33 (2016)
Hirama 2010	K. Hirama, K. Tsuge, S. Sato, T. Tsuno, Y. Jingu, S. Yamauchi, and H. Kawarada, Appl. Phys. Lett., **3**, 044001 (2010)
Hirth 1965	Hirth and Lothe, Theory of Dislocations, Krieger Publishing Company, 1982
Hoshino 2012	Y. Hoshino, H. Kato, T. Makino, M. Ogura, T. Iwasaki, M. Hatano, and S. Yamasaki, Phys. Status Solidi A, **209** (9), 1761 (2012)
Ikeda 2009	K. Ikeda, H. Umezawa, N. Tatsumi, K. Ramanujam, S-I. Shikata, Diam. Relat. Mater., **18**, 292 (2009)
Issaoui 2011	R. Issaoui, J. Achard, F. Silva, A. Tallaire, V. Mille, and A. Gicquel, Phys. Status Solidi A, **9**, 2023 (2011)
Iwasaki 2012	T. Iwasaki, Y. Hoshino, K. Tsuzuki, H. Kato, T. Makino, M. Ogura, D. Takeuchi, T. Matsumoto, H. Okushi, S. Yamasaki, and M. Hatano, Appl. Phys. Express, **5**, 091301 (2012).
Jelezko 2004	F. Jelezko, T. Gaebel, I. Popa, M. Domhan, A. Gruber, and J. Wrachtrup, Phys. Rev. Lett., **93**, 130501 (2004)
Jiang 2015	D. Jiang, W. Mu, S. Chen, Y. Fu, K. Jeppson, and J. Liu, IEEE Trans. Electron Dev., **36**, 499 (2015)
Jin 2012	H-H. Jin, H-D. Cho, S-C. Kwon, C. Shin, and J. Kwon, Mater. Lett., **89**, 133 (2012)
Johnston 1991	C. Johnston, C.G: Ayres, P.R. Chalker, J. Phys. IV, **1**, 915 (1991)
Kajihara 1993	S.A. Kajihara, A. Antonelli, and J. Bernholc, Phys. B Cond. Mater., **185**, 144 (1993)
Kamo 1983	M. Kamo, Y. Sato, S. Matsumoto, and N. Setaka, J. Cryst. Growth, **62**, 642 (1983)

Kasu 2004	M. Kasu, M. Kubovic, A. Aleksov, N. Teofilov, Y. Taniyasu, R. Sauer, E. Kohn, T. Makimoto, N. Kobayashi, Diamond Relat. Mater., **13**, 226 (2004)
Katagiri 2004	M. Katagiri, J. Isoya, S. Koizumi, and H. Kanda, Appl. Phys. Lett., **85**, 6365, (2004)
Kato 2005	H. Kato, S. Yamasaki, and H. Okushi, Diam. Relat. Mater., **14**, 2007 (2005)
Kato 2009	H. Kato, D. Takeuchi, N. Tokuda, H. Umezawa, H. Okushi, and S. Yamasaki, Diam. Relat. Mater., **18**, 782 (2009).
Kato 2012	H. Kato, T. Makino, M. Ogura, D. Takeuchi, and S. Yamasaki, Diam. Relat. Mater., 19. **27,** 2012
Kato 2015	Y. Kato, H. Umezawa, and S-I. Shikata, Diam. Relat. Mater., **57**, 22 (2015)
Kawano 2010	A. Kawano, H. Ishiwata, S. Iriyama, R. Okada, T. Yamaguchi, Y. Takano, and H. Kawarada, Phys. Rev. B **82**, 085318 (2010)
Kawarada 1993	H. Kawarada, H. Matsuyama, Y. Yokota, T. Sogi, A. Yamaguchi, A. Hiraki, Phys. Rev. B, **47**, 3633 (1993)
Kiran 2012	R. Kiran, L. Rousseau, G. Lissorgues, E. Scorsone, A. Bongrain, B. Yvert, S. Picaud, P. Mailley, and P. Bergonzo, Sensors, **12**, 7669 (2012)
Kitagoh 2010	S. Kitagoh, R. Okada, A. Kawano, M. Watanabe, Y. Takano, T. Yamaguchi, T. Chikyow, and H. Kawarada, Phys. C, **470**, S610 (2010)
klayout	www.klayout.de
Klippenstein 2006	S.J. Klippenstein, Y. Georgievskii, and L.B. Harding, Phys. Chem. Chem. Phys., **8**, 1133 (2006)
Kobachi 1988	K. Kobashi, K. Nishimura, Y. Kawate, and T. Horiuchi, Phys. Rev. B, **38**, 4067 (1988)
Koizumi 1997	S. Koizumi, M. Kamo, Y. Sato, H. Ozaki, and T. Inuzuka, Appl. Phys. Lett., **71**, 1065 (1997)
Koné 2010	S. Kone, G. Civrac, H. Schneider, K. Isoird, R. Issaoui, J. Achard, and A. Guicquel, Diam. Relat. Mater., **19**, 792 (2010)
Kreutz 1995	T. J. Kreutz, R. E. Clausing, L. Heatherly, Jr., R. J. Warmack, T. Thundat, C. S. Feigerle, and K. Wandelt: Phys. Rev. B, **51**, 14554 (1995).
Kumaresan 2010	R. Kumaresan, H. Umezawa, and S. Shikata, Diam. Relat. Mater., **19**, 1324 (2010)
Lagrange 1998	J.P. Lagrange, A. Deneuville, and E. Gheeraert, Diam. Relat. Mater., **7**, 1390 (1998)
Lai 2016	L. Lai, and A. S. Barnard, Nanoscale, **8**, 7899 (2016).

Landstrass 1993	M.I. Landstrass, M. A. Plano, M.A. Moreno, S.McWilliams, L..S. Pan, D.R. Kania, and S. Han, Diam. Relat. Mater., **2**, 1033 (1993)
Larson 1999	J.M. Larson, M.T. Swihart, and S.L. Girshick, Diam. Relat. Mater., **8**, 1863 (1999)
Lee 1999	S.-T. Lee, Z. Lin, X. and Jiang, Mater. Sci. Eng., R, **25**, 123 (1999).
Lee 2011	K.C. Lee, M.R. Sprague, B.J. Sussman, J. Nunn, N.K. Langford, X-M. Jin, T. Champion, P. Michelberger, K.F. Reim, D. England, D. Jaksch, and I.A. Walmsley, Science, **334**, 1253 (2011)
Lesik 2016	M. Lesik, T. Plays, A. Tallaire, J. Achard, O. Brinza, L. Williams, M. Chipaux, L. Toraille, T. Debuisschert, A. Gicquel, J.F. Roch, and V. Jacques, Diam. Relat. Mater., **56**, 47 (2015).
Liang 2014	Q. Liang, C-S. Yan, J. Lai, Y-F. Meng, S. Krasnicki, H. Shu, H-K. Mao, and R. Hemley, Cryst. Growth Des., **14**, 3234 (2014)
Lin 2011	J-Y. Lin, W-K. Lin, J-Y. Gan, J-C. Hwang, and C-S. Kou, Nanotechnology, **22**, 205707 (2011)
Liu 1995	H. Liu and D. Dandy, Diam. Relat. Mater., **4**, 1173 (1995)
Lodes 2015	M.A. Lodes, F.S. Kachold, and S.M. Rosiwal, Phil. Trans. R. Soc. A, **373**, 20140136 (2015)
Long 2008	R. Long, Y. Dai, M. Guo, L. Yu, B. Huang, R. Zhang, and W. Zhang, Diam. Relat. Mater., **17**, 234 (2008)
Lu 2012	Y.-G. Lu, S. Turner, J. Verbeeck, S.D. Janssens, P. Wagner, K. Haenen, G. van Tendeloo, Appl. Phys. Lett., **101**, 041907 (2012).
Ma 2008	J. Ma, J.C. Richley, M.N.R. Ashfold, and Y.A. Mankelevich, J. Appl. Phys., **104**, 103305 (2008).
Ma 2009	J. Ma, M.N.R. Ashfold, and Y.A. Mankelevich, J. Appl. Phys., **105**, 043302 (2009)
Maida 2008	O. Maida, H. Miyatake, T. Teraji, and T. Ito, Diam. Relat. Mater., **17**, 435, (2008)
Makino 2005	T. Makino, H. Kato, M. Ogura, H. Watanabe, S.G. Ri, S. Yamasaki, and H. Okushi, Jap. J. Appl. Phys. Lett. **44**, L1190 (2005)
Makino 2009	T. Makino, S. Tanimoto, Y. Hayashi, H. Kato, N. Tokuda, M. Ogura, D. Takeuchi, K. Oyama, H. Ohashi, H. Okushi, and S. Yamasaki, Appl. Phys. Lett., **94**, 262101 (2009)
Makino 2014	T. Makino, K. Oyama, H. Kato, D. Takeuchi, M. Ogura, H. Okushi, and S. Yamasaki, Jap. J. Appl. Phys., **53**, 05FA12 (2014)

Martineau 2009	P. Martineau, M. Gaukroger, R. Khan, and D. Evans, Phys. Status Solidi C, **6**, 1953 (2009)
Matsumoto 1982-a	S. Matsumoto, Y. Sato, M. Tsutsumi, and N. Setaka, J. Mater. Sci., **17**, 3106 (1982)
Matsumoto 1982-b	S. Matsumoto, Y. Sato, M. Kamo and N. Setaka, Jap. J. Appl. Phys. Let., **21**, L183 (1982)
Matthews 1974	J.W. Matthews, and A.E. Blakeslee, J. Cryst. Growth, **27**, 118 (1974)
May 2010-a	P.W. May, J.N. Harvey, N.L. Allan, J. C. Richley, and Yu. A. Mankelevich, J. Appl. Phys., **108**, 014905 (2010)
May 2010-b	P.W. May, J.N. Harvey, N.L. Allan, J. C. Richley, and Yu. A. Mankelevich, J. Appl. Phys., **108**, 014909 (2010)
McMaster 1995	M.C. McMaster, W.L. Hsu, M.E. Coltrin, D.S. Dandy, C. And Fox, Diam. Relat. Mater., **4**, 1000, (1995)
McSkimin 1972	H. J. McSkimin and P. Andreatch, J. Appl. Phys. **43**, 2944 (1972)
Miyatake 2007	H.Miyatake, K. Arima, O. Maida, T. Teraji, and T. Ito, Diam. Relat. Mater., **16**, 679 (2007)
Mochalin 2012	V.N. Mochalin, O. Shenderova, D. Ho and Y. Gogotsi, Nature Nanotechnology, **7**, 11 (2012)
Morse 2010	J. Morse, B. Solar, and H. Graafsma, J. Synchrotron Radiat., **17**, 456 (2010)
Muret 2011	P. Muret, P.N. Volpe, T.N. Tran-Thi, J. Pernot, C. Hoarau, F. Omnès, and T. Teraji, Diam. Relat. Mater., **20**, 285, (2011).
Muret 2015	P. Muret, A. Traoré, A. Maréchal, D. Eon, J. Pernot, J. C. Pinẽro, M. P. Villar, and D. Araujo, J. Appl. Phys., **118**, 204505 (2015)
Netto 2005	A. Netto, and M. Frenklach, Diam. Relat. Mater., **14**, 1630 (2005)
Neumann 2008	P. Neumann, N. Mizuochi, F. Rempp, P. Hemmer, H. Watanabe, S. Yamasaki, V. Jacques, T. Gaebel, F. Jelezko, and J. Wrachtrup, Science, **320**, 1326 (2008)
Ohmagari 2011	S. Ohmagari, T. Tejari, and U. Koide, J. Appl. Phys., **110**, 056105, (2011).
Omnès 2011	Franck Omnès, Pierre Muret, Pierre-Nicolas Volpe, Mamadou Wade, Julien Pernot, and François Jomard, Diam. Relat. Mater., **20**, 912 (2011)
Ozpineci 2011	B. Ozpineci, and L. Tolbert, IEEE Spectrum, 2011

Pernot 2008	J. Pernot and S. Koizumi, Appl. Phys. Lett. **93**, 052105 (2008)
Pernot 2010	J. Pernot, P.N. Volpe, F. Omnès and P. Muret, Phys. Rev. B, **81**, 205203 (2010)
Pimpinelli 1998	A. Pimpinelli and J. Villain, Physics of Crystal Growth (cambridge University Press, Cambridge, UK, 1998).
Powell 1966	C.F. Powell, Chemical Vapor deposition (Vapor Depostion, C.F. Powell, J. H. Oxley and J. M. Blocher, Jr., eds., John Willey & Sons, New York, 1966).
Prings 1988	F. Prings, Phys. Rev. B, **38**, 5576 (1988)
Prokhorov 2013	I.A. Prokhorov, V.G. Ralchenko, A.P. Bolshakov, A.V. Polskiy, A.V. Vlasov, I.A. Subbotin, K.M. Podurets, E.M. Pashaev, and E.A. Sozontov, Chystal. Rep. **58**, 1010 (2013)
Ratnikova 2011	A.K. Ratnikova, M.P. Dukhnovsky, Y.Y. Fedorov, V.E. Zemlyakov, A.B. Muchnikov, A.L. Vikharev, A.M. Gorbachev, D.B. Radishev, A.A. Altukhov, and A.V. Mitenkin, Diam. Relat. Mater., **20**, 1243 (2011).
Rawles 1997	R.E. Rawles, S.F. Komarov, R. Gat, W.G. Morris, J.B. Hudson, and M.P. D'Evelyn, Diam. Relat. Mater., **6**, 791 (1997)
Rhoderick 1978	E. H. Rhoderick, Metal Semiconductor contacts. Oxford University Press, 1978
Richley 2012	J.C.Richley, J.N. Harvey, M.N.R. Ashfold, J. Phys. Chem. C, **116**, 18300, (2012)
Sato 2014	K. Sato, T. Iwasaki, Y. Hoshino, H. Kato, T. Makino, M. Ogura, S. Yamasaki, S. Nakamura, J. Ichikawa, A. Sawabe, and M. Hatano, Jap. J. Appl. Phys., **53**, 05FP01 (2014).
Sauer 2003	R. Sauer, in: C.E. Nebel, J. Ristein (Eds.), Thin-Film Diamond. I. Semiconductor and Semimetal, vol. **76**, Elsevier, 2003
Sawada 2001	H. Sawada, H. Ichinose, H. Watanabe, D. Takeuchi, and H. Okushi, Diam. Relat. Mater., **10**, 2030 (2001).
Schaffer 2012	M. Schaffer, B. Schaffer, and Q. Ramasse, Ultramicroscopy, **114**, 62 (2012)
Scheel 2010	H. J. Scheel, P. Capper, and P. Rudolph, in Crystal Growth Technology: Semiconductors and dielectrics, edited by. H. J. Scheel and P. Capper (Wiley-VCH, Weinheim, 2010), p. 141.
Scheffler 1987	M. Scheffler, Physica B, **B146**, 176 (1987)
Schwander 2011	M. Schwander, and K. Partes, Diam. Relat. Mater., **20**, 1287 (2011)

Schwen 2012	D. Schwen, E. Bringa, J. Krauser, A. Weidinger, C. Trautmann, and H. Hofsass, Appl. Phys. Lett., **101**, 113115 (2012).
Siegert 2015	K.S. Siegert, F.R.L. Lange, E.R. Sittner, H. Volker, C.E. Scholockermann, T. Siegrist, and M. Wuttig, Rep. Prog. Phys., **478**, 013001 (2015)
Silva 2006	F. Silva, J. Achard, X. Bonnin, A. Michau, A. Tallaire, O. Brinza, and A. Gicquel, Phys. Statatus Solidi A, **203** (12), 3049 (2006)
Silva 2008	F. Silva, X. Bonnin, J. Achard, O. Brinza, A. Michau, and A. Gicquel, J. Cryst. Growth, **310**, 187 (2008)
Silva 2009	F. Silva, J. Achard, O. Brinza, X. Bonnin, K. Hassouni, A. Anthonis, K.D. Corte, and J. Barjon, Diam. Relat. Mater., **18**, 683(2009)
Spear 1994	K.E. Spear and J. P. Dismukes, Synthetic Diamond: Emerging CVD Science and Technology, Wiley, 1994
Steeds 1998	J.W. Steeds, A. Gilmore, J.A. Wilson, and J.E. Butler, Diam. Relat. Mater., **7**, 1437 (1998)
Sutcu 1992	L.F. Sutcu, C.J. Chu, M.S. Thompson, R.H. Hauge, J.L. Margrave, and M.P. D'Evelyn, J. Appl. Phys., **71**, 5930 (1992)
Suzuki 2013	M. Suzuki, T. Sakai, T. Makino, H. Kato, D. Takeuchi, M. Ogura, H. Okushi, and S. Yamasaki, Phys. Stat. Solidi A, **210**, 2035, (2013)
Takami 1999	T. Takami, K. Suzuki, I. Kusunoki, I. Sakaguchi, M.N. Gamo, and T. Ando, Surf. Sci., **440**, 103 (1999).
Takeuchi 2000	D. Takeuchi, H. Watanabe, S. Yamanaka, H. Okushi, and K. Kajimura, Diam. Relat. Mater., **9**, 231 (2000)
Takeuchi 2014	D. Takeuchi, T. Makino, H. Kato, M. Ogura, N. Tokuda, T. Matsumoto, D. Kuwabara, H. Okushi, and S. Yamasaki, Physica status Solidi A, **211**, 2251 (2014)
Tallaire 2008	A. Tallaire, M. Kasu, K. Ueda, and T. Makimoto, Diam. Relat. Mater., **17**, 60, (2008).
Tallaire 2013	A. Tallaire, J. Achard, O. Brinza, V. Mille, M. Naamoun, F. Silva, and A. Gicquel, Diam. Relat. Mater., **33**, 71 (2013)
Tallaire 2016	A. Tallaire, T. Ouisse, A. Lantreibecq, R. Cours, M. Legros, H. Bensalah, J. Barjon, V. Mille, O. Brinza, and J. Achard, Cryst. Growth Des., **16**, 2741 (2016)
Tallaire 2017	A. Tallaire, O. Brinza, V. Mille, L. William, and J. Achard, Adv. Mater., 1604823 (2017)
Tamor 1994	M.A. Tamor and M. P. Emerson, J. Mater. Res., **9**, 1839 (1994)

Teraji 2003	T. Teraji, S. Mitani, and T. Ito, Phys. Stat. Sol. A, **198**, 395 (2003
Teraji 2004	T. Teraji and T, Ito, J. Cryst. Growth, **271**, 409 (2004).
Teraji 2012	T. Teraji, M.Y. Liao, and Y. Koide, J. Appl. Phys., **111**, 104503 (2012)
Thion 2011	F. Thion, K. Isoird, D. Planson, M.L. Locatelli, and H. Ding, Diam. Relat. Mater., **20**, 729 (2011)
Thonke 2003	K. Thonke, Semiconductor Science and Technology, **18**, S20 (2003)
Tian 2007	R-H. Tian and J-F. Zhi, Electrochem. Commun., **9**, 1120 (2007)
Tokuda 2007-a	N. Tokuda, H. Umezawa, T. Saito, K. Yamabe, H. Okushi, and S. Yamasaki, Diam. Relat. Mater., **16**, 767 (2007)
Tokuda 2007-b	N. Tokuda, H. Umezawa, K. Yamabe, H. Okushi, and S. Yamasaki, Jpn. J. Appl. Phys. **46**, 1469 (2007).
Tokuda 2008	N. Tokuda, H. Umezawa, S-G. Ri, M. Ogura, K. Yamabe, H. Okushi, and S Yamasaki, Diam. Relat. Mater., **17**, 1051 (2008)
Tokuda 2009	N. Tokuda, H. Umezawa, H. Kato, M. Ogura, S. Gonda, K. Yamabe, H. Okushi, and S. Yamasaki, Appl. Phys. Express, **2**, 055001 (2009)
Tokuda 2010	N. Tokuda, H. Umezawa, K. Yamabe, H. Okushi, and S. Yamasaki, Diam. Relat. Mater., **19**, 288 (2010)
Tokuda 2012	N. Tokuda, T. Makino, T. Inokuma, and S. Yamasaki, Jap. J. Appl. Phys. Lett., **51**, 090107 (2012)
Tokuda 2016	N. Tokuda, M. Ogura, T. Matsumoto, S. Yamasaki, and T. Inokuma, Phys. Stat. Solidi A, **213**, 2051 (2016)
Tolbert 2005	L.M. Tolbert, T.K. King, B. Ozpineci, G. Muralidharan, D. T. Rizy, A.S. Sabau, H. Zhang, W. Zhang, X. Yu, H.F. Huq, H. Liu, Oak ridge national laboratory ut-batterelle us departement of energy, 2005
Traoré 2014	A.Traore, P. Muret, A. Fiori, D. Eon, E. Gheeraert, and J. Pernot, Appl. Phys. Lett. **104**, 052105 (2014)
Traoré 2015	A. Traoré, PhD Thesis, Université Grenoble, 2014
Tsubouchi 2008	N. Tsubouchi, and M. Ogura, Jpn. J. Appl. Phys. **47**, 7047 (2008).
Tsuno 1994	T. Tsuno, T. Tomikawa, S. Shikata, and N. Fujimori, J. Appl. Phys., **75**, 1526 (1994)
Tsuno 1996	T. Tsuno, H. Shiomi, Y. Kumazawa, S. Shikata, and S. Akai, Jap. J. Appl. Phys. Lett., **35**, 4724 (1996)

Ueda 2006	K. Ueda, M. Kasu, Y. Yamauchi, T, Makimoto, M. Schwitters, D.J. Twitchen, G.A. Scarsbrook and S.E. Coe, IEEE Electron Dev. Let., **27**, 570 (2006)
Ueda 2007	K. Ueda, M. Kasu, and T. Makimoto, Appl. Phys. Lett., **90**, 122102 (2007)
Umezawa 2007	H. Umezawa, T. Saito, N. Tokuda, M. Ogura, S-G. Ri, H. Yoshikawa, and S. Shikata, Appl. Phys. Lett., **90**, 073506 (2007)
Umezawa 2009	H. Umezawa, K. Ikeda, N. Tatsumi, K. Ramanujam, S-I. Shikata, Diam. Relat. Mater., **18**, 1196 (2009)
Umezawa 2012	H. Umezawa, M. Nagase, Y. Kato, andS. Shikata, Diam. Relat. Mater., **24**, 201 (2012)
Umezawa 2013	H. Umezawa, and Y. Kato, Appl- Phys. Express, **6**, 3 (2013)
Umezawa 2014	H. Umezawa, S-I. Shikata, and T. Funaki, Jap. J. Appl. Phys., **53**, 05FP06 (2014)
Uzan-Saguy 1998	C. Uzan-Saguy, R. Kalish, R. Walker, D.N. Jamieson, and S. Prawer, Diam. Relat. Mater., **7**, 1429 (1998)
Vegard 1921	L. Vegard, Z. Phys., **5,** 17 (1921).
Vescan 1994	L. Vescan, Mater. Sci. Eng. B, **28**, 1, (1994)
Volpe 2010	P-N. Volpe, P. Muret, J. Pernot, F. Omnès, T. Teraji, Y. Koide, F. Jomard, D. Planson, P. Brosselard, N. Dheilly, B. Vergne, and S. Scharnholz, Appl. Phys. Lett., **97,** 223501 (2010)
Watanabe 1999	H. Watanabe, D. Takeuchi, S. Yamanaka, H. Okushi, K. Kajimura, and T. Sekiguchi, Diam. Relat. Mater. **8**, 1272 (1999)
Wild 1994	C. Wild, R. Kohl, N. Herres, W . Müller-Sebert, and P. Koidl, Diam. Relat. Mater., **3**, 373 (1994).
Williams 1996	D.B. Williams, C.B. Carter, Transmission Electron Microscopy, Plenum Press, New York, (1996)
Wojewoda 2008	T. Wojewoda, P. Achatz, L. Ort ega, F. Omne`s, C. Marcenat, E. Bourgeois, X. Blase, F. Jomard, and E. Bustarret, Diamond Relat. Mater. **17**, 1302 (2008)
Wolff 1962	G.A. Wolff and J.G. Gualtieri, Am. Mineral., **47**, 562 (1962)
Xie 2015	Z.Q. Xie, J. Bai, Y.S. Zhou, Y. Gao, K. Park, T. Guillemet, L. Jiang, X.C. Zeng, and Y.F. Lu, Sci. Rep., **28**, 1665 (2015)
Yamada 2007	H. Yamada, A. Chayahara, and Y. Mokuno, J. Appl. Phys., **101**, 063302 (2007)

Yamada 2011	H. Yamada, A. Chayahara, Y. Mokuno, and S. Shikata, Jpn. J. Appl. Phys., **50**, 01AB02 (2011)
Yamada 2012	H. Yamada, Jpn. J. Appl. Phys., **51**, 090105 (2012)
Yan 2002	Ch. Yan, Y.K. Vohra, H. Mao, R.J. Hemley, Proc. Natl. Acad. Sci. **99** (2002) 12523
Yang 2015	Springer International Publishing Switzerland 2015, N. Yang (ed.), Novel Aspects of Diamond, Topics in Applied Physics 121
Yokoya 2005	T. Yokoya, T. Nakamura, T. Matsushita, T. Muro, Y. Takano, M. Nagao, T. Takenouchi, H. Kawarada, and T. Oguchi, Nature, **438**, 647 (2005)
Zaitsev 2001	A. M. Zaitsev, Optical properties of diamond. A data handbook. (Springer-Verlag Berlin Heidelberg 2001)
Zhang 1999	Y. Zhang, H. Ichinose, M. Nakanose, K. Ito, and Y. Ishida, J. Electron Microsc., **48,** 245 (1999)
Zhang 2001	X. F. Zhang and Z. Zhang, in Progress in Transmission Electron Microscopy: Concepts and Techniques, edited by G. Ertl, R. Gomer, H. Lüth, and D. L. Mills (Springer, Berlin, 2001), p. 263.
Zhang 2011	Q. Zhang, V.N. Mochalin, I. Neitzel, I.Y. Knoke, J. Han, C.A. Klug, J.G. Zhou, P.I. Lelkes, and Y. Gogotsi, Biomaterials, **32**, 87 (2011)
Zhou 2007	H. Zhou, J. Watanabe, M. Miyake, A. Ogino, M. Nagatsu, and R. Zhan, Diam. Relat. Mater., **16**, 675 (2007).
Zhu 2011	X.B. Zhu, S. Saito, A. Kemp, K. Kakuyanagi, S. Karimoto, H. Nakano, W.J. Munro, Y. Tokura, M.S. Everitt, K. Nemoto, M. Kasu, N. Mizuochi, and K. Semba, Nature, **478**, 221 (2011)
Zou 2016	Y. Zou and K. Larsson, J. Phy. Chem. C, **120**, 10658 (2016)

LLORET VIEIRA Fernando

✉ fernando.lloret@uca.es

WORK EXPERIENCE

2017	**Teaching Assistant**
2015–2017	**Research assistant**, Universidad de Cádiz, Cadiz (Spain)
2015-2017	**Research visitor**, Institut Néel, Grenoble (France)
2012–2015	**Research assistant**, Foundation for Research and Technology Hellas, Heraklion (Greece)
2011–2012	**Research assistant**, Universidad de Cádiz, Cádiz (Spain)

EDUCATION AND TRAINING

2014–2017	**PhD** Doctor en Ciencias/Doctor en Physique **PhD on co-tutelle in between the Universidad de Cadiz (Spain) and the Université Grenoble-Alpes (France)**.
2011–2012	**MSc** in Science and Technologies of Chemistry, Universidad de Cádiz, Cádiz (Spain)
2004–2011	**Physics Bachelor Degree,** Universidad de Sevilla, Sevilla (Spain)

INTERNATIONAL EXPERIENCE

2015–2017	**Institute Néel-CNRS,** Grenoble, France (12 months)
2012–2015	**FORTH,** Foundation for Research and Technology Hellas, Heraklion, Greece (31 months)

PUBLICATIONS

- F. Lloret, M. Gurtierrez, D. Araujo, D. Eon, and E. Bustarret, “MPCVD diamond lateral growth through microterraces to reduce threading dislocations density”, **Physica Status Solidi A**, 1700242 (2017) [DOI: 10.1002/pssa.201700242].
- F. Lloret, D. Araujo, D. Eon, M.P. Villar, and E. Bustarret, “Transmission electron microscopy study of defects generated during chemical vapor deposition diamond lateral growth.” **European Microscopy Congress 2016: Proceedings.** 364–365.
- F. Lloret, A. Fiori, D. Araujo, D. Eon, M.P. Villar, and E. Bustarret, "Stratigraphy of a diamond epitaxial three-dimensional overgrowth using doping supperlattices", **Applied Physics Letter**, 108, 181901, (2016).
- **Cover** of the May 2016 issue of **Applied Physics Letter** journal.
- F. Lloret, D. Araujo, D. Eon, M.P. Villar, J.M. Gonzalez-Leal, and E. Bustarret, “Influence of methane concentration on MPCVD overgrowth of 100-oriented etched diamond substrates” **Physica Status Solidi A**, 213, 2570, (2016).
- F. Lloret, D. Araujo, M.P. Alegre, J.M. Gonzalez-Leal, M.P. Villar, D. Eon, and E. Bustarret, "TEM study of defects versus growth orientations in heavily boron-doped diamond", **Physica Status Solidi A,** 11, 2468-2473 (2015)

- F.Lloret, D. Araujo, M.P. Villar, L.Liu, and K. Zekentes , “Si NWs conversion to Si-SiC core-shell NWs by MBE”, **Materials Science Forum**, 821-823, 965-969, (2015)
- M.P. Alegre, D. Araujo, A. Fiori, J.C. Piñero, F. Lloret, M.P. Villar, P. Achatz, G. Chicot, E. Bustarret, and F. Jomard, “Critical boron-doping levels for generation of dislocations in synthetic diamond", **Applied Physics Letters**, 105, 173103 (2014)
- F. Lloret, J. Piñero, D. Araujo, M.P. Villar, E. Gheeraert, A. Vo-Ha, V. Soulière, M. Rebaud, D. Carole, and G. Ferro, “Diamond as substrate for 3C-SiC growth: A TEM study", **Physica Status Solidi A**, 211, 2302 (2014)
- F. Lloret, D. Araujo, M.P. Villar, J.G. Rodríguez-Madrid, G.F. Iriarte, O.A. Williams, and F. Calle, “Diamond underlayer microstructure effect on the orientation of AlN piezoelectric layers for high frequency SAW resonators by TEM", **Micreoelectronic Engineering**, 112, 193 (2013).

HONOURS AND AWARDS

Diamond prize to the best PhD student speech on the conference “MRS Spring meeting & Exhibit”, 2016, Phoenix, USA